

DISSERTATION
EXTENDING THE PERFORMANCE OF NET SHAPE MOLDED FIBER
REINFORCED POLYMER COMPOSITE VALVES FOR USE IN INTERNAL
COMBUSTION ENGINES

Submitted by
Richard Theodore Buckley
Department of Mechanical Engineering

In partial fulfillment of the requirements
For the Degree of Doctor of Philosophy
Colorado State University
Fort Collins, Colorado
Summer 2007

UMI Number: 3281638

Copyright 2007 by
Buckley, Richard Theodore

All rights reserved.

INFORMATION TO USERS

The quality of this reproduction is dependent upon the quality of the copy submitted. Broken or indistinct print, colored or poor quality illustrations and photographs, print bleed-through, substandard margins, and improper alignment can adversely affect reproduction.

In the unlikely event that the author did not send a complete manuscript and there are missing pages, these will be noted. Also, if unauthorized copyright material had to be removed, a note will indicate the deletion.

UMI[®]

UMI Microform 3281638

Copyright 2007 by ProQuest Information and Learning Company.

All rights reserved. This microform edition is protected against unauthorized copying under Title 17, United States Code.

ProQuest Information and Learning Company
300 North Zeeb Road
P.O. Box 1346
Ann Arbor, MI 48106-1346

Copyright by Richard T. Buckley 2007

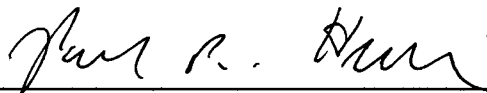
All Rights Reserved

COLORADO STATE UNIVERSITY

June 28, 2007

WE HEREBY RECOMMEND THAT THE DISSERTATION PREPARED UNDER OUR SUPERVISION BY RICHARD T. BUCKLEY ENTITLED "EXTENDING THE PERFORMANCE OF NET SHAPE MOLDED FIBER REINFORCED POLYMER COMPOSITE VALVES FOR USE IN INTERNAL COMBUSTION ENGINES" BE ACCEPTED AS FULFILLING IN PART REQUIREMENTS FOR THE DEGREE OF DOCTOR OF PHILOSOPHY.

Committee on Graduate Work



Dr. Paul Heyliger, Committee Member



Dr. Patrick Fitzhorn, Committee Member



Dr. Rudolf Stanglmaier, Advisor



Dr. Donald Radford, Co-Advisor and Acting Department Head

ABSTRACT OF DISSERTATION

EXTENDING THE PERFORMANCE OF NET SHAPE MOLDED FIBER REINFORCED POLYMER COMPOSITE VALVES FOR USE IN INTERNAL COMBUSTION ENGINES

Fiber Reinforced Composite (FRC) materials offer the possibility of reduced mass and increased structural performance over conventional metals. When used in reciprocating components of internal combustion engines, this may enable increased power and mechanical efficiency. Previously published work on FRC engine valves has both shown structural and thermal limitations.

A net-shape resin transfer molded intake valve has been developed, using a single-piece carbon fiber preform and the high temperature polymer PETI-RFI. Structural design issues have been overcome. Performance has been validated through static testing and dynamic testing. Testing culminated with an intake valve operating for four hundred continuous minutes in an engine without failure.

High engine load conditions resulted in thermal failure of FRC valves. Extensive thermal modeling was conducted to simulate the effect of fiber orientation and coating combinations on transient thermal performance of FRCs. One dimensional modeling has predicted FRC valve surface temperatures to be 120°C higher than that of a steel valve. Simply re-orienting conductive fiber along the heat path may reduce the temperature rise to below that of steel.

Two dimensional transient FRC and coatings thermal analysis has resulted in a novel method of evaluating thermal performance. Using the unitless ratio of thermal resistance at the coating surface and at the interface boundary, designated B_b , an accurate prediction of the interface temperature can be obtained. From this, relative temperature gradients in both the coating and core materials can also be estimated. Analysis shows that for values of $B_b < 1$, interface temperature is high and heat is transmitted to the core. For values of $B_b > 1$, interface temperature is lower, a large temperature gradient exists in the coating, and the core material is more thermally isolated. Testing of coupon samples in the cylinder head of a running engine has verified the trends shown.. Using this methodology a fiber and coating structure is proposed that reduces FRC core temperature by 80%. It has been shown through analysis and experimentation that careful selection of fiber orientation and coating materials can enable a polymer matrix composite material to withstand the structural and thermal environment of an IC engine combustion chamber.

Richard Theodore Buckley

Department of Mechanical Engineering

Colorado State University

Fort Collins, Co 80523

Summer 2007

LIST OF ABBREVIATIONS

Acronyms:

A	Area
Bi	Biot number
Bb	Interface resistance ratio = Bi/St
BMEP	Brake Mean Effective Pressure
BMI	Bismaleimide
BP	Brake Power
CAD	Computer Aided Design
C-C	Carbon carbon
CMC	Ceramic Matrix Composite
CVD	Chemical Vapor Deposition
CVI	Chemical Vapor Infiltration
DAQ	Data Acquisition
DSC	Differential Scanning Calorimetry
F	Force
FD	Finite Difference
FE	Finite Element
FEA	Finite Element Analysis
FMEP	Friction Mean Effective Pressure

Fo	Fourier number, unitless time
FRC	Fiber Reinforced Composite
IC	Internal Combustion
IMEP	Indicated Mean Effective Pressure
IP	Indicated Power
L	Length
LaRC	Langley Research Center
MMC	Metal Matrix Composite
N ₂	Diatomic nitrogen
PETI	Phenyl Ethynyl Terminated Imide
PI	Polyimide
PMC	Polymer Matrix Composite
PR	Published Reduction
RPM	Revolutions per minute
RTM	Resin Transfer Molding
SCRIMP	Seemann Composites Resin Infusion Molding Process
SiC	Silicon Carbide
St	Stanglmaier number
SWNT	Single wall nanotube
T	Temperature
TGA	Thermo Gravimetric Analysis
DTMA	Dynamic Thermal Mechanical Analysis
T _g	Glass transition temperature

V Shear Force
 VARTM Vacuum Assisted Resin Transfer Molding
 WOT Wide Open Throttle

Symbols:

α = thermal diffusivity (m^2/s)
 f = coefficient of friction
 h = convective heat transfer coefficient (W/m^2K)
 k = conductive heat transfer coefficient (W/mK)
 g = rate of heat generation per unit volume (W/m^3)
 m = mass
 n = rotating speed (revolutions/second)
 η_{ti} = indicated thermal efficiency
 η_c = combustion efficiency
 η_m = mechanical efficiency
 η_v = volumetric efficiency
 ρ = density (kg/m^3)
 P = bearing load
 q = heat flux
 Q = heat flux
 R^* = unitless length, percentage of length in the radial direction
 τ = shear stress
 $\bar{\tau}_q$ [s] = phase lag in the heat flux vector
 $\bar{\tau}_g$ [s] = phase lag in the temperature gradient

T_f	=	friction torque
Θ	=	ratio of temperature rise relative to the boundary conditions
μ		fluid viscosity
ω		natural frequency
X^*		unitless length, percentage of length in the axial direction

Other terms:

Core: refers to the primary material the solid is made of

Coating: refers to the thin coating material on the surface of the core

TABLE OF CONTENTS

ABSTRACT OF DISSERTATION	iii
TABLE OF CONTENTS	ix
LIST OF FIGURES	xvii
1 Introduction and Background	1
1.1 Fiber Reinforced Composite (FRC) Materials	1
1.1.1 General classification of FRCs	2
1.1.2 Polymer Matrix Composites	3
1.1.3 Metal Matrix Composites	3
1.1.4 Ceramic Matrix Composites	3
1.1.5 Why Choose Composite Materials?	4
1.1.6 Resin Transfer Molding	8
1.2 Background - Internal Combustion Engines	10
1.2.1 Mechanical Efficiency	12
1.2.1.1 Bearing Friction	14
1.2.1.2 Additive nature of mass reduction to reciprocating mass	15
1.2.2 Valve Dynamics	19
1.2.2.1 Valve Train Friction	23
1.2.2.2 Benefits of Reduced Mass Valve Train Components	24
1.2.3 Traditional Metal Poppet Valves	29

1.2.3.1	History of Poppet Valve Manufacture	30
1.2.3.2	Modern Metal Valve Manufacture	32
1.3	History of FRC Research in Internal Combustion Engines	34
1.3.1	Previous FRC Poppet Valves.....	41
1.3.1.1	Polimotor Research, Inc.	43
1.3.1.2	Langley Research Center (LaRC)	44
1.4	Thermal Analysis of Composite Materials	45
1.4.1	Thermal Modeling of Composite Materials.....	47
1.4.2	Material Developments for Thermal Management	48
1.4.3	Applications.....	51
1.4.4	Coatings for Composites.....	53
1.5	Hypothesis.....	54
2	Modeling and Analysis.....	56
2.1	Introduction.....	56
2.2	Prediction of Mass Reduction	57
2.2.1	Potential Mass Reduction by direct substitution	58
2.2.1.1	Methodology for determining weight savings:.....	58
2.2.2	Quantifying Mass reduction using the “additive effect”	61
2.2.2.1	Assumptions:	61
2.2.2.2	Methodology	62
2.2.3	Prediction results.....	64
2.2.3.1	Results of mass reduction by direct substitution.....	64
2.2.3.2	Results of “Additive Effects” Mass reduction	66

2.2.4	Inertial and frictional power losses	66
2.2.5	Reciprocating power losses	67
2.2.5.1	Frictional Power Losses.....	67
2.2.6	Limits to engine performance.....	70
2.2.7	Other possibilities not quantified	70
2.3	Structural Design of an FRC Intake Valve	71
2.3.1	Valve Requirements.....	72
2.3.1.1	Design Process	73
2.3.1.2	Valve Requirements: Loads.....	73
2.3.1.3	Valve Requirements: Temperature	77
2.3.1.4	Fatigue strength.....	79
2.3.1.5	Chemical environment.....	80
2.3.1.6	Manufacturability	80
2.3.1.7	Validation of FEA for metal valve.....	80
2.3.2	Material Selection and Fiber Placement.....	83
2.3.2.1	Fiber selection	83
2.3.2.2	Matrix Selection	85
2.3.2.3	Fiber Placement Analysis Using FEA	88
2.3.2.4	Fatigue Strength	95
2.4	Thermal Modeling.....	95
2.4.1	Initial Transient Thermal Analysis	96
2.4.2	Initial Transient Thermal Analysis Results	98
2.5	Detailed Analysis of FRCs and Coatings.....	100

2.5.1	Purpose of this Study	100
2.5.1.1	Choosing the Model.....	100
2.5.1.2	Modeling Material Properties	104
2.5.2	Analysis.....	105
2.5.2.1	Model Setup	105
2.5.2.2	Steady State Analysis.....	109
2.5.2.3	Transient Analysis	112
2.5.3	Results and Discussion.....	113
2.5.3.1	Results - Axial Heat Path.....	113
2.5.3.2	Results - Radial Heat Path	126
2.5.4	Example – In the Combustion Chamber	138
2.6	Discussion of Modeling Results.....	142
3	Process Development.....	145
3.1	Resin Transfer Molding (RTM)	145
3.2	RTM Process Development.....	148
3.2.1	Fiber holding strategies.....	148
3.2.1.1	Injection and Fiber Placement Experiments	149
3.2.1.2	Injection and Fiber Placement Results	151
3.2.2	Mold Design	154
3.2.2.1	Mold requirements.....	154
3.2.2.2	Prototype Mold Design	155
3.2.2.3	Intermediate Mold Design.....	157
3.2.2.4	Final Mold Design.....	160

3.2.3	Other Process Developments	160
3.2.4	Final Manufacturing Process.....	163
3.3	Processing of PETI-RFI.....	165
3.3.1	Background.....	167
3.3.1.1	Background - High Temperature Composites.....	168
3.3.1.2	Background - PETI-RFI	169
3.3.2	Material Properties and Processing	170
3.3.3	Objective of Research.....	172
3.3.4	Experimentation	172
3.3.4.1	Material Characterization.....	172
3.3.4.2	Dynamic Thermal Mechanical Analysis (DTMA).....	173
3.3.4.3	Differential Scanning Calorimetry (DSC)	176
3.3.4.4	Thermo Gravimetric Analysis.....	178
3.3.4.5	Vacuum/Pressure Chamber Cure Cycle Experiments..	178
3.3.4.6	Hot Press Experiments	180
3.3.4.7	Optical Microscopy	181
3.3.5	Results and Discussion.....	181
3.3.5.1	Dynamic Thermal Mechanical Analysis (DTMA).....	181
3.3.5.2	Differential Scanning Calorimetry (DSC)	183
3.3.5.3	Thermo gravimetric Analysis	189
3.3.5.4	Vacuum/Pressure Chamber Cure Cycle Experiments..	190
3.3.5.5	Hot Press Experiments	193
3.3.5.6	Optical Microscopy	193

3.3.5.7	Processing Parameters	197
3.4	Discussion of Process Development Results	199
4	Experimentation and Testing	204
4.1	Introduction.....	204
4.2	Static testing	205
4.2.1.1	Initial Static Testing Results.....	205
4.2.1.2	Follow-on Static Testing	206
4.3	Motored Dynamic Testing.....	209
4.4	Fired Engine Testing	210
4.5	Failure Analysis	213
4.6	Temperature Measurement of Valves in an Operating Engine	215
4.6.1	Introduction and Background	215
4.6.1.1	Valve Temperature Measurement Techniques.....	215
4.6.2	Experimental Setup and Procedure	218
4.6.2.1	Objective.....	218
4.6.2.2	Instrumentation of Steel Valves	219
4.6.2.3	Instrumentation of the Engine.....	221
4.6.2.4	Data Acquisition.....	223
4.6.3	Results and Discussion.....	229
4.6.3.1	Steady State - Intake Valve Temperatures	230
4.6.3.2	Steady State - Exhaust Valve Temperatures.....	231
4.6.3.3	Steady State- Engine Temperatures	233
4.6.3.4	High Sampling Rate - Intake Valve Temperatures.....	234

4.6.3.5	High Sampling Rate - Exhaust Valve Temperatures	235
4.7	In-Engine Composite Coating Experiments	238
4.7.1	Introduction and Purpose	238
4.7.2	Test Setup.....	238
4.7.2.1	Test Matrix.....	240
4.7.2.2	Sample preparation	242
4.7.2.3	Cylinder head preparation	243
4.7.2.4	Test Preparation	244
4.7.2.5	Data Acquisition and Instrumentation	245
4.7.3	Results and Discussion.....	245
4.7.3.1	Effect of fiber orientation on temperature distribution ...	247
4.7.3.2	Effect of Bb on Interface temperature.....	249
4.7.3.3	Other observations	253
4.8	Discussion of Experimentation and Testing Results.....	253
5	Dissertation Discussion	256
5.1	Literature Review.....	256
5.2	Modeling and Analysis.....	257
5.3	Process Development	260
5.4	Experimentation and Testing	263
5.5	Recommendations for Future Work.....	265
6	Conclusions	268
	References	275
	Appendices.....	285

Appendix 1: references for Figure 16, Figure 17, Figure 18, and Table 5.....	285
Appendix 2: tabulated mass reduction by material substitution	289
Appendix 3: Stress Plots for FRC valve structural design.....	290
Appendix 4: Complete Thermal Analysis Plans	296
Appendix 5: Normalized data for axial heat path cases	312
Appendix 6: Normalized data for radial heat path cases.....	322

LIST OF FIGURES

Figure 1. Specific modulus of metals and composite materials.	5
Figure 2. Schematic of resin transfer molding apparatus.	9
Figure 3. Power losses in a typical engine, adapted from Mistry.	13
Figure 4. Generic Stribeck curve, adapted from Juvinall and Marshek.	15
Figure 5. Piston velocity vs.. crank angle degrees (CAD).	16
Figure 6. Piston acceleration vs. crank angle degrees (CAD)	17
Figure 7. Piston inertial force vs. engine speed for varying piston mass.	18
Figure 8. Connecting rod load vs. RPM for varying connecting rod mass.	19
Figure 9. Additive effects of reducing component mass	20
Figure 10. Camshaft Torque vs.. camshaft angle, from Mufti.	24
Figure 11. Effects of reduced valve mass on engine performance.	25
Figure 12. Advantages of lightweight valves, adapted from Tominaga.	26
Figure 13. Maximum engine RPM for varying valve mass and spring stiffness, adapted from Miwa.	28
Figure 14. Camshaft torque vs.. position for varying spring stiffness.	29
Figure 15. Polimotor Lola II at Road America 500, August 1984 ⁵³	36
Figure 16. Timeline of Metal Matrix composite research.	39
Figure 17. Timeline of Carbon-Carbon composite research.	40
Figure 18. Timeline of polymer matrix composite research.	40
Figure 19. Relative mass for valves made of high-performance materials compared to steel.	42
Figure 20. The Polimotor 3-piece composite intake valves.	44

Figure 22. Thermal conductivities of metals and fibers, adapted from Bertram. .	48
Figure 23. Specific power vs. percent mass reduction.	69
Figure 24. Valve position and acceleration plots versus crankshaft angle for engine #1, 7200 rpm (redline).....	74
Figure 25. Free body diagram of the valve.	75
Figure 26. Plot of valve displacement and valve seat force vs.. camshaft angle illustrating valve bounce.	76
Figure 27. Temperature and heat flow for a metal exhaust valve in a gasoline engine.....	78
Figure 28. Valve static tensile test apparatus.	81
Figure 29. Schematic of the valve static tensile test setup.	82
Figure 30. Peak failure index for all plies in the valve, model 1.	91
Figure 31. Failure Index for each ply, model 1.....	91
Figure 32. Stress in Fiber Direction (σ_{xx}) for each ply,.....	92
Figure 33. In-plane transverse shear stress (σ_{xy}) for all plies, model 1.....	93
Figure 34. In-plane transverse normal stress (σ_{yy}) for all plies, model 1.....	93
Figure 35. Plane wall with convective heat transfer, adapted from Incropera & DeWitt.....	96
Figure 36. Calculated temperature distribution across the valve face for three different materials.	99
Figure 37, Thin and Thick model geometry and surface definitions.....	106
Figure 38. Axial and radial heat paths.	106
Figure 39. Steady state thermal circuit for uncoated, axial cases.....	110

Figure 40. Steady state thermal circuit for coated, axial cases.....	111
Figure 41. Orthotropic vs. Isotropic material response for axial heat path.....	114
Figure 42. Normalized temperature distribution for uncoated, isotropic materials under steady state conditions.	115
Figure 43. Normalized temperature distribution for coated, isotropic materials under steady state conditions.	116
Figure 44. Steady state interface temperature for varying B_b and thickness ratio.	117
Figure 45. Transient Temperature Distribution for uncoated, isotropic materials.	119
Figure 46. Transient Temperature Distribution for uncoated, isotropic materials.	119
Figure 47. Transient temperature distribution for coated, isotropic solid.	122
Figure 48. Temperature profile for $B_b < 1$ showing uniform coating temperature.	123
Figure 49. For $B_b = 1$, coating and core temperature rise together.	123
Figure 50. For $B_b > 1$, Surface temperature rises quickly, core temperature stays low and a large temperature gradient exists in the coating.....	124
Figure 51. Peak Interface temperature vs. B_b for varying time.....	125
Figure 52. Axisymmetric model layout.....	127
Figure 53. Thick and thin 3-D plot layout.....	127
Figure 54. Example 2-D temperature profile plot.....	128
Figure 55. 2-D temperature distribution for a thin isotropic solid.....	129

Figure 56. 2-D temperature distribution for a thick isotropic solid.	130
Figure 57. Coated isotropic materials, radial heat path.	131
Figure 58. Orthotropic uncoated materials, radial heat path.	132
Figure 59. Thick Orthotropic composite with insulating coating, $B_b > 1$	134
Figure 60. Thick orthotropic composite with conductive coating, $B_b < 1$	135
Figure 61. Peak core temperature vs.. F_o for uncoated, insulated and conducting coatings.	136
Figure 62. Peak core temperature vs. F_o for uncoated, insulated and conductive coating.	137
Figure 63. Schematic of resin transfer molding apparatus.	147
Figure 64. Injection molder in load frame.	150
Figure 65. Fiber placement trial #8.	152
Figure 66. Polystyrene valve with a carbon fiber preform pushed to the side...	153
Figure 67. Fiber clamping rings in place on the fiber preform.	154
Figure 68. Wire frame model of the initial one-piece mold design.	156
Figure 69. Photo of prototype mold showing gate and runner orientation.	157
Figure 70. Exploded view of the intermediate, modular mold design.	159
Figure 71. Intermediate modular mold design shown with flat end plates used for valve curing.	159
Figure 72. Final modular mold design.	161
Figure 73. Schematic of the FRC valve manufacture process.	164
Figure 74. As-molded carbon-fiber PETI-RFI valves.	165

Figure 75. Photo of the stem of a carbon-fiber/PETI-RFI valve showing surface porosity	166
Figure 76. Surface porosity on the face of a carbon-fiber/PETI-RFI valve.....	167
Figure 77. Pin-in-cup sample mounted in the TMA SS120C.	174
Figure 78. The Seiko Instruments TMA SS120C.....	175
Figure 79. Schematic of the vacuum/pressure vessel test setup.....	179
Figure 80. Photo of the vacuum/pressure chamber.....	180
Figure 81. Relative viscosity of several thermoplastics.	182
Figure 82. Viscosity versus Temperature for PETI-RFI showing minimum viscosity range.....	182
Figure 83. PETI-RFI DSC plot in uW/mg versus time for varying ramp rates. ...	184
Figure 84. DSC plot in uW/mg versus temperature for varying ramp rates.	184
Figure 85. DSC data for PETI-RFI with varying peak temperature. Ramp rate = 3°C/min.....	186
Figure 86. DSC versus time for varying peak temperature.....	186
Figure 87. Glass Transition Temperature (T_g) of PETI-RFI versus peak cure temperature.	188
Figure 88. DSC vs. temperature for neat PETI-RFI, with mold release and with carbon fiber. Constant ramp rate of 10°C/min.....	188
Figure 89. Thermogravimetric data for PETI-RFI.....	190
Figure 90. 1000x image of cured neat PETI-RFI polymer. The lines are polishing marks.....	194
Figure 91. 1000x magnification image of PETI-RFI with carbon fiber.....	196

Figure 92. 50x magnification image of un-reinforced PETI-RFI. Large black spots are voids. This sample was cured without degassing.....	196
Figure 93. Carbon Fiber reinforced PETI-RFI valve cured in the stainless steel mold, free of voids.	203
Figure 94. Valve P-14 proof-load, load and displacement vs.. time.....	206
Figure 95. Valve P-15 proof-load, load vs.. crosshead displacement.	206
Figure 96. Valve P-12, load and displacement vs. time.....	207
Figure 97. Valve P-12 crosshead and extensometer displacement vs.. time. ..	208
Figure 98. Motored Test Rig.	209
Figure 99. Dynamic Motored Test Profile.	210
Figure 100. Small engine dynamometer used for fired engine testing.....	211
Figure 101. Valve P-14 after running engine test. Note the small hole burned from the face and exposed fiber.	213
Figure 102. Valve P-14 immediately after the fired engine test. Note the location of the hole in the intake valve (bottom).....	214
Figure 103. Fluctuations in intake and exhaust valve temperatures in a running diesel engine published in 1945.	216
Figure 104. Exhaust valve temperature contours and heat paths.....	217
Figure 105. Exhaust and intake valve thermocouple locations.	220
Figure 106. Instrumented intake valve mounted in the engine.	220
Figure 107. Instrumented intake and exhaust valves mounted in the engine. ...	221
Figure 108. Engine block thermocouple locations.	222
Figure 109. Cylinder head thermocouple locations.....	223

Figure 110. Screen shot of the LabView VI used for steady state valve temperature measurements.....	224
Figure 111. Briggs raptor published torque curve (reference).	225
Figure 112. Briggs Raptor torque curve adjusted for altitude.	225
Figure 113. Briggs Raptor test points.	226
Figure 114. High-sampling rate VI.	227
Figure 115. Measured torque and HP curves for the Briggs Raptor engine.	229
Figure 116. Intake valve temperature profiles, part throttle.	230
Figure 117. Intake valve temperature profiles, full throttle.	231
Figure 118. Exhaust Valve temperature profiles, part throttle.....	232
Figure 119. Exhaust valve temperature profiles, full throttle.....	233
Figure 120. Cylinder head temperatures.	234
Figure 121. Valve seat temperatures vs.. RPM.	234
Figure 122. Intake valve temperature versus time, sampled at 125kHz.	236
Figure 123. Exhaust Valve temperature versus time, 125kHz sampling rate, unsynchronized data	236
Figure 124. Schematic of coupon test setup.	239
Figure 125. Photograph of a coated coupon test sample.	239
Figure 127. Modified cylinder head showing sample mounting locations.	244
Figure 128. Raw data, temperature vs.. time for alumina silicate coated samples.	246
Figure 129. Effect of fiber orientation on temperature drop across the samples for uncoated samples.	247

Figure 130. Effect of fiber orientation on temperature drop across the sample for stainless steel coated samples.	248
Figure 131. Effect of fiber orientation on temperature drop across the sample for alumina silicate coated samples.	248
Figure 132. Interface versus Bb at peak EGT.....	250
Figure 133. Steady state Interface temperature vs. Bb.	251
Figure 134. Bb vs.. interface temperature for analysis results and experimental test results.	251
Figure 135. Interface temperature vs.. Bb, scaled analysis results and experimental data.	252

LIST OF TABLES

Table 1. Properties of selected metals and composites (Matweb).....	6
Table 2. Engine Efficiencies and typical values.....	11
Table 3. Percent contribution of engine systems to FMEP.....	13
Table 4. 1973 cost per pound of valve material based on temperature range, adapted from Danis.....	33
Table 5. Summary of published mass reductions by component and material...	41
Table 6. Maximum service temperature of common fiber and matrix materials..	46
Table 7. Thermal properties of different grades of carbon fibers.....	49
Table 8. Lycoming 540 series baseline engine data.....	59
Table 9. Density ratios for metals to FRC substitution.....	60
Table 10. Summary of weight reduction using direct substitution.....	65
Table 11. Predicted Reduction of reciprocating mass	66
Table 12. Increased efficiency attainable as a result of reduced reciprocating mass.....	69
Table 13. Summary of valve Load scenarios.....	77
Table 14. Fiber selection results.....	84
Table 15. Material selection for the intake and exhaust valves.....	88
Table 16. Fiber model progression, configuration and failure mode(s).....	90
Table 17. Values used for transient heat transfer analysis.....	98
Table 18. Material properties used for transient thermal analysis.....	98
Table 19. Boundary conditions for the model.....	107
Table 20. Thermal properties of common engineering materials.....	108

Table 21. Material properties for isotropic materials.	108
Table 22. Material properties for orthotropic materials.	108
Table 23. Coated isotropic materials.	109
Table 24. Coated orthotropic material properties.....	109
Table 25. Transient analysis time steps.	113
Table 26. Intake valve operating conditions.	139
Table 27. Material properties for the uncoated FRC intake valve.	140
Table 28. FRC valve design changes for thermal management.....	142
Table 29. Fiber holding strategies ranked	148
Table 30. Injection mold fiber placement test conditions.	150
Table 31. Average void content and fiber content for different processing methods of PETI-RFI.....	195
Table 32. Motored engine test results.	210
Table 33. Fired engine test results.	212
Table 34. Briggs test points. All values are in lb-ft torque.....	226
Table 35. Data acquisition parameters, single thermocouple high sampling rate, based on 5500 RPM engine speed.	228
Table 36. Data acquisition parameters for four-thermocouple high sampling rate, based on 5500 RPM engine speed.	228
Table 37. Minimum, maximum and average exhaust valve temperatures. 5250 RPM, WOT full load.....	237
Table 38. Test matrix for in cylinder fiber orientation, matrix and coating evaluation.	241

Table 39. Material properties used for in-engine coating analysis. 246

ACKNOWLEDGEMENTS

I would like to sincerely thank Dr. Rudy Stanglmaier and Dr. Don Radford for their constant guidance, enthusiasm and insight in all areas of this project.

I would also like to thank; the Air Force Institute of Technology for making the civilian institutions program possible, LtCol Keith Bearden for the support and perseverance to getting me into the AFIT/CI program, Firewall Forward, Inc. and Mr. Matthew Fitzhorn for access to their aircraft engines, and Betty Tung from Imitec, Inc. for providing PETI-RFI. Thank you to Jason Miwa for help with the valve mold manufacture and excellent machining skills, Jake Nelson for assistance with TMA and DSC experiments, Blake Teipel for his assistance in running parts of the Fluent analysis. Thank you to Darin Cate and Andy Grabher for assistance in running the in-engine coating and valve temperature tests.

Most of all I'd like to thank my wife, April and my daughters, Maggie and Ivy for their patience and understanding and for their support on late nights and weekends when I was doing homework and research.

1 Introduction and Background

Engineering fiber reinforced composite (FRC) materials offer, when properly designed, the opportunity to reduce component mass and in many cases, increase material strength and stiffness. State of the art for FRC materials has steadily advanced over the past 50 years to the point that FRC applications are no longer exotic, and can be found in everyday items from cell phones to personal transportation. However, many applications still challenge engineers, including the use of composites at elevated temperatures and in harsh environments.

Internal combustion engine performance and efficiency can be significantly improved by reducing the mass of reciprocating components. Despite the apparent benefits, FRC materials have found only very limited use in internal combustion engines. The severe environmental requirements inside the engine, and in particular the combustion chamber of a running engine are part of this challenge. Advances in thermal management of FRC materials may open the door to operation in the challenging thermal oxidative environment of the combustion chamber

1.1 Fiber Reinforced Composite (FRC) Materials

In general, reinforced composite materials refer to any two or more materials combined together. Engineered composite materials typically result in

the composite system having superior performance, in some required area, than the individual constituent materials. Fiber reinforced composite materials refer to the subset of engineering composite materials which use some type of fibrous reinforcement in a non-fibrous matrix material or binder. Alternative reinforcements exist in the form of particle reinforced composites (PRCs). Engineered FRC materials inhabit a broad spectrum and may be as diverse as straw reinforced mud bricks used for housing, re-bar reinforced concrete used for heavy construction, glass fiber reinforced nylon used in boat hulls, or carbon fiber reinforced graphite used in high performance aircraft and spacecraft. For the application to engine components and specifically engine valves, the FRCs discussed are typically on the more exotic end of the spectrum and fall into the category of Advanced Composite Materials. Fibers discussed are high strength, light weight engineered fibers such as carbon. Matrix materials are also highly engineered, typically polymers.

1.1.1 General classification of FRCs

For the purpose of this discussion, fiber reinforced composites are divided into three very broad categories; polymer-matrix composites, metal-matrix composites and ceramic-matrix composites. In addition, each of these categories can contain long (continuous) fibers or short (less than 1 cm) fibers. Fiber length is typically a good indicator of manufacturing process, with short fiber composite manufacturing dominated by the formation of the matrix (injection molding or casting), and long fiber composite manufacturing dominated by fiber placement (filament winding or pre-preg layup).

1.1.2 Polymer Matrix Composites

Polymer-matrix composites (PMCs) typically use glass, carbon and/or aramid fibers embedded in a thermoset or thermoplastic matrix. Perhaps the most common PMCs seen in internal combustion engine research applications are carbon-fiber/epoxy combinations. PMCs are characterized by extremely high strength and stiffness combined with low densities. They can also be designed to have a “graceful,” rather than catastrophic failure. Historically, PMCs were temperature limited to about 300°C, however, new resins are pushing this limit to higher temperatures¹. PMCs using continuous fiber seem to be the material of choice for composite connecting rods².

1.1.3 Metal Matrix Composites

Metal-Matrix composites (MMCs) most commonly use short or continuous ceramic fibers in a metal matrix. The most frequently seen combination is crystalline alumina and/or silicon carbide fibers embedded in an aluminum matrix to increase stiffness and improve high temperature creep resistance of the metal. MMCs are typically performance limited by the operating temperature of the metal matrix. MMCs have been used extensively in piston crowns for diesel engines and have found some high performance racing applications. Both continuous fiber preforms and short-fiber reinforcement have been used^{3,4}.

1.1.4 Ceramic Matrix Composites

Ceramic-matrix composites are typically a ceramic fiber embedded in a ceramic matrix. This aids in slowing crack growth and improving the toughness

of the ceramic matrix. Common combinations are silicon carbide or alumina fibers in a silicon carbide matrix. The most common high temperature composite seen in engines research is carbon-carbon. Carbon-carbon (C-C) is a carbon fiber embedded in a relatively isotropic graphitic carbon matrix. C-C composites are characterized by extremely high strengths, low density (1.8 g/cc) and extremely high temperature operation (2000° C - 3000°C). Unfortunately, the temperature capability is much more limited in an oxidizing environment. Both continuous and chopped fiber carbon-carbon pistons have been fabricated^{5,6}.

1.1.5 Why Choose Composite Materials?

Fiber reinforced composites (FRCs) are attractive to the design engineer for a number of reasons. FRC materials have the unique ability to provide a specific strength (strength per unit density) and specific stiffness (modulus per unit density) significantly higher than those of conventional materials. Figure 1 is a graphical comparison of specific strength of some composite materials and conventional metals. In addition, the anisotropic nature of FRC behavior allows the designer to tailor these properties so that there is a high strength or stiffness where it is needed along a component load path and lower strength or stiffness where it is not needed. It is also possible to take advantage of this same anisotropy to tailor thermal properties of a FRC. These and other properties of FRCs offer a flexibility in design which has traditionally been used to reduce mass, to reduce part count, and to provide performance not possible with traditional metal design.

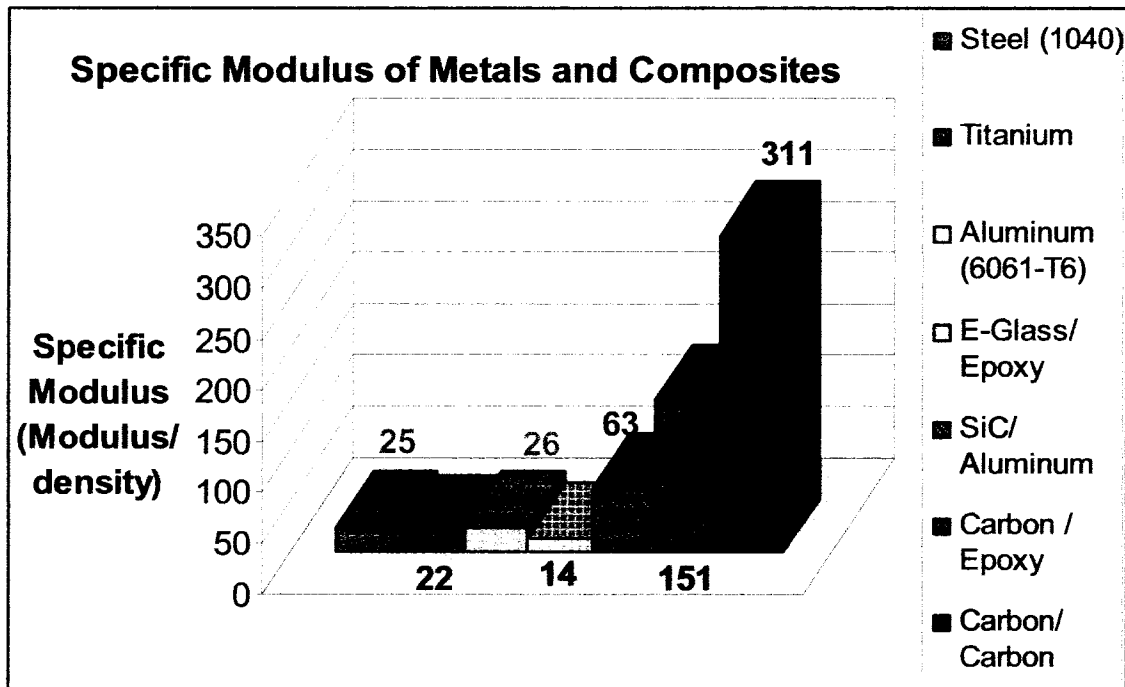


Figure 1. Specific modulus of metals and composite materials⁷.

FRCs have demonstrated the properties needed for operation in harsh environments such as those found in the internal combustion engine. Single cycle and fatigue strengths are far superior to metals. A comparison of relative strength and moduli of FRC materials and metals is shown in Table 1. It should be noted that FRC material properties listed in Table 1 are in the fiber direction and that properties will be reduced if loaded in a different direction. Chemical resistance can be comparable or superior to that of metals⁸. It has been shown that composites are significantly better than metals in damping⁹ and that FRC materials can be used as bearing materials¹⁰ FRC materials also enable reduced friction on bearing surfaces^{11,12}.

Table 1. Properties of selected metals and composites (Matweb)

	MODULUS (GPA)	FAILURE STRENGTH (MPA)	DENSITY (G/CC)	SPECIFIC MODULUS	SPECIFIC STRENGTH
Steel (1040)	200	415	7.9	25	53
Aluminum (6061-T6)	69	255	2.7	26	94
Titanium	116	140	4.5	26	31
E-Glass /epoxy*	30	550	2.1	14	264
SiC / Al **	203	1560	3.2	63	488
Carbon /Carbon***	590	1600	1.9	311	842
	Composite Properties are in the fiber direction. Properties in other directions will be different.				
	*Owens Corning Glass Fiber reinforced Epoxy (Filament Wound) 80 wt %				
	**3M Nextel TM 720 Composite Ceramic Fiber with 6061-T6 matrix				
	*** 70% P-120 with pyrolitic graphite matrix				

FRC materials are rarely used in modern internal combustion engines. The few exceptions are lightly reinforced metal matrix components and some ancillary parts and covers. The most probable reason for this is the historically high cost of composite fabrication. While this is a significant challenge to the use of FRCs, it will not be addressed.

A number of more exotic composites also offer superior high temperature performance compared to metals. For this reason, FRCs have been embraced in the space industry. Composites like carbon-carbon are the norm for rocket nozzles, radiators and structural applications in rockets and satellites¹³.

The benefits of using FRCs for weight reduction are well documented. Mass reduction of over 50% over a traditional steel or aluminum part is the norm.

Engineers have long recognized the potential benefit for using FRCs in internal combustion engines. Reduced reciprocating mass enables lower inertial loads. This results in lower stresses on all components and a reduction in cross-section of components. Reduced reciprocating mass also enables higher operating speeds which typically lead to higher power output, with reduced weight¹⁴. A more detailed discussion of the effects of reducing reciprocating mass is presented in chapter 2.

In addition, the use of FRCs for engine components enables improvements in several other areas of vehicle performance. Several items of significant importance are:

- Reduced manufacturing and lifecycle cost, including recycling
- Increased fuel economy. A common rule of thumb is that a 50kg vehicle weight reduction yields 0.3mpg increase for small cars, 0.15mpg for a mid size car¹⁵.
- Increased power output/ higher power density.
- Noise and comfort. A 60% reduction in reciprocating mass yields a 6dBa reduction in passenger compartment noise¹⁶.

- Increased service life.
- Reduced emissions during processing/manufacture.

The automotive industry has seen a consistent growth in the size, expected performance and luxury of passenger vehicles. At the same time Corporate Average Fuel Economy (CAFÉ) standards have increased. As a result, there has been an increase in the use of alternate materials and reducing mass components. FRCs offer an attractive alternative and the opportunity to continue “lightweighting” into the engine itself.

1.1.6 Resin Transfer Molding

Resin Transfer Molding is a process for manufacture of FRC components where a preform of fiber (dry or partially wetted) is placed in a mold and liquid resin is pumped into the mold under pressure. The resin is allowed to cure in the mold to form a solid composite¹⁷. In practice, RTM is similar to injection molding. Variations on the process depend on the particular part being molded. Some variations use an open mold and a vacuum bagged part (SCRIMP) or vacuum assisted resin transfer (VARTM) in a mold, Advantages of RTM include:

- Ability to mold complex shapes
- High level of automation possible enabling high volume production
- Ease of fiber lay-up (using preforms)
- Reduced process time
- High fiber volume-fractions are possible
- Reduced emissions¹⁷

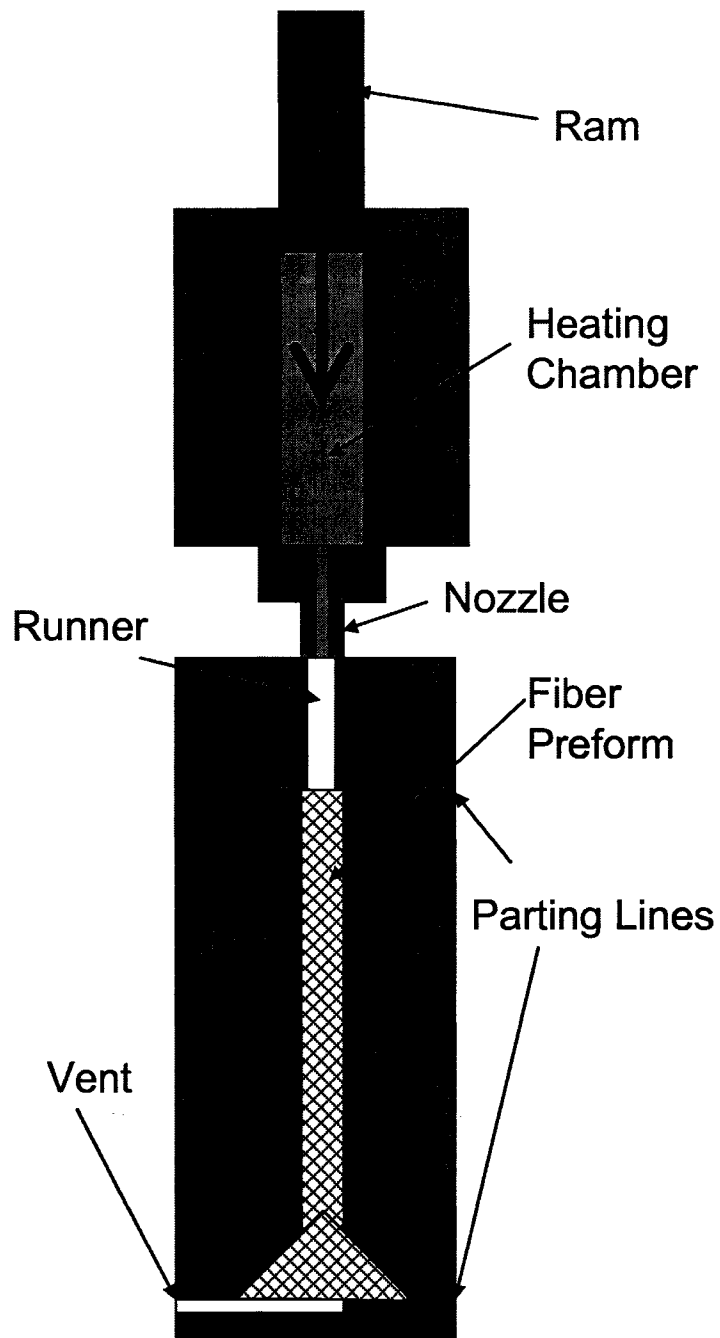


Figure 2. Schematic of resin transfer molding apparatus.

Some of the apparent advantages over traditional valve manufacturing techniques (discussed later in this chapter) are:

- Molded parts are near-net shape directly out of the mold, reducing the need for additional finish machining.

- Surface finish of a molded part is excellent, again reducing additional finish machining.
- The process is well suited to mass-production and production can be highly automated.

A more detailed description of the method used for this study is described in chapter 3.

1.2 Background - Internal Combustion Engines

The performance of internal combustion engines can be summarized using the following equation for Brake Power (BP)¹⁸:

$$BP = \eta_{ii} \cdot \eta_c \cdot \eta_m \cdot \eta_v \cdot \rho_{air} \cdot D \cdot \left(\frac{N}{2}\right) \cdot \left(\frac{F}{A}\right) \cdot LHV_F \quad \text{Equation 1}$$

Where:

ρ_{air} = density of air

D = displacement of the engine

N = engine speed

F/A = fuel/air ratio

LHV_F = lower heating value of the fuel

and the efficiencies listed in Table 2.

Any improvement in the power output of an engine must therefore be encompassed by one of the terms above. Modern engines benefit from over one hundred years of research into all of these areas, yet still have what may appear to be relatively low overall efficiencies. As an example: “the most powerful and most efficient prime-mover in the world today”¹⁹ has a thermal efficiency of 50%. Typical automotive engines have thermal efficiencies in the range of 30%¹⁹. In

the engines industry, gains in overall efficiency of 1% are huge. Large amounts of energy are expended to make small efficiency gains. For example, in 1991, Toyota redesigned the cooling system in their 4A-GE engine and added piston-cooling oil jets in order to increase compression ratio (affecting thermal efficiency) from 10.3:1 to 10.5:1. This resulted in a BSFC improvement of 1%²⁰. Toyota also developed a resin coating for a piston skirt that improves fuel efficiency 0.5%²¹.

Table 2. Engine Efficiencies and typical values.

EFFICIENCY	NAME	EXPLANATION	TYPICAL VALUE
η_{ti}	Indicated thermal efficiency	From the thermal indicator (P-V) diagram: W_{out}/Q_{in}	0.3
η_c	Combustion Efficiency	the ratio of chemical energy in the fuel to heat energy released by the combustion process	0.7
η_m	Mechanical Efficiency	the ratio of work produced at the piston to work available at the engine output shaft	0.8
η_v	Volumetric Efficiency	The ratio of air volume brought into the engine to the theoretical max air volume for an adiabatic, reversible engine. Volumetric efficiencies can be greater than 1.	0.9

Entire fields of research are devoted to the improvement of each of the efficiencies listed above. Implementing FRC engine components would likely

have little or no effect in increasing thermal, combustion, or volumetric efficiencies of an engine. However the possibility reducing mass and increasing stiffness and strength of using FRCs components has the potential for significant improvements in the mechanical efficiency of the engine. In order to gain a better understanding of this,

1.2.1 Mechanical Efficiency

Mechanical Efficiency is defined as the ratio of power (or work) produced at the piston to power (or work) available at the engine output (typically the crankshaft).

$$\eta_m = \frac{IP}{BP} = \frac{IMEP}{BMEP} \quad \text{Equation 2}$$

where:

IP = indicated power (power produced at the piston)

BP = brake power (power available at the crankshaft output)

IMEP = indicated mean effective pressure

BMEP = brake mean effective pressure

The primary sources of reductions in mechanical efficiency are:

- friction losses (sliding friction)
- inertial losses

A common way of quantifying friction losses is through the use of friction mean effective pressure (FMEP).

$$FMEP = IMEP - BMEP \quad \text{Equation 3}$$

In an engine friction forces are generally the result of sliding contact between lubricated bearing surfaces. Extensive work has been done to quantify the contribution to FMEP of different engine components or groups of components. Figure 3 shows the percent of total engine power consumed by different engine subsystems. From the figure above, we can calculate the percentage contribution to total FMEP from each system. These results are shown in Table 3.

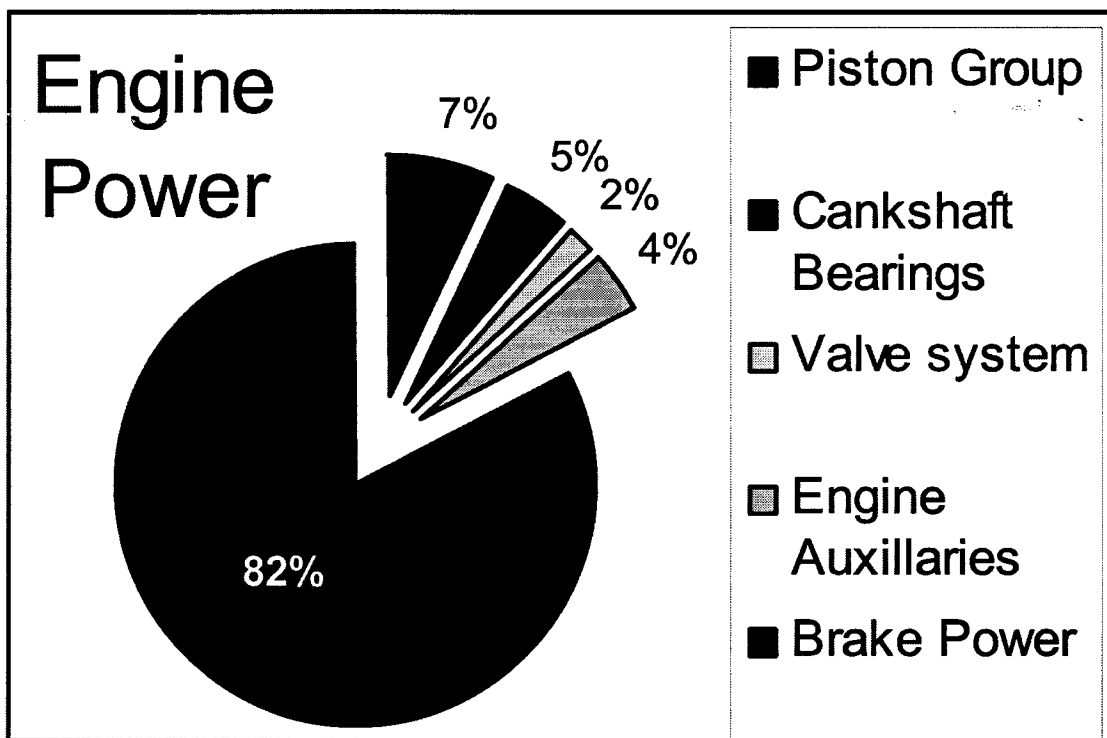


Figure 3. Power losses in a typical engine, adapted from Mistry²².

Table 3. Percent contribution of engine systems to FMEP.

SYSTEM	% OF FMEP
Piston Group	17 – 19
Crankshaft bearings	35 – 45
Valve System	20 – 30
Engine Auxillaries	7 – 10

Each of these contributions is a function of many variables such as mass, engine speed, geometry and engine design and the values given above should be taken as estimates. Other authors estimate piston friction at 30% of total FMEP²³ (Xu, 2004).

1.2.1.1 Bearing Friction

Nearly all sliding surfaces in the reciprocating are lubricated. Typical friction between sliding, lubricated surfaces is described by the Stribeck curve shown in Figure 4. The vertical axis is the coefficient of friction, the horizontal axis is a dimensionless load factor²⁴, where:

μ = viscosity of the fluid

n = rotating speed (revolutions per second)

P = Bearing unit load (bearing load divided by projected bearing area)

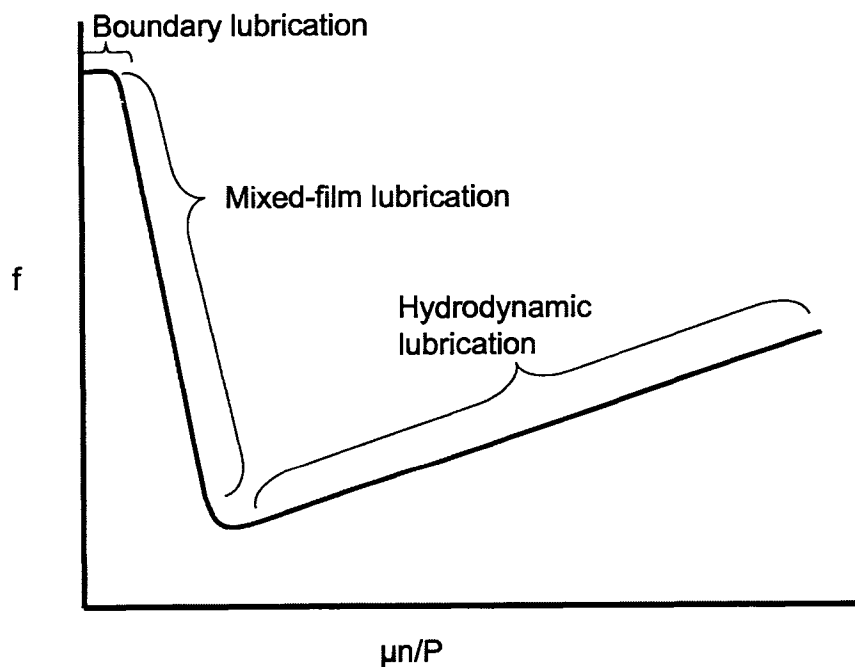


Figure 4. Generic Stribeck curve, adapted from Juvinall and Marshek²⁴.

The overall objective of bearing design is to, whenever possible, design the operating condition of the component to be at or near the “knee” of the Stribeck curve and thus minimize coefficient of friction and friction load. In addition, friction torque defined by the Petroff equation is:

$$T_f = fWR \quad \text{Equation 4}$$

Where:

F = coefficient of friction

W = Radial load

R = Radius of the shaft

Thus, both the coefficient of friction and the friction torque are functions of the load on the rotating shaft. The use of composite materials allows the drastic reduction of inertial loads, effectively decreasing W, and reducing the friction torque in the rotating components of the engine.

1.2.1.2 Additive nature of mass reduction to reciprocating mass

Reducing the reciprocating mass of an engine has an additive effect on the loading of reciprocating components, and on the overall engine structure. Inertial forces caused by the reciprocating assembly are less than forces due to combustion. However, inertial forces increase with the square of engine speed to the point that they are of the same magnitude as forces due to combustion.

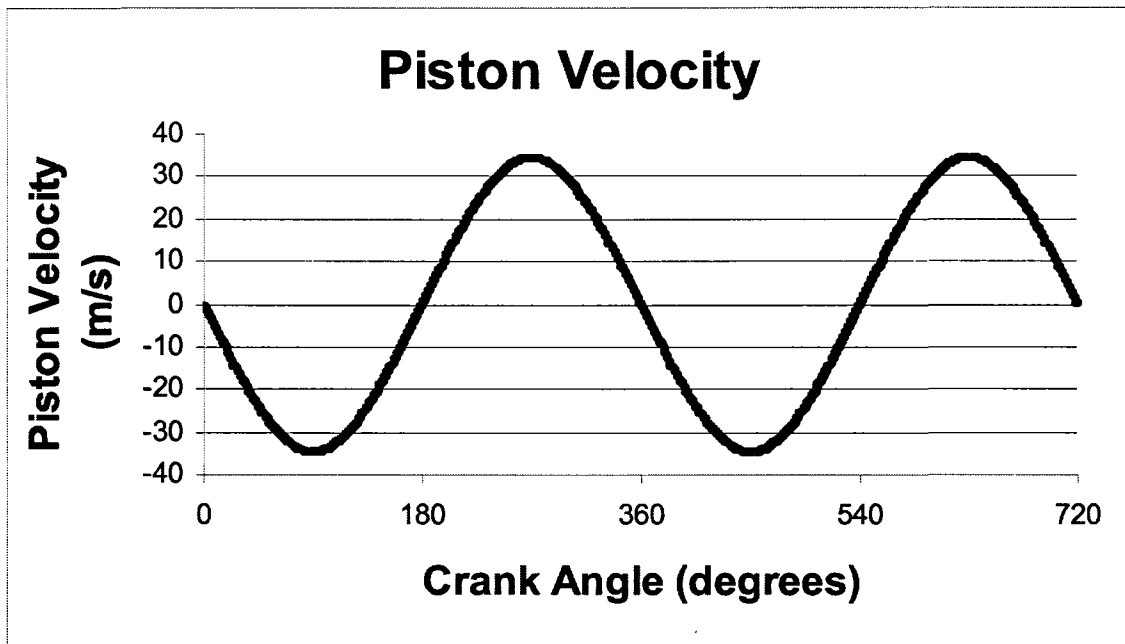


Figure 5. Piston velocity vs.. crank angle degrees (CAD).

Figure 5 and Figure 6 show the velocity and acceleration of a piston with the same dimensions as the baseline aircraft engine (described in more detail in the next section). 720 degrees of rotation represent the 4 strokes of the Otto cycle. This was developed using the equations for a classic 4-bar linkage²⁵ and is consistent for engines with a large stroke. It should be noted that the piston velocity and acceleration is not purely sinusoidal.

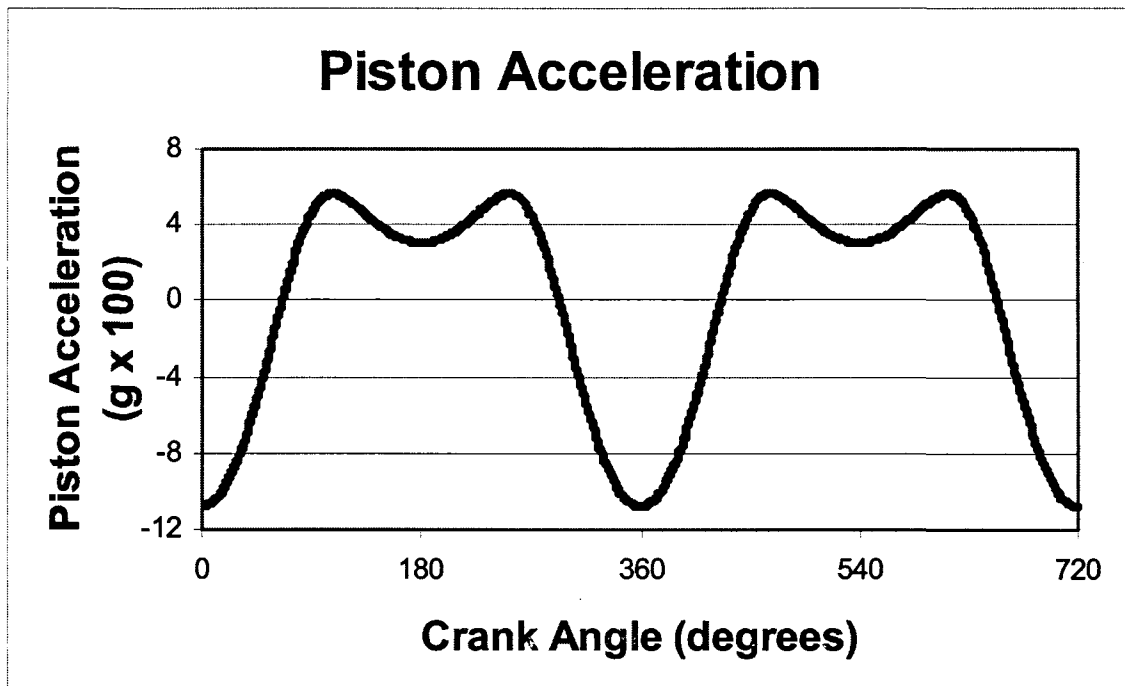


Figure 6. Piston acceleration vs. crank angle degrees (CAD)

For this example, Top Dead Center (TDC) of the compression stroke is at the point corresponding to 360 crank angle degrees (CAD) on both plots. This point will correspond to the highest magnitude forces the piston will see as a result of combustion pressure and inertial forces.

Although the forces due to combustion remain relatively constant with increasing engine speed, inertial forces increase significantly. Figure 7 illustrates how the magnitude of the maximum inertial acceleration on the piston increases as a function of engine speed, and how decreasing piston mass dramatically decreases the force experienced by the entire mechanism.

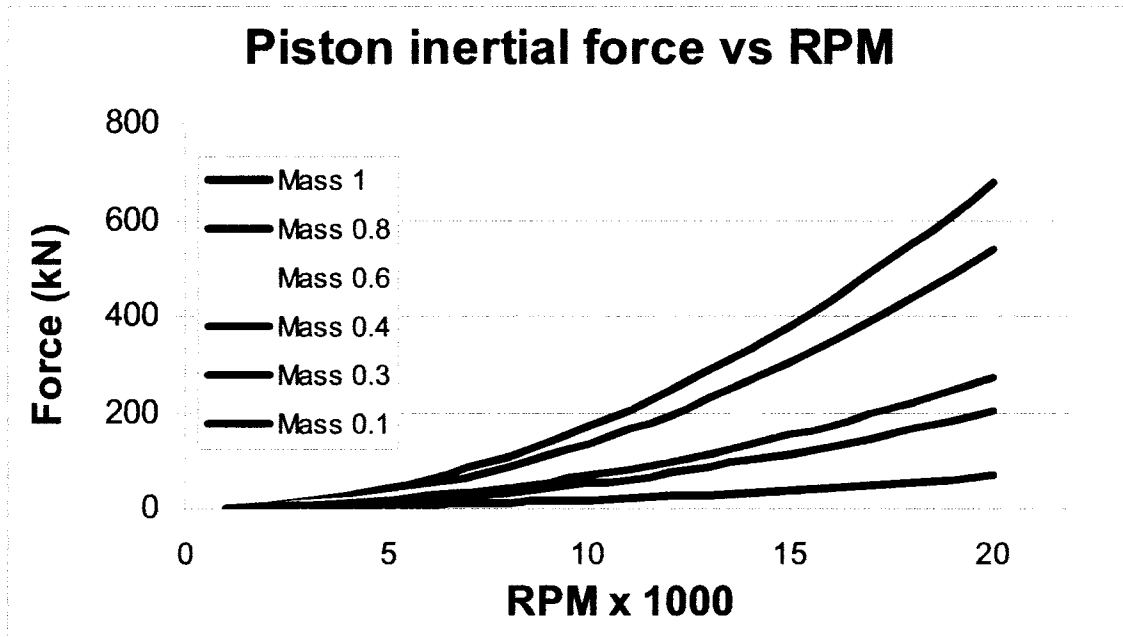


Figure 7. Piston inertial force vs. engine speed for varying piston mass.

The inertial forces created by the motion of the piston are transmitted to the connecting rod, which must be designed to handle this load as well as the load generated by its own mass. Figure 8 shows the maximum inertial force on a connecting rod for varying connecting rod masses and engine speeds.

This additional load must then be transmitted to the crankshaft, which must be designed to handle the loading for all the reciprocating components. As a result, the crankshaft is typically a very heavy, monolithic piece of steel. An illustration of these additive effects of reciprocating component mass on the remainder of the system is shown Figure 9.

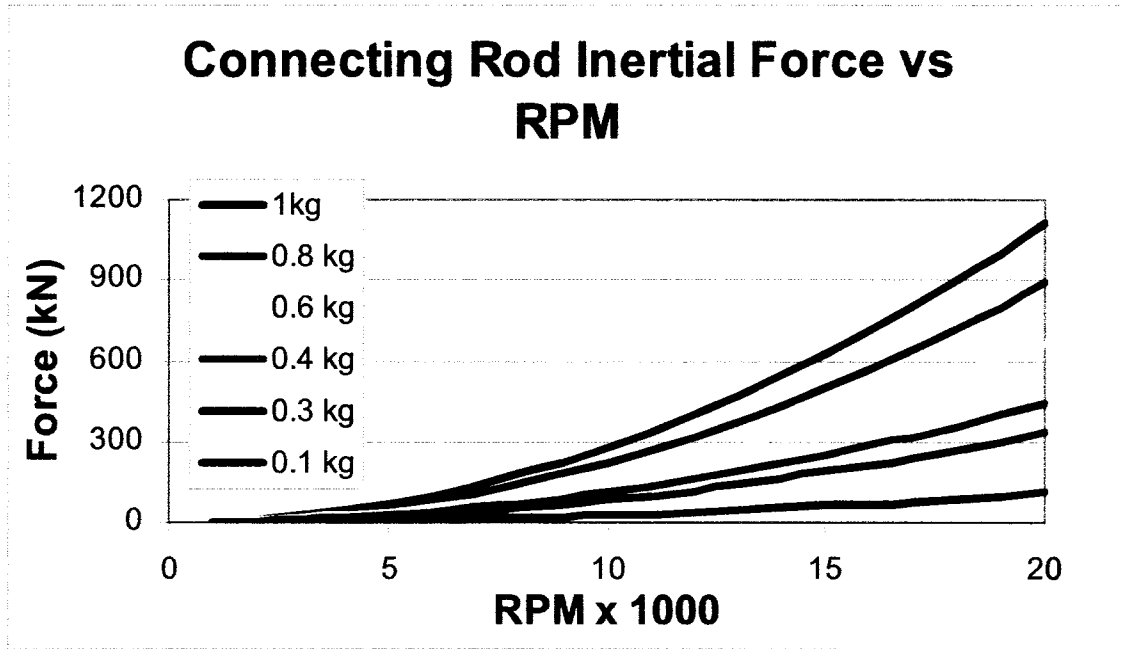


Figure 8. Connecting rod load vs. RPM for varying connecting rod mass.

With published mass reductions of at least 50% for each of the reciprocating components in an engine, it is clear that using FRCs for reciprocating components in the engine has the ability to greatly reduce the loading on many engine components. This will have a cascading effect that will enable further mass reduction.

1.2.2 Valve Dynamics

Katz, writing for Race Engine Technology wrote, *“Like it or not, the top end of a racing engine’s rpm range remains a direct function of the speed with which it’s reciprocating valves can be pushed open and sprung closed-reliably, at least for the duration of the race”*²⁶.

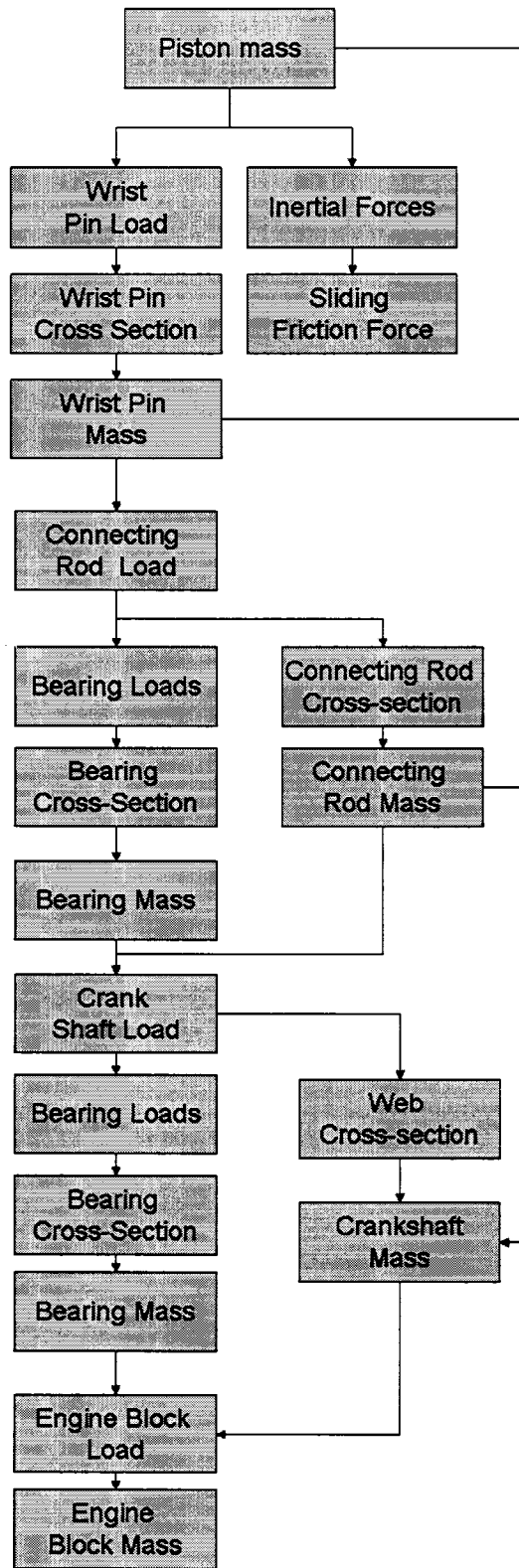


Figure 9. Additive effects of reducing component mass

With a few exceptions, the RPM limit of most modern high-performance engines is governed by the speed at which the valve train becomes unstable. Valve jump and bounce are governed by the mass and stiffness of the valve train components. Using a very simplistic view, the natural frequency of the valve train, ω , is defined as;

$$\omega = \sqrt{\frac{k}{m}}, \quad \text{Equation 5}$$

where k = the stiffness of the system, and m = the mass of the system. Decreasing the mass of the valve train should increase the operating speed of the engine. Likewise, increasing the stiffness of the valve train will have the same effect. Although the actual dynamics of the system are much more complex, this basic premise has been shown to be true. A number of workers have developed dynamic models of valve train systems that predict valve jump and bounce based on the mass and stiffness of the components^{38,37,27}. It has been shown using multi-mass and stiffness models that the onset of valve bounce and jump occurs at higher engine speed for a stiffer system³⁶.

In the quest for greater power, racers and engine builders have always pushed the limits of technology, using new, lighter and stronger materials throughout the engine. For valve materials, steel is still the most predominant material used. However, stainless steel is not uncommon, providing increased wear resistance and heat transfer with nearly the same valve mass. Titanium valves are becoming more common in racing and high performance applications, and offer a mass reduction of roughly 40% over steel valves²¹. A potential drawback is that titanium does not have the high-cycle fatigue performance of

steel and wear surfaces require surface hardening treatments²⁸. Ceramic and ceramic-head valves have been demonstrated and offer a mass reduction of roughly 60% over steel²⁹. However, the brittle failure mode of a ceramic valve can have devastating consequences for the rest of the engine. Formula one race teams have, in previous seasons, almost exclusively use a specially developed intermetallic compound called titanium aluminide, developed specifically for valve applications³⁰. Titanium Aluminide compounds enable a mass reduction of 15% from Titanium, or 42-45% from steel³¹. FRC valves offer the opportunity for an 80% mass reduction over steel, while potentially increasing reliability.

Racers are not the only ones concerned with valve mass and reductions in valve train losses. Using Toyota as an example again, engineers have published several papers detailing reductions in mass and the accompanying efficiency improvements for production car engines^{20,21}. Toyota has spent a significant amount researching lightweight valves. Titanium Boron valves were developed for the specific purpose of mass reduction. The result was a 40% mass reduction, which resulted in an increase in power of 6% and reduced engine noise by 3dB. This work was done on the Toyota 4AGE engine, used in the ever popular MR2 model and contributed to then highest power-density for a production automotive engine⁶⁰. In addition, reduced mass valve train components have been demonstrated to reduce the sliding friction in the valve train by 40% and increase fuel economy by 2.5%³². The benefit of lightening the valve train seems to be common knowledge in the race community. The stated

objective of race engine valve manufacturers is to “reduce reciprocating mass and increase stiffness”²⁶.

1.2.2.1 Valve Train Friction

As shown previously in Figure 3, in an average engine, friction power is roughly 17-19% of total horsepower. The valve system represents 7-10% of this power²². Although sliding friction is present in the valve system, the primary source of power loss is in the acceleration of the valve and the compression of the valve spring. Reduction of valve mass reduces the power consumed by the valve train in accelerating the valve open. In addition, lighter valves enable the use of softer valve springs. This again results in reduced power consumption by the valve train and more power available at the crankshaft.

Friction in the valve train is complex and highly dependent on the configuration of the valve actuation mechanism. Common practice is to measure the contribution of the valve train to engine friction in terms of camshaft torque. Contributions to camshaft torque can be divided into two distinct sources³³:

- Sliding friction losses due to the contact between the cam and follower.
- Inertial losses from accelerating the valve and compressing the valve spring.

For most valve mechanisms, the dominant friction losses are in the camshaft-follower interface. In general, work exerted in compressing the valve springs is largely regained when the valve closes and the springs “return” torque to the camshaft. **Error! Reference source not found.** shows a plot of camshaft torque versus camshaft angle for a single cylinder automotive production-based engine.

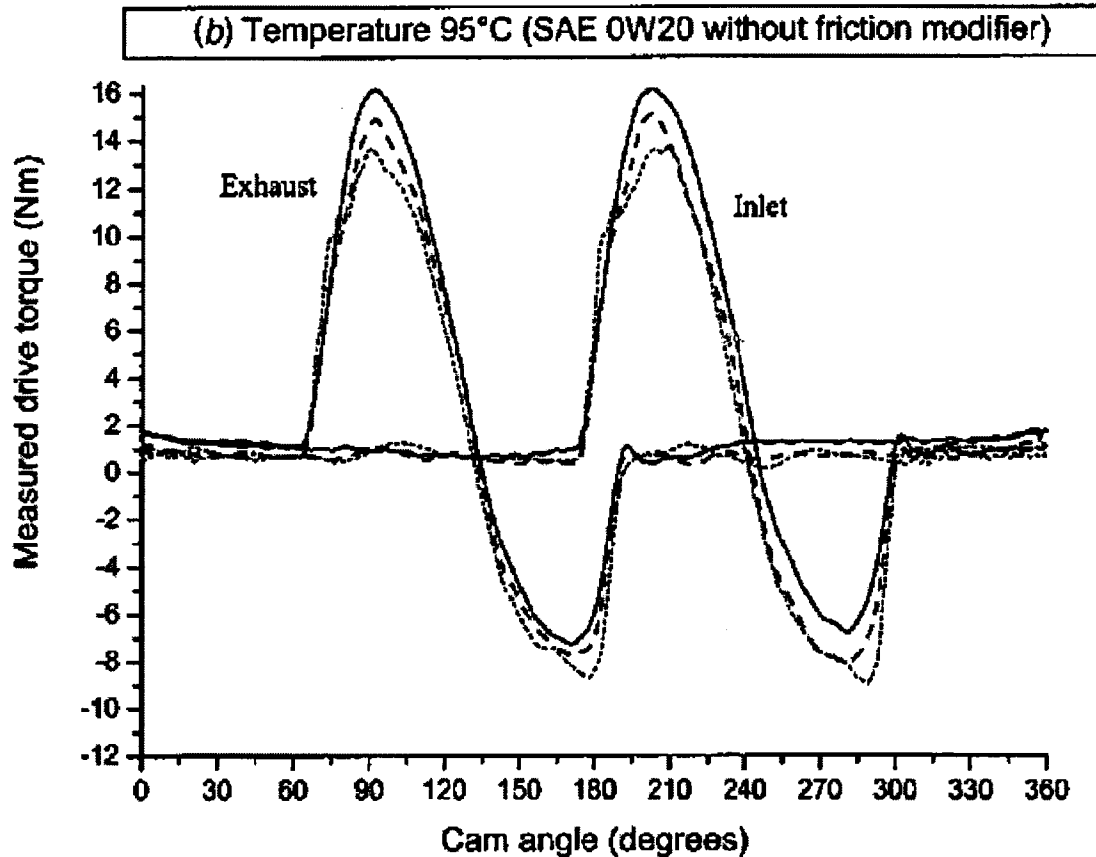


Figure 10. Camshaft Torque vs.. camshaft angle, from Mufti³⁴.

(—— 800 rpm, — — — 1500 rpm, · · · · 2500 rpm)

1.2.2.2 Benefits of Reduced Mass Valve Train Components

Reducing the mass of the valve, and other valve train components, affects both sources of losses outlined above in the following ways. Figure 11 is a graphic representation of the different ways in which reducing valve mass affects mechanical efficiency and engine performance.

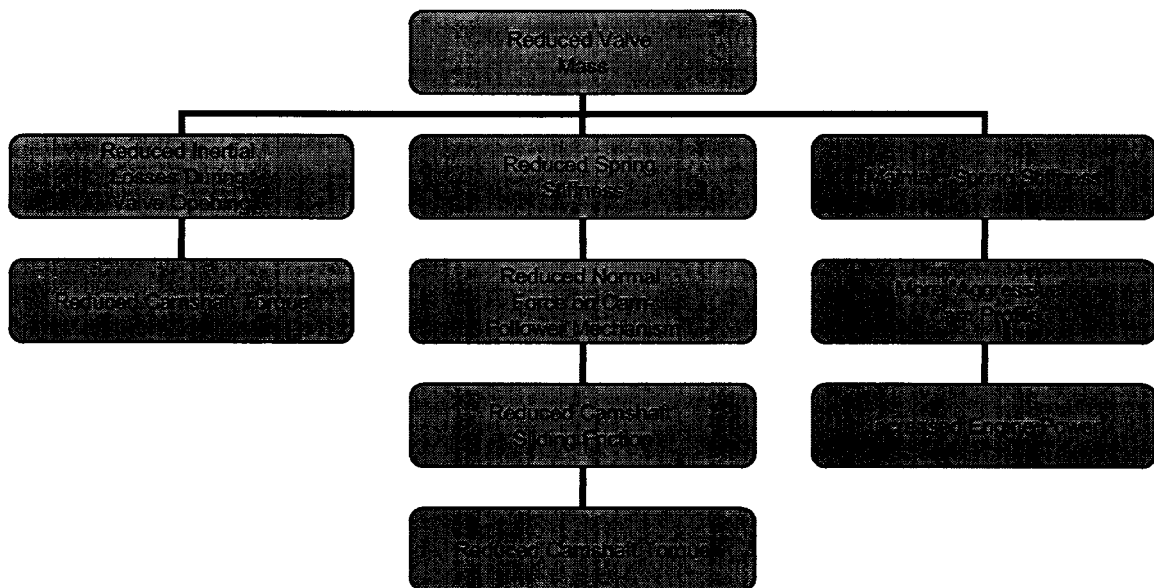


Figure 11. Effects of reduced valve mass on engine performance.

Essentially there are two benefits of using reduced mass valves. They are: 1) The reduced valve mass reduces the inertial loading during valve opening, and thus reduces camshaft torque. 2a) If the designer chooses to maintain peak engine peak rpm, reduced valve mass enables this while the using softer valve springs. The result is reduced normal force at the follower and thus reduced sliding friction. 2b) Alternately, the designer may choose to use stiffer springs, increasing the peak RPM of the engine and (typically) increasing power. This topic is discussed in more detail in the next section.

As mentioned earlier in section 1.2.2.1, there are a number of potential advantages to using reduced mass valves. Figure 12 shows these advantages in the form of a flow chart. The primary advantages in high performance engines are:

- Reduced valve mass enables the use of softer springs, reducing the camshaft torque required and increasing the mechanical efficiency of the engine.
- Reducing valve mass while maintaining or slightly reducing spring stiffness enables higher operating speeds and more “aggressive” cam profiles, enabling greater engine power.

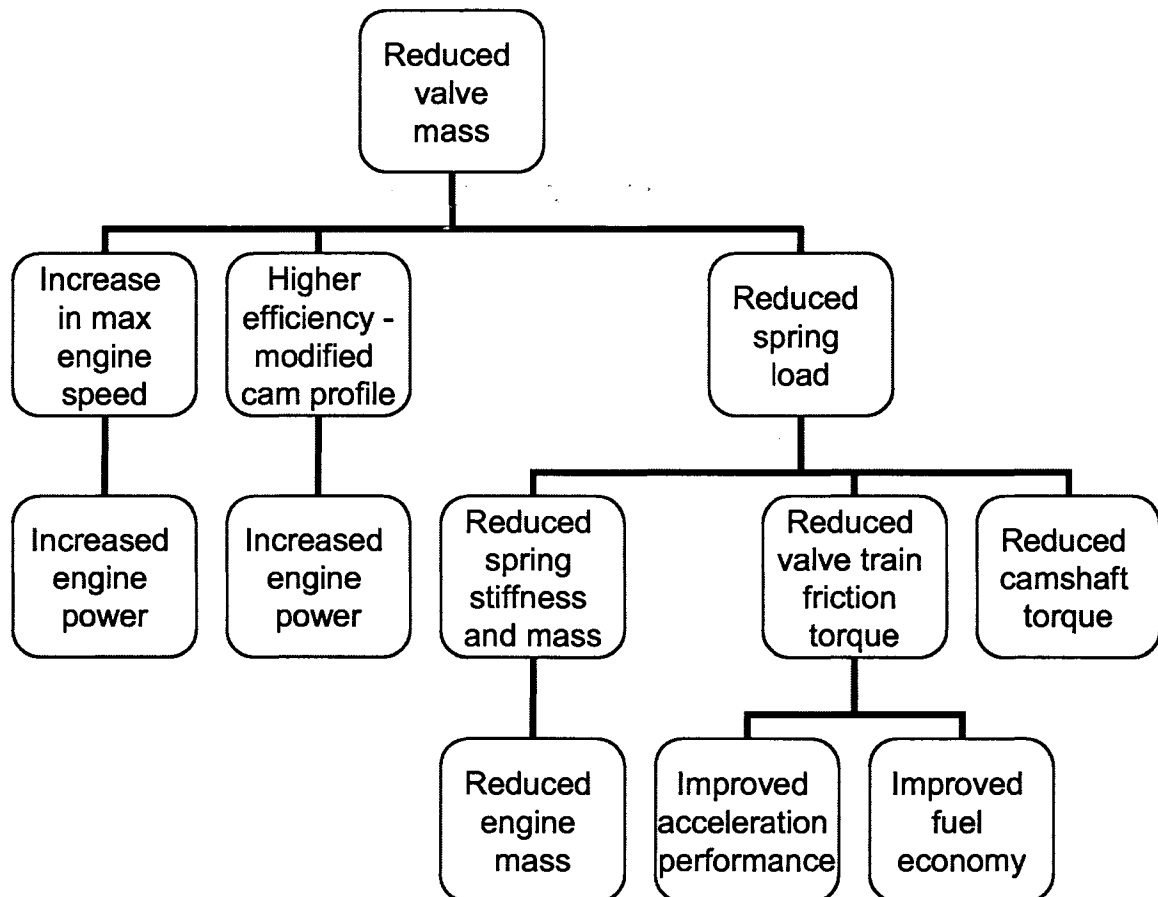


Figure 12. Advantages of lightweight valves, adapted from Tominaga²⁸.

A kinematic model of a single cylinder race engine was developed by Jason Miwa during M.S. research³⁵ to quantify the potential benefits of reduced mass valves. This model was validated using a motored engine test rig equipped with a laser displacement sensor and crankshaft position encoder in order

measure valve displacements and the onset of abnormal valve behavior (bounce and jump). Valve jump is a condition when the valve actuation mechanism loses contact with the valve, essentially “launching” the valve during high speed operation. In many cases this causes the valve to slam against the valve seat and open again. This is referred to as bounce^{36,37}. Details of the model, test rig, and tests conducted are documented in a separate paper³⁸ and M.S. thesis by Jason Miwa³⁵.

Using the model, maximum engine speed was calculated for the test engine with varying combinations of valve mass and spring stiffness. The results of these simulations are shown in Figure 13. In the figure, the downward sloping lines represent constant spring stiffness. From the model, reducing valve mass by 50% (roughly that of a titanium valve) and maintaining stock spring stiffness allows a maximum RPM increase from 10,000 RPM to about 12,500 RPM. Reducing the valve mass by 75% (attainable through the use of composite valves), and reducing the spring stiffness by 50% will still give an increased maximum engine speed of roughly 1,000 RPM³⁸.

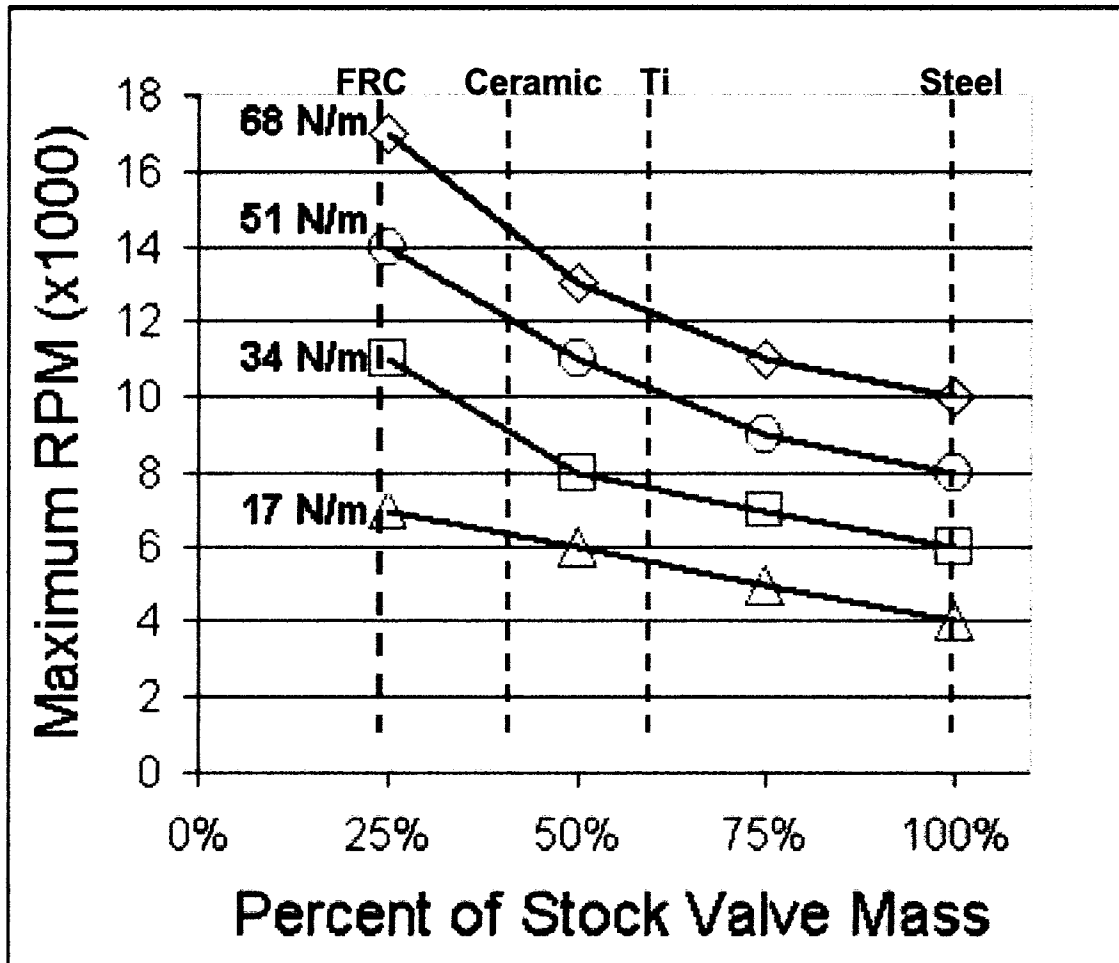


Figure 13. Maximum engine RPM for varying valve mass and spring stiffness, adapted from Miwa³⁸.

Reduced mass valves and reduced spring stiffness also reduces the loading on the valve train. Figure 14 is a plot of the torque required to drive the camshaft versus camshaft angle for the same spring stiffness values. Reducing the spring stiffness by 75% reduces peak camshaft torque by about 63%. However, this has a minimal effect on engine brake power since the negative portion of the curve represents torque returned to the engine³⁸.

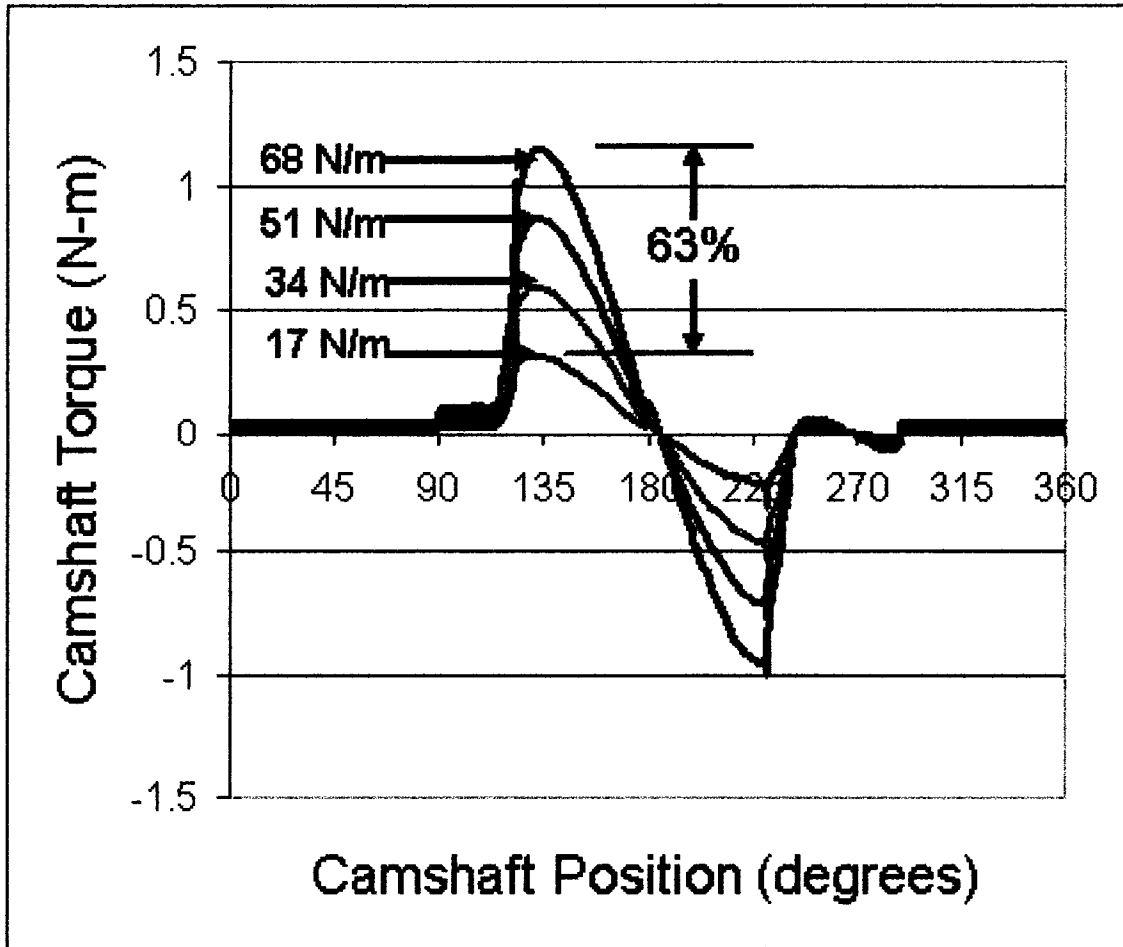


Figure 14. Camshaft torque vs.. position for varying spring stiffness³⁸.

1.2.3 Traditional Metal Poppet Valves

At first glance, the poppet valve is a fairly simple design. However, closer inspection reveals a very specialized device that has evolved dramatically in just over a century since adoption for use in internal combustion engines.

Rather than a homogeneous piece of metal from tip to head, the physical properties of the valve must change along its length. The tip of the valve must be hardened to resist the high contact stress associated with the actuating mechanism. The head of the valve must be tougher, to withstand the fatigue associated with closing, yet must also have a high surface hardness to resist

wear against the seat. Surface finish of the stem must be extremely fine to reduce sliding friction. In addition tolerances must be extremely tight since a small eccentricity of the stem and head will cause improper sealing and potentially lead to bending of the valve³⁹. Thermal stresses cannot be neglected either. High temperature performance is necessary since combustion gasses regularly reach 2000 to 3000 °C. Sustained operating temperatures for an exhaust valve can be as high as 760°C⁴⁰.

Given these facts, it seems incredible that one of the many valve manufacturers makes over 300 million reliable valves per year⁴¹.

1.2.3.1 History of Poppet Valve Manufacture

The dawn of the automotive era saw the basic form of the valve take shape. Cone shaped valve seats began appearing in 1912 to reduce pitting and produce a better seal. The importance of material properties was beginning to be recognized. Built-up valves were made using two different materials, one for the head and another for the stem which were then welded together in a heated die. The brittle behavior of steel was a significant issue. Observations showed that valve deformation and shape could cause improper seating and blow-by. At this early stage, manufacturing was crude. Valves were heated and stamped in a multi-step process. Slots were cut in the valve face to allow holding and locating for later grinding. The head was ground and the seat was cut on a lathe to rough finish. Heat treating the ends and seat was done with an oxy-acetylene torch. The manufacturing process produced internal stresses that bent the valve stem. In many cases a hammer was used to straighten it again⁴².

By the 1930s, the problem had changed. *"The problem today is not one of design, but is one of production, for motor valves must be made accurately in very large lots"*⁴³. Manufacture was done on specialized machinery, but was largely very operator dependent. Most valves were forged, rolled, and heat treated. Final machining was done in a centerless grinder. End hardening by heating electrically or by oxy-acetylene torch while valves were held in a cooling tank⁴³.

The 1940s saw a reduction in processing time by using drop forging. *"This method is claimed to be superior to any other because it enables the fibres to be placed in the strongest orientation"*⁴⁴. (Note: in this context, *fibres* refer to the metal grain boundaries created by the forging process, not to any engineered fiber). Hardened tips were welded to austenitic stems to reduce tappet wear⁴⁴. More specialized materials began to appear as well. "Tranco" valves made outside London in Farnborough used five basic materials for different applications ranging from light duty gasoline and diesel valves, to more specialized materials for continuous high temperature operation. Manufacturing still averaged 15 operations per valve and as many as 25 or 30 for complex shapes⁴⁵.

By the 1960s, valve manufacture was completely automated and made of different materials were flash welded together. Two-angle diamond grinding of seats became common. Visual and automated mechanical inspection also became the norm⁴⁶.

1.2.3.2 Modern Metal Valve Manufacture

Modern poppet valves are typically made from a variety of steels and contain some portion of iron, nickel, manganese, and many other metals. Composition is tailored based on the environment encountered, strength and fatigue requirements, and desired heat transfer characteristics.

A typical valve manufacture process flow might follow a process similar to this^{42,61,31,45}

- Rod stock is forged to shape in a number of steps.
- The stem is rough ground to size, typically on a centerless grinder.
- The stem is straightened by rolling through a press.
- Rough facing of head is accomplished, centered on the previously ground stem.
- The valve head is ground concentric with the stem, again centered on the previously ground stem.
- The valve stem is cut to final length.
- The stem is finish ground to final size and finish.
- The valve seat is ground, typically using a 2-angle or 3-angle grinder.
- The collet/keeper notch is ground into the stem.
- Bevel/chamfer is ground onto the end.

In some high-heat applications, sodium filled valves may be used to increase heat transfer away from the valve face. These particular designs take advantage of the high temperature phase transformation of sodium and convective heat transfer within the valve stem to draw heat away from the valve

seat and to the cooling passages around the valve stem. While this is an advantage, manufacturing is complex⁴⁰ and this type of valve is atypical for most common IC engine applications.

Table 4. 1973 cost per pound of valve material based on temperature range, adapted from Danis⁴⁰.

TEMPERATURE RANGE	COST PER POUND
-40 to 600F (-5 to 300C)	10 – 20 cents
600 to 1000F (300 to 550C)	20 – 45 cents
1000 to 1200F (550 to 650C)	50 - \$1.00
1200 to 1400F (650 to 750C)	70 - \$3.00
1400 to 1650F (750 to 900C)	\$1.00 - \$8.00
Above 1650F (above 900C)	?

Material costs are not insignificant. As one might expect, the cost of a material increases with operating temperature. Table 4 shows the cost per pound of metals as a function of temperature range. Although the numbers may be dated, this trend still exists.

Poppet valve production is a high-volume, low margin business. The number of valves manufactured for new vehicles every year is in the hundreds of millions. In the highly cost-competitive automotive industry, profit margins on individual valves are very low. Thus, any cost savings in the manufacturing

process from reduced machining operations should be a benefit. Manufacturer costs for individual valves are in order of the pennies per valve. Aftermarket cost for valves is a slightly higher profit margin. "High Performance" titanium racing valves cost on the order of \$100 or more per valve⁴⁷.

1.3 History of FRC Research in Internal Combustion Engines

As discussed above, FRC materials have been demonstrated to both reduce mass and increase performance of components in the aerospace industry. The advantage of reduced mass reciprocating components in an internal combustion engine has the potential for improved mechanical efficiency and increased performance. It appears then, that FRC materials and internal combustion engines would be a logical match. Based on this revelation an extensive literature review of previous work on development of FRC engine components was undertaken. The results of that literature review are documented below.

The oil crisis of the 1970's produced a renewed interest in FRCs because of the increased fuel economy made possible by reducing vehicle mass. A number of experimental vehicles and vehicle components were produced. Many, including the 1979 Ford "Carbon Car" and the Daimler Benz C111 used extensive use of FRCs for structural applications, but avoided the challenge of producing engine components from FRCs⁴⁸.

Perhaps the most famous effort to produce a composite engine was the Polimotor engine. Polimotor was the first to produce an "entire" engine out of composites. Owner/designer Matthew Holtzberg used a combination of carbon

fiber, Torlon®, epoxy, ceramic and metal. The first version of his engine was based on the Ford 2.3L Mustang engine. The engine block, cylinder head, valve spring retainers, timing gears intake valves with ceramic heads, and several other parts were made of FRCs. Hand lay-up of epoxy pre-preg for the engine block and cylinder head made production of an engine/head very time consuming. A single engine took over one week to fabricate⁴⁹. However the reciprocating mass of the engine was still entirely metal⁵⁰.

The second iteration of the Polimotor project was more extensive. A large number of injection-molded and carbon fiber prepreg parts were used. The engine produced was a 237 kW (318 HP) @ 9200rpm. Holtzberg produced the engine block, cylinder head, intake manifold, valve spring retainers, timing gears, piston skirts, rings connecting rods, intake valve stems, push rods, rocker arms, wrist pins, cam followers, turbo casings & impellers, out of FRCs, and plastics⁵¹. Metals were used for components that were exposed to temperatures above 260°C⁴⁸.

Holtzberg was fairly successful with this engine. It was campaigned in a Lola II chassis and run in several Grand Prix races in the 1980's. The engine weighed 168lbs (76kg) compared to the 350 lb metal engine it was based on. Holtzberg claimed a 60% valve train mass reduction 25% higher speed (14,000 RPM race), 50% reduction in reciprocating mass and 40% reduction in noise from piston slap. The engine even used Polyacrylonitrile (PAN) carbon-fiber based spark plug wires⁵². Figure 15 is a picture of the Polimotor car racing at the Road America 500 in August of 1985, where it finished in 17th place⁵³.

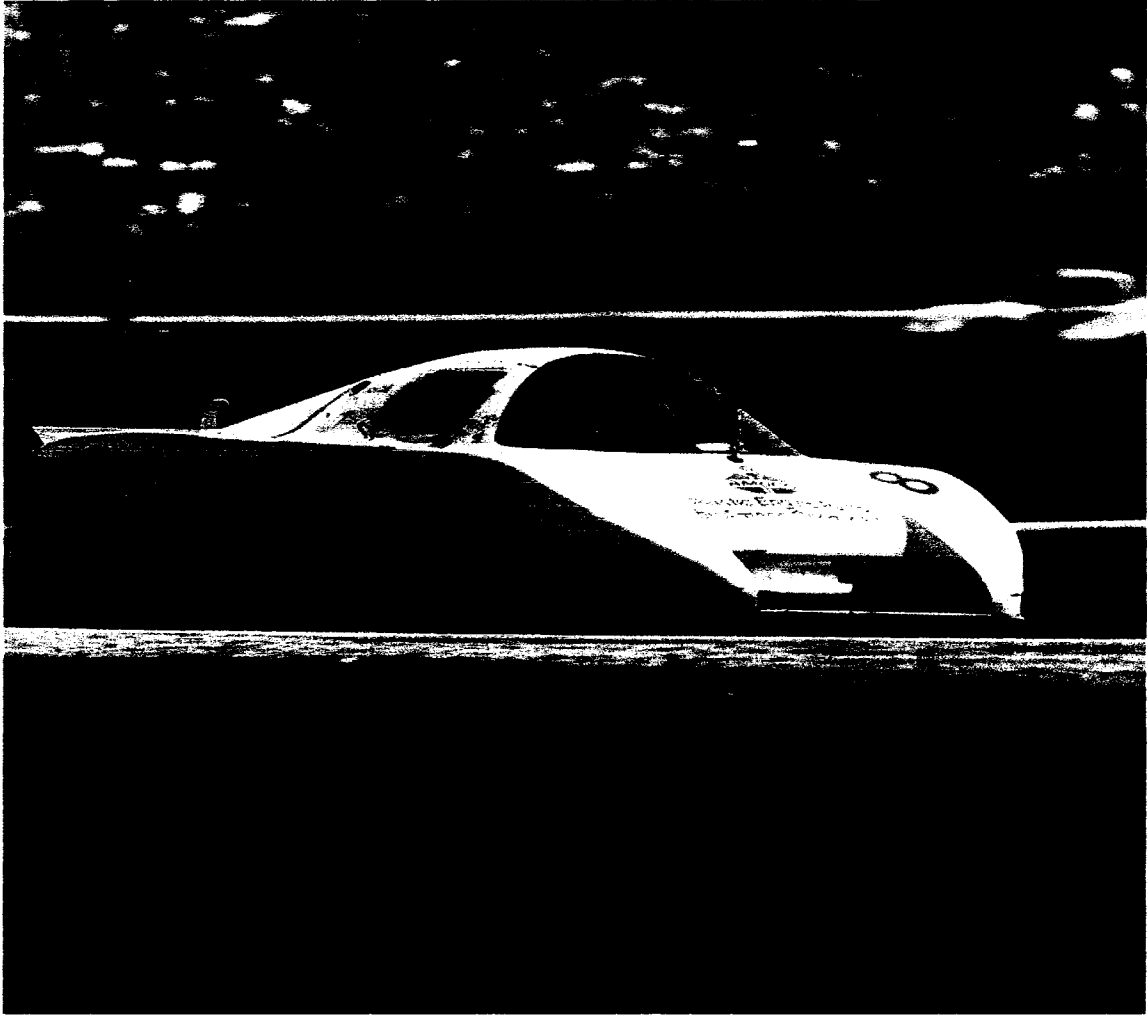


Figure 15. Polimotor Lola II at Road America 500, August 1984⁵³.

The early 1980s also saw a Japanese push towards the use of Metal Matrix composites (MMCs). A combined government/industry research effort was established and produced notable results. Honda produced the first MMC connecting rod using continuous stainless steel fibers in an aluminum matrix. This used 12-15% volume fraction of fibers and produced a 20% weight savings. Toyota was the first to mass-produce MMC diesel pistons beginning in 1982. A continuous fiber perform of 3.5% to 8% volume fraction alumina and carbon fiber was used to reinforce the aluminum piston crown. This enabled an aluminum piston to be used instead of steel and reduced the piston mass by 30%. Honda

was also the first to use Alumina/Carbon reinforced aluminum in cylinder sleeves in 1989, claiming a 20% weight reduction by using 12-15 volume % fibers. In 1991, Toyota also produced a crankshaft damper claiming 20% weight savings using short fiber reinforcement³.

In the late 1980s, Western Michigan University did extensive work with its polymer engine project. An injection molded piston with chopped graphite fibers was produced for use in a 5 HP Jacobsen 2-stroke engine. This was coated with a ceramic for thermal protection. A connecting rod was made using similar means and a crankshaft was made from pultruded vinylester and glass fiber⁵⁴. The existing aluminum engine block, cylinder sleeve and head were used. Weight savings was claimed at 40%¹⁰.

In the early 1990's the NASA Langley began the carbon-carbon engine project. This focused on the use of carbon-carbon composites in internal combustion engines. Extensive work was done on pistons and cylinder sleeves. A number of working prototypes were developed and an even greater number of patents were issued for things from carbon-carbon pistons to engine blocks. One of the primary focuses of the NASA project was to find a viable manufacturing process and bring down the cost of carbon-carbon pistons. Though initial costs were over \$200 per piston, estimates for mass produced chopped carbon fiber pistons were as low as \$20 per piston⁵⁵. With improvements in processing and matrix precursors, estimates for mass-produced pistons were eventually less than \$5 per piston, which is comparable to production aluminum pistons⁵⁶. This was achieved using Langley Research Center Soluble-Imide (LaRC-SI) as a

carbon matrix precursor and a hot isostatic-press manufacturing technique which greatly reduced manufacturing time⁶.

The NASA project also produced carbon-carbon cylinder liners with the intent of investigating the possibility of ring-less operation. This project was transferred to the Department of Energy (DOE) in 1999 where subsequent research focused on using carbon-carbon pistons to reduce emissions in diesel engines through a contractor in Hampton, Virginia⁵⁷.

In the early 1990s, Volkswagen experimented with carbon fiber/epoxy connecting rods and successfully demonstrated at least two versions. Rods consisted of a titanium eye and compression plate with a continuous carbon fiber perimeter wrap to carry tensile loads. These connecting rods underwent extensive testing with satisfactory results. Results showed a 70% weight reduction from steel, a 3dBA noise reduction, and a 15% reduction in mechanical losses. However it was deemed that the manufacturing challenges were too large at the time to pursue production^{58,59}.

Toyota has continued the use of short-fiber Alumina reinforced aluminum cylinder liners in the Celica model and claims small gains in fuel efficiency as a result⁶⁰. Reinforced aluminum pistons and filament wound carbon-fiber wrist pins have been used in F-1 racing engines, though details are difficult to come by⁶¹.

Figure 16, Figure 17, and Figure 18 illustrate a timeline of the work cited in the literature, broken down into the large categories of metal matrix, carbon-carbon, and polymer matrix composites. The numbers in the figure correspond to references cited in Appendix 1: references for Figure 16, Figure 17, Figure 18,

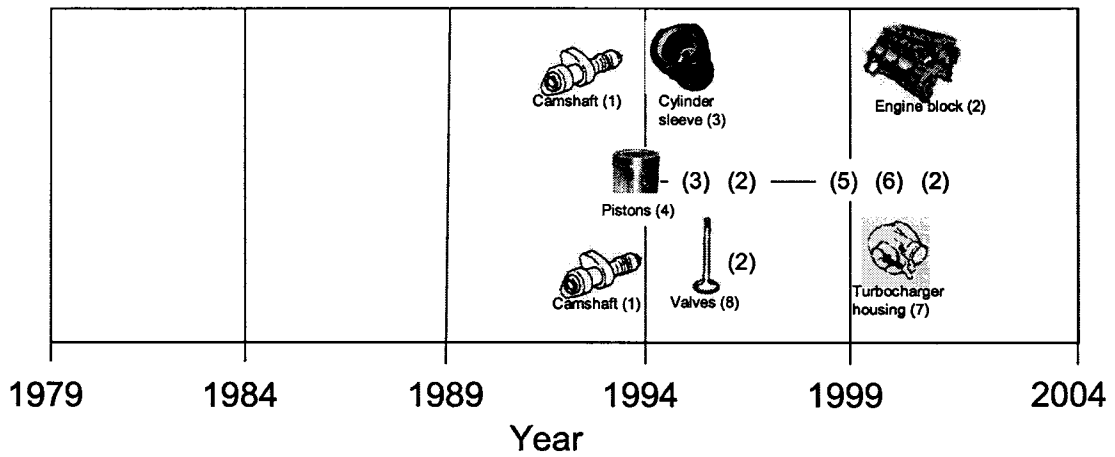


Figure 17. Timeline of Carbon-Carbon composite research.

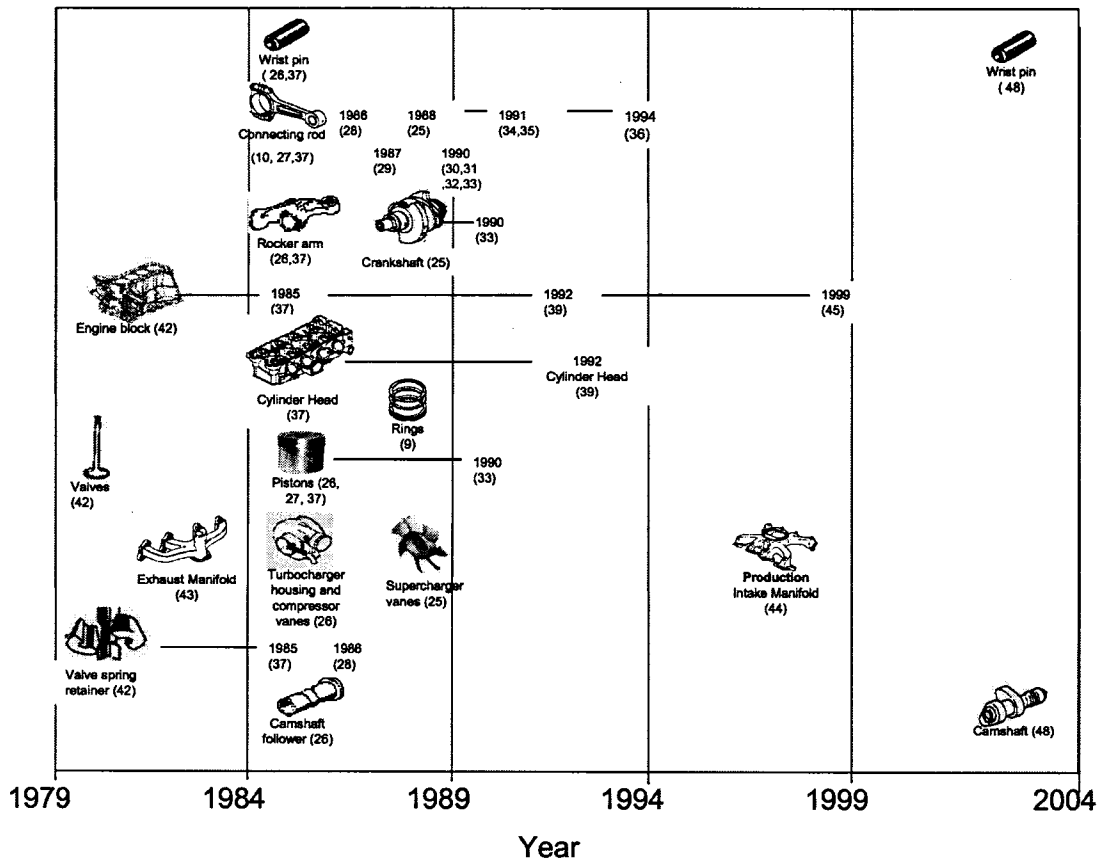


Figure 18. Timeline of polymer matrix composite research.

Despite the vast amount of work that has been done producing FRC engine components, there has been only one attempt to construct a complete engine using FRCs, (the Polimotor project). The question then arises, “what could be done if FRCs were used from the onset in the design an engine.” The answer to this question will be addressed in the next chapter on modeling.

1.3.1 Previous FRC Poppet Valves

As mentioned in the section on valve train, there are a number of advantages to reduced mass valves. Modern racing applications typically reduce valve mass by using smaller diameter steel and stainless steel valves, or titanium. Titanium nitride valves offer even greater mass reduction. Figure 19 shows the typical mass of valves made of high-performance materials relative to steel.

Table 5. Summary of published mass reductions by component and material.

PART	MMC WT % REDUCTION/ ORIGINAL MATERIAL	PMC WT % REDUCTION/ ORIGINAL MATERIAL	C-C WT % REDUCTION/ ORIGINAL MATERIAL	REFERENCE (SEE APPENDIX 1)
Camshaft			75/ steel	1
Connecting Rod	25-55/ steel	30-70/ steel		10, 13 ,14 ,15 , 27, 28, 30, 31, 36, 37
Crankshaft		40/ steel		25
Cylinder Sleeve	20/ steel			13
Cylinder Head		70/ steel		37
Damper	20/steel			13
Drive Shaft		40-50/ steel		28, 40
Engine Block/case		60-70/ steel		37, 42

Piston	5/Al – 18/Cast iron	70/ steel	45-60/ Al	44, 27
Pushrod	60/steel			23
Rocker Arms		70/ steel		37
Timing Gears		70/ steel		37
Valves		70/ steel	83/ steel	2, 37
Valve Retainers	60/ steel	70/ steel		23, 37
Wrist Pins		70 /steel		37

A number of candidate FRC materials offer the performance necessary for in-engine operation. Metal matrix composites such as Silica fibers in aluminum offer nearly twice the performance of conventional metals with improvements in creep resistance. More exotic materials such as carbon-carbon offer an order of magnitude improvement over metals as well as superior high-temperature performance when an oxidative barrier is used⁶².

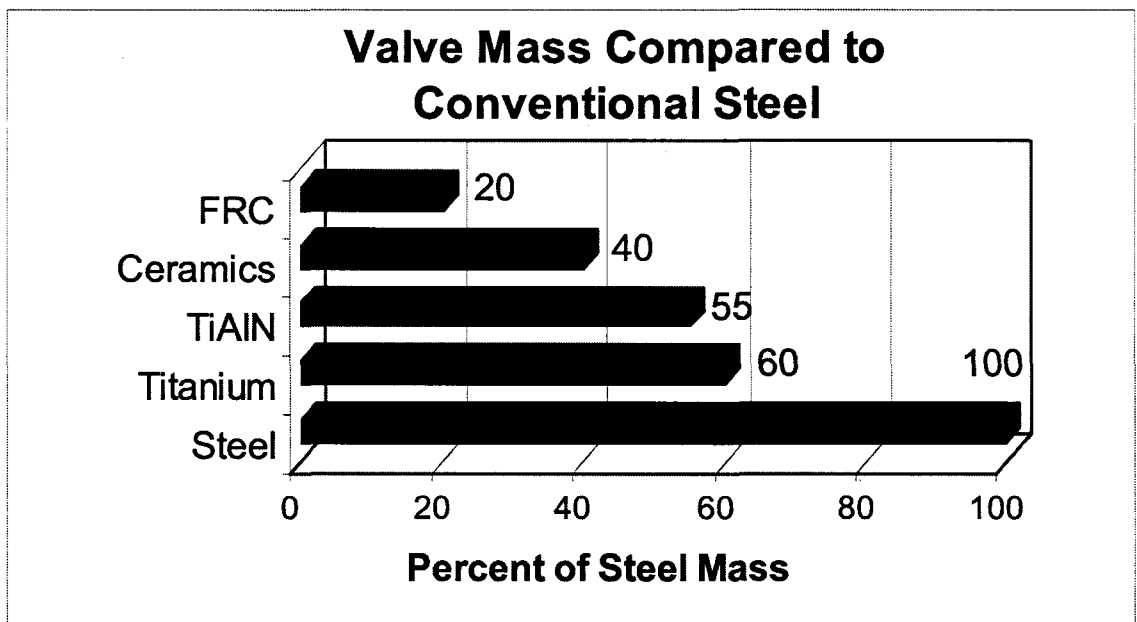


Figure 19. Relative mass for valves made of high-performance materials compared to steel.

There have been several attempts to design a FRC poppet valve for automotive engines. These are briefly summarized below.

1.3.1.1 Polimotor Research, Inc.

Polimotor Research, Inc., mentioned in section 1.3, developed a “composite” engine. Valves were made of “Torlon” which is a trade name for a high temperature thermoplastic, polyamide-imide (PAI). Intake valves were made from extruded Torlon with carbon fiber reinforcement, bonded to a ceramic valve head. This contributed to an inline 4-cylinder engine weighing 168 lb. The comparable metal production engine weighed in at 412 lb. The authors also claimed the engine was 30% quieter. The limiting factor in the performance of these valves was adhesive technology of the time⁵⁰. Plastics were not used in components that saw temperatures above 260°C, however at lower temperatures, the composite valves showed higher fatigue life than metal valves⁴⁸. More significant was the fact that valve train mass was reduced by 60% and operating speed was increased by 25%²². A picture of the Polimotor 3-piece valve is shown in Figure 20.

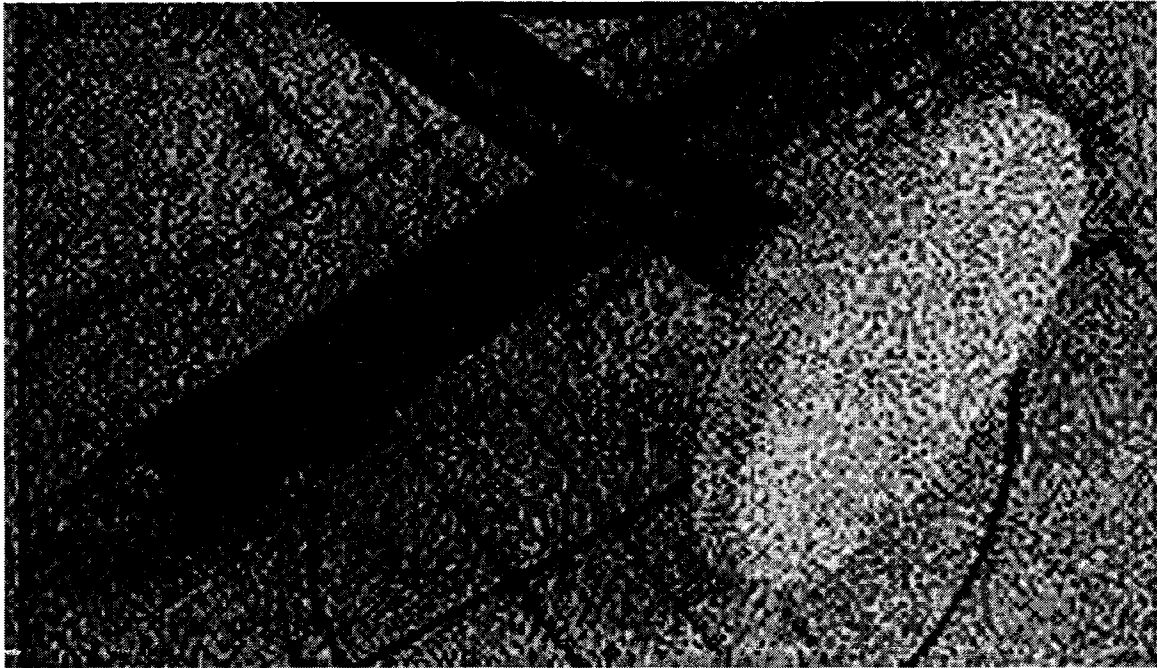


Figure 20. The Polimotor 3-piece composite intake valves⁵⁰.

1.3.1.2 Langley Research Center (LaRC)

During the late 1980s, the NASA Langley Research Center began a carbon-carbon engine project in which they produced a piston and cylinder sleeve for a small engine. The purpose of the project was to develop a manufacturing process for low-cost carbon-carbon. Two attempts were made create a carbon-carbon poppet valve. The first used a unidirectional carbon fiber in a valve for a small single cylinder engine. Testing showed failure transverse to the fiber direction at the junction between the stem and head⁶³. A second attempt used a 2-D weave of carbon fiber and produced valves for a small-block Chevrolet V-8. The resulting carbon-carbon valves weighed a mere 15 grams versus 90 grams for the stock steel valves. No performance details were available for these valves but it was noted that a coating would be required to prevent oxidation at temperatures above 400°C⁵⁶.

Based on this literature review, it appears a vast amount of work has been done demonstrating nearly every engine component made from FRC materials. The exception appears to be in those components that are exposed to the extreme environment of the combustion chamber. Those that have been demonstrated in the combustion chamber have had marginal success. Recognized improvements were required to operate for prolonged periods in the demanding thermal oxidative environment found in the combustion chamber.

1.4 Thermal Analysis of Composite Materials

FRCs often have a limited service temperature. This is especially true for polymer matrix composites. Table 6 lists some common fibrous materials, matrix materials, and coatings and their maximum service temperature in air. Typically, high temperature fiber and matrix materials are more exotic, often brittle, and also more expensive. Trends have shown that, as these materials are adopted, prices come down. As an example, carbon fiber sold for \$500/kg in the 1970s, now it sells for roughly \$4/kg⁸⁴ and is a commodity item.

The orthotropic nature of FRCs has long been recognized as being advantageous in the design of thermal management systems for numerous applications. While early work focused on aerospace applications, using FRCs for thermal management has become more mainstream every day. By 1992 the US Navy had developed numerous FRC applications for thermal management, ranging from electronics to missiles and satellite applications⁶⁴. A brief summary of some of the published work is described later in this document.

Table 6. Maximum service temperature of common fiber and matrix materials⁶⁵

Fiber Type	Maximum service temperature (deg C)
Boron	2300 (melt)
E-Glass	1800 (melt)
SiC (Nicalon)	1400
Carbon (T-300)	600
Matrix Type	
Ceramic (SiC)	1350
Bismaleimide	350 ⁶⁶
Epoxy	240
Polyester	120
Nylon 6	40-230

In general, the advances in understanding of thermal performance of FRCs can be divided into three generic areas:

- modeling FRCs as multilayer and orthotropic solids
- material development for thermal management
- specific designs that use multi-layers with orthotropic materials

A summary of the notable achievements in these three categories is discussed below.

Methods for coating FRCs have been developed and are in production; however the focus of the majority of the published research has been on other functions for the coatings such as friction, wear, or aesthetics⁹¹.

1.4.1 Thermal Modeling of Composite Materials

The late growth of FRC use in the 1970s and early 1980s, combined with the relatively small amount of computing power available led to a number of fundamental studies on transient thermal performance of composite materials. In many of these cases, the term “composite” refers to a solid made of two materials with different properties. Modeling of FRCs are typically described as orthotropic materials.

In many of these cases, the analysis was based on the transient performance of fundamental shapes. Focus of most of this work was in determining the temperature induced stress created by a thermal transient.

Some significant examples of these studies are:

- a multi-layer slab with contact resistance⁶⁷
- a composite band heater with heat source⁶⁸
- a composite slab with variable conductivity⁶⁹
- a graphite-epoxy plate using Mindlin Plate theory, developed FE and FD process⁷⁰
- 3-D carbon-carbon composites⁷¹
- 2 perfectly bonded cylinders⁷²
- an orthotropic circular cylinder⁷³
- an axisymmetric multilayer composite cylinder⁷⁴
- a multilayer hollow cylinder⁷⁵
- a rotating orthotropic circular cylinder⁷⁶

Many of the studies above developed the underlying mathematics for, or employed simple Finite Difference Method (FDM) or Finite Element Method (FEM) simulations and laid the groundwork for the more complex modeling used today.

1.4.2 Material Developments for Thermal Management

Traditional thermal management materials are characterized by high thermal conductivities. As a result, materials like copper, aluminum, and tungsten were the materials of choice. In general, materials used for heat sinks have conductivities less than 180W/mK ⁸². Figure 21 shows the relative conductivities of conventional metals used for thermal management, as well as that of several grades of fibrous reinforcement materials.

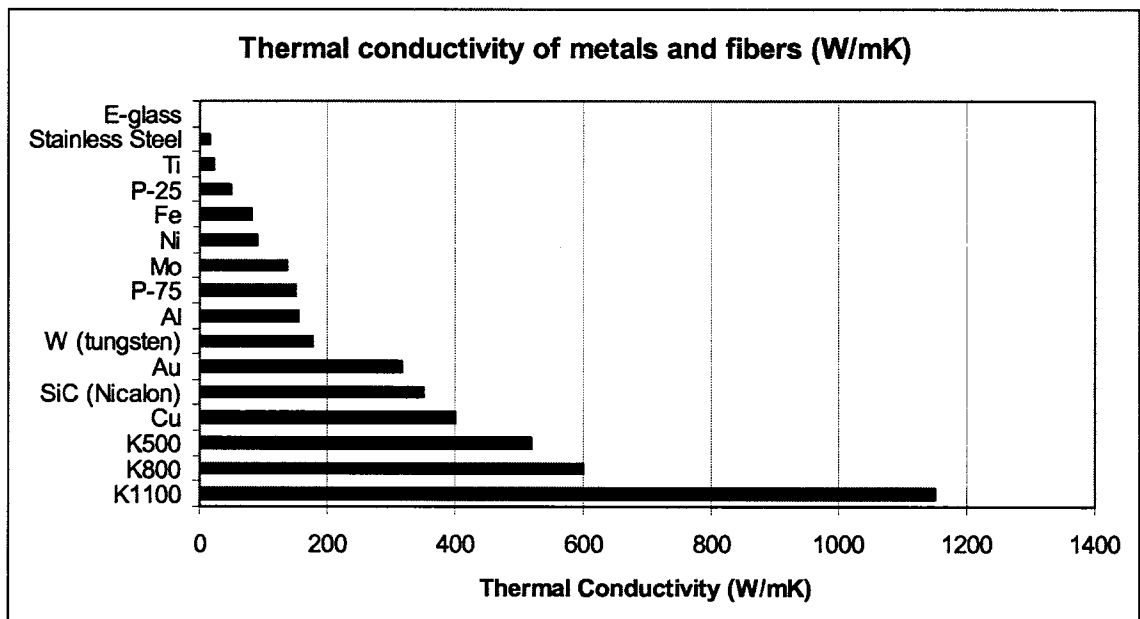


Figure 21. Thermal conductivities of metals and fibers, adapted from Bertram.

Carbon fiber and carbon-fiber composites have gained considerable attention since the mid 1980s for use as thermal management materials. Carbon

fiber has a maximum theoretical conductivity of 2000 W/mK⁶⁴, however different grades of carbon fibers have different thermal properties, based on processing methods, but all display highly orthotropic behavior. Table 7 lists the thermal properties of a number of different grades of carbon fiber.

As a result of the superior thermal and structural properties of carbon fibers, numerous carbon fiber composites have been developed and demonstrated with highly varying thermal properties. At one end of the spectrum, highly orthotropic, aligned carbon-carbon composites with axial conductivities between 400 W/mK and 1500 W/mK have been demonstrated. On the other end of the spectrum, nearly isotropic carbon-carbon composites have been developed with a highly tailorable coefficient of thermal expansion (CTE). CTE tailoring was done by impregnating the carbon composite with varying amounts of copper⁷⁷. In another example a 3-D carbon fiber preform in an Al-Si alloy matrix was developed as a replacement for tungsten. The result was a conductivity of 245 W/mK, higher than tungsten, with significantly lower mass⁷⁸.

Table 7. Thermal properties of different grades of carbon fibers.

Carbon Fibers	Axial Conductivity (W/mK)	Radial Conductivity (W/mK)
Single Wall Nanotubes	6000	50
K1100	1150	50
K800	600	50
P-100	520	not available
P-75	150	not available

Of special interest in the area of new materials for thermal management is the use of carbon nanotubes and nanofibers. Single wall carbon nanotubes, (SWNTs) are much more effective at increasing conductivity than larger carbon

fibers⁷⁹. This is in part because SWNTs have a theoretical maximum conductivity of 6600 W/mK⁸⁰. Published, measured conductivities for SWNTs are between 1100 and 1900 W/mK⁷⁹. Thus, creating a composite with even small volume fractions of nanotubes can bring a marked increase in conductivity of the bulk material. Using SWNTs in an epoxy matrix, a sharp increase in conductivity was measured with weight fractions between 0.1 and 0.2 wt% indicating formation of a percolation network⁷⁹. A composite consisting of 1% by weight SWNTs yielded a 70% increase in conductivity at 40°K, and a 125% in conductivity increase at 250K⁷⁹. Additional work has shown that aligned carbon nanotube films increase conductivity dramatically at 0.5 wt%⁸⁰. As a result of these stellar properties, carbon nanotube composites have been developed for applications such as semiconductor chip cooling where high conductivity, low CTE and low mass are of extreme importance⁸¹. Powder metal copper reinforced with carbon fiber has been demonstrated with conductivity of 454 W/mK using a K640 carbon fiber at 81% Vf. The authors claimed this novel metal matrix composite has the potential for a conductivity of up to 800 W/mK when using K1100 fiber. Similar bi-directional composites were demonstrated with conductivities of 321 W/mK and 158 W/mK in the primary and secondary directions respectively⁸².

Diamond is yet another form of carbon that has extremely high thermal conductivity (2300W/mK)⁸³ and yet is an electrical insulator. A diamond film manufactured through chemical vapor deposition (CVD) has been demonstrated with an estimated 1100W/mK thermally conductivity⁸². Commercial diamond

coated carbon fibers with $k = 2000\text{W/mK}$ have been developed for thermal management of electronic packaging where high thermal conductivity and electrical insulation is required⁸⁴.

Combining even more possibilities, squeeze cast diamond-aluminum composites have been demonstrated. Isotropic conductivities from 450 W/mK at 50% V_f of diamond have been achieved. CVD coated low-cost diamonds are coated to produce high conductivity. Higher volume fractions of diamond have produced isotropic conductivities up to 650 W/mK ⁸⁵.

1.4.3 Applications

In the electronics packaging industry especially, thermal management has been of increasingly significant importance. The combination of conventional materials and heat pipes have been applied in designs to take advantage of the energy released during phase change from liquid to gaseous state⁸⁶. However in many cases FRCs can be more efficient than heat pipes. For mounting semiconductors, coefficient of thermal expansion (CTE) is also of extreme importance to avoid thermal contact stresses and cracking. For electronic packaging the desired range of CTEs is 4-7 ppm/K, matched to silicon based semiconductors. The ability to tailor both CTE and thermal conductivity of carbon FRCs has led to numerous demonstrations. Orthotropic FRC materials designed for semiconductor mounting have been developed using both continuous and discontinuous fiber reinforcement. Continuously reinforced products have achieved axial conductivities of 890W/mK . Discontinuous reinforced composites have lower conductivity than continuous of same volume fraction⁸⁴.

Spacecraft applications have seen an increase in the use of carbon-carbon laminated plates for thermal and structural solutions. Production samples have achieved conductivities of 500 and 125 W/mK in the (laminate) x and y directions respectively. Additional applications for the same product included aircraft, nuclear reactors, electronic packaging, and chemical heat exchangers⁸⁷. In another spacecraft application, a carbon fiber face sheets with aluminum heat pipes embedded in an aluminum honeycomb core were developed to replace an older all aluminum design. The heat pipes use ammonia as the working fluid. The new design improved thermal performance significantly as well as reduced overall mass⁸⁸.

In the material processing industry, carbon fiber reinforcement has been used for thermal management during solidification of aluminum. Aluminum microstructure is a function of cooling and the formation of alpha aluminum forms on the freeze front. The carbon fiber was used to achieve higher dispersion of alpha aluminum than normally possible. A high fiber volume fraction was used to produce a uniform temperature distribution across the part, cooling the part uniformly⁸⁹.

In the automotive industry, SiC reinforcement of Al, Mg alloys have been used for diesel piston reinforcement for years. Due to the extreme environment seen by these parts, extensive thermal analysis has been done on these alloys. While conductivity is improved using SiC fibers, accelerated aging due to CTE mismatch between metal and fiber limits the component lifetime⁹⁰.

1.4.4 Coatings for Composites

Although numerous coatings are available for conventional metals and for plastics, the technology to coat FRCs is only now becoming commercially available. Typically, this is due to the difficulty in bonding to both the exposed fiber and matrix material. Thermal spray coatings have been demonstrated for FRCs which focus on increasing wear resistance. These coatings are typically metals such as nickel, chromium carbide, tungsten-carbide-cobalt⁹¹. The thermal spray process is flexible enough that just about any material can be thermal spray coated onto just about anything else⁹². Published performance of these materials has not addressed thermal performance other than peak operating temperatures.

A few specific applications of FRCs coated for thermal management have been published. A carbon fiber reinforced piston was developed at the Western Michigan University. For thermal protection the piston was coated with a 0.003 inch stainless steel layer followed by 0.1 in magnesium oxide zirconium oxide coating⁹³. For a satellite application, aluminum doublers were replaced with aluminum clad carbon-carbon composite resulting in a 19% mass reduction over aluminum⁹⁴. While this example is not strictly a coated FRC, it is functionally equivalent. Ceramic thermal barrier coatings have been used in Rolls-Royce jet engine combustion chamber and turbine stator blades. Fiber reinforced, coated blades outperformed metallic and monolithic ceramic blades under transient thermal conditions⁹⁵.

From the literature, it appears that the technical ability to tailor the thermal properties of FRCs has been established. The ability to coat FRCs with numerous materials has also been demonstrated. A handful of applications have been published that use the combination of tailored FRCs with coatings for thermal management.

1.5 Hypothesis

FRC materials offer the possibility to reduce mass and increase strength of reciprocating components in the internal combustion engine. The most challenging conditions seen are for those components exposed to the high temperature, pressure and oxidative environment inside of the combustion chamber. To date, the FRC materials chosen for in combustion chamber applications have been either ceramic matrix composites or carbon-carbon composites. These are energy intensive and time consuming to produce, can be very expensive, and are characterized by brittle failure modes which does not bode well for the rest of the engine. There is an opportunity to extend the performance of “lower performance” FRC materials that are more easily processed and have a more graceful failure mode. The hypothesis of this research then becomes;

“Structurally sound, one-piece, near net shape molded fiber reinforced polymer matrix composite IC engine valves can overcome the manufacturing complexities seen in previous attempts to reduce valve train reciprocating mass by using composite materials. Further, it is possible to extend the useable range of one-piece net shape resin transfer molded polymer matrix, fiber reinforced

composite materials by using a combination of coatings and tailored fiber placement to withstand the structural and thermal conditions in extreme thermal oxidative environments such as the combustion chamber of an engine.”

As a case study for much of the work presented, an engine intake valve was chosen. However, when this was not appropriate or prudent, alternate methods were used. Intake valves were chosen because:

- FRC valves are easily inserted into an existing engine.
- Net-shape FRC valves not have been (successfully) demonstrated to date.
- Validating FRC valve design is synergistic with existing valve dynamics and valve seat design work going on within the engines research group at the MERC.
- Potential research sponsor(s) are interested in applications of FRC valves in racing engines.

2 Modeling and Analysis

2.1 Introduction

In support of the hypothesis described in the previous chapter, both initial and detailed modeling and analysis has been accomplished. Initial structural modeling was used calculate the mass reduction enabled by the use of FRC engine components via direct substitution and if the components were redesigned with reduced inertial loads taken into account. In addition, an attempt was made to quantify the additional effects of reducing reciprocating mass. This work is detailed in section 2.2, "Prediction of Mass Reduction."

Detailed design of FRC components is possible with commercially available Computer Aided Design (CAD) software. A detailed structural design of a FRC intake valve was accomplished with the goal of meeting or exceeding the performance of the stock steel valve. This structural design work is documented in section 2.3 "Structural ."

Initial transient thermal analysis was conducted to determine the difference in surface temperature between a steel component and an FRC component exposed to the combustion chamber environment. Simple assumptions were made to determine the effect of fiber orientations on thermal performance. This work is detailed in section 2.4.1 "Initial Transient Thermal Analysis."

As a result of the initial thermal analysis, a much more in depth study on the response of uncoated and coated FRC materials under transient thermal loading was undertaken. This is detailed in section 2.5 “Detailed Analysis of FRCs and Coatings,” is by far the most in depth of the modeling undertaken and sheds insight into the performance of FRCs exposed to the combustion chamber-like environment. Although the modeling in this section is generic, a recommendation for an initial thermal design for an FRC intake valve is made.

2.2 Prediction of Mass Reduction

By necessity, the majority of the work done in developing FRC engine components to date has involved producing a component that will directly substitute for a metal part. Using this methodology, nearly all the reciprocating components in an engine have been produced. However, they have not been adopted for a host of reasons. One potential reason is that the benefit of replacing a single component in an engine system already designed for metal components has little advantage. The full advantage of using FRCs can only be realized through the additive effects of combining these components to maximize mass reduction.

In this section, a prediction of engine weight reduction is made for direct substitution of FRCs. An additional prediction is made to quantify the additive effects of mass reduction on component mass, and power. It is estimated that engine mass might be reduced by as much as 70% using FRCs and reciprocating mass might be reduced by as much as 90%. In addition, increased

mechanical efficiency on the order of 2% may be possible from reduced inertial and frictional loads.

2.2.1 Potential Mass Reduction by direct substitution

An exercise was undertaken to predict how much mass reduction would be possible if an entire engine were made using FRC components. The objective was to determine how much weight savings would be possible using direct substitution of FRCs for as many components as possible. It was assumed that component shapes remained unchanged and were not optimized for FRC use. An estimate of mass reduction for each component, and mass reduction for the entire engine was determined.

2.2.1.1 Methodology for determining weight savings:

A baseline engine, chosen to use as a reference, was a Lycoming 540 cubic inch (8.8L) series engine. General specifications for this engine are shown in Table 8.

This engine is fairly common for use in light civil aviation. Using the data discussed above, an estimate of weight reduction was made using FRCs for all the components of a modern aircraft engine.

Each component of the engine was weighed and its material noted. Based on engineering judgment, an appropriate composite material was chosen for substitution. For a component where existing published experimental data was available, that data was used to determine mass reduction values. Using the existing mass data, and experimental results from previous researchers,

mass reduction was calculated for each component and tabulated. The values shown in Table 5 were used in this step.

Table 8. Lycoming 540 series baseline engine data

MANUFACTURER	LYCOMING	
Configuration	Horizontally Opposed 6 cylinder	
Displacement	540 cubic inch	8849 cubic cm
Bore	5.41 inches	137 mm
Stroke	3.9 inch	99 mm
Power	235-360 HP	175-268 kW
Operating speed	2400-2600 RPM	
Compression Ratio	7.2:1 to 8.7:1	
Fuel Delivery	Carbureted or Throttle Body Injection	
Turbocharger	Optional	
Dry weight	364-536 lbs	165-243 kg

For example, the mass of an FRC piston or the baseline engine was calculated using the equation:

$$m_{FRC_piston} = m_{metal_piston} \times (1 - PR) \quad \text{Equation 6}$$

Where:

m_{FRC_piston} : predicted piston mass

m_{metal_piston} : mass of the original metal piston

PR: Published mass reduction

The piston of the baseline engine weighed 3 lbs and was made of aluminum. Table 5 shows a 60% reduction using Carbon-carbon composite. Using equation (1) results in a single FRC piston weighing 1.2 lbs and six FRC pistons weighing 7.2 lbs.

Where published experimental data was not available, a ratio of densities of the materials was used to calculate the mass of the replacement part. Density calculations were made using the following calculation:

$$m_{FRC_piston} = m_{metal_piston} \times Density_Ratio \quad \text{Equation 7}$$

Where:

$$Density_Ratio = \frac{\rho_{FRC}}{\rho_{metal}} \quad \text{Equation 8}$$

ρ_{FRC} = density of the composite material

ρ_{metal} = density of the metal

Table 9 shows the values used for the density ratio substitution.

Table 9. Density ratios for metals to FRC substitution.

TO: FROM:	ALUMINA/ ALUMINUM	GLASS/ EPOXY	CARBON/ EPOXY	CARBON/ CARBON
Steel	0.45	0.22	0.17	0.22
Cast iron	0.49	0.24	0.19	0.24
Aluminum 6061-T6	1.3	0.63	0.51	0.63
Cast Aluminum	1.25	0.60	0.49	0.61

For example, there is no experimental data for replacing steel pushrods with composites. The original steel pushrods weighed 0.25lb each. Based on the density ratios in Table 9, substituting the steel pushrods with a filament wound carbon/epoxy pushrod with 80% volume fraction carbon fiber would result in an 83% mass reduction. The resulting 12 pushrods would then have a total weight of 0.51 lbs. This methodology was repeated for all the engine components measured. Weights and materials of the original components, as well as the substitution details are shown in Appendix 2: tabulated mass reduction by material substitution.

2.2.2 Quantifying Mass reduction using the “additive effect”

An attempt was made to quantify how this “additive effect” would reduce the overall mass of the reciprocating components of an engine. The objective of this exercise was to determine how much weight savings could be achieved if each component were redesigned to take into account the reduced inertial load resulting from using FRCs for the other system components. The same baseline Lycoming engine was used as a reference.

2.2.2.1 Assumptions:

For the purpose of this exercise, the connecting rod was assumed to have 50% of its mass at the piston and 50% of its mass at the crankshaft. Thus, its motion was evenly divided between rotational and translational. While this is not completely accurate, it does give a reasonable approximation.

For all reciprocating components, the most extreme loads are experienced immediately after Top Dead Center when both combustion and inertial forces are accelerating the components downward.

Because fiber-reinforced composites have highly isotropic material properties, the maximum strength of the fibers (Table 1) were not used in these calculations. It was assumed that a “more isotropic” lay-up was used. A value of 70% of actual fiber strength was used for the composite strength. This is typical for a roughly 70% fiber volume fraction with pseudo-isotropic, $[0,+-45,90]_s$ layup.

Because loading on structural components of the engine (crankcase, cylinder head, engine mounts) is a function of the engine application and difficult to quantify, an estimate of mass reduction for these components was not attempted.

2.2.2.2 Methodology

Based on the engine dimensions and assumed combustion pressures, estimates of the dynamic loading of the piston, wrist pin, connecting rod and crankshaft were all calculated.

For each component, the major failure modes were determined. For example, potential failure modes for the piston wrist pin were; 1) material failure due to direct shear, 2) material failure bending, 3) excessive deflection due to bending. For each failure mode examined a potential mass reduction of the component was determined. For example, in direct shear, the stress on the wrist pin can be represented as:

$$\tau = \frac{V}{A} = \frac{F}{2A_{pin}}$$

Equation 9

Where:

F = Force on the piston due to combustion and inertia

A = the cross-sectional area of the wrist pin

Solving for the required cross sectional area of the wrist pin:

$$A_{pin} = \frac{V}{\tau} = \frac{F}{2\tau}$$

Equation 10

The ratio of areas for the new and old pin can be found:

$$\frac{A_{pin,new}}{A_{pin,old}} = \frac{F_{new}\tau_{old}}{\tau_{new}F_{old}}$$

Equation 11

Solving for the cross-sectional area of the “new” pin:

$$A_{pin,new} = A_{pin,old} \frac{F_{new}\tau_{old}}{\tau_{new}F_{old}}$$

Equation 12

Knowing the cross-sectional area of the new pin and using the definition of mass as the product of density and volume, and assuming length remains constant, the mass of the wrist pin can be calculated. Substituting and solving for the mass of the new wrist pin yields:

$$m_{pin,new} = m_{pin,old} \frac{(\rho A_{pin})_{new}}{(\rho A_{pin})_{old}}$$

Equation 13

A similar set of calculations was repeated for each possible failure mode. Based on these calculations, the most conservative estimate for mass reduction was chosen. This mass reduction was then rolled into the calculations for the next component (using Figure 9 as a guide). So reducing piston and wrist pin

mass reduced the inertial loading on the connecting rod and eventually the crankshaft. Using this methodology, and the same materials as in example 1, a total potential mass reduction was determined for the reciprocating components.

2.2.3 Prediction results

2.2.3.1 Results of mass reduction by direct substitution

Using the simple substitution method described above based on the work of previous researchers, an overall mass reduction was estimated. For the purpose of simplification, components were divided into sub categories based on function. The results of this exercise are summarized in Table 10. It can be seen that an overall mass reduction of 55% is predicted. More significant reductions in the reciprocating mass of 72% and in the structural mass of 68% are also predicted.

An examination of the component weights reveals that the crankshaft and engine block/cylinders and cylinder head combine for over 50% of the engine mass. Reducing these by 50% alone could decrease the mass by 25% and increase the power density of an engine. For the baseline engine, this results in an increase in power density from roughly 1 kW/kg to 2.2 kW/kg, an increase of over 100%. But, as illustrated above, the real improvements related to mass reduction come when the entire engine is considered as a system.

The method described above assumes a substitution with a pseudo-isotropic composite material, i.e. replacing the part with “black aluminum.” In reality, fiber orientation can typically be optimized, and further mass reduction

can be achieved. This is especially true of components under relatively simple, directional loading such as connecting rods and push rods. For components under more complex loads, such as an engine block or crankshaft, these predictions should be relatively accurate. These predictions are in-line with results that have been achieved using FRC materials for individual components in the aerospace industry as well.

Table 10. Summary of weight reduction using direct substitution

	MASS BEFORE (KG)	MASS AFTER (KG)	PRIMARY MATERIAL	% REDUCTION
Starter/ Alternator	30.0	30.0	None	0%
Accessories	24.5	12.5	PMC	49%
Intake/ Exhaust	69.5	26.5	PMC/ MMC	62%
Covers	30.5	8.6	PMC	72%
Miscellaneous	48.0	45.9	None	4%
Reciprocating Mass	53.35	14.91	C-C/ PMC	72%
Rotating Mass	91.0	50.2	MMC	45%
Structure	257.4	82.3	MMC	68%
Total:	604.25	271.0		55%

2.2.3.2 Results of “Additive Effects” Mass reduction

The results of these calculations are summarized in Table 11. Results are based on the baseline engine data running at 2500 RPM. Predicted reduction in total reciprocating mass is on the order of 90%.

Table 11. Predicted Reduction of reciprocating mass

	ORIG MASS (KG)	ORIG MATERIAL	FRC	END MASS (KG)	MASS RED.
Piston	1.36	Al	Carbon -carbon	0.41	70%
Wrist Pin	0.40	Steel	Carbon -epoxy	0.08	79%
Connecting Rod	1.36	Al	Carbon -epoxy	0.45	67%
Crank shaft	30.62	Stainless Steel	Carbon -epoxy	2.65	91%

Reduction in structural mass was not evaluated due to the complex loading of the engine block and cylinder heads. However the same type of reasoning can be used. Because of the nature of designing engine components with FRCs will involve some tradeoffs, it is reasonable to expect slightly different results. Even so, it is probably realistic to expect a 70-80% reduction in overall engine mass using FRC components.

2.2.4 Inertial and frictional power losses

In any engine, power is required to keep the mass of the reciprocating components in motion. In reducing the reciprocating mass of the engine, we can

expect to gain some increase in brake power due to decreased power to maintain the inertia of these components. This inertial power can be thought of as having two sources, reciprocating mass and rotating mass. Reciprocating mass includes the piston, wrist pin and some percentage of the connecting rod (assumed to be 50% for this exercise). Rotating mass includes the crankshaft, part of the connecting rod (again, 50%), flywheel and/or propeller in an aircraft. An attempt was made to quantify the power gains due to reduced reciprocating mass at constant engine speed.

2.2.5 Reciprocating power losses

Power required to move the reciprocating mass is fairly straightforward. For linear motion, power is defined as the product of force and speed. Force can be determined from the mass and acceleration of the components. Piston speed is easily determined knowing engine speed. For a balanced engine at constant velocity, the net acceleration of the components through one cycle is zero, thus there is no power loss. This will not be true for an accelerating engine.

2.2.5.1 Frictional Power Losses

Frictional losses in engines are a widely studied topic. Frictional power losses have been estimated at 17-19% of total engine power. Of that, 35-45% of friction is from the piston ring assembly. The crankshaft bearing system represents 20-30% of friction losses, the valve system 7-10%, and engine auxiliaries 20-25%²³.

2.2.5.1.1 Piston Friction

The frictional force caused by the piston rings is proportional to the normal load, which is in turn proportional to lateral acceleration and piston mass. Thus, reducing piston mass will have a direct effect on reducing frictional force and frictional power loss. For the baseline 6-cylinder engine this would translate to between 12.5 and 20 kW. The reduction in piston mass would correspond to 2.4kW or between 1% and 1.5 percent of BHP.

Friction Mean Effective Pressure (FMEP) is a function of piston mass and operating speed. Using previously tabulated data and extrapolating, at 2000 rpm a piston mass reduction of 70% (from Table 11) may yield a roughly 5% decrease in FMEP⁹⁶.

Using this information, reducing reciprocating mass by 70% we can reasonably expect an increase in output of about 0.3% or 0.5 to 1 kW.

2.2.5.1.2 Bearing Friction

Power loss in journal bearings is proportional to the loading factor and bearing speed. For a constant speed, reciprocating mass is proportional to the load. Reducing loading on the bearings by 70% will reduce power loss by 70%²⁴. This would correspond to roughly a 1% improvement in power transmitted. For the baseline engine this corresponds to 1.75 to 2.7 kW. Overall efficiency increases by about 1%.

If bearings are resized to have a smaller diameter, this can be reduced even further. Perhaps 1.5% less power lost. The results of the frictional and inertial power calculations are summarized in Table 12.

Table 12. Increased efficiency attainable as a result of reduced reciprocating mass.

	EFFICIENCY INCREASE
Ring Friction	0 - 1 %
Bearing Friction	0 - 1%
Total	0 - 2%

Increasing the role of FRCs in major engine components has the potential to significantly increase the power density of the engine. The baseline engine is not state-of-the-art in engine design but a much more traditional design. If the same type of analysis were applied to a more modern engine, the results would be similar with higher numbers for power density. Figure 22 shows the change in specific power as a function of the percent reduction in overall engine mass.

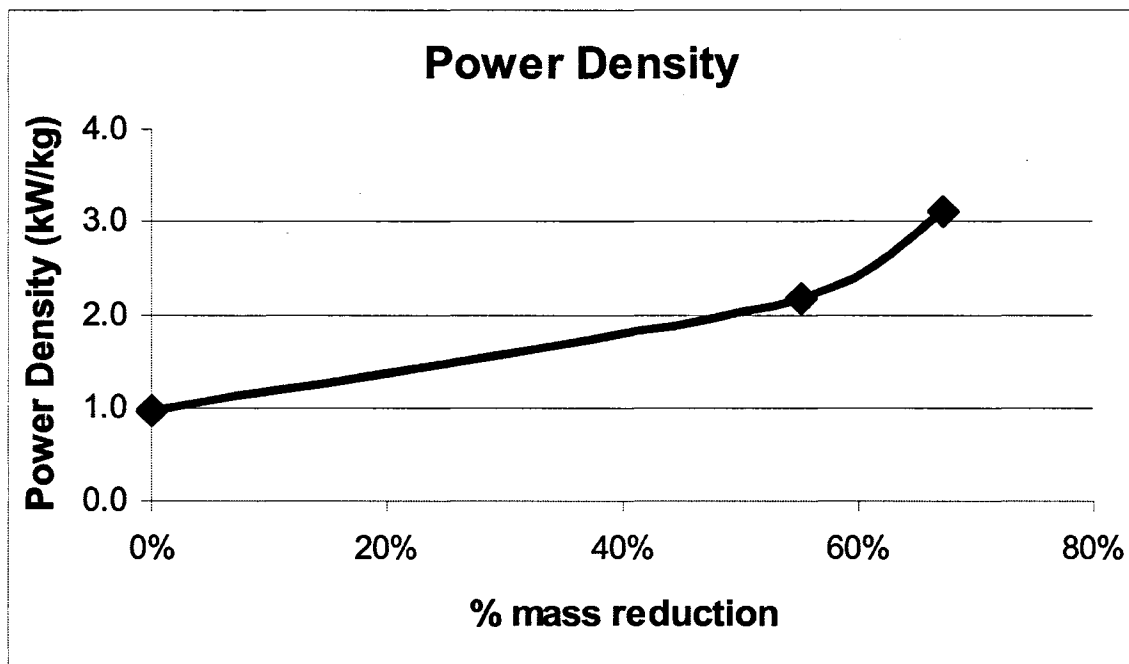


Figure 22. Specific power vs. percent mass reduction.

2.2.6 Limits to engine performance

The power benefit of reducing the mass of reciprocating components does eventually reach a limit. At some point, the limits to engine power are no longer governed by the ability to accelerate engine components, but by the ability to fill, burn and expel the fuel/air mixture in the combustion chamber. Extremely high speed, high performance engines such as those used in F-1 racing are reaching this limit above 20,000 RPM. However, the reduced mass made possible using FRCs will have more beneficial effects on overall vehicle acceleration, fuel efficiency and performance. These same concepts apply to “normal” passenger vehicles as well.

2.2.7 Other possibilities not quantified

FRCs enable other potential improvements to engine performance that are mentioned in the literature, but that have not been thoroughly explored. Some of these are:

The low coefficient of thermal expansion (CTE) available using carbon composites allows the possibility of extremely tight tolerances between the piston and cylinder wall. It is well documented that a portion of hydrocarbon emissions from spark ignition engines is a result of fuel/air mixture trapped in the top-land crevice. The tighter tolerances possible with FRCs may help in reducing the volume of this crevice, and thus reducing hydrocarbon emissions.

Currently, the fit of the piston/cylinder assembly is dominated by the CTE between the aluminum piston and steel cylinder wall. Constructing both of these components from low CTE composite materials has the possibility of reducing

piston friction, piston slap, and reducing the required ring tension. This, combined with the increasing popularity of low-friction coatings and/or self-lubricating composites opens the possibility of producing ring-less pistons. This has been explored as part of the NASA Langley effort⁵.

Tailoring thermal conductivity of composite materials in the combustion chamber, cylinder head and exhaust manifold offer the possibility of delivering more energy to a turbocharger. In a purpose-built composite engine, as much as a 20% improvement in thermal efficiency has been achieved using this method⁹⁷.

Less reciprocating mass in the engine compartment will mean greater life for those components. In addition to the benefits mentioned earlier, reducing the reciprocating mass reduces the magnitude of cyclic loading on all the components connected to the engine. This will help to increase fatigue life and durability, and reduce noise and vibration. Workers developing FRC engine components almost invariably mention reduced noise and vibration, though no work has been done to date to quantify this.

This discussion was based in the idea of substitution and redesign of existing components using FRCs. An engine designed from scratch, with the intent of using FRCs for the major components, may be able to make even larger steps in weight reduction.

2.3 Structural Design of an FRC Intake Valve

As mentioned in the previous chapter, an FRC intake valve for in an internal combustion engine was chosen to demonstrate the capability to withstand operation in the combustion chamber environment. Although a valve

may appear to be a trivial device, significant structural loading occurs during normal operation and extreme conditions. The design requirements and the process used for development of the FRC valve prototypes is discussed in this section, as well as material selection criteria for the fiber and matrix.

Resin transfer molding was chosen for the valve manufacture process for a number of reasons. The RTM process produces a one-piece net-shape part, requiring very little machining. The process is easily adaptable to prototype development and is scalable to high volume production.

2.3.1 Valve Requirements

The operating requirements for both an intake and exhaust valve were determined based on three target engines. These engines were:

1. 206 cc, single cylinder, 2-valve flat head utility engine
2. 2.0 liter, 45 degree V-twin, 2-valve/cylinder overhead valve motorcycle engine
3. A 2.4 liter , inline 4 cylinder, 4 valve/cylinder automotive engine

Of these three engines, engine #1, the flat head utility engine has the smallest diameter valve stem and most “square” valve profile. The load seen at valve bounce (discussed in the next section) is fairly constant over the three engines. As a result the state of stress seen in the valves in engine #1 represents the most severe loading condition in all three engines. For this reason, this valve was chosen as the focus of the design study. The presumption was that extending the design to a larger, less severely loaded valve would be a relatively simple exercise once the initial design was done.

2.3.1.1 Design Process

Structural design of the FRC intake valve was using the familiar steps in the engineering design process. The steps used in the design process were:

- Determine requirements, including loading, temperature, fatigue, corrosion, manufacturability requirements.
- Fiber Selection using evaluation of alternatives / Pugh Chart
- Matrix Selection using evaluation of alternatives / Pugh Chart
- Analysis and detailed design of fiber volume fraction and placement
- Validation of design

Methodology and results for each of these steps are presented in the following sections.

2.3.1.2 Valve Requirements: Loads

From the camshaft profile and valve train geometry, the position/velocity and acceleration profiles of the valve can be determined. Using this methodology and published peak engine speed, the worst case loading on the valve was determined. For engine #1, the valve acceleration profiles are shown below.

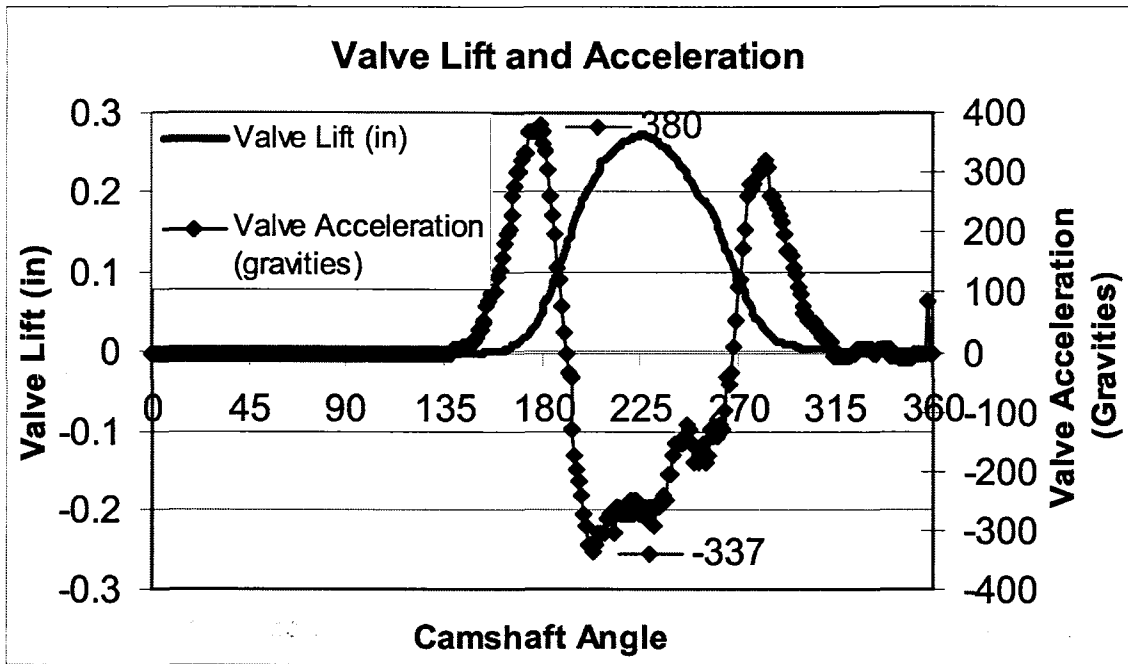


Figure 23. Valve position and acceleration plots versus crankshaft angle for engine #1, 7200 rpm (redline).

It can be seen from Figure 23 that the inertial loads on the valve are very high. Peaks in the acceleration occur at 380Gs and -337Gs.

Valve springs from the engine were also tested to characterize the spring stiffness. Knowing the spring stiffness, camshaft position (valve lift), valve acceleration and combustion pressure, it is possible to draw a dynamic free body diagram and determine the required rocker force to produce the force on the valve. Figure 24 is an example free body diagram of the valve.

From this free-body diagram, the equilibrium equation can be written by summing forces in the axial (y) direction.

$$F_{Actuator} + F_{Spring} + F_{y,Seat} + P_{Combustion} \cdot A_{Valve} = m_{Valve} \cdot a_{Body} \quad \text{Equation 14}$$

Where:

$F_{Actuator}$ = force exerted by the rocker on the valve tip

F_{Spring} = force exerted by the valve spring on the retainer

$F_{y,Seat}$ = the axial component of the force on the valve seat

$P_{Combustion}$ = the in cylinder combustion pressure

A_{Valve} = valve head surface area

M_{Valve} = the mass of the valve

a_{Body} = the acceleration of the valve

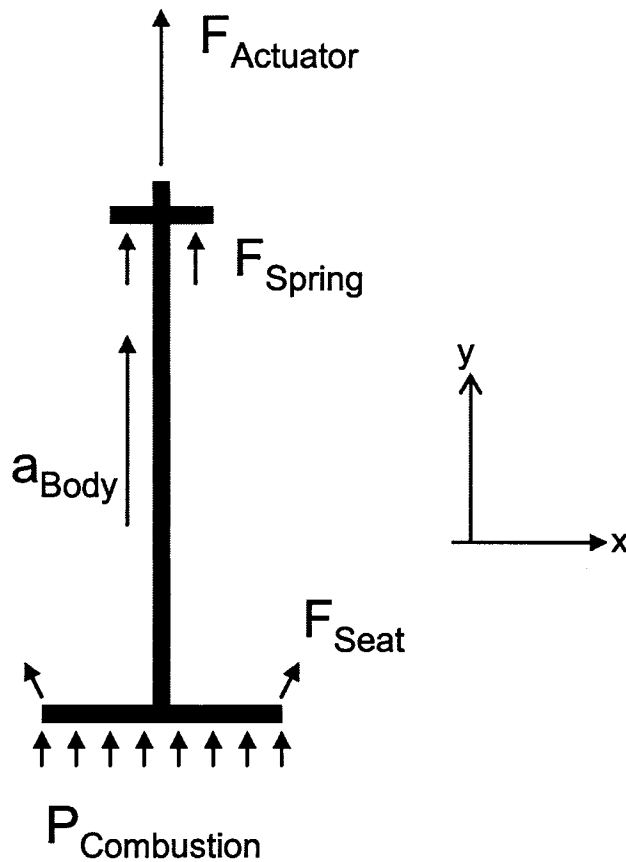


Figure 24. Free body diagram of the valve.

This was done at five points to determine the worst case load on the valve. These five load scenarios were:

1. Valve closed, combustion
2. Max positive acceleration

3. Max negative acceleration
4. Max valve lift
5. Valve Bounce

The loading in scenario #5 (bounce) was determined from previously published work which measured the force on the valve seat for a similar engine. Valve seat force was measured at between 2.5 and 3.0 kN at the start and end of bounce⁹⁸. An illustration of valve bounce is shown in Figure 25. A summary of forces on the valve for the five loading scenarios is shown in Table 13. It can be seen from the table that load scenario #5 (Bounce) is by far the most severe load the valve experiences.

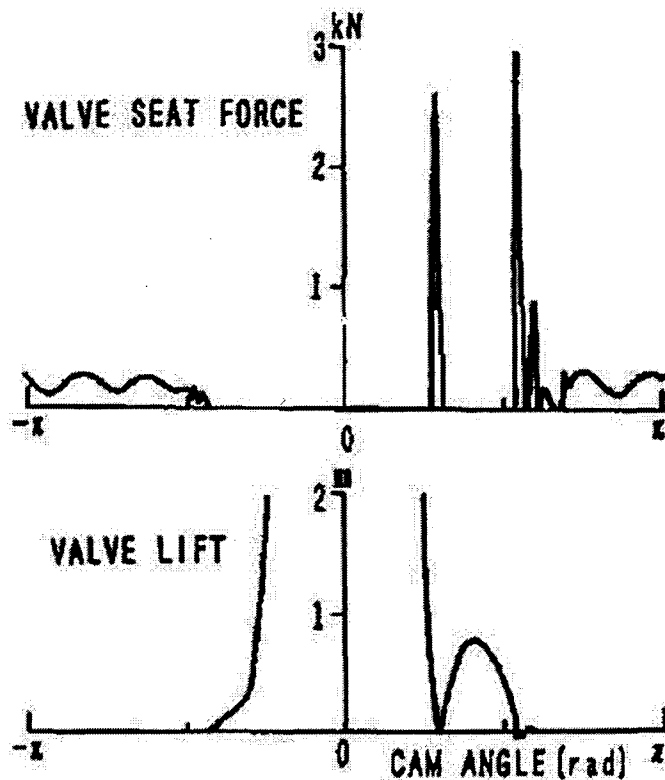


Figure 25. Plot of valve displacement and valve seat force vs. camshaft angle illustrating valve bounce³⁶.

Since the most severe loading was found to occur in load scenario #5 (valve bounce), all design work was done to this scenario.

Table 13. Summary of valve Load scenarios

LOAD SCENARIO	VALVE	F⁻ROCKER (KN)	F^S SPRING (KN)	F^YSEAT (KN)	P^CCOMBUST (MPA)	A^BODY (M/S² X 1000)
1	Intake	0.0	0.6	-0.6	10.1	0
1	Exhaust	0.0	0.6	-0.6	10.1	0
2	Intake	-1.6	0.7	0.0	0	-3.7
2	Exhaust	-2.2	0.6	0.0	1.01	-3.7
3	Intake	-1.6	1.0	0.0	0	3.7
3	Exhaust	-1.6	0.9	0.0	0	3.7
4	Intake	-2.5	1.1	0.0	0	-2.7
4	Exhaust	-2.2	1.0	0.0	0	-2.7
5	Intake	0.0	0.6	-6.0	0	-29.3
5	Exhaust	0.0	0.6	-6.0	0	-32.3

2.3.1.3 Valve Requirements: Temperature

Temperature requirements, especially on exhaust valves, are extremely severe. Previous work by Danis was done to characterize the temperature profile of a metal exhaust valve⁴⁰. Figure 26 shows the temperature and heat flow for a solid metal exhaust valve.

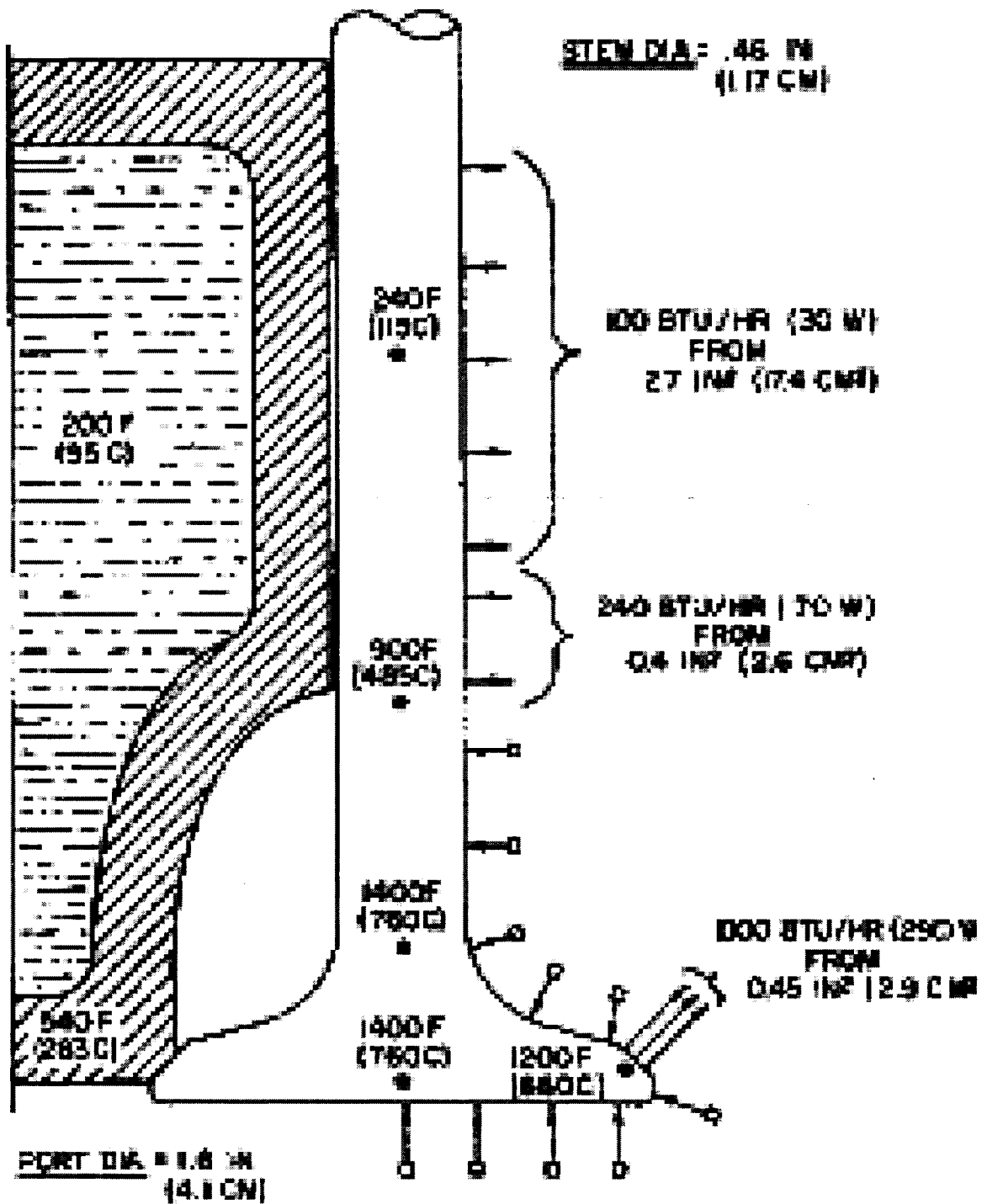


Figure 26. Temperature and heat flow for a metal exhaust valve in a gasoline engine⁴⁰.

It can be seen from Figure 26 that the surface temperature of a metal exhaust valve is in the range of 660°C in the combustion chamber and 95°C at the stem. This results in an internal valve temperature of up to 760°C. Intake valve temperatures are significantly lower due to the flow of the fresh air charge around the valve and on the backside. The only example found in the literature of intake valve temperatures in a gasoline engine measured temperatures at 370°C (700°F)⁹⁹. In designing a FRC valve, exhaust gas temperatures, and therefore valve surface temperatures may be similar, but internal temperatures will be different based on the thermal conductivity of the material chosen. Also, the primary path for cooling the valve is through the seat, and not through the stem as might be expected⁴⁰.

It will be seen later in this chapter and in subsequent chapters that this estimate of valve temperature was particularly low.

2.3.1.4 Fatigue strength

A calculation was done to determine the required fatigue life of a modern poppet valve. A valve in a modern passenger engine must last for 200,000 miles without replacement. For an engine running at 5000 rpm, this represents roughly 1 billion cycles over the valve lifetime. As a result, infinite fatigue life was chosen as a primary design requirement. In addition, the high temperature operation over this period makes resistance to creep a high priority as well. Certain composites, such as carbon-carbon, perform very well under these conditions.

2.3.1.5 Chemical environment

Typical valves are exposed to motor oil, gasoline, air and combustion products. High temperatures can make these very corrosive. The valve face is exposed to an oxidative environment. Resistance to these chemicals and to oxidation will be a requirement for the FRC valve.

2.3.1.6 Manufacturability

As previously mentioned, valve manufacture is a very slim margin industry. In order to be economically viable, manufacture of a FRC valve must offer significant performance advantage and/or cost reduction over a metal valve. This implies a near-net shape molded part with little machining required after removing the valve from the mold.

2.3.1.7 Validation of FEA for metal valve

A finite element model of the exhaust valve from engine #1 was constructed. The “bounce” loading scenario was examined and displacement versus load was plotted for the FEA model. A static test rig was constructed to perform tensile tests on the valve in a load frame. Figure 27 shows a picture of the valve static test apparatus. Load was applied to the valve as in the FEA model, with the keeper constrained and load applied to the valve seat. Displacement of a section of the valve was measured using a clip gage extensometer. A schematic of the test setup is shown in Figure 28. Testing showed that the load-displacement curves for the FEA model corresponded well to the test data for the same valve.

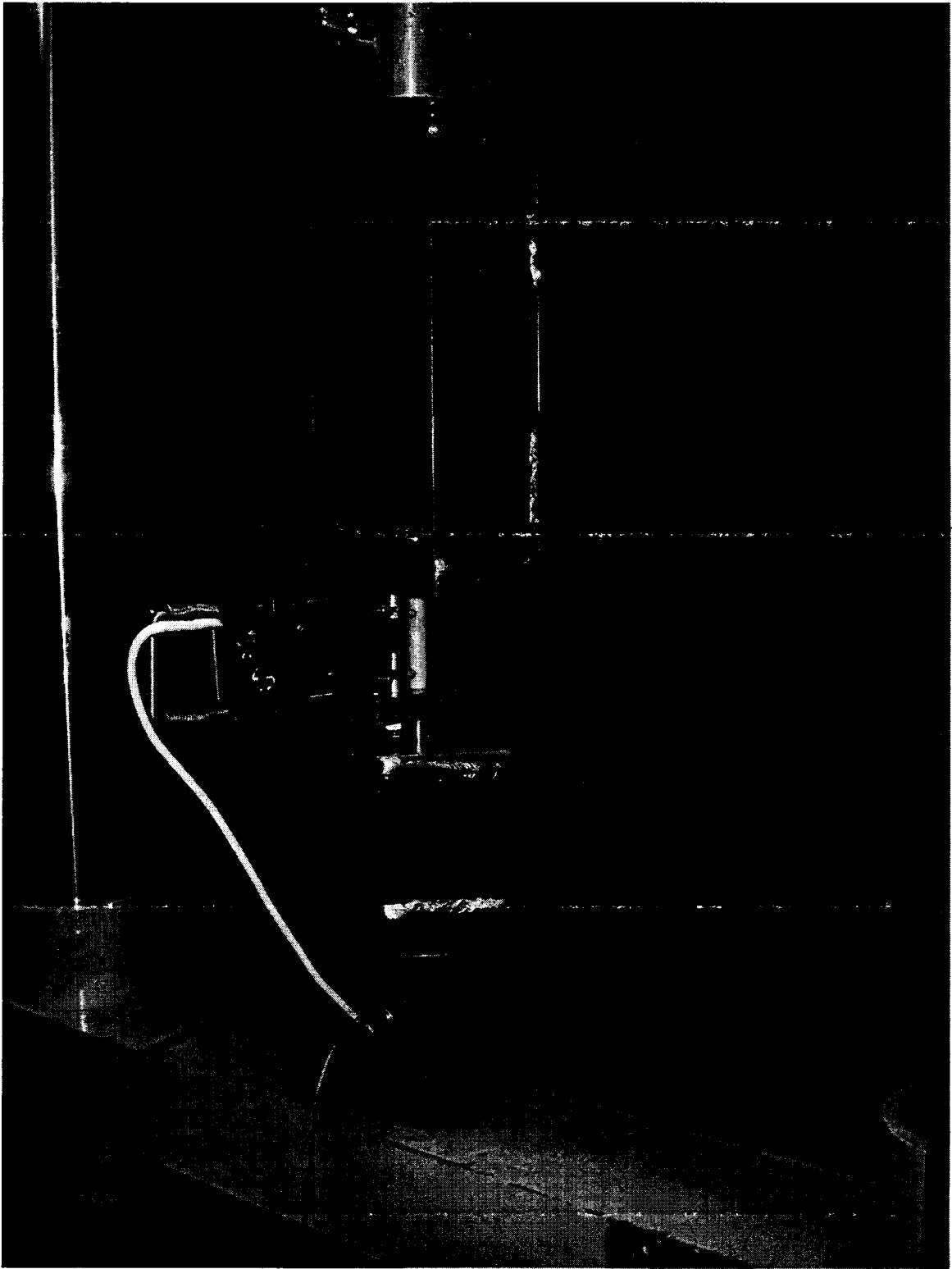


Figure 27. Valve static tensile test apparatus.

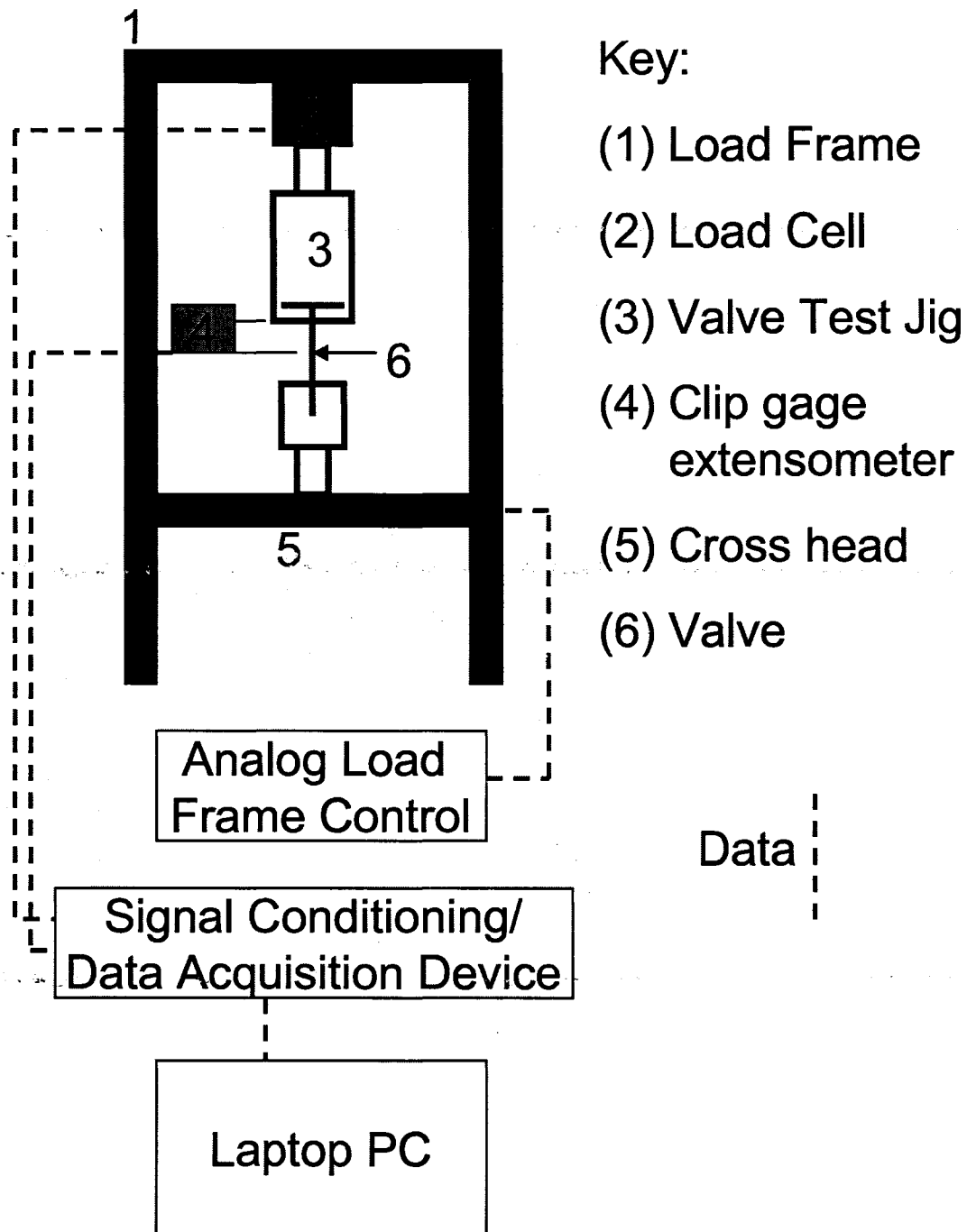


Figure 28. Schematic of the valve static tensile test setup.

2.3.2 Material Selection and Fiber Placement

Once the design requirements for the FRC valve were understood, the design process and tools were used to find suitable solutions to meet the requirements for fiber and matrix selection. That process and solutions are detailed below.

2.3.2.1 Fiber selection

There are a many potential fibers that can be used for reinforcement in a composite material. The fibers considered for reinforcement of the RTM valve were:

- Glass
- Carbon
- Metal
- Kevlar
- Alumina/Silica

Evaluation of fiber alternatives was first done by comparing fiber performance to valve operating conditions. The two primary concerns in this area were:

1. The fiber must have the ability to withstand the high operating temperatures associated with operation in an internal combustion engine.
2. The fiber must have a specific modulus and specific strength higher than that of conventional metals. Choosing a fiber that does not meet this requirement would result in a valve inherently weaker than a metal valve.

Since the fibers are embedded in a polymer matrix material, corrosion and oxidation requirements were not considered. Requirement #1 for temperature immediately eliminated glass and Kevlar fibers. Kevlar fibers maximum service temperature is 149°-177°C, well below the temperature requirement for a valve. Glass fibers typically melt at around 1725°C, however the glass transition temperature (the point at which viscosity decreases) is significantly lower typically below 300°C and as low as 140°C ⁷.

Hence, the two possible candidates for fiber reinforcement became carbon fiber and Alumina/Silica fiber. Since both are ceramics, they have high temperature resistance and very high specific strength/specific modulus. Table 14 shows the ranking of fibers based on performance and the significant performance criterion used.

Table 14. Fiber selection results.

FIBER	RANK	FAILURE STRENGTH (MPA)	MAX SERVICE TEMPERATURE (°C)
CARBON	1	1600	1900
ALUMINA/SILICA	2	1560	1175
E-GLASS*	3	550	140
KEVLAR-49*	4	300	149 - 177
* DO NOT MEET TEMPERATURE REQUIREMENTS			

2.3.2.2 Matrix Selection

For the purpose of this discussion, matrix materials refer to the material used to bond fibers together and fill the mold. Evaluation of matrix alternatives was first done by comparing matrix performance to valve operating conditions.

The three primary concerns in this area were:

1. The matrix must be capable of withstanding the normal valve operating temperature
2. The matrix must be compatible with the fiber chosen
3. The matrix must have a working viscosity low enough to enable Resin Transfer Molding and complete fiber wetting

Corrosion and oxidation resistance were considered, but with lower importance. For matrix selection, the temperature requirement is different for the intake and exhaust valve. Metal exhaust valves regularly see temperatures above 700°C, far above the range of traditional polymers. However, intake valves are subjected to far lower temperatures. High-temperature polymers are capable of sustained performance at 350°C, which is above the requirements for an intake valve.

The matrix materials considered were:

- Aluminum
- Bismaleimide (BMIs) – a cross-linked thermoset
- Polyimide (PI) – a high temperature thermoplastic
- Langley Research Center Soluble-imide (LARC-Si)
- PMR-15 (a high-temperature polyimide)

- PMR-II (similar to PMR-15 but with reduced carcinogens)
- LaRC PETI-RFI (a high-temperature polyimide viscosity modified for resin transfer molding)
- Silicon Carbide (SiC)

Of the matrix materials considered, PMR-15 has been shown to be capable of operation at 350°C and at 371°C for 100 hours¹⁰⁰. However, other sources report that it withstands sustained use at 288°C¹⁰¹. In addition, PMR-15 contains known carcinogens, a definite drawback.

BMIs and PI have achieved glass transition temperatures of 300°C¹⁰². Condensation Polyimides have achieved operating temperatures in the 343° to 371°C range, but processing requires high temperature and high pressure cures such as in a hydroclave, thermoclave or compression molding. PMR-II is similar to PMR-15 and is good for operating temperatures from 288°-343°C. However, inert-environment high temperature (500°C) post-cures of both PMR-15 and PMR-II have resulted in glass transition temperatures of 427°C¹⁰¹. BMI matrix materials also have strengths higher than high-strength epoxies and moduli comparable to epoxies at high temperature¹⁰³.

Property data of matrix materials can be difficult to compare. Table 5 is a summary of high-temperature thermoplastics compiled by Mangalgi¹⁰⁴. It can be seen that glass transition temperatures (T_g) peak at 290°C for PAI, and service temperatures peak at 270°C for PAI¹⁰⁴. This is significant in that typical service temperatures for polymers are 20°-30°C below the glass transition temperature.

Although aluminum has been used successfully in metal-matrix composite components for engines, including connecting rods and pistons, the high loading and high temperature combination seen in a valve was deemed too severe.

Aluminum melts at 660°C, and significant creep occurs at lower temperatures.

SiC offers outstanding matrix properties, however it was eliminated because it requires a Chemical Vapor Deposition (CVD) or Infiltration (CVI) process to produce. This is time consuming and is not compatible with the RTM process.

	TYPICAL PRODUCT	T_g (°C)	MELT POINT (°C)
Polysulphone (PSU)	Udel P1700 (Amoco)	190	--
Polyethersulphone (PES)	Victrex 4100G (ICI)	220	--
Polyamideimide (PAI)	Torlon (Amoco)	290	--
Polyetherimide (PEI)	Ultem (GE)	217	--
Thermoplastic Polyimide (TPE)	Avimid KIII (DuPont)	250	--
Thermoplastic Polyimide (LaRC-TPI)	Aurora (Mitsui)	260	388
Polyketone	Victrex-HTX (ICI)	205	285
PEKEKK	Ultrapek (BASF)	175	375
Polyetherether-ketone	Victrex-PEEK (ICI)	143	343

Table 5, Thermoplastic matrices for high-temperature applications,
adapted from Mangalgi¹⁰⁴.

After considering the vast amount of data on high-temperature polymers it was decided that, for the intake valve, LaRC-PETI-RFI, should be used because

of the high operating temperature, ability to be resin transfer molded and local experience with the material¹⁰⁵.

The exhaust valve sees a much more severe environment, one that no current thermoset or thermoplastic can withstand. However, it is possible to create a carbon matrix from a polymer precursor. For this reason, it was decided that the matrix material for the exhaust valve should be graphitic carbon, made from an injection molded LARC-Si precursor. This will require high-temperature pyrolyzation and later Chemical Vapor Infiltration (CVI) to densify the matrix. The carbon matrix will also require coating for oxidation protection. Final matrix material selections are shown in Table 15.

Table 15. Material selection for the intake and exhaust valves.

Valve	Fiber	Matrix
Intake	Carbon	LaRC- PETI-RFI
Exhaust	Carbon	Carbon (LaRC-Si precursor)

2.3.2.3 Fiber Placement Analysis Using FEA

A finite element model was used to design the composite valve based on the worst case loading scenario (bounce) and the required fatigue life. Material used in the model was carbon fiber in an epoxy matrix. This should produce a conservative result, since the strength and modulus of the PETI-RFI matrix material is higher than that of epoxy.

2.3.2.3.1 Methodology

The methodology was to start with a minimum of fiber and place additional fiber layers based on where and how the fiber was predicted to fail by the FEA model. For each, the failure index was plotted along the length of the valve. The Tsai-Wu failure criterion was used for this problem. This gave an indication of where the fiber/matrix would be expected to fail first. From this data, ply-by-ply analysis was conducted to determine the failure mode or modes that were most likely to occur. For all the models, the peak stress occurred at the base of the valve stem and the dominant failure modes were transverse normal stress in each ply and in-plane shear stress for plies oriented at an angle to the valve axis. An example of this process is shown for model 1 below. A summary of the model progression and failure modes is shown in Table 16.

2.3.2.3.2 Structural Design Example - Model 1

Model 1 consists of a single layer of unidirectional carbon fiber, 0.125mm thick on the valve surface, with epoxy filler for the remaining volume of the valve. For the purpose of simplifying the analysis and reducing computation time, one half of the valve was modeled with a mirror constraint on the mid-valve cut surface. The valve keeper groove was constrained and a load of 3000N was placed on the valve seat, along the axis of the valve, placing the valve in tension.

From this model, the failure index was plotted for each ply in the model where:

$$Failure_Index = \left(\frac{actual_stress}{failure_stress} \right) \quad \text{Equation 15}$$

Table 16. Fiber model progression, configuration and failure mode(s)

Model #	Fiber and Orientation	Failure Location	Failure Mode(s)	Peak Failure Index
1	Single Uniaxial Fiber layer	Stem Base	Transverse fiber failure	8.7
3	Single Braid +/- 30	Stem Base	Transverse fiber failure and in-plane shear	5.24
4	Single braid +/- 30 and single uniaxial sleeve	Stem Base	Transverse fiber failure and in-plane shear	4.96
6	Two braids +/- 30, One braid +/-45 in stem base, fabric face	Stem Base	Transverse fiber failure and in-plane shear	3.99
8	Stem: Two braids of +/-30, Base, [+30/0/90]s	Stem Base	Transverse fiber failure	1.49
12	Stem: Two braids of +/-30 and 1.5mm uniaxial tow Base: 0,[-60/60/-60/60/-30/30]s	Stem Base	Transverse fiber failure	0.56

Figure 29 shows a plot of peak failure index of all plies in the model. It is clear that the area with the highest stress is at the base of the valve stem where the stem transitions to the valve head. Figure 30 shows an X-Y plot of failure index along the length of the valve stem. The left hand side of the plot represents the valve head; the right hand side represents the tip of the valve. This plot allows pin-pointing the ply in which failure occurs. Because this model consists of a single unidirectional ply, ply 1 represents the carbon fiber layer, and ply 2 represents the epoxy filler.



Figure 29. Peak failure index for all plies in the valve, model 1.

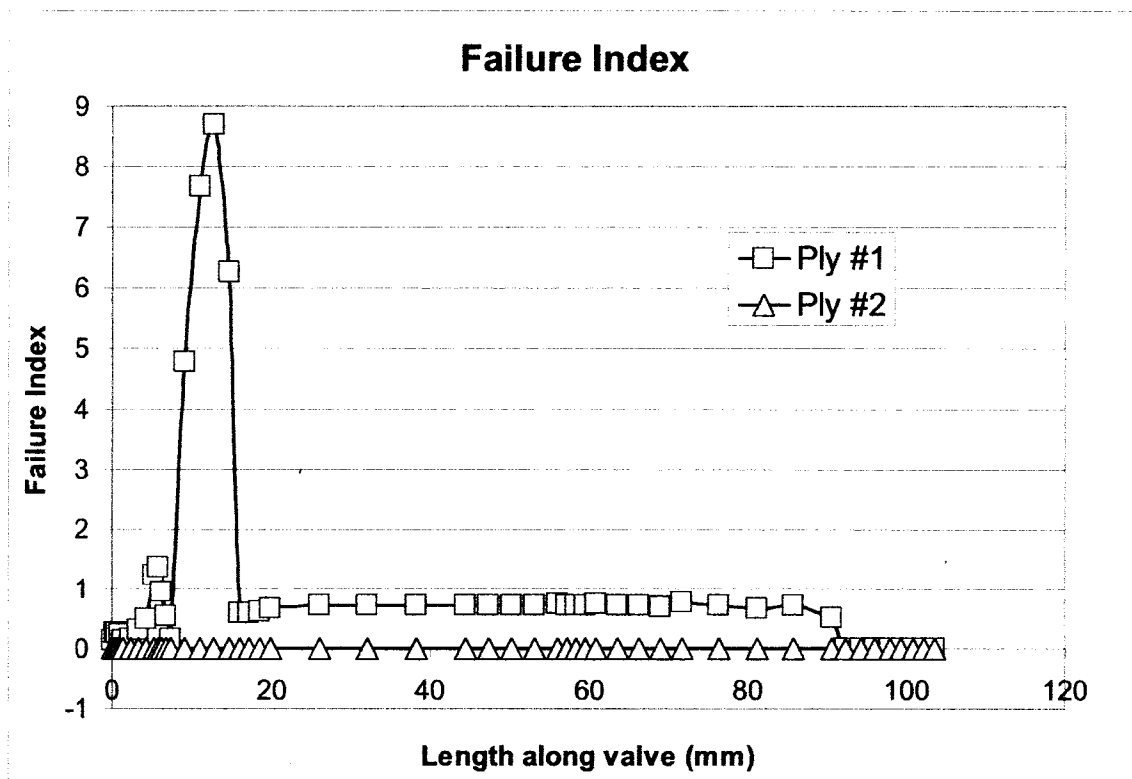


Figure 30. Failure Index for each ply, model 1.

From Figure 30 it is clear that failure occurs in the fiber layer, although the mode of failure is still unknown. The next step was to look at the specific stresses in each fiber layer. All plots of stress are done relative to fiber direction so that they can be compared to the Tsai-Wu failure criterion. Figure 31, Figure 32 and Figure 33 are plots of the stress in the fiber direction (σ_{xx}), in-plane transverse shear stress (σ_{xy}), and transverse normal stress (σ_{yy}) respectively.

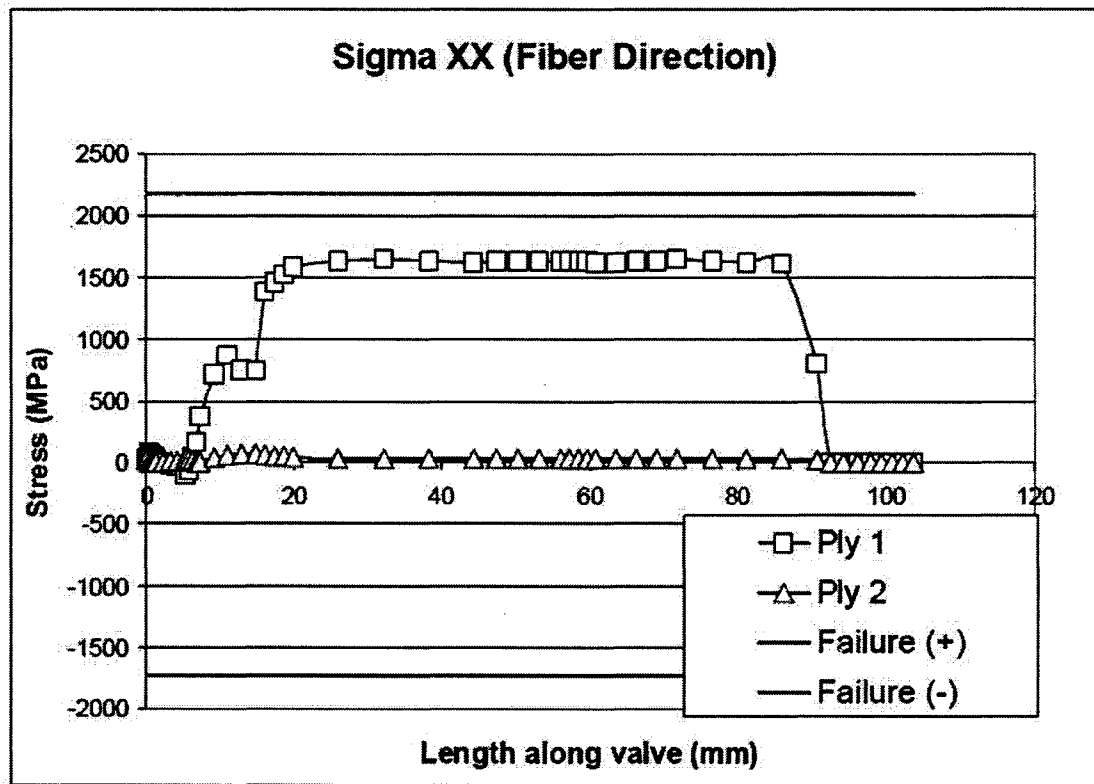


Figure 31. Stress in Fiber Direction (σ_{xx}) for each ply,

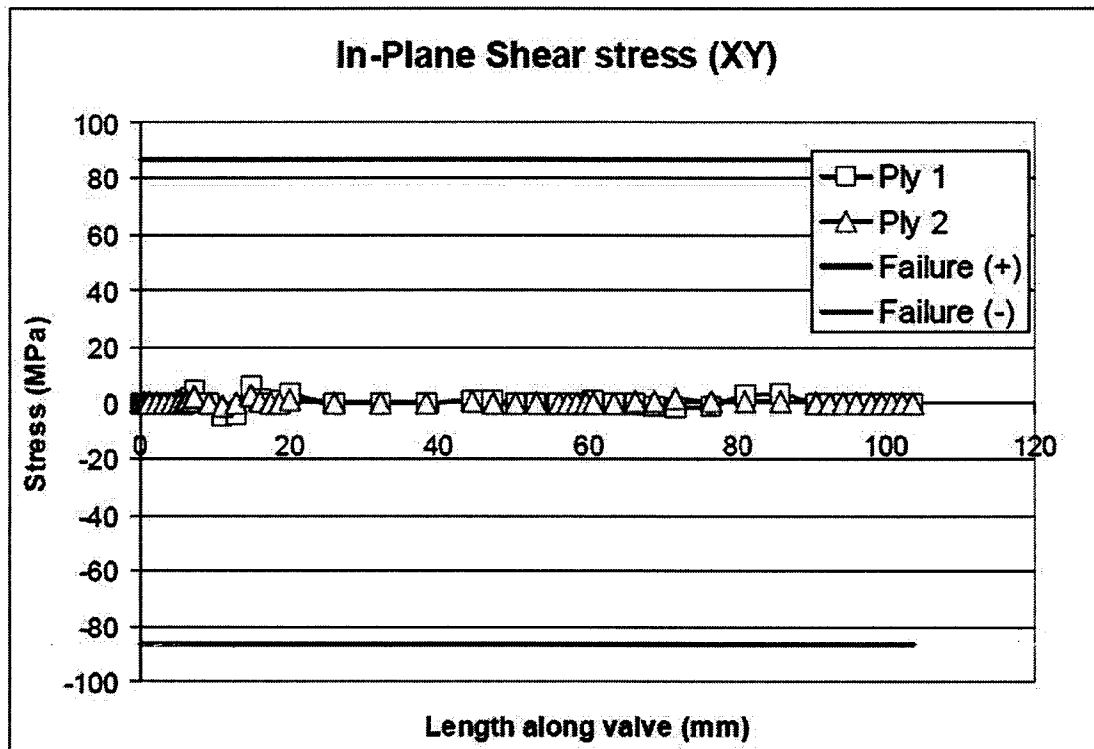


Figure 32. In-plane transverse shear stress (σ_{xy}) for all plies, model 1

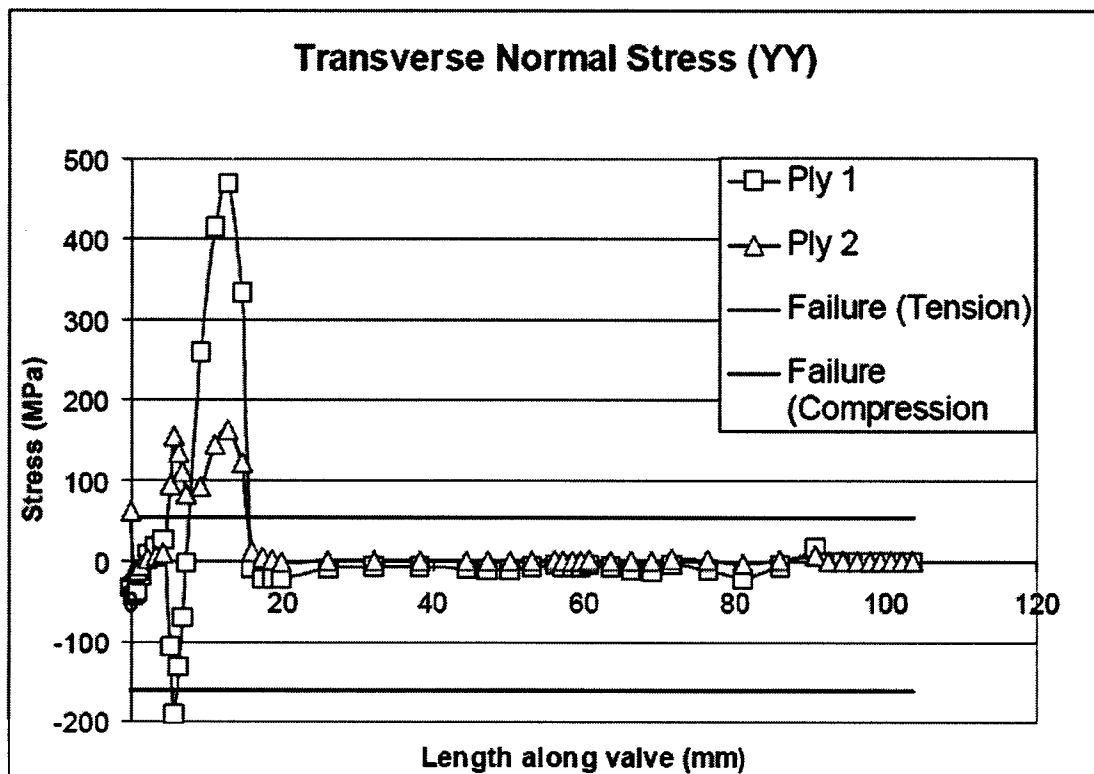


Figure 33. In-plane transverse normal stress (σ_{yy}) for all plies, model 1

It can be seen from these figures that, for model #1, failure is predicted to occur in the fiber layer, as a result of transverse normal stress, at the base of the stem. As expected from a laminated plate model, through-ply normal and shear stresses were insignificant.

This methodology was used for each model developed. A summary of the model progression, failure modes and peak failure index for some of the models is presented in Table 16. Braided sleeves were used in the model because of the ease of fiber placement and orientation in the mold. The table clearly shows the progressive reduction in the failure index as more fiber was added. Plots of Failure Index, and appropriate stresses for all 12 models are shown in 0, Appendix 3: Stress Plots for FRC valve structural design.

From the FEA analysis described above and progression shown in Table 16, the fiber orientation decided on for the current design was determined to be:

- Stem: [+30/+30/0]
- Stem base and seat: [+60/+60/+30]_s/0.

The CAD model of the valve predicts a mass of 18.3 grams. This represents a mass reduction of 50% over the stock steel valve.

In practical terms for assembly of the fiber preform, the final fiber design is:

In the stem:

- 2 x 1/4 in braided sleeves
- 120k axial UD tow [± 30 / ± 30 / 0]

In the transition area:

- 3 layers of braided sleeve
- 120k axial UD tow [$\pm 60/\pm 60/\pm 30/0$]s

2.3.2.4 Fatigue Strength

Carbon fiber has been shown to have effectively infinite fatigue life when loaded to 95% of failure strength in the axial direction¹⁰⁶. Since the failure index for the fibers in the axial direction in all plies of the laminate is theoretically well below 95% of failure strength, fatigue life is expected to be infinite. Based on the loads seen under normal operating conditions, transverse shear and normal stresses are also sufficiently low to ensure infinite fatigue life. However, continued operation at the “bounce” loading condition will produce failure after several hundred thousand cycles.

2.4 Thermal Modeling

Because the FRC material chosen for the valve has different thermal conductivity than the steel valve, thermal performance will be different. The goal of the analysis presented was to understand the thermal behavior of FRCs, and to understand the failure mode observed in the running engine. This should enable design of a solution that will allow performance of FRC valves under the thermal and structural loading experienced in a running engine. Thermal failures of the carbon PETI-RFI intake valve, discussed in chapter 4 also drove the need for a more in-depth thermal analysis. The analysis presented consists of two parts; 1) an initial transient thermal analysis using a basic one-dimensional model and simple tools and, 2) an in depth analysis of FRC materials and coatings to

understand the fundamental relationship and design criteria necessary for designing a generic composite material for thermal management and for operation in the extreme conditions of the combustion chamber. In addition, an initial thermal design for a FRC valve is presented.

2.4.1 Initial Transient Thermal Analysis

A simple transient, flat plate analysis was conducted to determine the approximate temperature of the valve face and the temperature profile through the valve. The purpose was to compare the thermal conductivity and resulting temperature distribution of the FRC valve to a standard steel valve. The valve was modeled as a plane wall with convective heat transfer as shown in Figure 34.

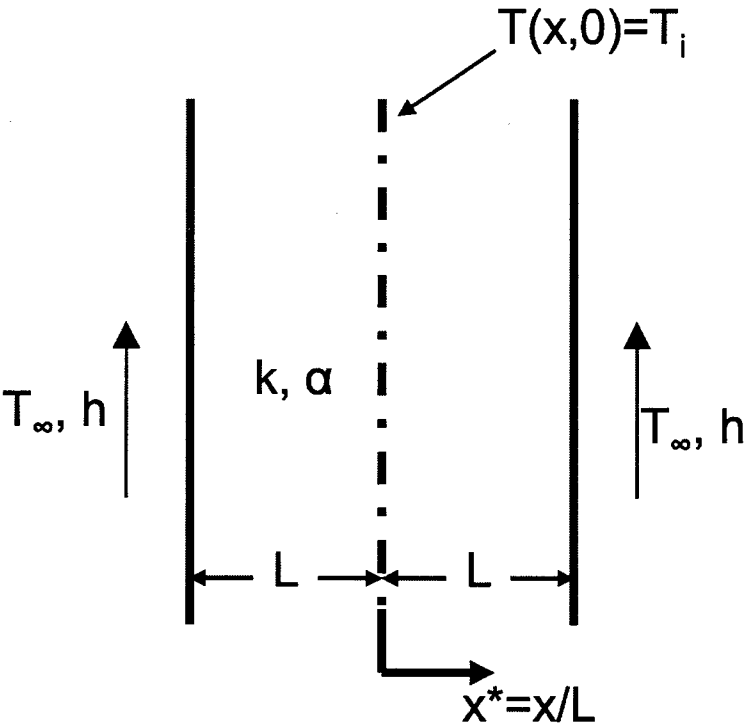


Figure 34. Plane wall with convective heat transfer, adapted from Incropera & DeWitt¹⁰⁷.

In the diagram above, the variables described are:

T_{∞} [K] Ambient fluid temperature

T_i [K] Mid-plane temperature

h [W/m²K] Convective heat transfer coefficient

k [W/mK] Conductive heat transfer coefficient

L [m] distance to the midplane

α [m²/s] thermal diffusivity

In this analysis, the temperature distribution at any instant and position in the plate is defined by the equation:

$$\Theta^* = \frac{\Theta}{\Theta_i} = \frac{T - T_{\infty}}{T_i - T_{\infty}} \quad \text{Equation 16}$$

Θ^* , the non-dimensional temperature distribution is defined as:

$$\Theta^* = \sum_{n=1}^{\infty} C_n \exp(-\xi_n^2 F_0) \cos(\xi_n x^*) \quad \text{Equation 17}$$

This produces a series solution that is the product of the Fourier number, F_0 , (a non-dimensional time constant) and a cosine term that is a function of distance from the mid-plane and ξ_n . ξ_n terms are a function of the ratio of conductive to convective heat transfer at the plate surface¹⁰⁷.

A simple analysis was conducted comparing the steel valve and two FRC valves, one with carbon fiber oriented parallel to the valve face and another with the fiber oriented perpendicular to the valve face. The values used for this analysis are shown in Table 17.

Table 17. Values used for transient heat transfer analysis.

VARIABLE	VALUE
h	490 W/m ² K
Lc	3.175 mm
T _∞	600 K
T _i	0 K
t	0.06 sec

The time, t of 0.06 seconds, corresponds to longest time the valve would be exposed to combustion and exhaust gasses. This represents 180 crank angle degrees at idle speed.

The material properties used are shown in Table 18. The two values of conductivity and diffusivity for the carbon/epoxy composites vary greatly because carbon fiber has an extremely high thermal conductivity along the fiber axis, but a much lower conductivity perpendicular to the fiber axis. The values used correspond to a 30% volume fraction of carbon fiber. Epoxy was used because appropriate data was not available for PETI-RFI.

Table 18. Material properties used for transient thermal analysis.

	STAINLESS STEEL	CARBON/EPOXY PARALLEL	CARBON/EPOXY PERPENDICULAR
K [W/mK]	50	0.456	24.5
α [m ² /s]	1.88x10 ⁻⁵	3.30x10 ⁻⁷	1.76x10 ⁻⁵

2.4.2 Initial Transient Thermal Analysis Results

The results of the transient thermal analysis for steel and for the two carbon/epoxy composites are shown in Figure 35. In this figure, the left side of

the plot represents the face of the valve, exposed to the combustion chamber. The right side of the plot represents the mid-plane temperature of the valve, at a depth equal to the thickness of the valve seat. This can be assumed to be the steady-state temperature of the valve.

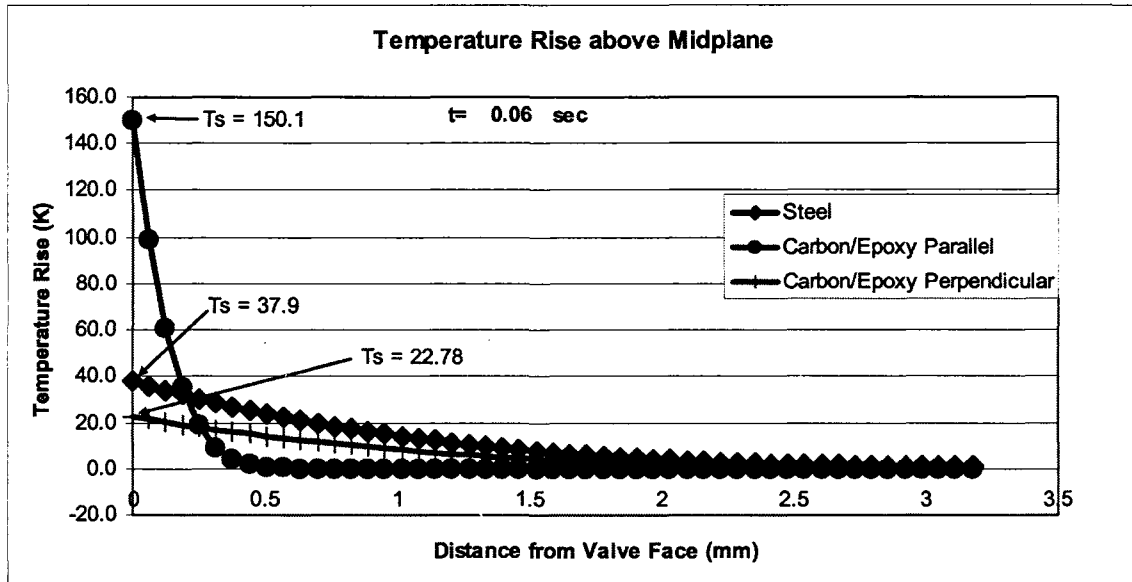


Figure 35. Calculated temperature distribution across the valve face for three different materials.

It becomes immediately apparent from this plot that the decreased thermal conductivity of the FRC valve in the configuration used (with fibers parallel to the face) does not allow heat transfer back through the valve seat. The result is a much higher surface temperature than the steel valve. This simplified analysis shows that the temperature at the face of the steel valve rises a mere 38°C above the steady-state valve temperature, whereas the carbon/epoxy with fibers parallel to the face experiences a temperature rise of 150°C. It is also interesting note that, by changing the fiber orientation in the valve face so that the fibers run perpendicular to the valve face, the axial conductivity of the valve increases and

the result predicted is a valve face temperature slightly higher (23°C temperature rise) than that of the steel valve.

It should be noted that these values represent a temperature rise above the steady-state temperature of the valve. It is still not clear from analysis how the steady state temperature of the FRC valve will compare to that of a steel valve.

2.5 Detailed Analysis of FRCs and Coatings

2.5.1 Purpose of this Study

The research presented in this section is two fold; 1) gain a fundamental understanding of the steady state and transient thermal behavior of orthotropic composite materials with and without coatings and, 2) apply this knowledge to the design of an FRC valve that will withstand operation in the extreme thermal environment of the combustion chamber. From the literature review, presented in section 1.4, there does not appear to be a comprehensive study on the performance of tailored FRCs with coatings for thermal management. This work attempts to fill that void.

2.5.1.1 Choosing the Model

Three fundamental transient heat transfer models were considered for the basis of the analysis. The models were the classical Fourier model, the Hyperbolic model and the Dual Phase Lag (DPL) model. Each of these is discussed briefly below.

2.5.1.1.1 The Fourier Model

The classical Fourier based model is well understood and forms the basis for most modern thermal analysis. The Classical Fourier equation for conduction can be expressed as:

$$q_n = \frac{Q_n}{A_n} = -k \frac{\partial T}{\partial n} \quad \text{Equation 18}$$

Where:

q_n [W/m²] is the rate of heat flow per unit area normal to the n direction

Q_n [W] is the rate of heat flow across the normal area A_n

A_n [m²] is the cross-sectional area

k [W/mK] is the thermal conductivity of the material

$\frac{\partial T}{\partial n}$ [K/m] is the temperature gradient in the n direction

For an orthotropic composite material, the generalized form of the Fourier equation in Cartesian coordinates becomes¹⁰⁸:

$$\vec{q} = \begin{Bmatrix} q_x \\ q_y \\ q_z \end{Bmatrix} = - \begin{bmatrix} k_{11} & k_{12} & k_{13} \\ k_{21} & k_{22} & k_{23} \\ k_{13} & k_{23} & k_{33} \end{bmatrix} \begin{Bmatrix} \frac{\partial T}{\partial x} \\ \frac{\partial T}{\partial y} \\ \frac{\partial T}{\partial z} \end{Bmatrix} = -[K] \begin{Bmatrix} \frac{\partial T}{\partial x} \\ \frac{\partial T}{\partial y} \\ \frac{\partial T}{\partial z} \end{Bmatrix} \quad \text{Equation 19}$$

The Fourier model is the basis for thermal simulation in most Finite Element Method (FEM) and Finite Difference Method (FDM) codes. It has been verified as appropriate for calculating transient temperature distributions in 2-D and 3-D composite plates¹⁰⁸. An alternative approach to multi-dimensional

problems involves using a separation of variables approach. This essentially solves three one-dimensional problems. The resulting temperature distribution is then product of solution functions in three directions¹⁰⁹.

For transient heat conduction with generation and constant conductivity, the Fourier model can be written as:

$$\nabla^2 T + \frac{\dot{g}}{k} = \frac{1}{\alpha} \frac{\partial T}{\partial t} \quad \text{Equation 20}$$

Where:

α [m²/s] is the thermal diffusivity of the material

g [W/m³] rate of heat generation per unit volume

t [sec] time

This is referred to as the Fourier-Biot Equation⁸³. The Fourier model assumes infinite speed of propagation, and that heat flux and temperature change occur at the same time¹¹⁰.

2.5.1.1.2 The Hyperbolic Model

The Hyperbolic conduction model suggests that heat flux and temperature change do not occur simultaneously and introduces a phase lag between the two terms. The hyperbolic heat equation can be written as¹¹⁰:

$$\frac{1}{\alpha} \frac{\partial T}{\partial t} + \frac{\bar{\tau}_q}{\alpha} \frac{\partial^2 T}{\partial t^2} = \nabla^2 T + \frac{g}{k} + \frac{\bar{\tau}}{k} \frac{\partial g}{\partial t} \quad \text{Equation 21}$$

Where:

$\bar{\tau}$ [s] is the thermal relaxation time of the solid

2.5.1.1.3 The Dual Phase Lag Model

The Dual Phase Lag (DPL) model does goes a step further and suggests that there is a phase lag associated with both temperature change and heat flux¹¹¹: The Dual phase lag heat conduction equation can be written as:

$$\frac{1}{\alpha} \frac{\partial T}{\partial t}(t, \vec{r}) + \frac{\bar{\tau}_q}{\alpha} \frac{\partial^2 T}{\partial t^2}(t, \vec{r}) = \nabla^2 T(t, \vec{r}) + \bar{\tau}_T \frac{\partial}{\partial t} [\nabla^2 T(t, \vec{r})] + \frac{1}{k} \left[g + \bar{\tau}_g \frac{\partial g}{\partial t}(t, \vec{r}) \right]$$

Equation 22

Where:

$\bar{\tau}_q$ [s] is phase lag in the heat flux vector

$\bar{\tau}_g$ [s] is phase lag in the temperature gradient

Notice that, in the absence of a temperature gradient phase lag, this equation collapses to the hyperbolic heat equation. In the absence of both phase lags, the equation collapses to the Fourier equation.

Extensive simulations of the dual-phase lag model have been conducted by Hader et al. Simulations of heat transfer through a single thin layer¹¹¹, a dual layer slab similar to a solid with a coating¹¹², and a homogeneous composite with heat generation¹¹⁰ have all been conducted. Results show that deviations between the Fourier model and the DPL model appear at very fast heating rate and very thin layers. Examples provided of high heating rate are laser and microwave heating of semiconductors and films. The effect becomes significant when the heating frequency $\omega > \frac{\alpha}{L^2}$. For thin metal films, $\alpha \cong 10^{-4}$ and $L \cong 10^{-8}$.

Therefore it becomes necessary to use the DPL model at frequencies larger than

10^{12} Hz. Recalling the purpose of this study was to understand coatings and FRC performance in the thermal environment of an engine combustion chamber, this would imply that, for phase lag effects to be significant the engine would have to run at 10^{14} RPM. Peak speed of even the most high performance engines is in the order of 2×10^4 RPM.

Based on the previously published work described above it was decided that a Hyperbolic model or Dual-phase lag model was not necessary. Using a Fourier based FE model with bulk material properties will introduce only a small amount of error which is acceptable to this analysis.

2.5.1.2 Modeling Material Properties

Testing, modeling and analysis of spacecraft designs have shown that 1-D circuit analysis and FEA are appropriate tools when using an equivalent thermal conductivity for FRC panels⁸⁸. That is, it is not necessary to model fiber-matrix interface conditions, bulk thermal properties based on constituent material properties and volume fractions are appropriate for design.

Balageas conducted a fundamental study to measure the apparent diffusivity of fiber reinforced composites under transient heating conditions. Results showed that, apparent flash diffusivity of the composite can range from 0.5 to 1.5 of steady state diffusivity. Limits of homogeneous property model were shown and proposed changes in techniques were discussed. The ratio of fiber size and spacing to part thickness is of particular importance. As the thickness of the part becomes large relative to the fiber spacing, apparent diffusivity approaches steady-state diffusivity¹¹³. Additional studies have also shown that

inter-constituent temperature gradients are considerable within distance of yarn spacing from the surface⁷¹.

The analysis conducted deals with FRCs with a thickness of 2mm and 200mm respectively. Typical fiber diameters range from 7um for carbon fiber to 200um for CVD Boron fibers¹¹⁵. Assuming moderate volume fractions of fiber and fiber consolidation, there are still several orders of magnitude difference between the fiber spacing and part thickness. Thus it was deemed that use of steady state material properties was appropriate.

2.5.2 Analysis

2.5.2.1 Model Setup

In order to quantify the affect of coatings and fiber orientation on transient heat transfer, two generic axisymmetric models were built. Two basic models were used, a thin plate and a thick plate. Each had a diameter of 1 meter. The thin plate had a thickness of 2mm yielding an aspect ratio of 500:1. The thick plate had a thickness of 20mm, yielding an aspect ratio of 5:1. These two combinations were chosen to represent a generic “thin” and “thick” composite. For all cases with a coating, a coating thickness of 0.1mm was used. Figure 36 is a representation of both the thick and thin models.

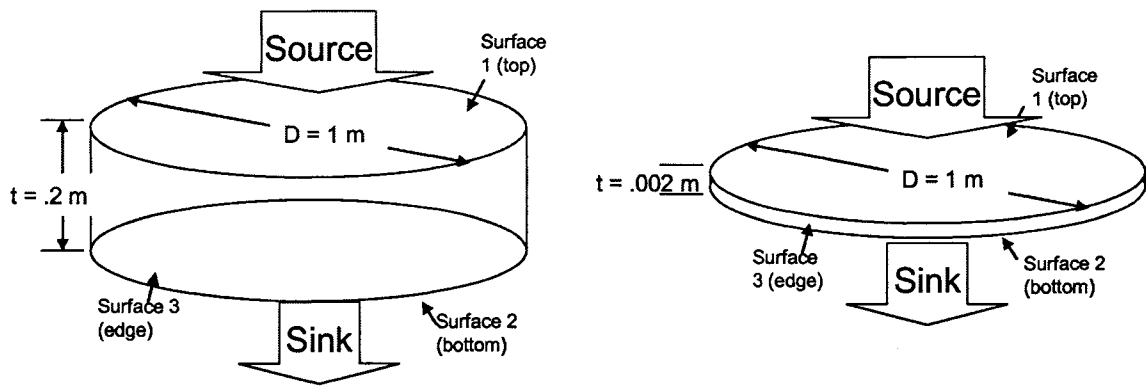


Figure 36, Thin and Thick model geometry and surface definitions.

2.5.2.1.1 Boundary Conditions

For all analyses, there are only two sets of boundary conditions. The first set of boundary conditions represents an axial heat path, in which the only path for heat conduction through the composite is through the thickness of the solid. The second represents a radial heat path in which the only path for heat transfer is radially through the edge of the solid. Figure 37 is a graphic representation of the axial and radial heat transfer cases. For all cases, boundary conditions were modeled as convective heat transfer with matched heat flux into and out of the solid. To accomplish this, the convective heat transfer coefficient of the sink was changed so that the product $h \cdot A$ was equal for the source and sink. Table 19 is a summary of the boundary conditions used for the model.

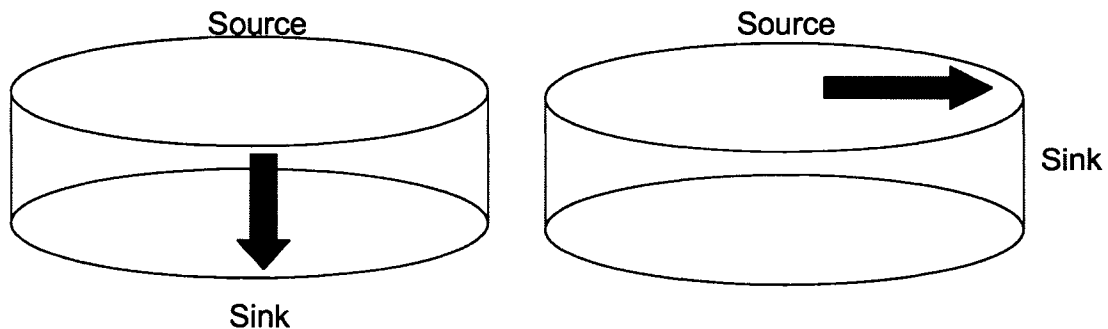


Figure 37. Axial and radial heat paths.

Table 19. Boundary conditions for the model.

	Axial cases	Radial cases
Source	Surface 1	Surface 1
h ($W/m^2\cdot K$)	500	500
T_{∞} ($^{\circ}K$)	1300	1300
Sink	Surface 2 (bottom face)	Surface 3 (edge)
h ($W/m^2\cdot K$)	500	62500 (thin) 625 (thick)
T_{∞} ($^{\circ}K$)	300	300
Insulated ($h = 0$)	Surface 3 (edge)	Surface 2 (bottom face)

2.5.2.1.2 Material Properties

For each model and set of boundary conditions, a set of generic isotropic material properties and orthotropic material properties were chosen that span the known range of typical material properties. Table 20 lists the properties of common engineering materials spanning the range of material thermal properties. Table 21 lists the material properties used to model isotropic materials, and Table 22 lists the material properties used for orthotropic materials. In each case, density and specific heat were held constant and only thermal conductivity was changed with the differing materials. For orthotropic materials, both axial and radial conductivity were varied such that the ratio of conductivities in the principal directions was changed such that the ratio of axial to radial conductivity varied from 1:1000 to 1000:1. This spans the ranges typically seen in all composite materials.

Table 20. Thermal properties of common engineering materials.

	Min	Material Name	Max	Material Name	Maximum Ratio (Max/Min)	Minimum Ratio (Min/Max)
k (W/mK)	0.0017	Evacuated Silica Powder	2300	Diamond	1.4E+06	7.4E-07
density (kg/m ³)	16	Polystyrene, molded rigid beads	21450	Platinum	1.3E+03	7.5E-04
Specific Heat, cp (J/kgK)	116	Uranium	2010	Soft Rubber	1.7E+01	5.8E-02
thermal diffusivity, alpha (m ² /s)	1.41E-07	sulfur	1.74E-04	silver	1.2E+03	8.1E-04

Table 21. Material properties for isotropic materials.

Material Name - Isotropic Materials	density, rho, (kg/m ³)	Specific heat, Cp (J/kgK)	thermal conductivity k (W/mK)	thermal diffusivity, alpha (m ² /s)
iso 1	10	1000	0.001	1.00E-07
iso 2	10	1000	0.01	1.00E-06
iso 3	10	1000	0.1	1.00E-05
iso 4	10	1000	1	1.00E-04
iso 5	10	1000	10	1.00E-03
iso 6	10	1000	100	1.00E-02
iso 7	10	1000	1000	1.00E-01

Table 22. Material properties for orthotropic materials.

Material Name - Orthotropic Materials	density, rho, (kg/m ³)	Specific heat, Cp (J/kgK)	axial thermal conductivity k _a (W/mK)	radial thermal conductivity k _r (W/mK)	axial thermal diffusivity, alpha _a (m ² /s)	radial thermal diffusivity, alpha _r (m ² /s)	conductivity ratio k _a /k _r	diffusivity ratio alpha _a /alpha _r
ortho 1	10	1000	1.0E+02	1.0E-01	1.0E-02	1.0E-05	1.0E+03	1.0E+03
ortho 2	10	1000	1.0E+01	1.0E+00	1.0E-03	1.0E-04	1.0E+01	1.0E+01
ortho 3	10	1000	1.0E+00	1.0E+01	1.0E-04	1.0E-03	1.0E-01	1.0E-01
ortho 4	10	1000	1.0E-01	1.0E+02	1.0E-05	1.0E-02	1.0E-03	1.0E-03

2.5.2.1.3 Coating Properties

For isotropic coated materials, the coating conductivity was also varied in decades in the opposite direction as the core material properties. This enabled a

set of analysis that spanned the range from a conductive coating on an insulating core to an insulating coating on a conductive core. Table 23 is an example of the material properties used for isotropic, coated models.

Table 23. Coated isotropic materials.

Test Name	Coating material name	Core Material name	k-coating (W/mK)	k-core (W/mK)	density (kg/m ³) [core and coating]	Specific Heat, cp (J/kgK) [coating and core]	coating thermal diffusivity, alpha (m ² /s)	core thermal diffusivity, alpha (m ² /s)
thick_iso_coat_a_1	iso_7	iso_1	1000	0.001	10	1000	1.E-01	1.E-07
thick_iso_coat_a_2	iso_6	iso_2	100	0.01	10	1000	1.E-02	1.E-06
thick_iso_coat_a_3	iso_5	iso_3	10	0.1	10	1000	1.E-03	1.E-05
thick_iso_coat_a_5	iso_3	iso_5	0.1	10	10	1000	1.E-05	1.E-03
thick_iso_coat_a_6	iso_2	iso_6	0.01	100	10	1000	1.E-06	1.E-02
thick_iso_coat_a_7	iso_1	iso_7	0.001	1000	10	1000	1.E-07	1.E-01

In order to limit the number of analysis cases required for orthotropic materials, the four generic orthotropic materials described in Table 22 were used each with either a conductive or insulating coating. Table 24 is an example of the material properties used for the orthotropic, coated cases.

Table 24. Coated orthotropic material properties.

Material: thick_ortho_coat_a	Core material	k-axial	k-radial	coating	k coating	ratio k_coating / k_axial	Bi-coat
1	ortho_1	100	0.1	iso_2	1.00E-02	1.00E-04	5.00E+00
2	ortho_2	10	1	iso_2	1.00E-02	1.00E-03	5.00E+00
3	ortho_3	1	10	iso_2	1.00E-02	1.00E-02	5.00E+00
4	ortho_4	0.1	100	iso_2	1.00E-02	1.00E-01	5.00E+00
5	ortho_1	100	0.1	iso_6	1.00E+02	1.00E+00	5.00E-04
6	ortho_2	10	1	iso_6	1.00E+02	1.00E+01	5.00E-04
7	ortho_3	1	10	iso_6	1.00E+02	1.00E+02	5.00E-04
8	ortho_4	0.1	100	iso_6	1.00E+02	1.00E+03	5.00E-04

2.5.2.2 Steady State Analysis

Simple steady state analysis was conducted for each of the axial cases to gain an understanding of how material properties change the performance of the material, as well as to understand the equilibrium condition that the transient cases are approaching. It was also used for verification of the transient analyses. Figure 38 is the diagram and thermal circuit used for the uncoated,

steady state temperature calculations. Figure 39 is the diagram and thermal circuit used for the coated, steady state calculations. Results from each model and material were calculated, normalized and plotted for comparison.

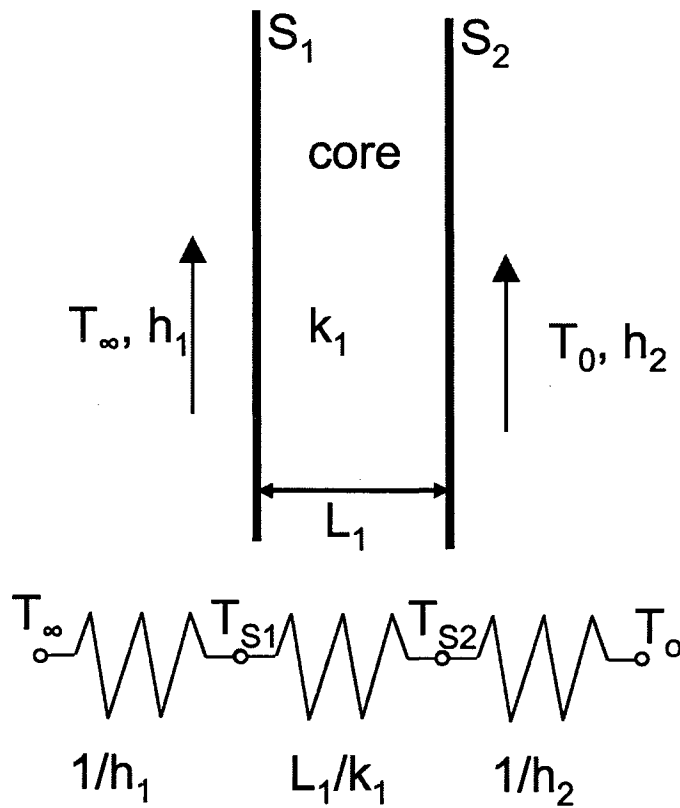


Figure 38. Steady state thermal circuit for uncoated, axial cases.

In transient heat transfer analysis, Biot number, or the dimensionless heat transfer coefficient, is defined as:

$$Bi = \frac{hL}{k} \quad \text{Equation 23}$$

This represents the ratio of convective heat transfer at the surface of the body to conduction within the body⁸³. Typically, Biot numbers greater than 0.1 imply conduction is greater than convection at the boundary and temperature gradients inside the body are negligible. The Biot number enables calculation of the transient temperature distribution through the thickness of the plate. For the

purpose of this analysis, a modified Biot number, referred to as the Stanglmaier number, St , is defined as:

$$St_{core} = \frac{\left(\frac{L_1}{k_1}\right)}{\left(\frac{1}{h} + \frac{L_2}{k_2}\right)} \quad \text{Equation 24}$$

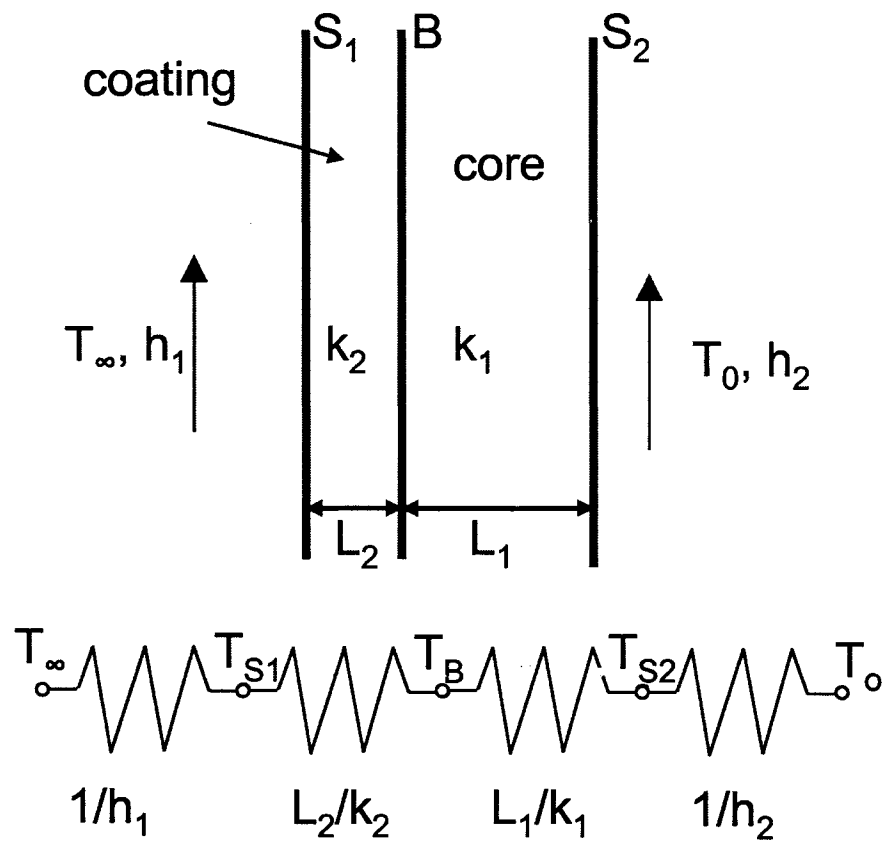


Figure 39. Steady state thermal circuit for coated, axial cases.

At the boundary between two materials, this unitless number represents the ratio of heat transfer into the boundary to the heat transfer out of the boundary. Similarly, a high Stanglmaier number would imply uniform temperature distribution in the core material. Using the same methodology as in

the Biot analysis, the Stanglmaier number enables calculation of the transient temperature distribution through the thickness of the coated plate.

The ratio of the surface coating Biot number to the core material Stanglmaier is defined as Bb , where:

$$Bb = \frac{Bi_{coating}}{St_{core}} \quad \text{Equation 25}$$

Simplifying yields:

$$Bb = \left(\frac{k_1}{L_1} \right) \left(\frac{L_2}{k_2} \right) \left(1 + h \frac{L_2}{k_2} \right) \quad \text{Equation 26}$$

This ratio, Bb , represents the ratio of the heat carrying capacity of the coating to the heat carrying capacity of the core material under convective heat transfer conditions. Thus, if the Biot number enables calculation of the transient temperature distribution in an uncoated plate, and the Stanglmaier number enables calculation of the transient temperature distribution in the coated plate, the ratio of the two numbers, Bb , should provide some understanding of the relative temperature profiles in both the core and coating materials.

Using the steady state-circuit diagram temperatures at the surfaces and interface were calculated for each set case described in the previous section. Using the dimensionless parameters described, plots of normalized temperature distribution were generated.

2.5.2.3 Transient Analysis

The Finite Element and Computational Fluid Dynamics software, Fluent™, was used to conduct transient analysis for the cases described above. For each

case described in 2.5.2.1, a transient analysis was run using the time step scheme presented in Table 25. Results were collected, normalized and plotted.

Table 25. Transient analysis time steps.

Run #	Time step (sec)	# of time steps	Total Elapsed time (sec)
1	10-5	1000	10-2
2	10-4	900	10-1
3	10-3	900	1.0
4 (thick cases only)	10-2	900	101
5 (thick cases only)	10-1	900	102

For complete details of all the analysis cases, please refer to Appendix 4: Complete Thermal Analysis Plans.

2.5.3 Results and Discussion

2.5.3.1 Results - Axial Heat Path

In an orthotropic material with a linear, axial heat path, the orthotropic composite material behaves as an isotropic material. Material performance is only affected by materials in the direction of the heat path. Properties perpendicular to the heat path do not affect the result. As a result the case collapses to a 1-D solution with no differences between isotropic and orthotropic cases. Figure 40 illustrates this fact. The plot on the left is of an orthotropic composite material with axial conductivity of 0.1 W/mK and radial conductivity of 100 W/mK. The plot on the right is the corresponding isotropic material with $k =$

0.1 W/mK. The plots are identical. As a result of this, orthotropic materials are not discussed in the context of an axial heat path.

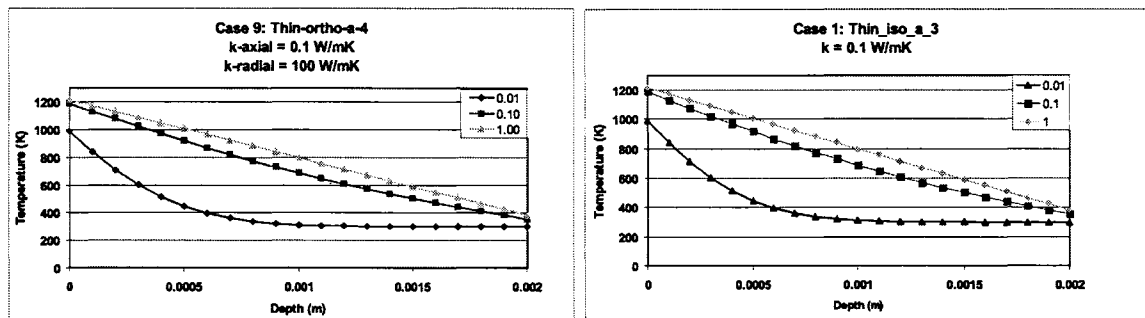


Figure 40. Orthotropic vs. Isotropic material response for axial heat path.

2.5.3.1.1 Steady State Analysis

Simple steady state analysis was conducted for each of the axial cases to gain a better understanding of how material properties change the performance of the material, as well as to understand the equilibrium condition that the transient cases are approaching. It was also used for verification of equilibrium for the transient analyses. Results were normalized and plotted in terms of Biot number, unitless length, x^* and unitless temperature Θ . Data was combined for the thick and thin models. Figure 41 is a plot of the steady state temperature distribution for uncoated, isotropic materials.

Figure 41 shows that under steady state conditions, for increasing Bi , the surface temperature of the material increases until it is equal to that of the ambient air temperature while back side temperature decreases until it is equal to that of the ambient air of the sink. As Bi decreases, the steady state temperature approaches $\Theta = 0.5$. That is, the temperature of the solid is exactly midway between that of the source and sink. Thus, if the design goal is to lower the

surface temperature in a material, we have three options. Recalling that $Bi = hL/k$, these three options are; 1) decrease the heat transfer coefficient h , 2) decrease the thickness of the material, L , or 3) increase the conductivity of the material k .

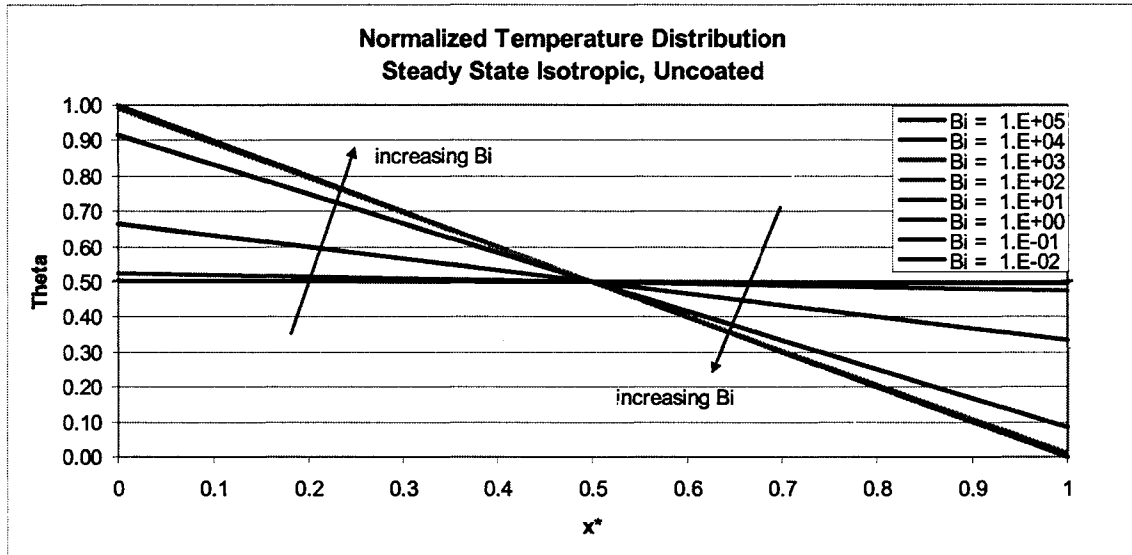


Figure 41. Normalized temperature distribution for uncoated, isotropic materials under steady state conditions.

2.5.3.1.1.1 Effect of Bb on Temperature Profile

Normalizing the data for the thick and thin cases results in two sets of plots which overlap; this data was combined and is presented in Figure 42. A clear trend is apparent from this figure. The demarcation line where the core material and coating behave as one is at $Bb = 1$. For values of $Bb < 1$, the temperature distribution in the coating is essentially uniform, with the peak core temperature being equal to the surface temperature. This represents a combination where the coating material has a thermal conductivity greater than that of the core. For values of $Bb > 1$, there is a larger temperature gradient in the coating, with the peak core temperature dropping as Bb increases. These

cases represent a combination where the coating material has a thermal conductivity less than that of the core. Thus, if the goal of the designer is to “protect” the core, increasing the value of B_b will have the desired effect.

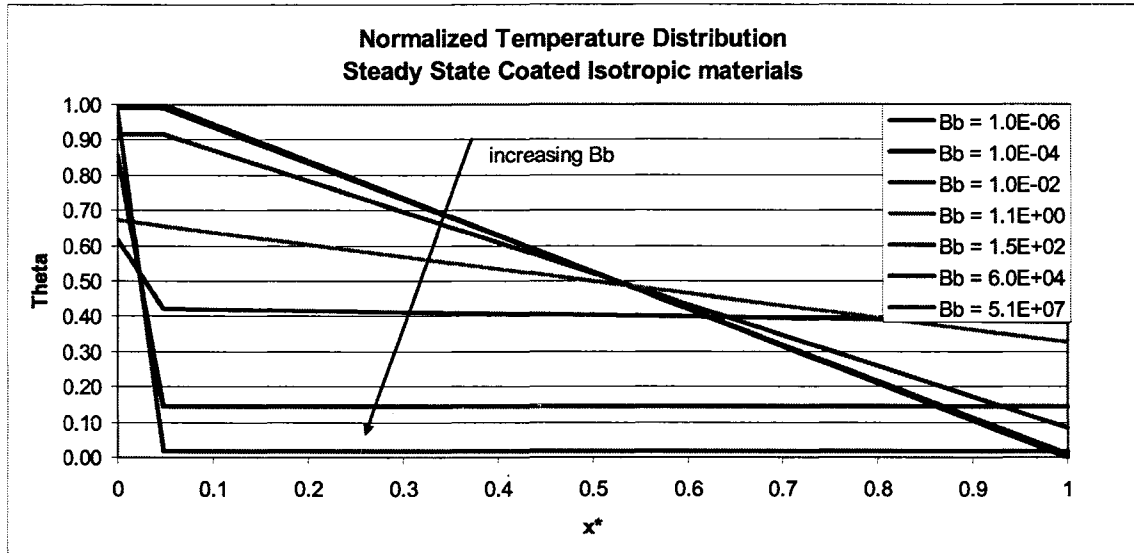


Figure 42. Normalized temperature distribution for coated, isotropic materials under steady state conditions.

2.5.3.1.1.1.2 Effect of Thickness Ratio on Interface Temperature

For steady state analysis only, the thickness ratio, defined as $\frac{L_1}{L_2} = \frac{L_{core}}{L_{coating}}$

was varied in decades from 2 to 2000. Dimensionless interface temperature (at the boundary between the core and coating) was plotted for varying B_b . Results are presented in Figure 43.

From this plot, it is apparent that increasing the thickness ratio increases the interface temperature for a given $B_b < 1$, and decreases the interface temperature for $B_b > 1$. If the design goal is to lower interface temperature and “protect” the core, for a larger thickness ratio, a B_b closer to one will work well. For the range of materials and thickness ratios, a $B_b > 100$ will result in interface

temperature $\Theta_B < 0.15$. If the design goal is to transmit heat to the core, for the range of materials and thickness ratios, $Bb < 0.1$ will result in interface temperature $\Theta_B > 0.85$ and for $Bb < 0.01$ will result in interface temperature $\Theta_B > 0.90$.

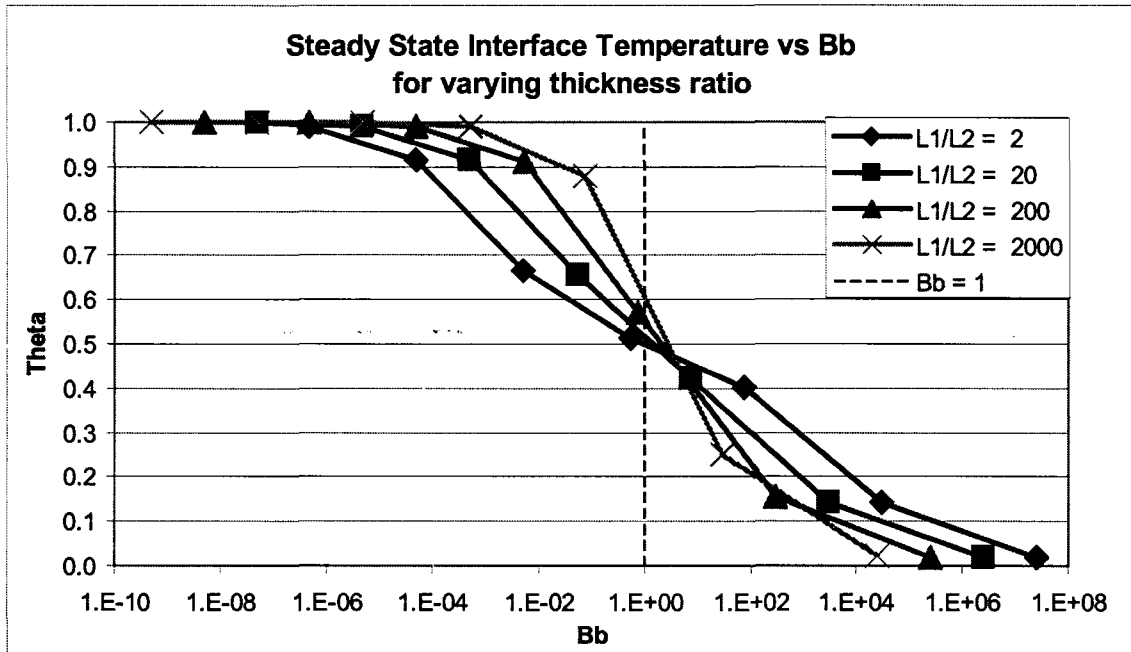


Figure 43. Steady state interface temperature for varying Bb and thickness ratio.

2.5.3.1.2 Results - Transient Analysis

In steady state situations, material performance is dependent only on conductivity, k , and specific heat, c_p . During transients, thermal diffusivity, α , and effusivity, β dominate material response¹¹³. Referring to the material properties used for this analysis in Table 21 and Table 22, material density, ρ , and specific heat, c_p are held constant across all the materials used. This has the simplifying effect of constraining changes in material performance to changes in thermal

conductivity only. For transient material performance, data is presented in terms of the unitless time measure, the Fourier number, Fo defined as:

$$Fo = \frac{\alpha \cdot t}{L} \quad \text{Equation 27}$$

2.5.3.1.2.1 Uncoated Material Response

Figure 44 is a series of plots for an uncoated, isotropic solid representing the temperature distribution through the thickness of the solid. In each sub-plot, Bi is constant, that is the material properties do not change. Each series in the sub-plot represents an increment in time, or an increasing Fo . As in the steady state plots, increasing the Bi number of the material results in increased temperature gradient and increased surface temperature in the solid. This data was verified with against a 1-D finite difference model as well as a traditional Biot model used to model transient temperature distribution in a flat plate with convection.

Figure 45 is the same data presented slightly differently. Here each sub-plot can be thought of as a snapshot in time. Each series on the sub-plot can be thought of as a set different of materials or boundary conditions that change the Biot number. Thus, for the same time, a material with a larger Biot number will have a larger temperature gradient, and a higher peak temperature. Lower Fourier numbers yield lower temperatures. Lower Bi numbers also yield lower temperatures.

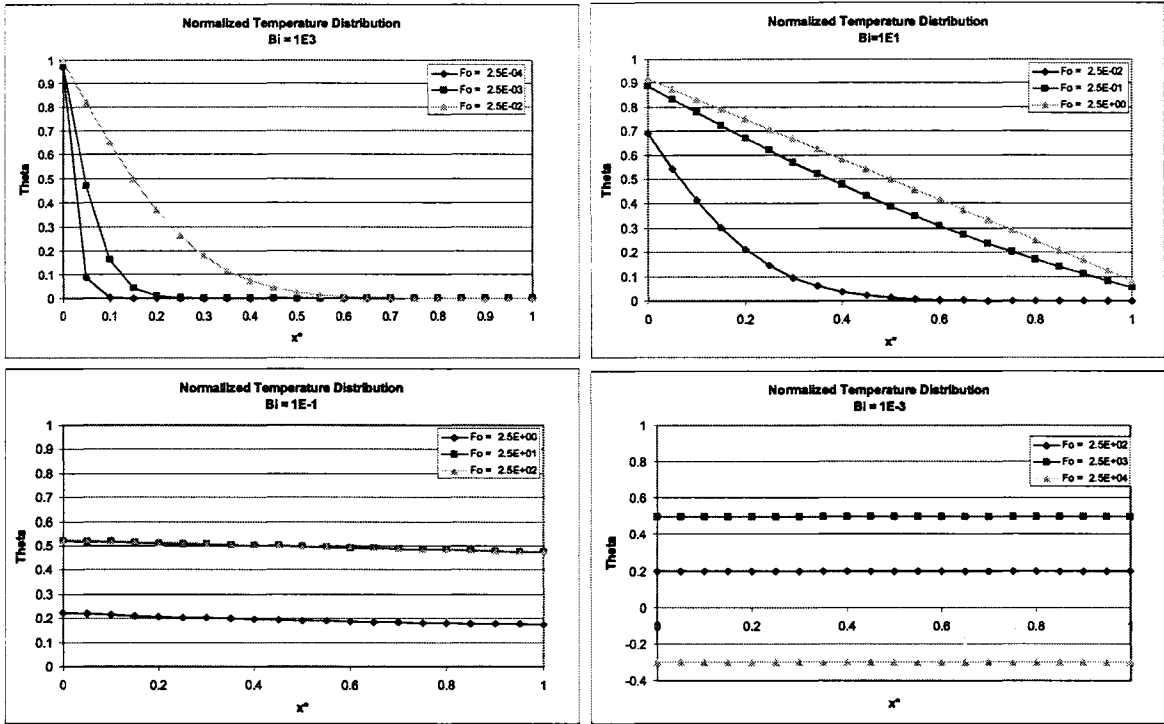


Figure 44. Transient Temperature Distribution for uncoated, isotropic materials.

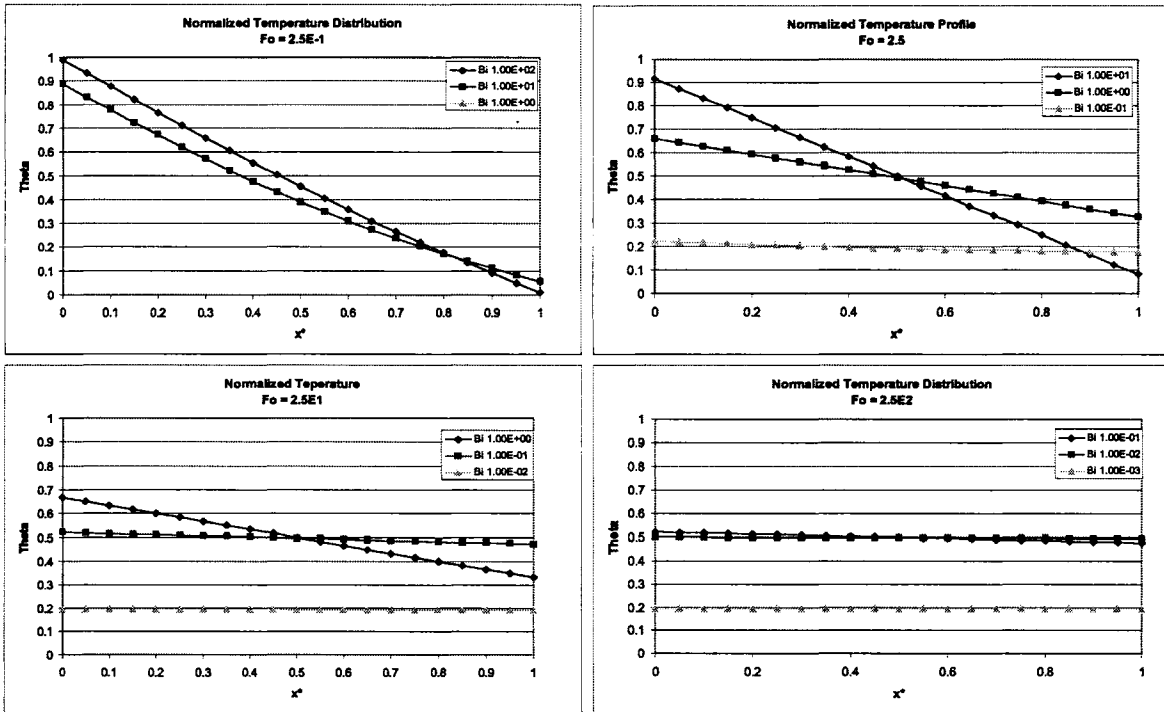


Figure 45. Transient Temperature Distribution for uncoated, isotropic materials.

2.5.3.1.2.2 Coated Material Response – Effect of Bb on Temperature Profile

For presenting transient response, it may seem logical to compare the Fourier numbers of the coating and core material. If we introduce yet another ratio of unitless numbers, called Ff, defined as:

$$Ff = \frac{Fo_{coat}}{Fo_{core}} = \frac{\alpha_2 t}{L_2} \cdot \frac{L_1}{\alpha_1 t} = \frac{\alpha_2}{L_2} \cdot \frac{L_1}{\alpha_1} \quad \text{Equation 28}$$

Recall that $\alpha = \frac{k}{\rho \cdot c_p}$, substituting yields $Ff = \left(\frac{k}{\rho \cdot c_p L} \right)_2 \cdot \left(\frac{\rho \cdot c_p L}{k} \right)_1$

For the materials modeled in this study $\rho_1 = \rho_2$ and $c_{p1} = c_{p2}$. Thus the ratio of Fourier numbers, Ff simplifies to:

$$Ff = \frac{k_2 L_1}{L_2 k_1} \quad \text{Equation 29}$$

This is the inverse of the first two terms in Bb and neglects the change in convective heat transfer coefficient. As a result, transient data will be presented in terms of Bb. For all of the data presented below, the time increment chosen was the Fourier number for the coating, Fo-coat. This was chosen because the thickness of the coating, and therefore Fo, was the same for the thin and thick models. Figure 46 is a series of plots of the temperature distribution through the thickness of the coated solid. Bb is increasing from top left to bottom right. In each plot, the successive series are decade increments of Fo-coat. Notice the drastic change in temperature profile that occurs from Bb = 1 (top right plot) to Bb = 6 (bottom left plot). For Bb < 1 the temperature distribution in the coating is essentially uniform and peak core temperature is equal to the surface

temperature. For $Bb > 1$, there is gradient in the coating and peak core temperature is less than the surface temperature. This gradient increases with increasing Bb .

Figure 47 is the top left plot from Figure 46. Here $Bb < 1$ and the result is that the temperature distribution at all Fourier numbers is essentially constant in the coating and equal to the surface temperature. The coating material transmits heat to the core material very effectively.

Around $Bb = 1$, things there is a continuous transition from one temperature profile to the other that is also a function of Fo (time). Figure 48 is a similar plot where Bb is roughly one for all plots. Fourier number is increasing from the bottom to top curve. From this plot it can be seen that, for $Bb \approx 1$, low Fourier numbers result in a gradient in the coating, that is, a temperature distribution similar to $Bb > 1$. High Fourier numbers result in a uniform coating temperature, with a gradient in the core material, that is, a temperature distribution similar to $Bb < 1$.

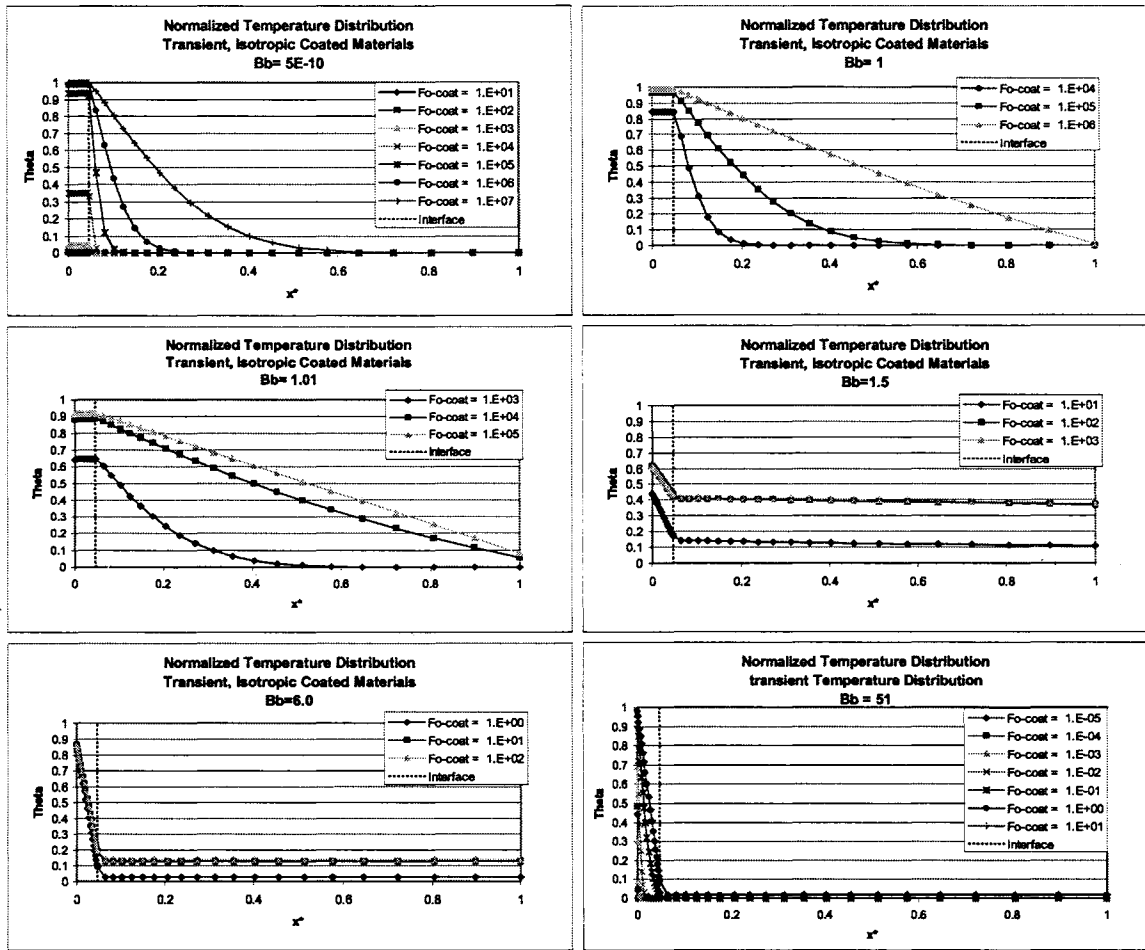


Figure 46. Transient temperature distribution for coated, isotropic solid.

Figure 49 is the bottom right plot from Figure 46. In this plot $Bb > 1$, thus, for all Fo , there is a steep temperature gradient in the coating, and peak core temperature is significantly less than the surface temperature.

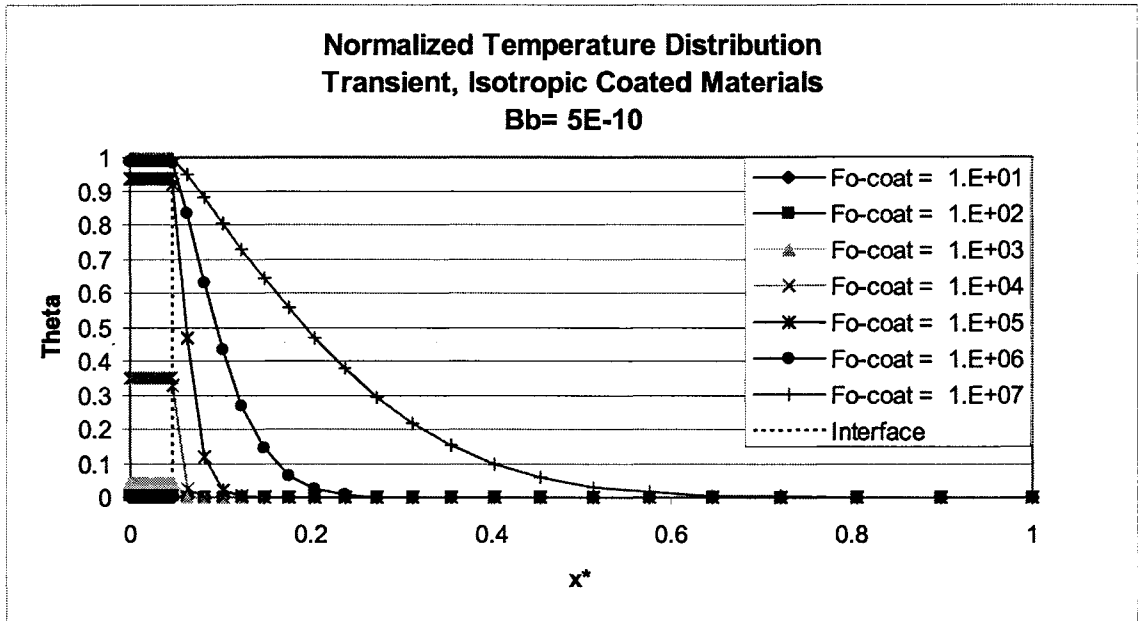


Figure 47. Temperature profile for $Bb < 1$ showing uniform coating temperature.

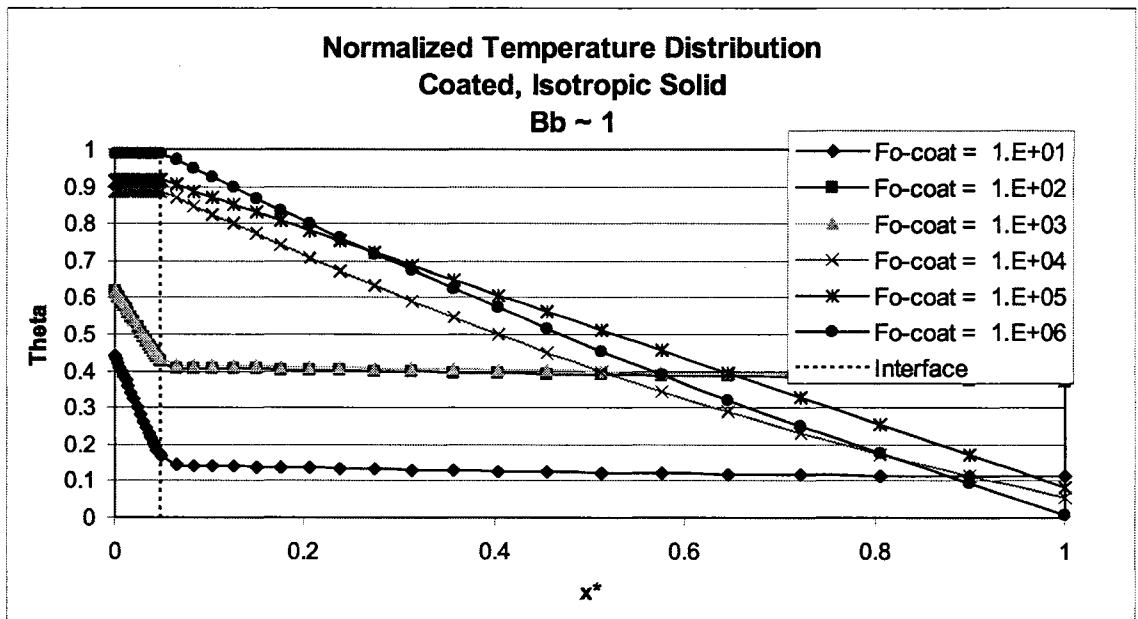


Figure 48. For $Bb=1$, coating and core temperature rise together.

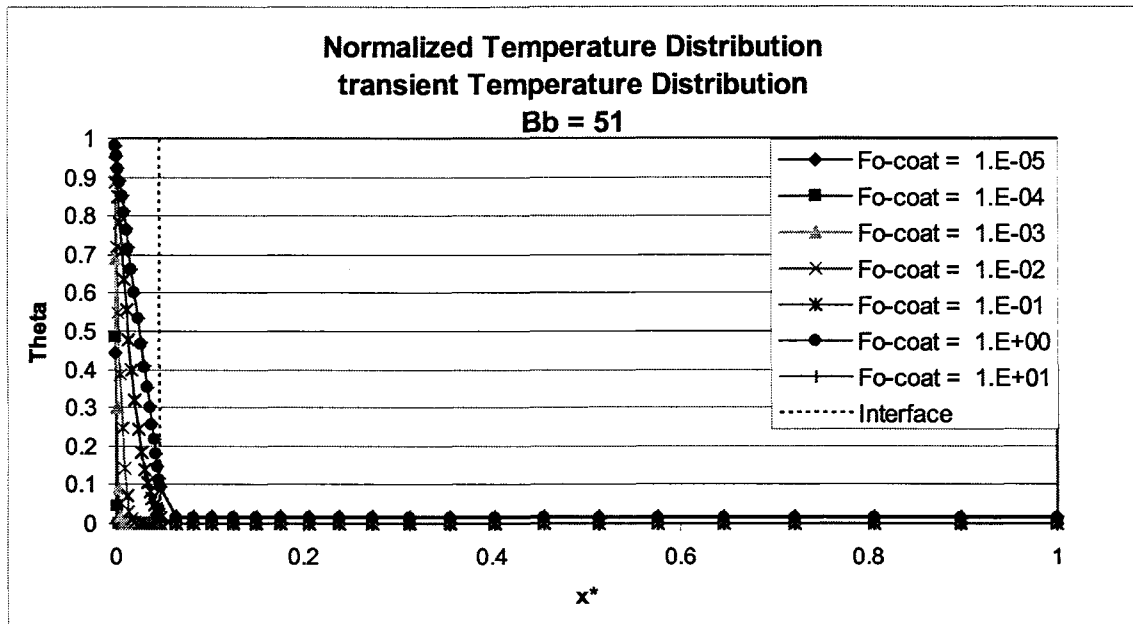


Figure 49. For $Bb > 1$, Surface temperature rises quickly, core temperature stays low and a large temperature gradient exists in the coating.

As the ratio Bb increases, gradient increases and peak core temperature decreases. This looks remarkably like the steady state diagram because it is a high Fo number for the core.

2.5.3.1.3 Effect of Bb on Interface Temperature

For nearly all composite coating designs with an axial heat path, the peak temperature in the core material will be at the interface between the core and coating material. Figure 50 is a plot of peak interface temperature vs.. Bb for successive time steps. From this plot the progression of temperature at the interface becomes clearer. As stated earlier, $Bb < 1$ results in a high peak core temperature roughly equal to the surface temperature and heat is transmitted to the core. For $Bb > 1$, interface temperature is lower than the surface temperature and heat is not transmitted to the core.

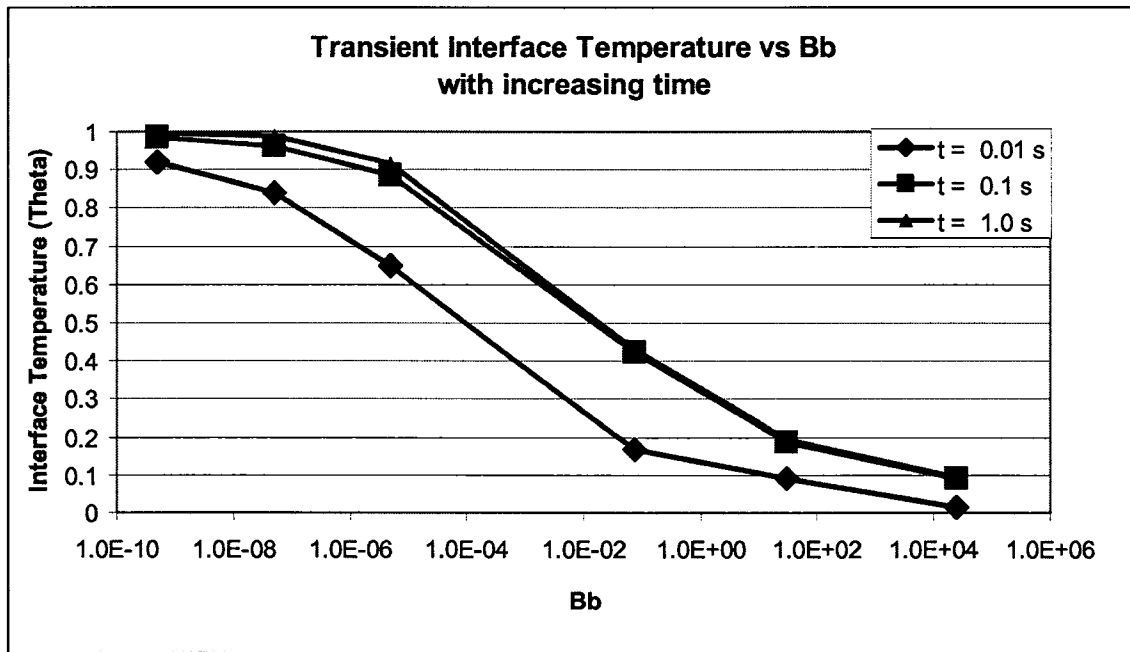


Figure 50. Peak Interface temperature vs. Bb for varying time.

2.5.3.1.4 Discussion – Axial heat path

In designing the combination of a FRC with a coating for thermal management, an initial engineering assessment might be to choose a coating and core material based solely on the conductivities of the materials. However, the data has shown that a better approach is slightly more refined. By comparing the ratio of heat transfer into and out of the material interface, Bb, a more accurate assessment of performance can be obtained. If the goal of the designer is to protect the core material, increasing Bb above unity will more effectively reduce the interface temperature. Looking at the definition of Bb, this involves several options:

$$Bb = \left(\frac{k_1}{L_1} \right) \left(\frac{L_2}{k_2} \right) \left(1 + h \frac{L_2}{k_2} \right) \quad \text{Equation 26}$$

- Increase k_1 – make the core more conductive

- Decrease L_1 – make the core thinner
- Decrease k_2 – make the coating less conductive
- Increase L_2 – make the coating thinner
- Increase h – increase the convective heat transfer coefficient

The last suggestion, increasing the convective heat transfer coefficient, may be initially counterintuitive. This approach will only work under the specific circumstances where $Bb > 1$ and $h_{\text{source}} \leq h_{\text{sink}}$. If the inverse is true, that is $Bb < 1$, and/or $h_{\text{source}} \geq h_{\text{sink}}$, then increasing the convective heat transfer coefficient will have the opposite effect of raising the interface temperature. If the goal of the designer is to increase heat transfer to the core, then the inverse applies for all conditions.

2.5.3.2 Results - Radial Heat Path

For the radial heat path case, isotropic and orthotropic materials behave differently. Presentation of the results for isotropic materials will be covered only briefly. The discussion will focus on the effect of the orthotropic nature of FRCs and the effect of coatings on material response be spent on orthotropic material response.

2.5.3.2.1 Reading the plots

Recall from the model description section that the simulation conducted was a transient, axisymmetric model with “thin” and “thick” configurations. Refer to Figure 36 for the model geometry and boundaries. For the purpose of presenting the temperature profile data in the radial heat path cases, the model is

rotated 90 degrees and a cross section is taken. See Figure 51 for a representation. The two dimensional temperature data is then plotted as an elevation change from this base plane. The aspect ratio of the plots is varied for the thin and thick cases see Figure 52, although these are not the actual aspect ratios of the model.

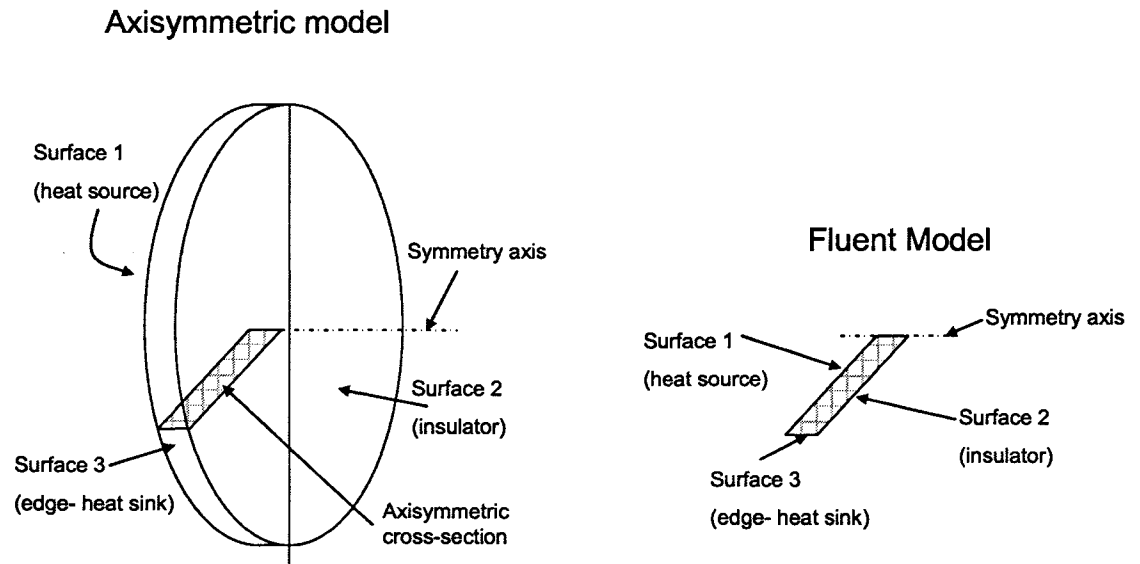


Figure 51. Axisymmetric model layout.

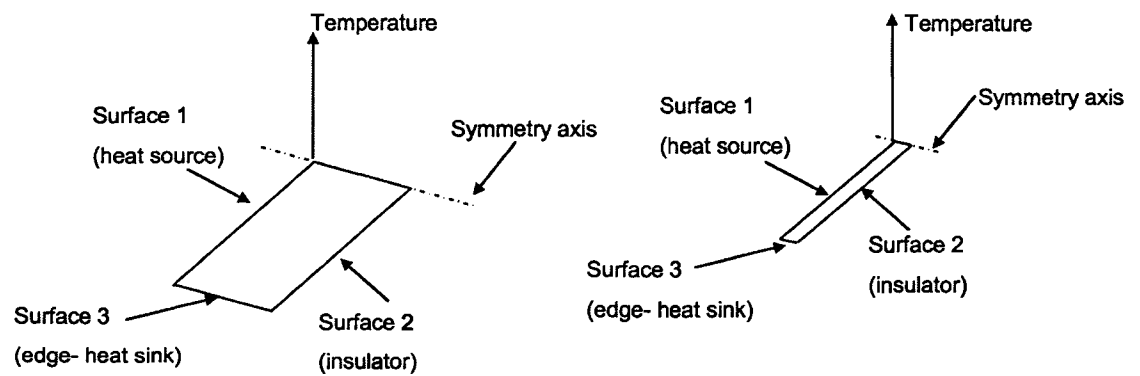


Figure 52. Thick and thin 3-D plot layout.

As shown in Figure 52, all plots are displayed with the heat source (surface 1) on the left rear face of the base plane, the sink (surface 3) on the left front face, the symmetry axis on the right rear face and the insulated surface (surface 2) on the right front plane. For clarity, a single example plot is shown in Figure 53.

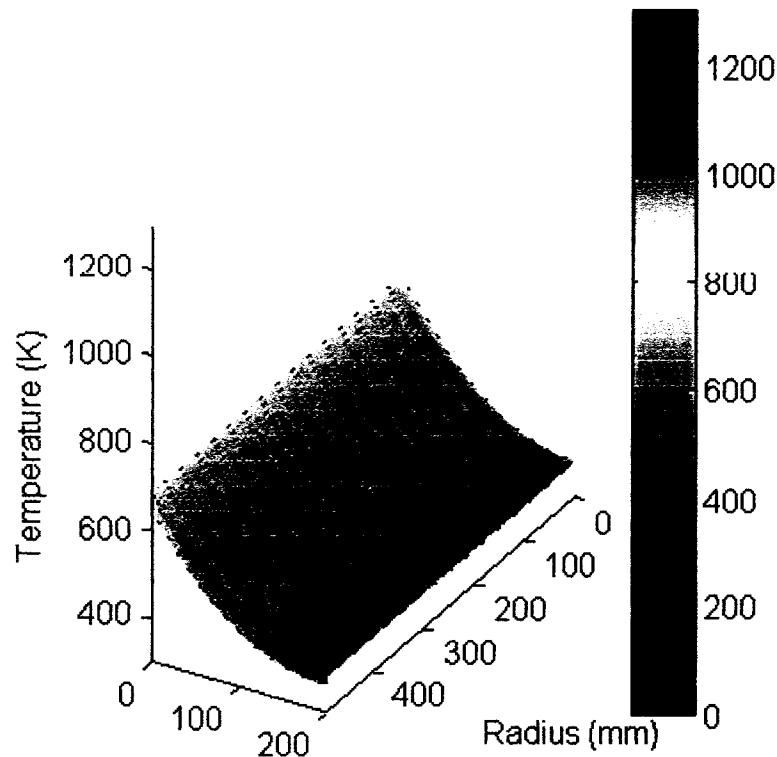


Figure 53. Example 2-D temperature profile plot.

2.5.3.2.2 Results – Temperature Distribution in Uncoated Isotropic Materials

For presentation of results, all data was normalized in terms of dimensionless temperature change Θ , axial distance x^* , and radial distance R^* . Figure 54 and Figure 55 are a subset of the results plotted for thin and thick cases respectively. In each plot, Biot number increases with each vertical row, and Fourier number increases with each column from the left. The same trends

that were shown in previous section with an axial heat path are apparent with a radial heat path as well, only now there are two temperature gradients present, one each in the axial and radial directions. From Figure 54 and Figure 55, it can be seen that temperature gradient away from the source in the axial direction and away from the sink in the radial direction increases with increasing Biot number. At higher Fourier numbers, temperature distribution across the solid is nearly uniform, and this effect is exacerbated at higher Biot numbers. There exists what one might label a “taper distance” from the sink surface. This is the distance in the radial direction necessary for the solid to reach nearly uniform temperature distribution through the axial thickness. This taper distance appears to be a function of both Biot number and aspect ratio. Attempts were made to quantify this distance, but were unsuccessful.

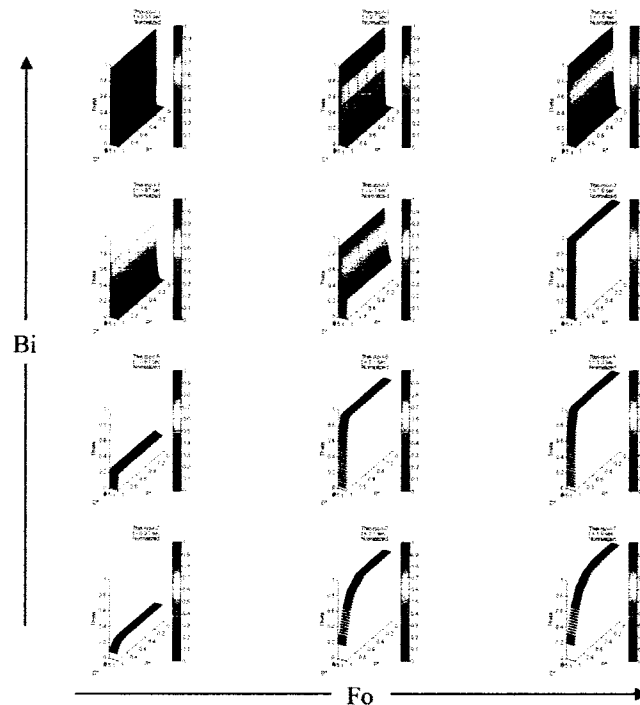


Figure 54. 2-D temperature distribution for a thin isotropic solid.

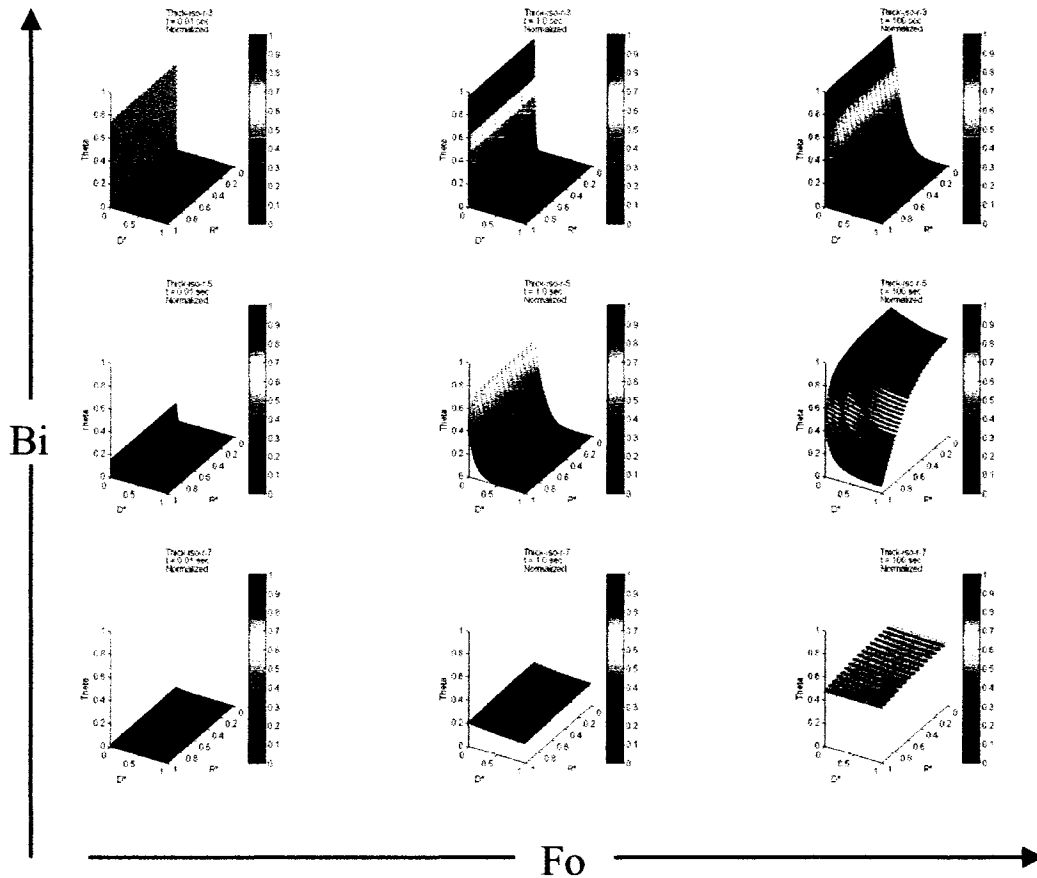


Figure 55. 2-D temperature distribution for a thick isotropic solid.

2.5.3.2.2.1.1 Temperature Distribution in Coated Isotropic Materials

Similar normalized 2-D plots were generated for the coated isotropic material cases. As in the 1-D axial heat flow cases, the unitless ratio of heat flow into and out of the interface boundary, B_b is used as a unit of comparison. It is possible to generate two values for B_b for each case, on each in the radial and axial directions. However, because the critical length of the core and coating is equal in the radial direction this ratio becomes less useful. As a result, the ratio B_b in the axial direction is used for comparison on all of the coated radial heat path cases. In the name of simplicity and space, only a subset of the results

from the thick aspect ratio cases is presented here. For the plots in Figure 56, the material properties for the core material are the same as those in Figure 54 and Figure 21 however on the plots the thermal properties of the coating are varied in the opposite direction of the core. Refer to Table 23 for details.

2.5.3.2.2.1.2

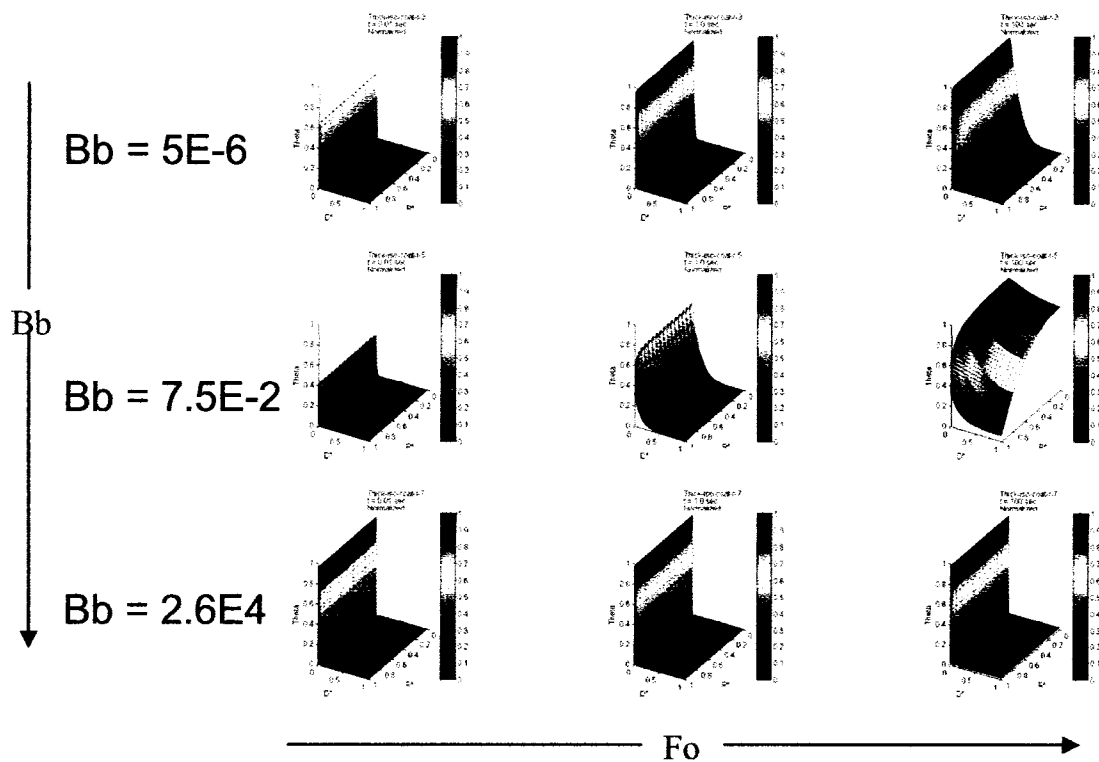


Figure 56. Coated isotropic materials, radial heat path.

Notice that the same trends are apparent as in the axial heat path. For $Bb < 1$ the temperature distribution in the coating is essentially uniform and peak core temperature is equal to the surface temperature. At higher Fourier numbers, the temperature distribution appears to be almost identical to that in the uncoated cases. For $Bb > 1$, there is a large gradient in the coating and peak core temperature is less than the surface temperature. This gradient increases with

increasing Bb and the core temperature stays lower than the uncoated cases even at higher Fourier number. Aspect ratio of the part still plays a role in lowering the temperature near the sink, but for at some point the temperature distribution through the part in the axial direction becomes uniform. Thus, for isotropic coated materials with a radial heat path, the same guidelines that were described in the previous section still apply.

2.5.3.2.3 Results - Orthotropic materials

2.5.3.2.3.1 Transient Temperature Distribution in Uncoated Orthotropic Materials

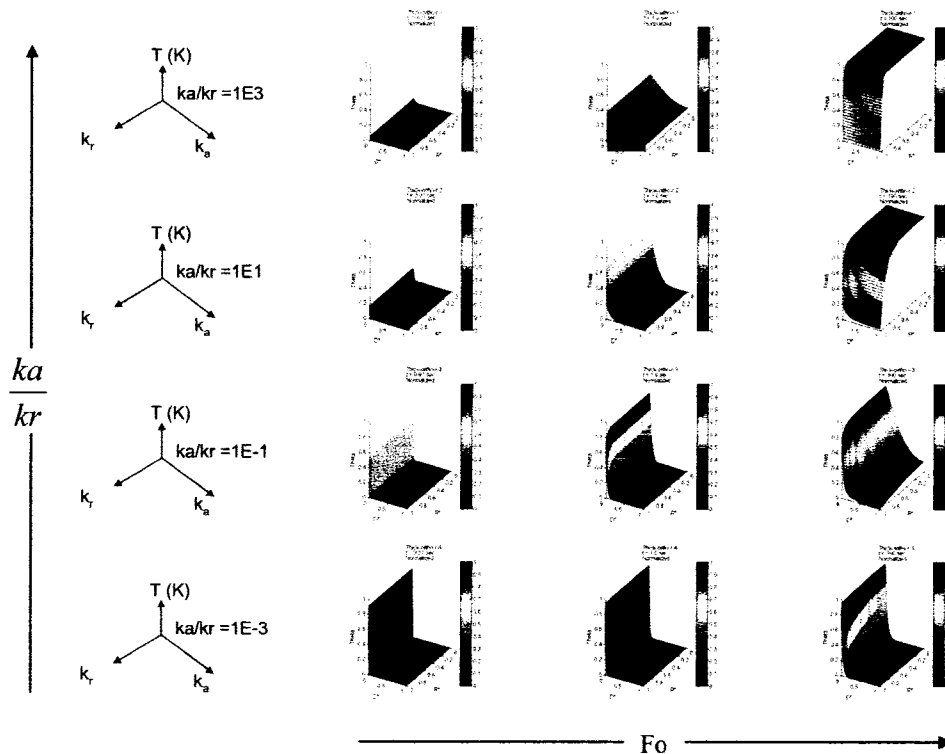


Figure 57. Orthotropic uncoated materials, radial heat path.

Figure 57 is a series of plots showing the temperature distribution in orthotropic materials with a radial heat path. As in the previous plots, Fourier number increases from left to right. For the orthotropic materials modeled,

thermal conductivity was varied in decades from 0.1 to 100 in the radial direction and 1000 to 0.1 in the axial direction. (refer to Table 22). The resulting plots are presented in the same order. The far left column shows the ratio of axial to radial conductivities k_a/k_r . Thus the top row in Figure 57 is of a material with a high axial conductivity and a low radial conductivity. The bottom row is of a material with a low axial conductivity and a high radial conductivity. From this figure we see that as k_a/k_r increases, the through thickness gradient decreases and the radial temperature gradient increases. As k_a/k_r decreases, the through thickness temperature gradient increases while the radial temperature gradient decreases. For all radial cases, there is a distance from the sink in which temperature distribution through thickness is essentially uniform. This distance increases with increasing radial conductivity, or decreasing k_a/k_r . As in the isotropic material cases, an attempt was made to quantify this distance, but was not successful.

Looking at the far right column (highest Fo) in Figure 57 we see what is essentially the steady state temperature distribution for the solid. For $k_a/k_r > 1$ this steady state temperature through thickness is essentially constant (top right plot). For $k_a/k_r < 1$ steady state temperature distribution consists of a sharp gradient through the thickness of the composite.

2.5.3.2.3.2 Transient Temperature Distribution in Coated Orthotropic Materials

For ease of presenting data, the coated orthotropic cases are presented in two series of plots. In each case, the core material has the same properties as those shown in Figure 57. This was done to enable a direct visual comparison. Figure 58 is the same set of core materials with an insulating coating resulting in

$Bb > 1$. Figure 59 is the same set of core materials with a conducting coating resulting in $Bb > 1$. Refer to Table 24 for specific material properties.

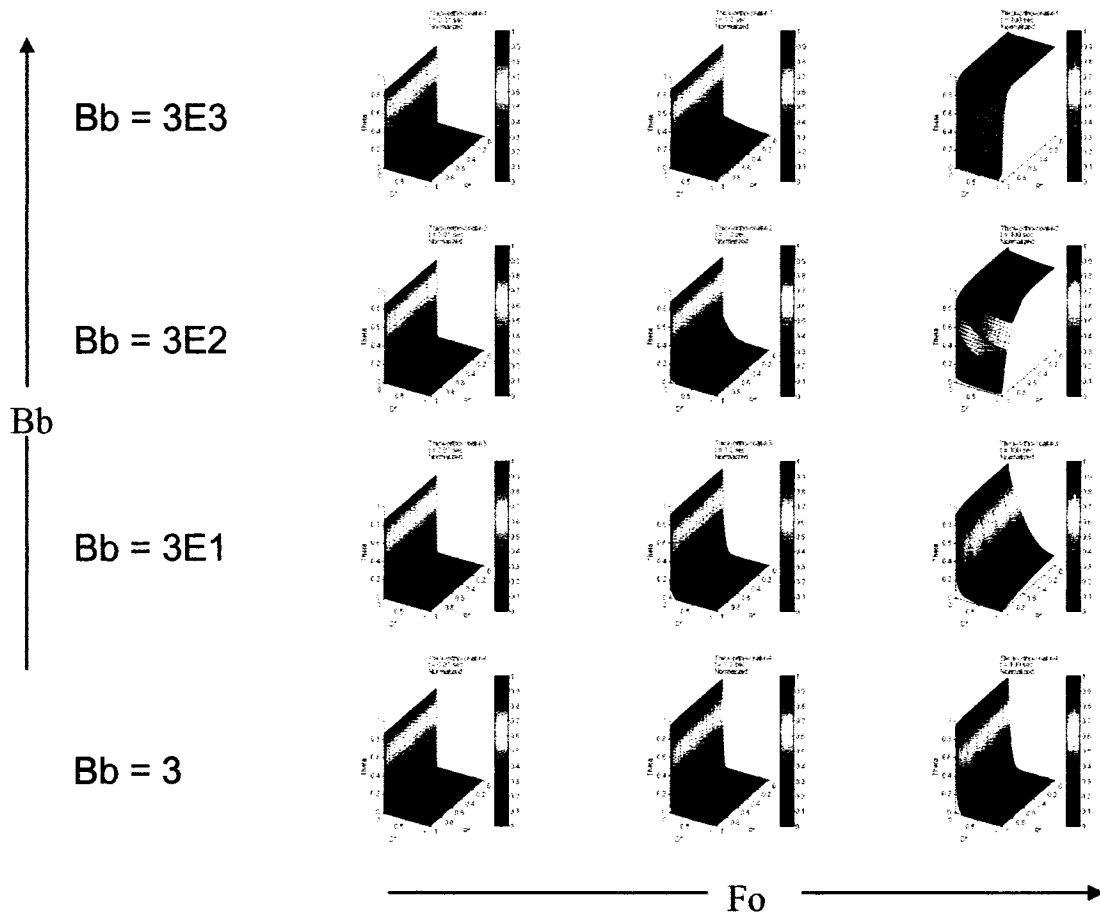


Figure 58. Thick Orthotropic composite with insulating coating, $Bb > 1$.

Compare Figure 57 to Figure 58. For all cases at low Fourier number (left column), the surface temperature is higher in the coated cases than in the uncoated cases. The core temperature is relatively low in all of these cases. However, at intermediate Fo (middle column), the surface temperature remains high, while the core temperature is significantly lower in the coated cases. Thus the insulating coating has the effect of reducing the temperature in the core at all Fourier numbers, yet raises the surface temperature in all cases.

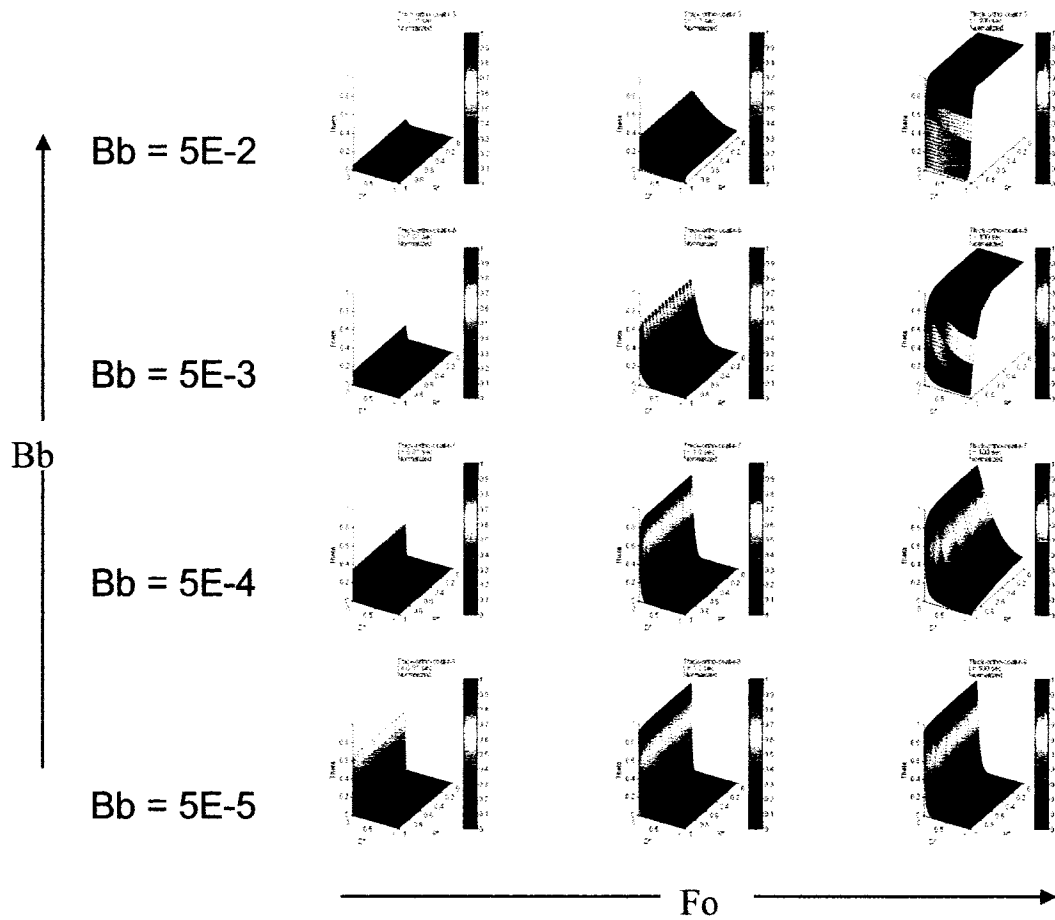


Figure 59. Thick orthotropic composite with conductive coating, $Bb < 1$.

Compare Figure 57 to Figure 59. For $k_a/k_r > 1$ (top two rows), the temperature distributions in both sets of plots appear almost identical, indicating that the conductive coating transmits heat to the core. Because the coating is thin relative to the thickness of the entire part, it is difficult to see this small change in profile. For $k_a/k_r < 1$ (bottom two rows), the surface temperatures actually drop from the uncoated to coated cases and the core temperature actually remains lower. It appears that in these cases the coating is acting as a heat path to the sink. The high radial conductivity and low axial conductivity of the core material contribute to keeping this heat path near the surface of the part.

The heat path is more effective at lower Fo , and penetration into the core increases with increasing Fo .

Additional data analysis was conducted to more thoroughly quantify these trends. Figure 60 is a plot of peak core temperature at the symmetry axis vs. Fourier number for the uncoated and two coated cases. This plot represents a composite with high conductivity parallel to the heat path. These data points were taken from the plots on the bottom rows of Figure 57, Figure 58, and Figure 59.

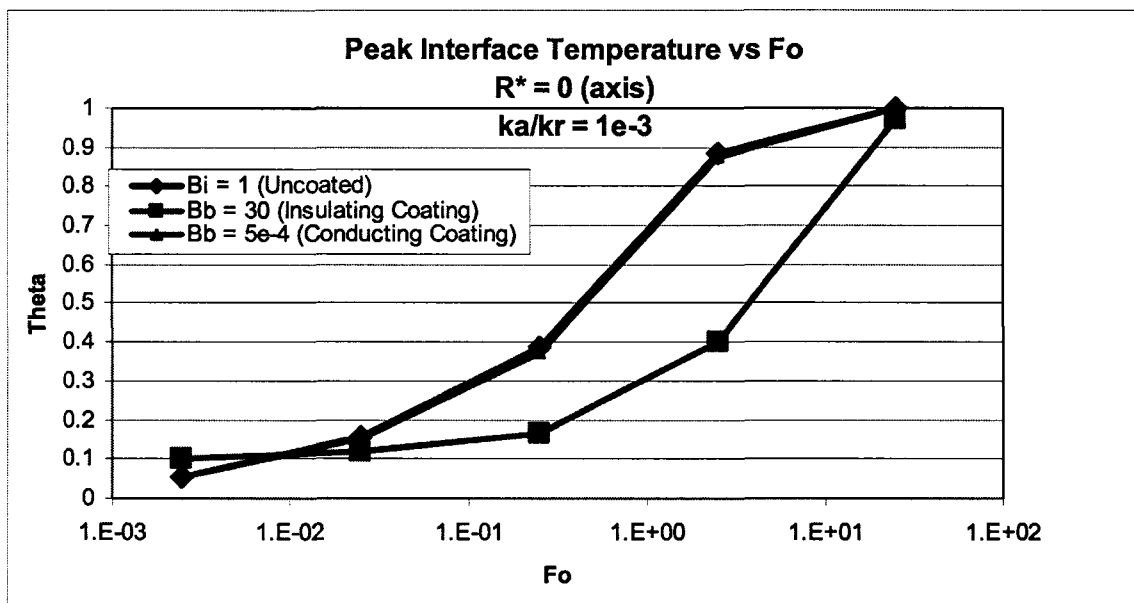


Figure 60. Peak core temperature vs.. Fo for uncoated, insulated and conducting coatings.

The dominant trend in this figure is that the insulating coating reduces the core temperature and delays the temperature rise in the core at Fourier numbers above roughly 0.15. However, at low Fourier numbers, the insulating coating actually increases the peak core temperature. This might be referred to as a “sweet spot” for sing a conductive coating on a FRC to reduce core temperature.

This result also agrees with experimental data published by Roberts in which a flat plate with a surface mounted heat source on one end, and a source on the other observed that, by locating high conductivity fibers near the surface and the source, heat spreading could be accomplished¹¹⁴.

Figure 61 presents the same data, but for the composite with opposite orientation, that is, the high conductivity perpendicular to the heat path. These data points were taken from the top rows of Figure 57, Figure 58, and Figure 59.

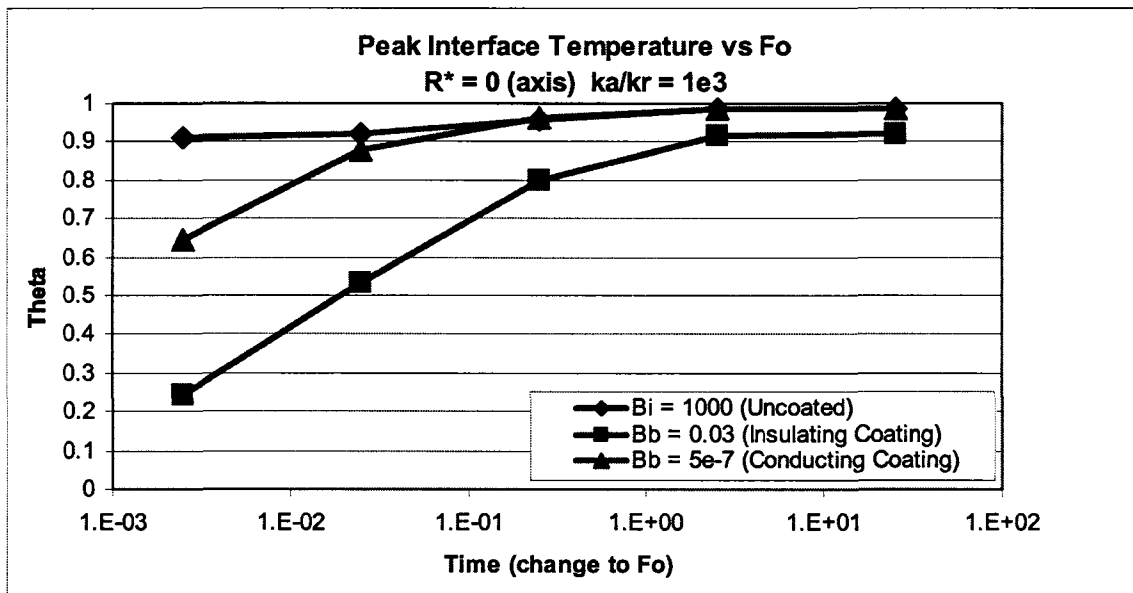


Figure 61. Peak core temperature vs. Fo for uncoated, insulated and conductive coating.

In Figure 61 there is no point where the insulating coating curve crosses the conducting coating curve. Thus there is no sweet spot. In all cases, the insulating coating reduces the core temperature and delays heat transfer to the core. At extremely low Fourier numbers, the conductive coating does a fair job of reducing temperature as well, however at $Fo > 1E-3$, this ability is lost.

2.5.3.2.4 Recommendations – Radial heat path

As in the axial heat path cases, by comparing the ratio of heat transfer into and out of the material interface, B_b , a more accurate assessment of performance can be obtained. Again, if the goal of the designer is to protect the core material, increasing B_b above unity will more effectively reduce the interface temperature. However, in the radial heat path cases there is more flexibility. At low Fourier numbers ($Fo < 10^{-3}$) a conducting heat path may reduce interface temperature enough to within satisfactory limits and may provide superior properties in other than thermal areas such as wear.

In all cases, increasing the axial conductivity of the core decreases peak temperature. This is not easily accomplished with traditional fiber polymer laminates, however small additions of high conductivity materials such as carbon nanotubes can have a dramatic effect on thermal performance of the material. This may also be counterintuitive. One would think that conductivity along the direction of the heat path is most critical. This is true; however a large mismatch (i.e. lower) in conductivity in the orthogonal direction to the heat path creates a large temperature gradient in that material direction. Thus, simply increasing the heat carrying capacity in the direction of the heat path may result in thermal stresses perpendicular to the heat path.

2.5.4 Example – In the Combustion Chamber

As an example, a FRC and coating combination was designed for an intake valve running in an internal combustion engine. The operating conditions for a reciprocating engine valve are a make for a difficult design problem. The

structural and thermal operating conditions are extreme. Table 26 is a summary of the thermal operating conditions that the intake valve is exposed to. This data is based on peak load conditions and corresponds to an engine speed of 5000 RPM. The convective heat transfer coefficient is an average across the entire engine cycle.

Table 26. Intake valve operating conditions.

Intake Valve operating conditions	
T-gas (deg C)	1000
T-ambient (deg C)	30
T-sink (deg C)	250
h (W/mK)	500
cycle time (sec)	0.024

Heat transfer in a valve face is a combination of axial and radial heat flow. The heat source is on the face of the valve, as in the model. The valve seat, back side and stem all act as heat sinks. Depending on operating conditions and valve geometry, roughly 30-40% of heat transfer is through the valve seat when the valve is closed, 40-60% is through convection on the back surface, and 10% is via conduction through the stem.⁴⁰ Thus the results of both the axial and radial analysis must be considered equally.

The initial structural design of the valve consists of T-300 carbon fiber in a high-temperature polyimide (PETI-RFI) matrix. Details of the material properties are shown in Table 27.

Table 27. Material properties for the uncoated FRC intake valve.

Uncoated Valve properties	
Radius (mm)	15
Thickness (mm)	3
Aspect ratio	5
Core Material Properties	
Fiber type	T300
k1 (W/mK)	200
k2 (W/mK)	50
Vf	0.3
Matrix Properties	
Name	PETI-RFI
k (W/mK)	0.7
diffusivity (m ² /s)	0.000583
Peak Service Temperature (deg C)	400
ka/kr	0.04
Bi (axial)	0.66
Fo (axial)	1.56

From this initial calculation of k_a/k_r , Bi and Fo for the uncoated valve, it is possible to get an understanding of the temperature profile in the valve under operating conditions. Referring to Figure 57, the operating conditions for the valve fall between the bottom two rows at the highest Fourier number. That is, there is a surface temperature roughly equal to the gas temperature and a large temperature gradient through the thickness of the valve. Alternately, one can look at the axial heat path temperature profiles. In Figure 44, the top right temperature profile at the highest Fourier number is closest to the operating conditions of the valve.

Based on the design goal of reducing the operating temperature of the core composite material, there are several options to pursue. Recall that, to reduce the temperature of the core material coatings should be chosen such that $Bb > 1$ and that this protection increases with increasing Bb . There are several

other design constraints for the valve as well. For design reasons that have to do with stability of running the engine, we would like to keep the face temperature of the valve as low as possible. High surface temperatures in the combustion chamber lead to auto-ignition of the fuel, known as knocking. Also, any material that contacts the valve seat should have a high toughness and wear resistance due to the mechanical loading of the valve.

The changes in design are shown in Table 28. Design #1 added a nickel coating to the FRC valve. This was chosen based on the logic that this might act as a heat path to the valve seat. However, inspection of the Fourier number reveals that this is far too high to be in the “sweet spot” described earlier. The goal of design change #2 was to increase the core conductivity by increasing fiber content and changing to a more conductive carbon fiber. This has the effect of bringing B_b closer to 1. Design change #3 changes the coating to a stainless steel, with a lower conductivity than Nickel. This increases B_b above 1. From Figure 50 we see that a value for B_b greater than 10 is necessary to drop core temperature significantly. Design change #4 does this by adding carbon nanofibers to the matrix material. This increases the core conductivity in all directions and increases B_b above 25. According to Figure 50, this should lower the interface temperature by roughly 80%. This should bring the core material temperature down to below 400°C, the maximum service temperature of the polymer.

Table 28. FRC valve design changes for thermal management.

	Design #1	Design #2	Design #3	Design #4
Fiber type	T300	K-1100	K-1100	Carbon Nanotubes
Fiber Vf	0.3	0.8	0.8	0.8
Coating type	Nickel	Nickel	Stainless Steel	Stainless Steel
Coating thickness (mm)	1.00E-04	0.1	0.1	0.2
Fo	4.86E+04	4.86E+04	9.60E+03	2.40E+03
Bb	0.07	0.41	2.30	25.16

2.6 Discussion of Modeling Results

Using basic mechanics, a prediction of mass reduction was made for a small aircraft engine. Using direct substitution of FRC materials for existing components, it is predicted that engine mass can be reduced by roughly 55%. A 72% mass reduction for the reciprocating mechanism is possible. Redesigning the system to take advantage of the reduced inertial loads enabled by FRC components may enable even further mass reduction. A conservative estimate using this shows 90% mass reduction of reciprocating mass may be possible.

A viable structural model for a FRC valve has been designed. While the structural design of FRCs using FEA is not new, this process was not trivial. Dynamic loading seen by the valve under normal operating conditions and under valve bounce conditions are severe. In addition, several new, novel ideas have been incorporated into this design to aid in manufacture with the goal of high-volume production. Recall that the two previous attempts at FRC valves were multi-part components bonded together. These new designs are:

- The fiber is designed to be a one-piece continuous fiber preform
- The valve will be a net-shape resin transfer molded valve, minimum machining will be required once removed from the mold.
- From the analysis, the structural design should equal or surpass that of a steel valve.

Initial transient thermal analysis using a one-dimensional flat plate with convective heat transfer showed that the decreased conductivity of the FRC matrix material causes a sharp temperature gradient near the exposed surface, increasing surface temperature. Initial results suggest that orienting conductive fibers along the heat path will help to alleviate this problem and that a temperature distribution similar to that in the steel component is attainable using FRC materials.

A comprehensive analysis has been undertaken to quantify the effects of coating and core material combinations on the thermal performance of FRCs with axial and radial heat paths. Specific emphasis has been placed on reducing the core temperature of the FRC material.

A novel method of quantifying performance of core/coating combinations has been developed which compares the ratio the heat carrying capacity of the coating to the heat carrying capacity of the core material under convective heat transfer conditions. This ratio is referred to as Bb and is defined as:

$$Bb = \left(\frac{k_1}{L_1} \right) \left(\frac{L_2}{k_2} \right) \left(1 + h \frac{L_2}{k_2} \right) \quad \text{Equation 30}$$

Analysis results have shown that for combinations of coating and core material, $Bb < 1$ will result in a higher interface temperature and $Bb < 0.1$, interface

temperature is effectively equal to surface temperature. In these cases, the coating material effectively transmits heat to the core. For $Bb > 1$, a large temperature gradient occurs in the coating material, effectively insulating the core material from the heat source. In addition, the highly orthotropic nature of FRCs greatly affects the thermal response of the material. While orienting fibers along the heat path reduces the temperature gradient in that direction, a FRC with a large ratio of conductivities in the orthogonal directions will experience a steep temperature gradient in the direction of the lowest conductivity, typically orthogonal to the fiber direction. This can again lead to high surface temperatures and high internal thermal stresses.

The methodology described allows the designer to more quickly focus the hone the design than by running numerous complex simulations of specific materials. This design methodology has been applied to the thermal design of a FRC intake valve. Initial estimates shown that, by changing fiber type and volume fraction, and by adding a metallic coating, the temperature experienced by the matrix material can be reduced by several hundred degrees, making the FRC valve thermally viable.

An initial thermal management for the FRC valve face has been presented which should reduce surface temperature and reduce coating interface temperatures by roughly 80%. This solution involves increasing the conductivity of the FRC in the face, as well as adding a stainless steel barrier coating on the face.

3 Process Development

As mentioned in the introduction, resin transfer molding was chosen for the valve manufacture process. A significant amount of process development was required to make this process work. Process parameters such as injection temperatures and pressures, fiber holding strategies and mold development were all required. Details of the process development, as well as several innovations in the RTM process are covered in this chapter. The majority of this work involved experimentation with process parameters and adjustment of the process to achieve the desired results. Although presented separately, development of the fiber holding strategy, mold design and process parameters were conducted in parallel. Detailed development of process parameters for PETI-RFI is covered as well.

3.1 Resin Transfer Molding (RTM)

Many of the high-temperature capable FRC materials mentioned previously, such as ceramics matrix composites, and carbon-carbon are time and energy intensive and difficult to produce. For that reason polymer matrix composites were chosen because they are relatively easy to work with.

Resin Transfer Molding is a process where a preform of fiber (dry or partially wetted) is placed in a mold and liquid resin is pumped into the mold. The resin is allowed to cure in the mold to form a solid composite¹¹⁵. In practice,

RTM is similar to injection molding. A schematic of an RTM apparatus is shown in Figure 62. Variations on the process depend on the particular part being molded. Some variations use an open mold and a vacuum bagged part (SCRIMP) or vacuum assisted resin transfer (VARTM) in a mold, Advantages of RTM include:

- Ability to mold complex shapes
- High level of automation possible
- Ease of fiber lay-up (using preforms)
- Reduced process time
- High fiber volume-fractions are possible
- Reduced emissions during manufacturing¹¹⁵

Some of the apparent advantages over traditional valve manufacturing techniques are:

- Molded parts are near-net shape directly out of the mold, reducing the need for additional finish machining.
- Surface finish of a molded part is excellent, again reducing additional finish machining.
- The process is well suited to mass-production and production can be highly automated.

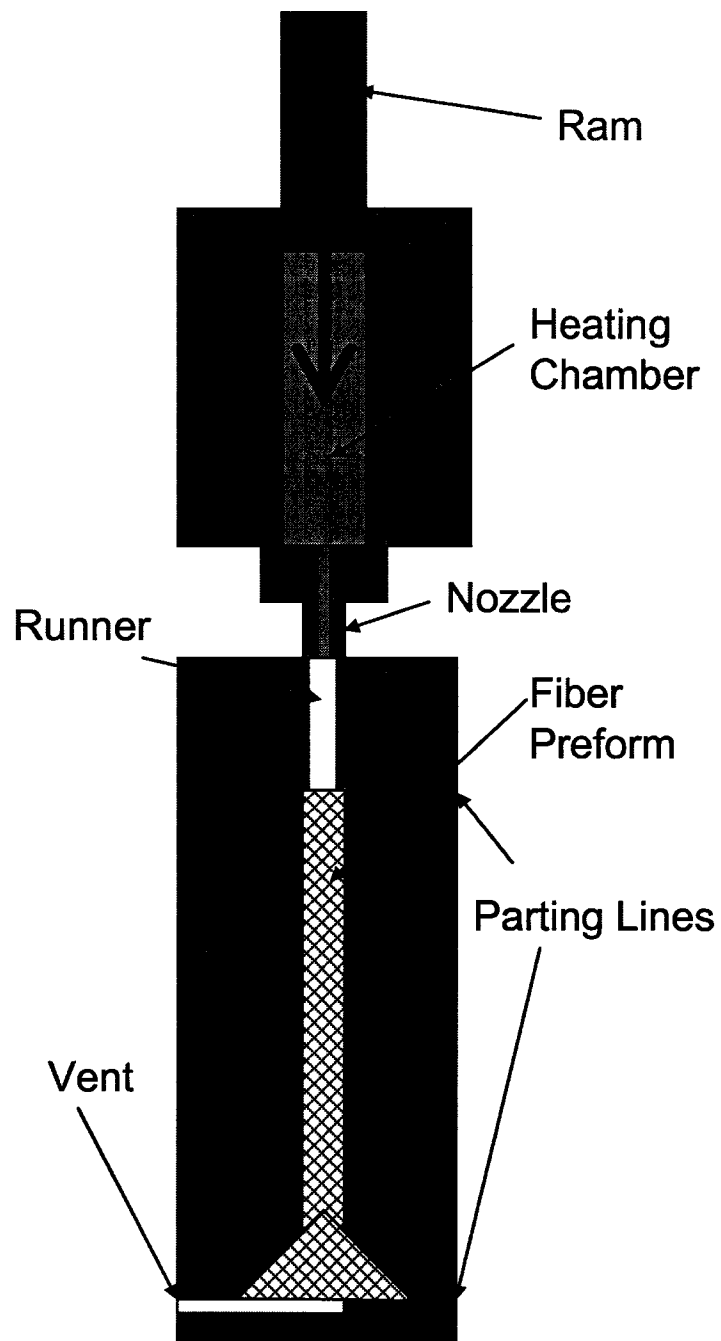


Figure 62. Schematic of resin transfer molding apparatus.

3.2 RTM Process Development

3.2.1 Fiber holding strategies

Even though the desired fiber orientations were now determined, it was unclear how the fibers would be placed in the mold and how fiber orientation would be maintained during the injection process. An evaluation of alternatives was performed to decide which method was most desirable from a manufacturing point of view. The results are tabulated in Table 29. Fiber holding strategies ranked. Most preferable was using a fiber/matrix preform which would then be inserted into the final mold and matrix injected to mold the valve to final shape. However, this effectively requires two molds, one for the preform and one for the final molded shape.

Table 29. Fiber holding strategies ranked

Concept	Rank	Primary Challenge
Fiber/ Matrix Preform	1	Preform Manufacture and wetting
Floating Fiber	1	Fiber Movement during injection
Fiber Ends Clamped	3	Sealing and Flash during injection
Very High Volume Fraction	4	Fiber Wetting and orientation

Equally appealing from a manufacturing point of view was having the fibers floating in the mold and injecting the matrix around and through the floating fibers. However, it was unclear if this method would be satisfactory in maintaining the fiber orientation.

A number of experiments were undertaken to evaluate the fiber placement options In Table 29. Because a limited supply of the chosen matrix material,

PETI-RFI, was available, these experiments were conducted using polystyrene and acrylic as the polymer.

3.2.1.1 Injection and Fiber Placement Experiments

To answer the question of whether a preform or floating fibers would be necessary, a series of trials was undertaken. Thermoplastics typically have a high viscosity. Therefore, the objective of these tests was to determine if fibers would maintain their orientation inside the mold and if fibers could be sufficiently “wetted” inside the mold.

Over twenty tests were performed. Each used a single braided fiber sleeve inside a mold of the valve. A single-shot experimental injection molder was used for these tests. A schematic of the one-shot injection molder is shown in Figure 62 and a picture is shown in Figure 63. The matrix was injected from either the valve face or the valve tip. The fiber braid was clamped in the mold to prevent the fiber from being pushed out of the mold. A vent was incorporated into the opposite end of the mold to allow air to release from the mold. Temperature of the matrix and mold were varied to see the effect on fiber orientation and fiber wetting. Table 30 shows the details of the five test conditions.

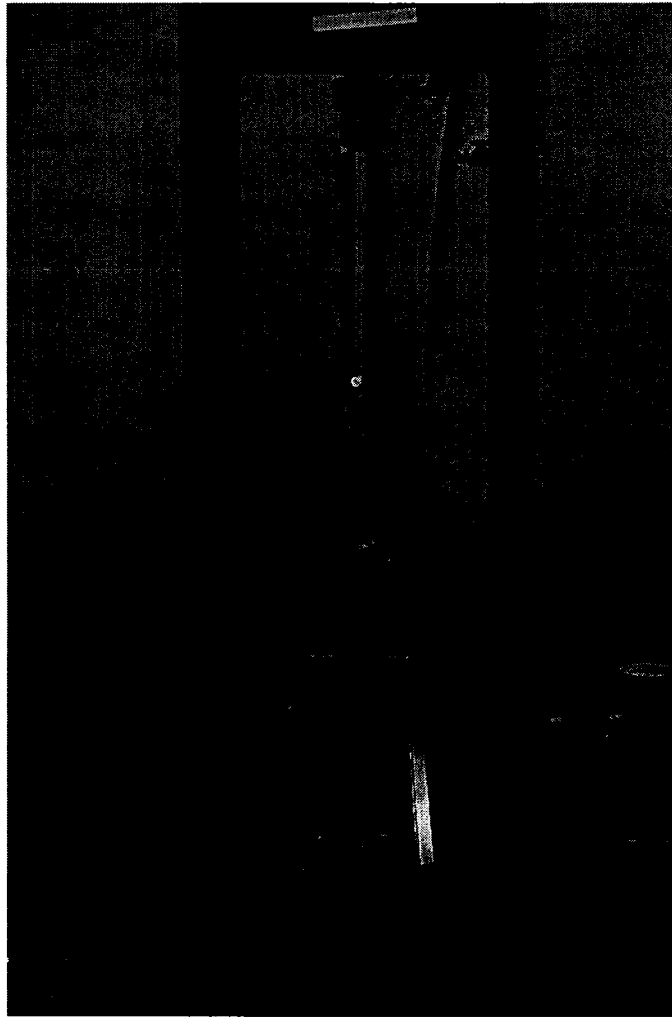


Figure 63. Injection molder in load frame.

Table 30. Injection mold fiber placement test conditions.

TEST #	MATRIX TEMP °C	MOLD TEMP °C	RAM SPEED (IN/SEC)	MOLD SOAK TEMPERATURE AND TIME
1	200	~25	5	NA
5	220	100	5	NA
10	200	200	2	5 min @ 185°C
13	200	200	2	10 min @ 190°C
21	200	225	2	5 min @ 225°C

3.2.1.2 Injection and Fiber Placement Results

A number of insights were gained from the fiber placement experiments. It was found that having low volume fraction of fibers in a preform tends

Tests showed that injecting from the valve face results in incomplete wetting of the fibers at the transition from the stem to the face. Conversely, injecting from the tip of the valve and soaking the mold at temperature for at least five minutes before cooling results in complete fiber wetting and mold filling through the entire valve.

At lower temperatures and high injection speeds, the matrix tends to push the fibers out of the way and does not wet the fiber at all. Increasing the temperature of the matrix, mold and fiber improves the penetration of the matrix into the mold and into the fiber. In addition, slowing the injection rate also increases the fiber wetting. Figure 64 is from injection trial #8. The black is the carbon fiber weave; the lighter color is the acrylic matrix material. The injection rate was slowed from previous trials. Fiber, mold and matrix were all at elevated temperature during injection. Close inspection reveals some penetration of the matrix into the fiber. From these initial trials, it was determined that a fiber preform would be needed to maintain fiber orientation during injection of the matrix.



Figure 64. Fiber placement trial #8

Additional experiments showed that the resin material must be injected through the preform in order to completely wet the fibers. Failure to do so will simply push the fibers out of the way. Figure 65 is a picture of a polystyrene valve in which the fiber preform was simply clamped to the side of the mold. The resin did not wet the fibers and simply pushed the preform to the side of the mold.

Failure to adequately hold the end of the preform in place during injection will push the preform down inside the mold. The result is a piece that is fiber-free at one end and a fiber-rich at the other end.

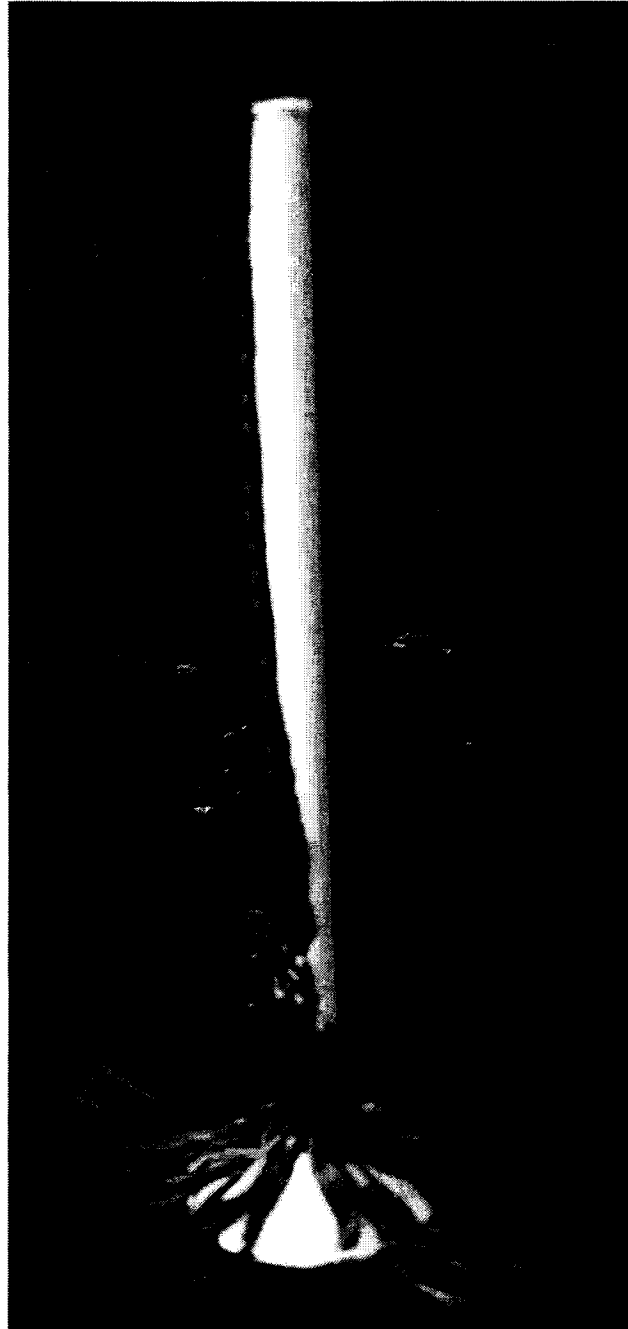


Figure 65. Polystyrene valve with a carbon fiber preform pushed to the side.

In the end, a solution was devised in which two compression-fit rings were used to clamp the fiber at the tip. This enables positive location of the fiber preform as well as the ability to inject the resin through the center of the preform. This setup forces infiltration of the resin through the fiber, wetting the fiber. Figure 66 is a picture of the fiber clamp on the end of the preform, prior to insertion into the mold. To the best of the authors knowledge, this is the first time such a fiber clamp has been used for holding and positively locating a fiber preform, and injecting through the center of the preform.

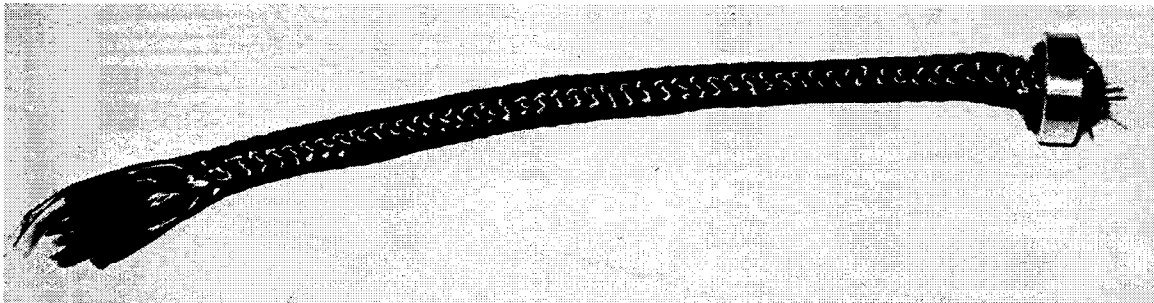


Figure 66. Fiber clamping rings in place on the fiber preform.

3.2.2 Mold Design

Once requirements for the valve were known, and a preliminary valve design was decided upon, processing requirements were determined and the same design process was used to design the mold.

3.2.2.1 Mold requirements

Mold functions and requirements were determined to be:

- Deliver the matrix material to the fiber
- Achieve tight dimensional tolerances
- Heat and/or cool the composite valve.

- Hold the fiber and maintain fiber orientation during the injection process.
- For the purpose of prototyping, the material should be easy to machine and of low cost.
- A Coefficient of Thermal Expansion (CTE) different from the fiber/matrix combination is desirable to ease in release of the valve from the mold.
- Surface finish of the molded valve should require little or no additional machining.
- The mold must fit within the geometric constraints of the existing injection molding machine.
- The mold must have provisions for ejecting the valve after molding.

3.2.2.2 Prototype Mold Design

Mold design was undertaken to satisfy the previously outlined requirements. The initial prototype mold was made of 6061-T6 aluminum.

Aluminum was chosen for the following reasons:

- Relatively inexpensive compared to other mold materials.
- It was readily available.
- Easily machinable for prototype development.
- Desirable Coefficient of Thermal Expansion (CTE) relative to matrix materials.

The mold was CNC machined to achieve tight dimensional tolerances and achieve a superior surface finish on the stem. The mold was designed with a

right-angle runner that clamps onto the valve head side of the mold (the right side in Figure 67). This was done to facilitate placement in the one-shot injection molder. The end cap was made removable to allow ejection of the valve using an ejector pin at the valve tip. Figure 67 is a wire frame model of the prototype mold. Figure 68 is a photo of the actual mold showing the runner for matrix delivery.

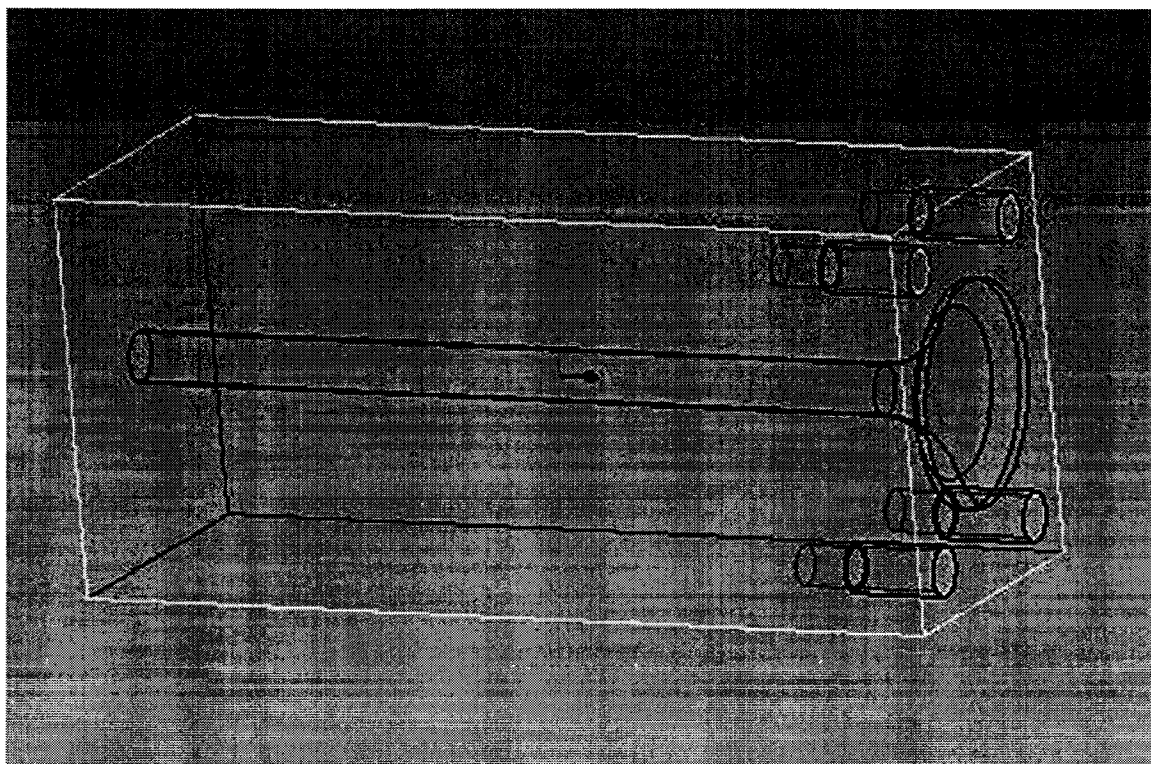


Figure 67. Wire frame model of the initial one-piece mold design.

Additional space was left around the valve stem for future placement of cartridge heaters and/or cooling lines. This was done because curing of high temperature polymers requires specific heating and cooling rates and times to achieve maximum strength.

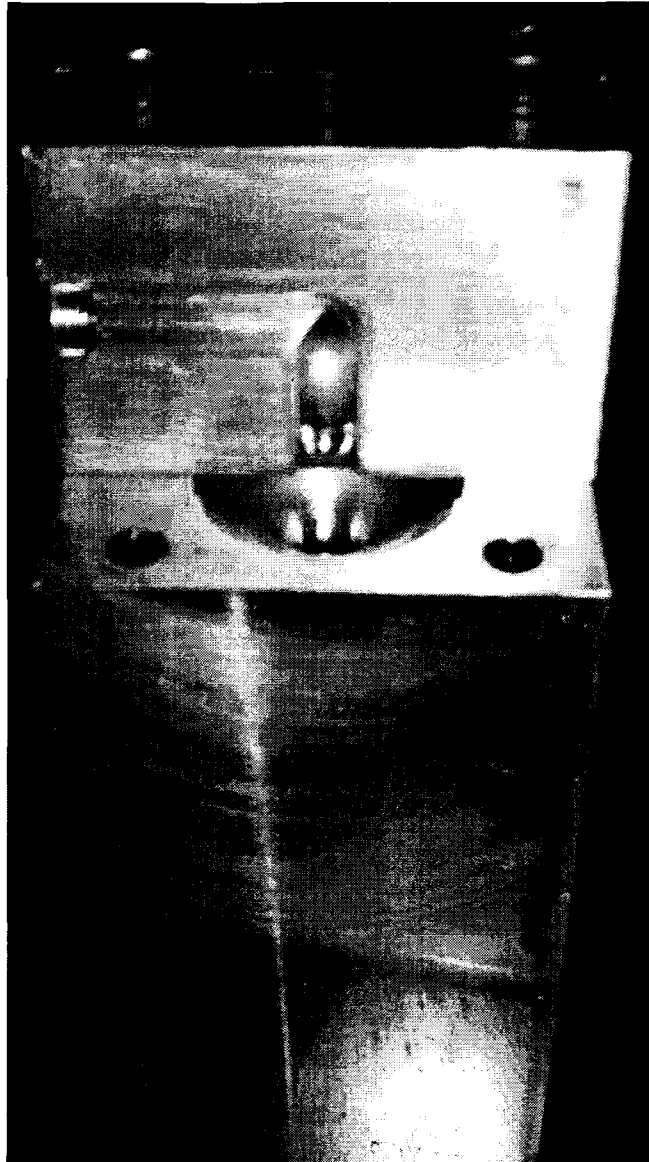


Figure 68. Photo of prototype mold showing gate and runner orientation.

3.2.2.3 Intermediate Mold Design

After many experiments, the mold design was refined to add the following features:

- A split mold design was selected to facilitate mold preparation and part ejection.

- Electric cartridge heaters were placed along the stem for even heating.
- Thermocouple holes were located along the stem for mold temperature monitoring and control.
- Injection ports were revised to allow injection from the tip of the valve.
- Clamping plates were incorporated to minimize flash of resin under high injection pressures.
- A quick-release union fitting was incorporated for separating the mold from the injection barrel.
- Vent size and location were revised for better mold filling and fiber wetting.
- A two-piece end cap at the valve face was developed to allow compression of fibers into the larger volume of the valve face, increasing fiber volume fraction in the face.

An exploded view of the intermediate mold design is shown in Figure 69.

A photo of the intermediate mold design with end-caps in place for curing is shown in Figure 70.

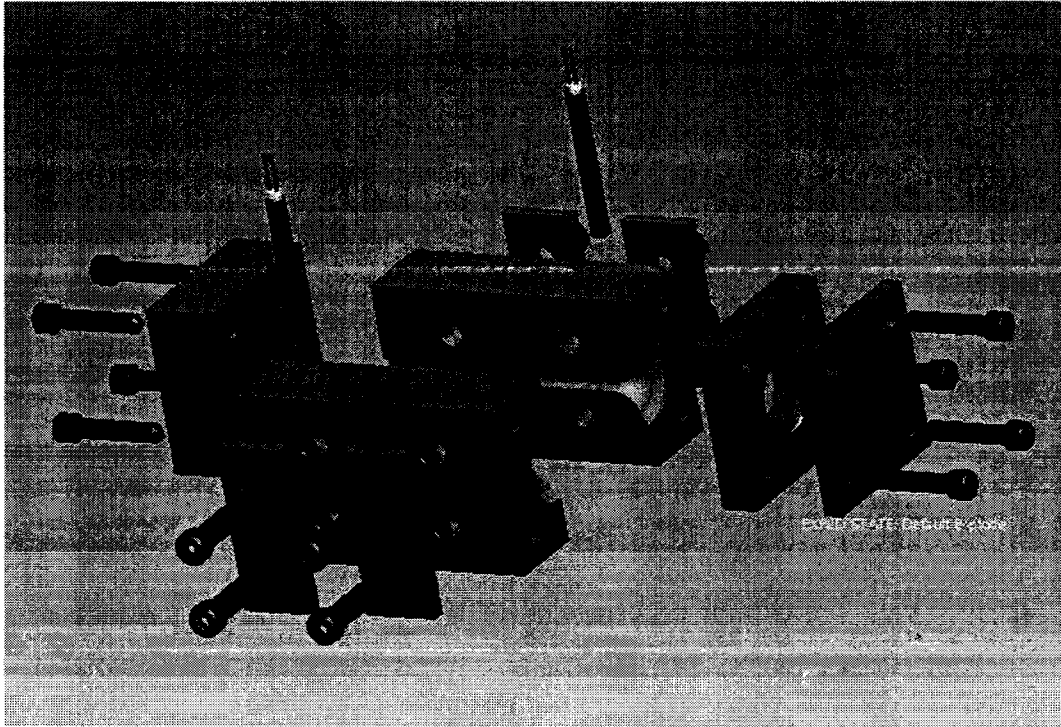


Figure 69. Exploded view of the intermediate, modular mold design

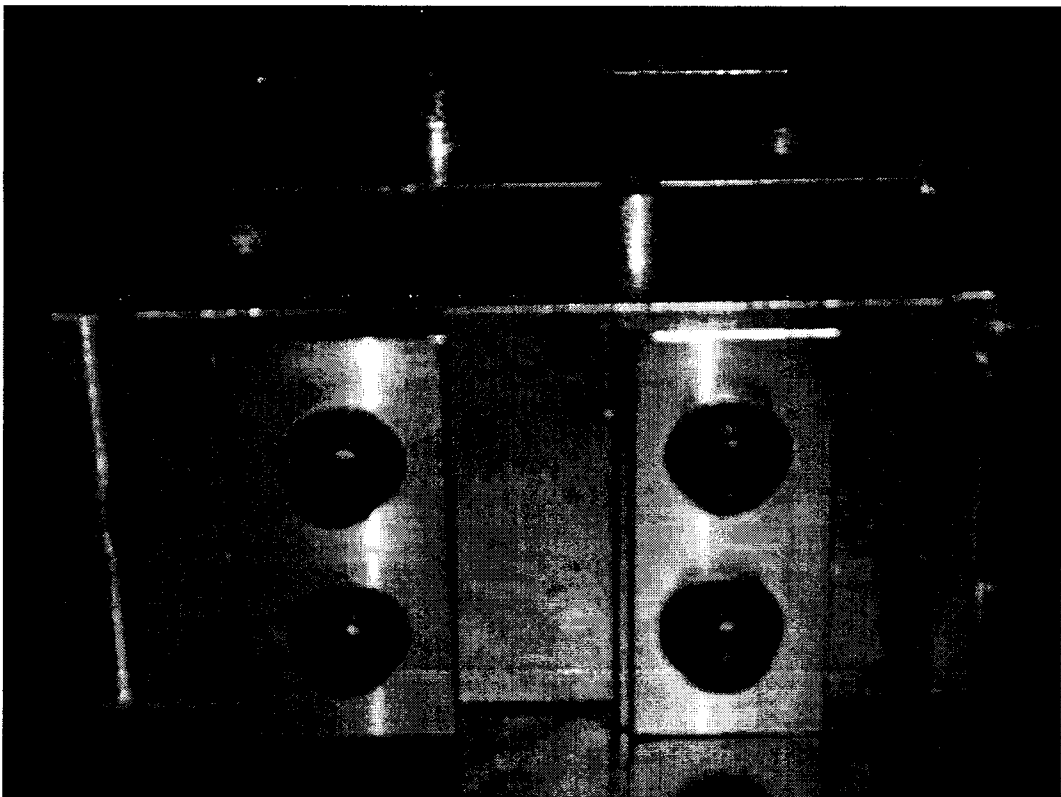


Figure 70. Intermediate modular mold design shown with flat end plates used for valve curing.

3.2.2.4 Final Mold Design

Still more improvements were made after the manufacture of nearly 20 carbon fiber reinforced PETI-RFI valves. A number of additional improvements were made including:

- A modular valve face section that enables that manufacture of both intake and exhaust valves.
- Locating pins for precise alignment
- Stainless steel mold material for increased durability, and the ability to mold different matrix materials.

An exploded view of the final mold design is shown in Figure 71.

3.2.3 Other Process Developments

A number of additional process developments were made that do not fall into the two categories above.

Recall from the structural analysis of the FRC valve presented in section 2.3 that the stem to face transition area of the valve was reinforced with an additional two layers of carbon fiber braid. Because the outer diameters of the valve stem and face are only 0.25 inch in and 1.125 inch respectively and this transition area is roughly 0.5 inch long, assembling the preform in this configuration turned out to be extremely difficult. Carbon fiber braid is very “slippery” and unravels easily. Thus placing the extra fiber layers in this section was nearly impossible. To alleviate the problem, an alternative technique was developed. Discs of carbon fiber and PETI-RFI “prepreg” were made by melting the PETI-RFI in thermoplastic form into sheets of carbon fiber weave.

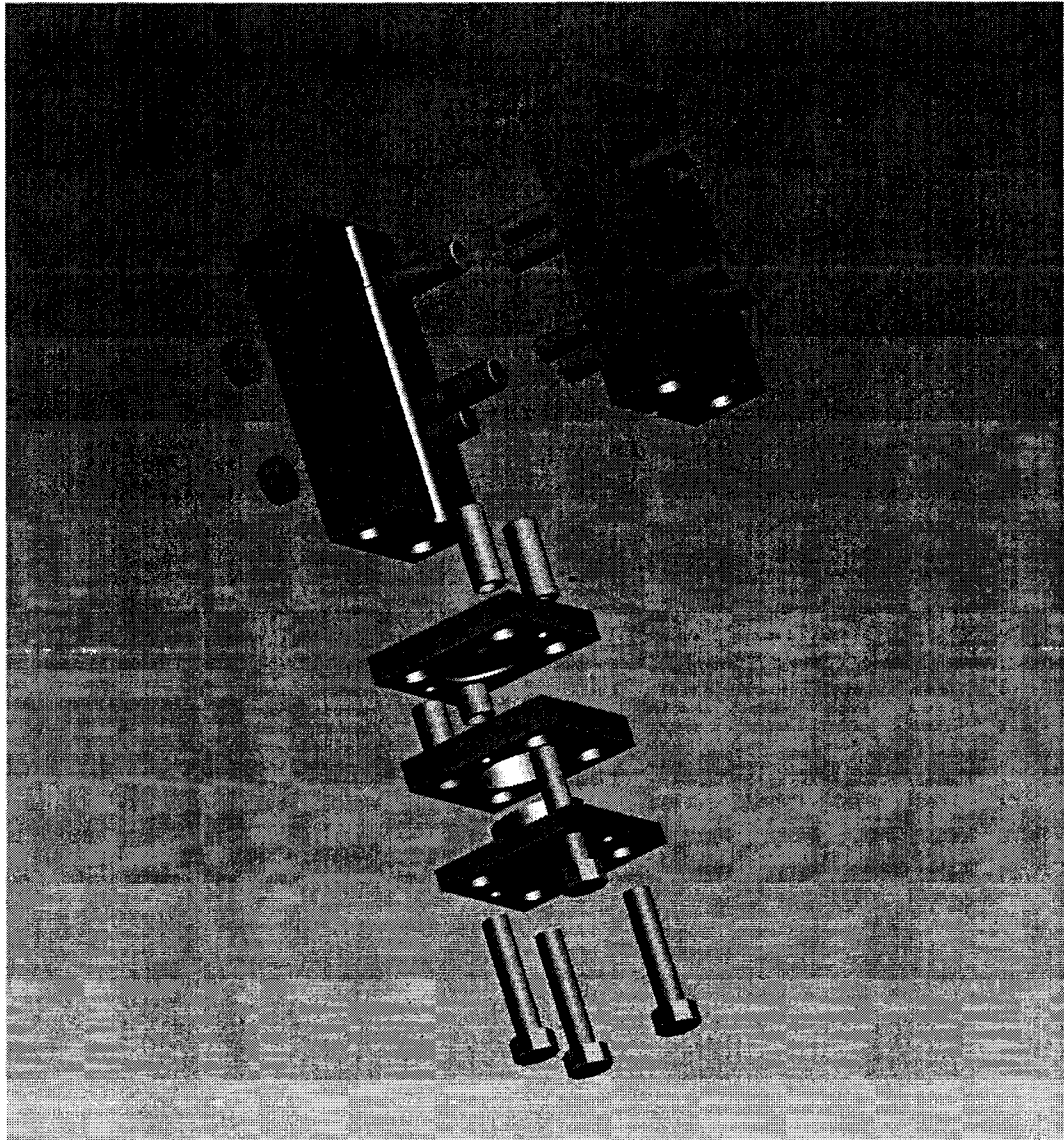


Figure 71. Final modular mold design.

Discs the diameter of the valve face were cut or punched from these sheets. These prepreg discs were then placed into the face of the valve mold during assembly, in place of the stem reinforcement, prior to injection. When the thermoplastic resin was injected into the mold, the resin in the prepreg discs melted together with the resin introduced during RTM. Curing of the valve at high temperature produced a one-piece mold and no evidence of the separate 'parts' was visible. These prepreg discs served the same structural purpose as

the extra layers of fiber braid mentioned above, but also increased the bending stiffness of the valve face. Discs were used to increase the fiber fraction in the face of the valve, thereby increasing strength and stiffness.

Although the use of prepreg is common in the composites industry it is typically done with a lay-up type part production. The use of sections of prepreg material in a RTM part is a new development and adds greater flexibility to the manufacture process. This technique could also be used to add other functional components to the part, such as tailored wear surfaces or different conductivity materials to further improve the part performance. This is the technique the author would recommend to place carbon nanotubes or nanofibers into the face of the valve to increase conductivity, as mentioned in section 2.5.4. In addition, this type of insert could also be added after the injection process, but prior to the final cure.

Most FRC components are relatively thin and uniform in thickness. As a result, uniform fiber placement and volume fraction is typically not a problem. In the valve, the transition from the 0.25 inch diameter stem to the 1.125 inch diameter causes a problem. The use of a one-piece continuous fiber preform ensures fiber placement and a uniform amount of fiber through the valve profile. The increase in cross sectional area at the valve transition coupled with the constant amount of fibers causes a decrease in the volume fraction of fibers and a corresponding decrease in strength in this area. In addition to the prepreg discs discussed in the previous paragraph, a device was incorporated into the face of the valve mold. An extra-long fiber preform was manufactured and the

excess fiber from the preform was pressed into the face using a disc-in-cup type arrangement, effectively producing randomly oriented fibers in the interior of the part. This increased the fiber fraction and thus the strength in the valve face and transition area.

3.2.4 Final Manufacturing Process

The process of manufacture for the FRC valve under development follows the steps below:

- A fiber preform is assembled from unidirectional fiber and fiber braid.
- The fiber preform is placed inside the mold.
- Polymer resin at high temperature (245°C) is injected into the mold, under high pressure, infiltrating the fiber preform, and filling the mold.
- The mold is cooled to allow the polymer to harden.
- The ends of the mold are removed and replaced with sealing caps.
- The entire mold is placed in an oven and the resin is processed at elevated temperature (360°C) for two hours.
- The mold is cooled and the valve is removed from the mold.
- Parting lines, which contain only small amounts of excess polymer, are removed from the valve stem.
- The tip is sanded to final length.

The valve is removed from the mold with the proper seat angle and the keeper geometry already molded in place. Figure 72 is a schematic of the manufacture process. Figure 73 shows four valves immediately after being

removed from the mold. The finished valves weigh a mere 7.3 grams each. This is an 81% mass reduction over the stock steel valve weighing over 38.4 grams.

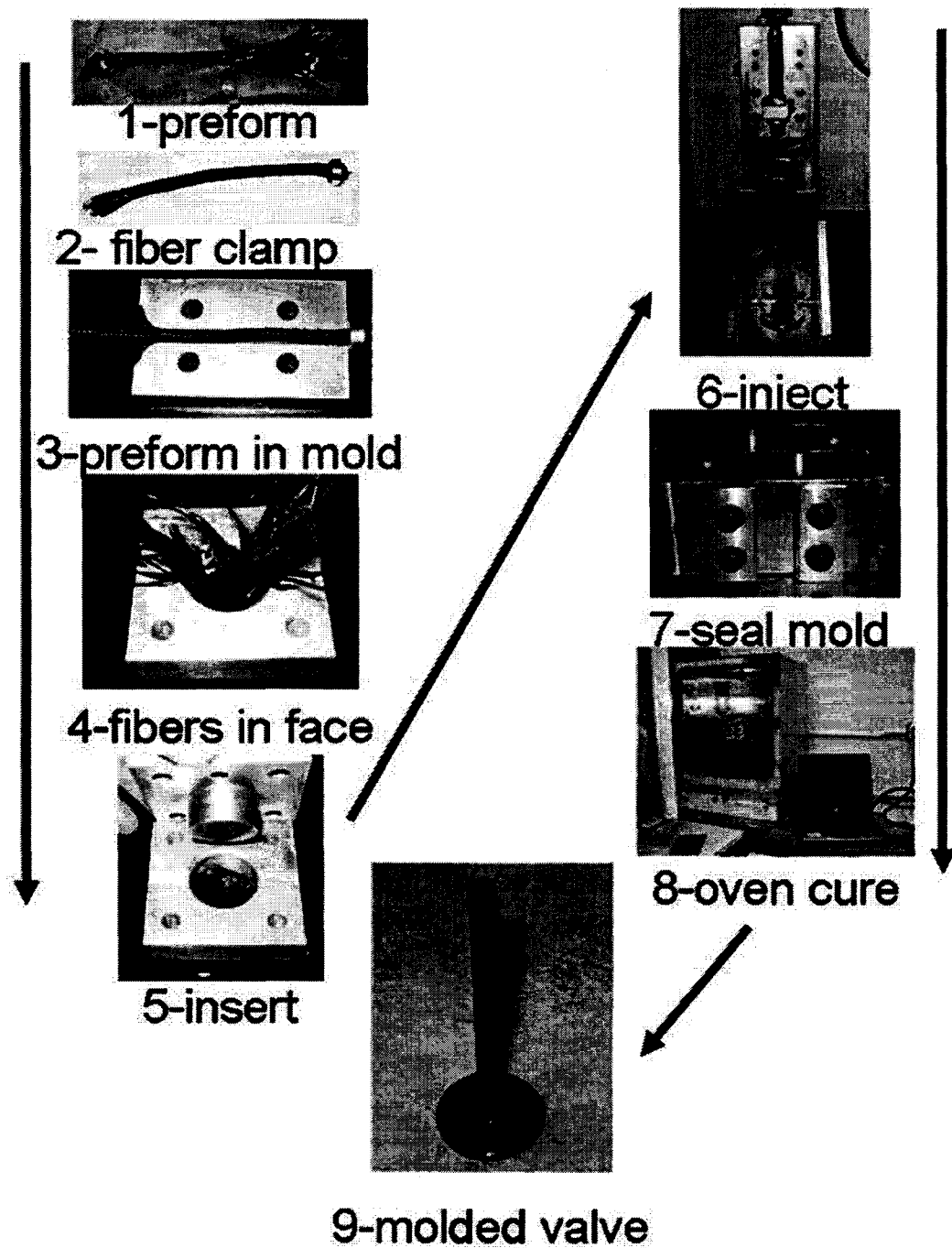


Figure 72. Schematic of the FRC valve manufacture process.

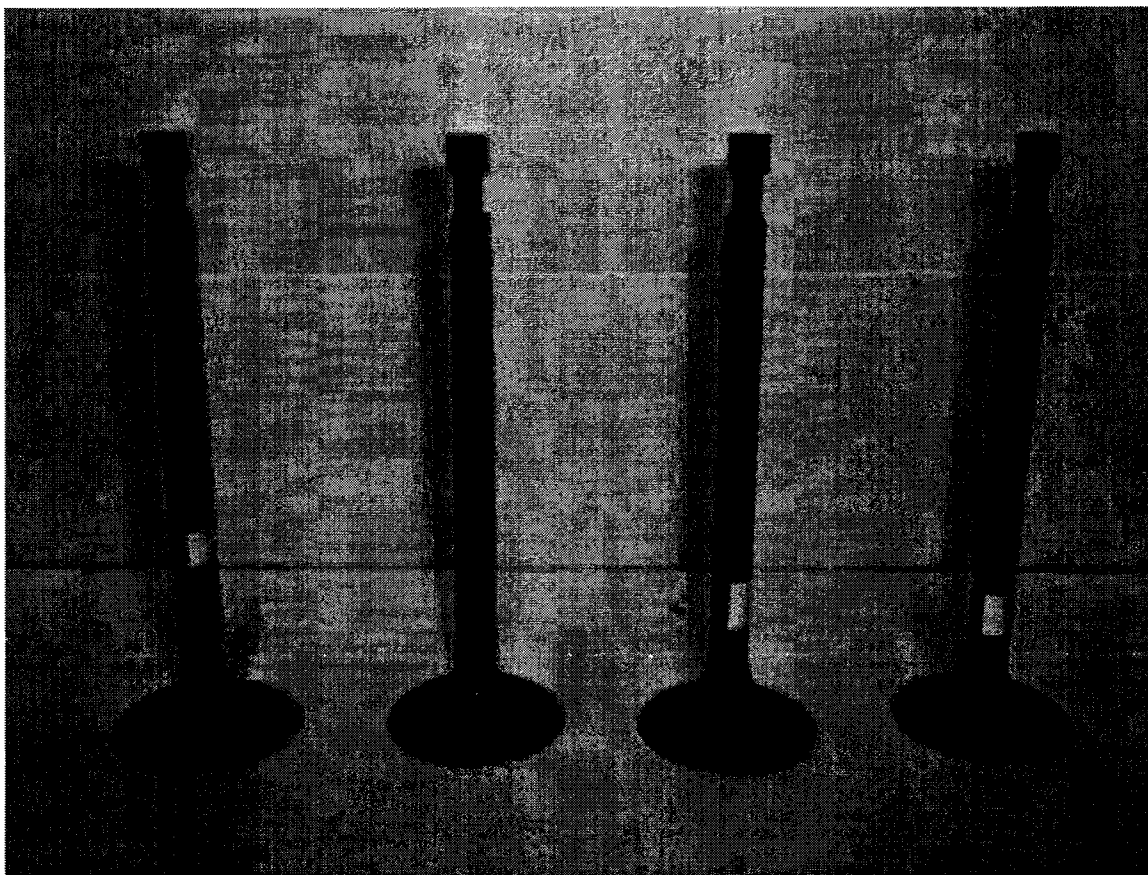


Figure 73. As-molded carbon-fiber PETI-RFI valves.

3.3 Processing of PETI-RFI

Once the manufacture process for carbon-fiber reinforced PETI-RFI valves has been demonstrated, valve manufacture began in earnest. During this process, small changes were made, primarily to the cure cycle, to improve processing and valve quality. All of the valves manufactured and mentioned in the previous section had a small amount of surface porosity. An example of the surface porosity on the stem of a valve is shown in Figure 74 and porosity on the face is shown in Figure 75. This surface porosity did not appear to affect the performance of the valves, discussed in the following chapter. However, the size and quantity of surface voids began increasing with increased number of valves

manufactured. Eventually, porosity increased to the point that the cause and a solution needed to be addressed in order to produce high quality valves. As a result, an in-depth processing study of PETI-RFI was conducted. The process described in this chapter alone took the better part of one year to accomplish.

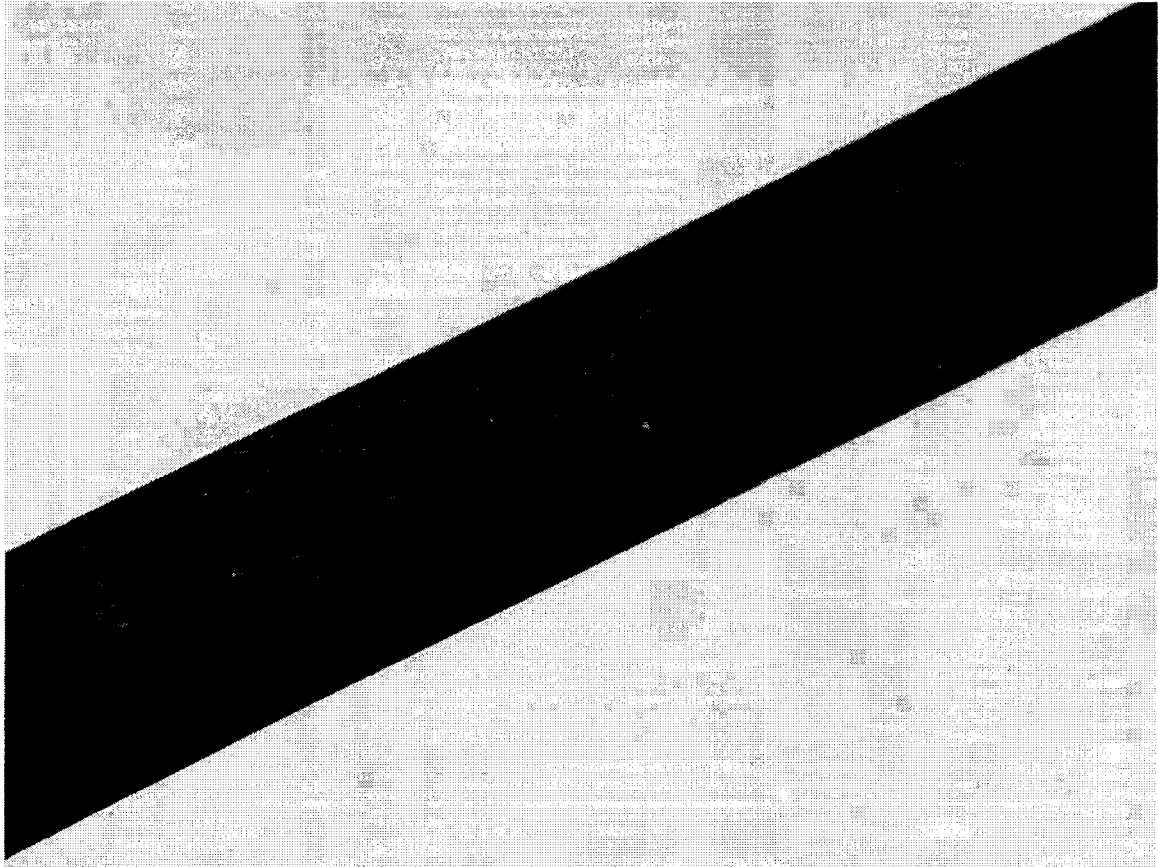


Figure 74. Photo of the stem of a carbon-fiber/PETI-RFI valve showing surface porosity

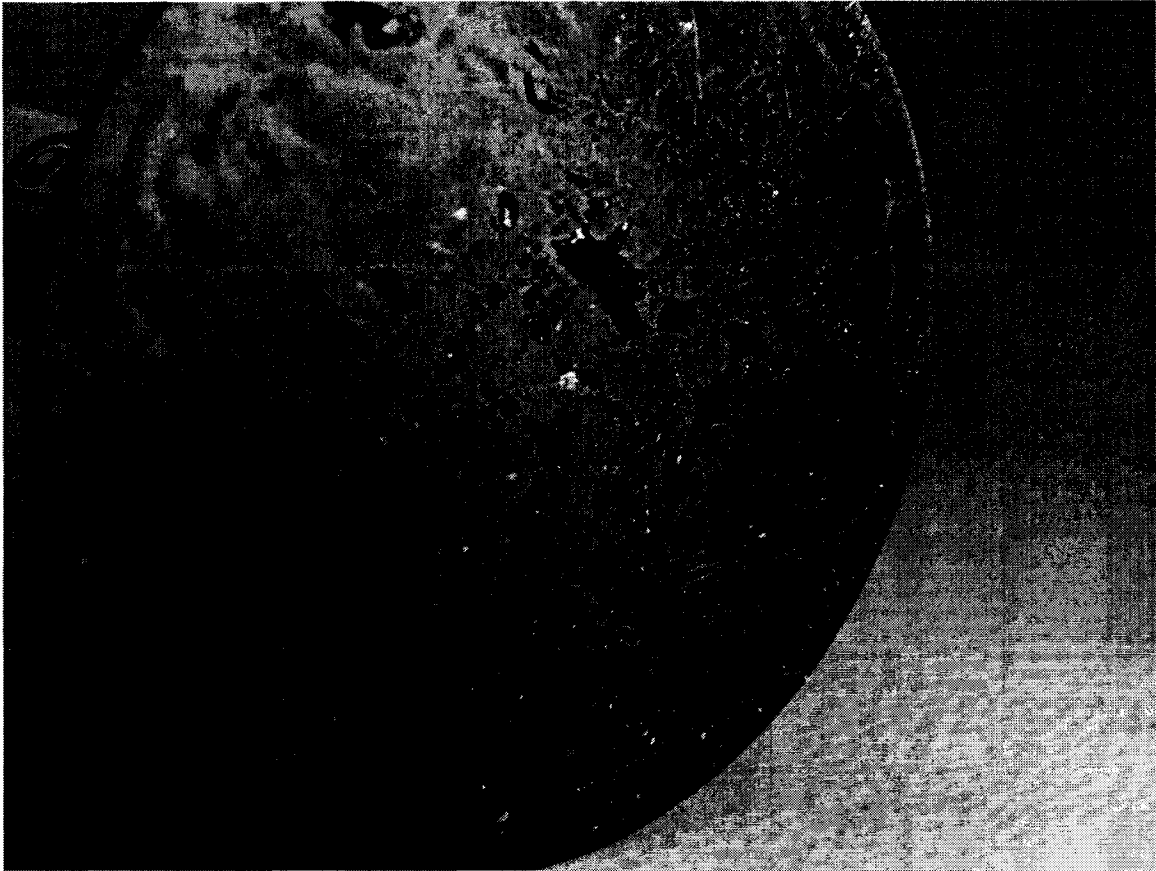


Figure 75. Surface porosity on the face of a carbon-fiber/PETI-RFI valve.

3.3.1 Background

PETI-RFI is a variant of the polymer PETI-5 developed by NASA and viscosity modified for resin transfer molding. The polymer has characteristics of a thermoplastic at low temperature, and high temperature processing results in cross-linking. The cured polymer retains its strength and does not degrade at high-temperature (400°C). Previous work with PETI-RFI has focused on compression molding and vacuum assisted compression molding of simple shapes. This section details the development of a resin-transfer molding process for carbon-fiber reinforced PETI-RFI and the process parameters for removing voids, including injection parameters such as temperature and pressure. Results

of Differential Scanning Calorimetry (DSC), Thermo-Gravimetric Analysis (TGA) and optical microscopy are presented. Several processing options for resin-transfer molding are recommended which lead to reduced void content..

3.3.1.1 Background - High Temperature Composites

High temperature composite materials have been under development since the 1960's and rapid progress has been made in a number of areas with the primary focus being on aerospace applications. However, the number of, and classes of high temperature composite systems is still fairly limited. Carbon-carbon and high temperature ceramics exhibit high strength above 2000°C. For this reason, these materials have found use in satellite and rocket applications. Manufacture of these materials is time consuming and energy intensive. High temperature conversions, up to 3000°C, and additional CVD infiltration and densification steps are required¹¹⁶. In addition, uncoated carbon-carbon begins to degrade at 600°C in an oxidative environment¹¹⁷.

For (relatively) lower temperature applications, such as jet engines, high temperature polymers have been the focus of research. In general, amorphous polymers have a usable temperature range roughly 25°C below the glass transition temperature (T_g). Semi crystalline polymers have usable temperature ranges determined by melting temperature. Typically, high temperature polymers require even higher temperature processing. For processing above 400°C, the melt process begins to compete with the degradation process¹¹⁸. Epoxy blends are relatively common and have been demonstrated with T_g in excess of 300°C¹¹⁹. Another class of high temperature polymers, bismaleimides

(BMIs) have also shown promise. BMIs have seen use in jet engines and can withstand temperatures to 180°C – 200°C, however BMIs can be relatively brittle¹²⁰. Polyimides such as PMR-15 and PMR-II have also been evaluated for use in jet engines and exhibit high strength and fracture toughness when reinforced¹²¹. Many condensation polyimides have a useable range to 350°C. However, the condensation cure reaction produces solvents that are difficult to remove during processing and can result in voids¹²².

PETI refers to the family of phenylethynyl-terminated imide (PETI) oligomers and are a sub group of polyimides that can be thermally cured, rather than condensation cured. This has the possibility to reduce the amount of solvents produced during cure and thus reduce the propensity for voids¹²².

3.3.1.2 Background - PETI-RFI

PETI-RFI is a variant of the polymer PETI-5. It was developed by NASA at the Langley Research Center (LaRC) and is modified for injection molding. Whereas PETI-5 has a molecular weight of 5000 g/mol, PETI-RFI has a molecular weight of 1250g/mol and a correspondingly lower process viscosity. It behaves as a thermoplastic at temperatures below 280°C. High temperature curing, at above 300°C, converts the polymer to a crosslinked thermoset. This thermoset is then stable in an inert environment to 460°C¹²⁰.

PETI oligomer species exhibit a stable melt viscosity below 300°C of below 6.0 Pa·s, and often lower. When cured at 371°C, the resulting polymer has a glass transition temperature (T_g) of 236°C¹²³. The polymers require degassing prior to injection¹²³. The resulting cured polymer has favorable mechanical

properties with a tensile modulus, $E = 3.48 \text{ GPa}$, and an ultimate strength of $\sigma_U = 94.4 \text{ MPa}$.

Previous work has concentrated on the combined vacuum-hot press technique with immediate curing of the polymer. (Immediate curing suggests processing the material from room temperature through the molding temperature range, $240^\circ\text{C} - 280^\circ\text{C}$, and then continuing heating to the curing temperature 370°C). While this procedure works well for parts of reasonably simple shape, it can result in a large amount of wasted polymer. For this reason, the single step curing approach is not desirable for production or for more complex part geometries. The focus of this work was to define a process which is more applicable to resin-transfer molding and mass production applications.

3.3.2 Material Properties and Processing

Extensive information on the constituent materials, manufacture, and characterization of processing of PETI-RFI and PETI-RTM was previously published by Criss et al.¹²³. Some of the notable properties that make PETI-RFI attractive for resin transfer-molding are:

- Viscosity @ 250°C 9 Pa·s
- Viscosity @ 280°C 1.5 Pa·s

This melt viscosity (280°C and below) is stable for at least two hours before appreciable increase in viscosity.

The previously published processing practices for PETI-RFI involve the following steps:

- Degas the resin under vacuum at 280°C for at least 1 hour

- Evacuate the mold
- Under pressure, inject the resin into the mold
- Upon filling the mold immediately raise the temperature to 371°C and cure for one hour under hydrostatic pressure.

This process above involved vacuum-bagging the part during processing. The vacuum bagged part was then placed in an autoclave where the injection and curing took place. Flat panels of various sizes as well as I-beams were manufactured. This process resulted in a cured polymer with the following properties:

- Porosity 0.8%
- T_g $\geq 236^\circ\text{C}$
- Degradation Temperature 416°C in N_2
- Flexural Strength 933 MPa
- Flexural Modulus 46.5 GPa
- Compressive Strength 629 MPa
- Compressive Modulus 92.3 GPa

(Mechanical properties are for a carbon fiber reinforced specimen, 52% Vf IM-7, 5HS fabric.)¹²³

The same group successfully demonstrated RTM of a large I-beam section using vacuum assisted resin transfer molding of a PETI-RTM, which has a lower melt viscosity (0.6 Pa-s @ 280°C)⁵.

Other work at Georgia Tech successfully demonstrated RTM of PETI-RFI (JC-272-39) with small carbon fiber fractions (0.6 and 0.62 wt%). A 50 ton

Wabash vacuum hot press was used for injection and 4.5 inch diameter x 0.1 in thick flat discs were produced. The part was cured in-place at 353°C immediately after injecting. It was noted that the seals on the mold were prone to failure, presumably due to the extreme processing requirements, and as a result it was difficult to maintain pressure during the injection process.¹²⁴

3.3.3 Objective of Research

In light of the previously published work, and motivated by the difficulties with bubble and void formation during the processing of PETI-RFI, the objectives for this research were defined as:

- Determine the timing of bubble formation in the RTM and cure processes
- Devise a method for processing that eliminates voids
- Develop a method for separating the injection and cure process
- Reduce the complexity of tooling and introduce flexibility into the manufacturing process for PETI-RFI

3.3.4 Experimentation

3.3.4.1 Material Characterization

Material analysis and testing was undertaken to determine the most appropriate injection and cure parameters. Early trials produced samples with excessive bubbling that appeared to form during the cure process. As a result of these early experiments avoiding the production of bubbles during the injection and curing process became of paramount importance. Quantitative thermal

analyses were used to investigate the processing parameters. This approach was critical, especially given the limited quantities of the polymer available.

3.3.4.2 Dynamic Thermal Mechanical Analysis (DTMA)

Dynamic Thermal Mechanical Analysis (DTMA) was conducted to determine the viscosity versus temperature profile of the polymer. This data was used to determine the temperature range for minimum viscosity of the uncured polymer and thus the optimum injection temperature and appropriate temperature for removing bubbles during the degassing process. DTMA was conducted using a Seiko Instruments SSC/5200 system TMA/SS120C. This analysis of viscosity was done using a pin-in-cup technique. The pin was excited in a sinusoidal motion at a frequency of 0.1 Hz with amplitude of 50 μ m. The resulting force required to move the pin was measured. Temperature was increased at 10°C/min from room temperature to 300°C. A N₂ purge of 15cc/min was used for all tests.

Post processing calculations converted this force and velocity data to viscosity trends. Although this test does not give a traceable measurement of absolute viscosity, relative viscosities of polymers can be compared. A photograph of the pin-in-cup setup is shown in Figure 76. Figure 77 is a picture of the TMA SS120C.

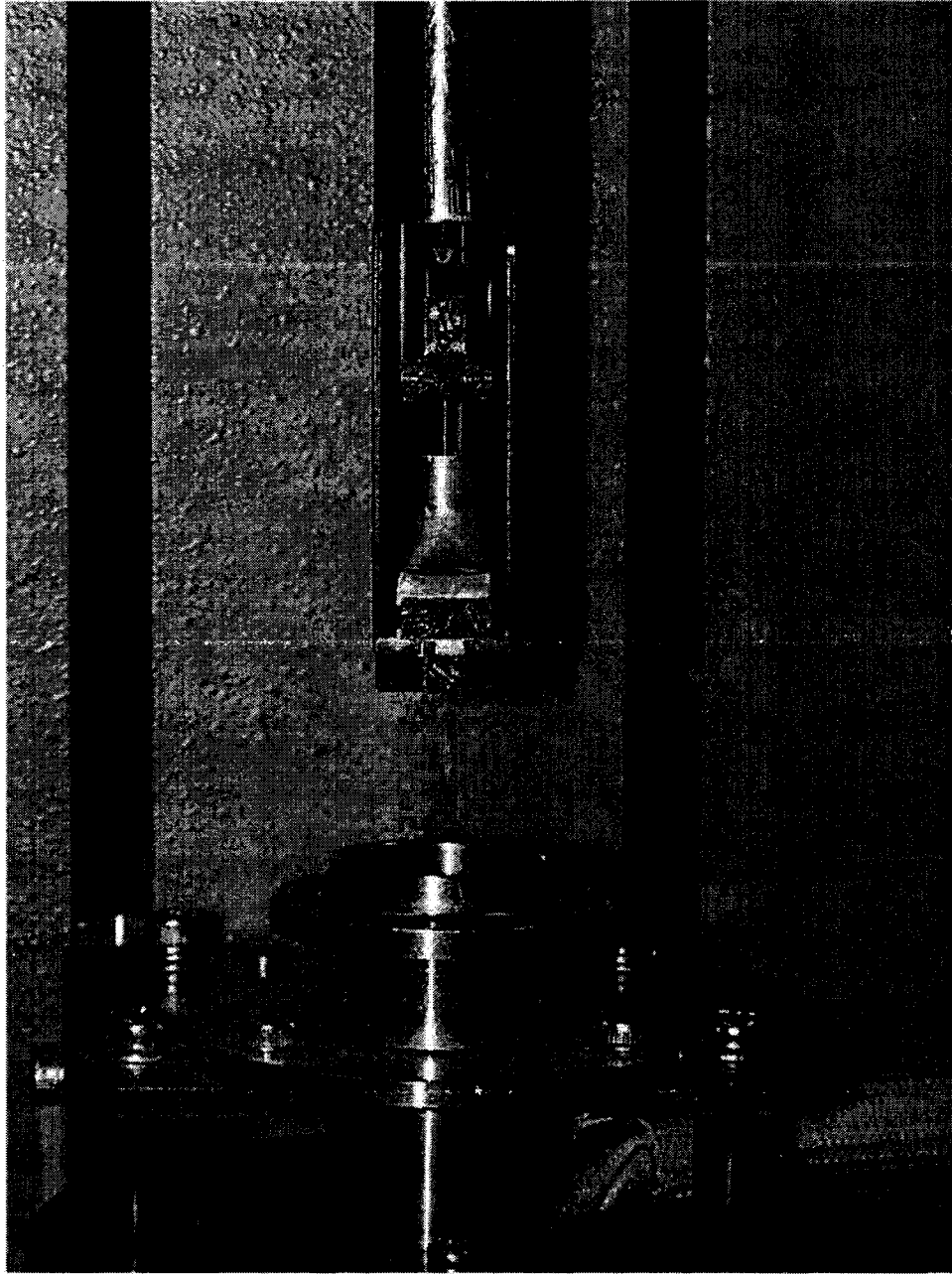


Figure 76. Pin-in-cup sample mounted in the TMA SS120C.

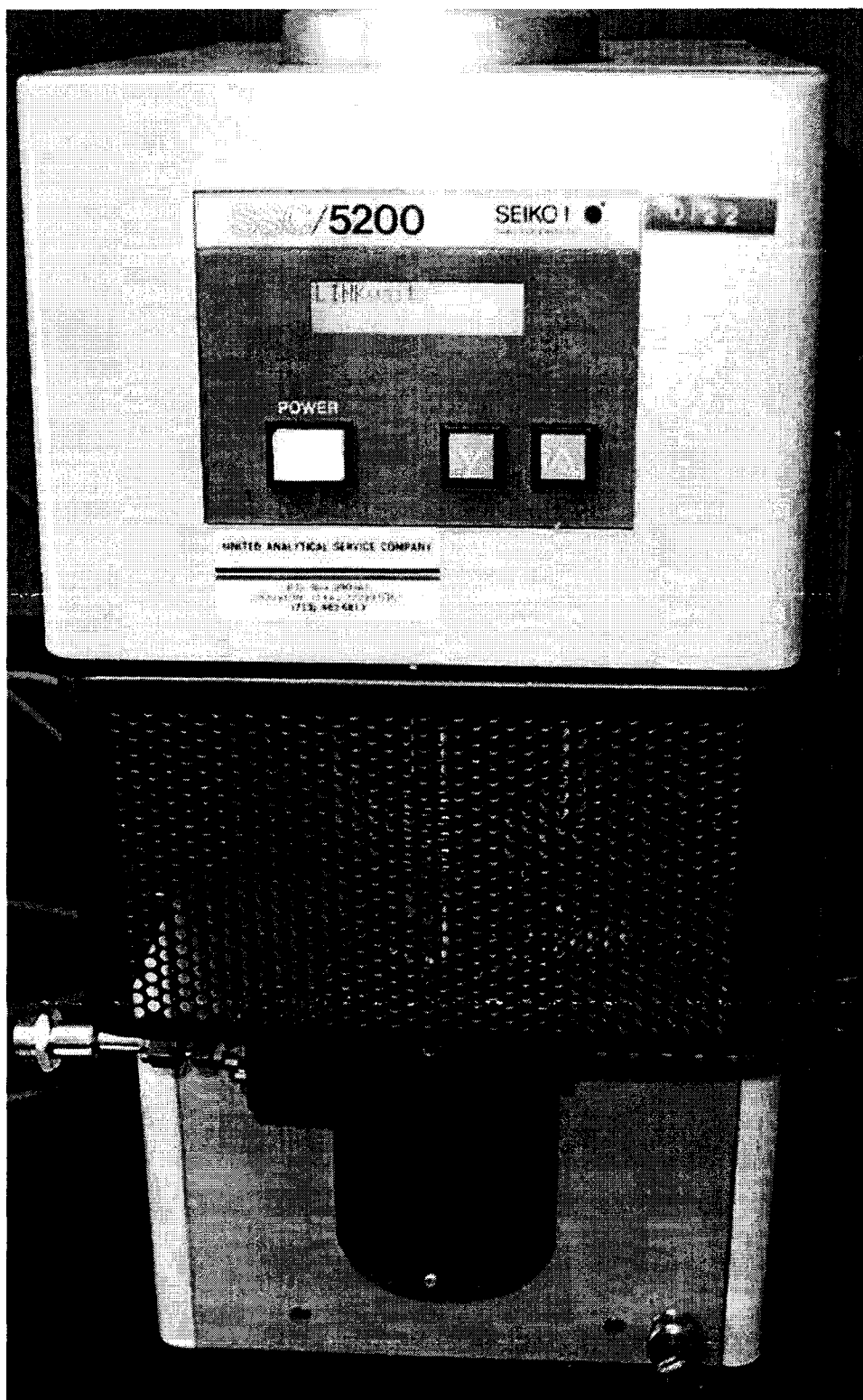


Figure 77. The Seiko Instruments TMA SS120C.

3.3.4.3 Differential Scanning Calorimetry (DSC)

Differential Scanning Calorimetry (DSC) measurements were performed with three different objectives, to investigate:

- Effect of heating rate and peak temperature on reaction rate
- Interactions between constituent materials
- Effect of peak cure temperature on the polymer properties

All DSC tests were performed using a Seiko Instruments SSC/5200 system, DSC220C. N₂ purge gas at a flow rate of 15cc/min was used for all tests. A sample mass of roughly 10mg was used for all tests. Test parameters were varied based on the test objectives. Details of the different tests are described below.

3.3.4.3.1 Effect of Heating Rate and Peak Temperature on Reaction Rate

Experiments were conducted to test the hypothesis that bubbles formed during the cure process were the result of a fast reaction rate and an inability of the surrounding polymer to absorb the reaction products. The implication is that faster reaction rates would have a higher probability of producing voids in the polymer, and that by slowing the reaction rate, production of bubbles could be reduced or eliminated.

In separate experiments, heating rate was varied in three steps at 3°C/min, 4°C/min, and 5°C/min from room temperature to a maximum of 355°C. Additional tests were conducted with the ramp rate held constant at 3°C/min. In these tests peak cure temperatures were varied between 308°C and 388°C in

roughly 10°C increments. Normalized DSC plots versus temperature and time were produced and compared.

3.3.4.3.2 Interactions Between Constituent Materials

Experiments were conducted to test the hypothesis that reactions between the polymer, carbon fiber and mold release might lead to the formation of bubbles during processing. These reactions would show up as variations from the baseline DSC curve for the neat polymer. To test this hypothesis, DSC measurements were performed on the neat polymer, polymer with carbon fiber and polymer with mold release (AirTech Inc. Release-All #50). These tests were performed at a ramp rate of 10°C/min to a peak temperature of 355°C. Normalized DSC plots versus temperature and time were produced.

3.3.4.3.3 Effect of Peak Cure Temperature on Polymer T_g

In many polymers, the peak cure temperature of the polymer has a strong effect on the glass transition temperature (T_g) of the polymer. Increasing the T_g may extend the useable range of the polymer, thus knowing the effect of cure temperature, the process designer can tailor the processing parameters to meet performance requirements of the polymer.

In order to understand the effect of cure temperature on T_g, a series of samples were cured using a standard cure cycle. The cure cycle used was:

- Heat at 10°C/min to 280°C
- Hold at 280°C for 30 minutes
- Heat at 3°C/min to peak cure temperature

- Hold at peak cure temperature for 60 minutes

Peak cure temperature was varied in 10°C increments from 310°C to 390°C. 390°C was chosen as the highest cure temperature because previous tests had shown the degradation begins at higher temperatures.

Following the cure cycle, an additional DSC run was performed on each sample. The sample was heated from 100°C to 500°C at 10°C/min. A DSC versus Temperature trace was used to find the T_g . The T_g was calculated from the midpoint of the inflection curve. Transition temperature T_t and end temperature T_e , were also recorded.

3.3.4.4 Thermo Gravimetric Analysis

Thermogravimetric analysis was performed to determine the degradation temperature of the cured polymer and hence the usable range. TGA was done using a Seiko Instruments SSC/5200 system TG/DTA 220. N₂ purge gas was used for all experiments at a flow rate of 15cc/min. A heating rate of 1°C/min was used from room temperature to 500°C. The sample size of the cured polymer was about 10 mg.

3.3.4.5 Vacuum/Pressure Chamber Cure Cycle Experiments

In order to observe the cure process and to identify the factors associated with bubble formation during cure, a vacuum/pressure chamber with an integral heat source and a viewing window was designed and constructed. This apparatus was similar to an autoclave, without the ability to vacuum bag the part. This enabled a series of experiments where the heating rate, intermediate dwell,

and chamber pressure were varied. The samples were observed through the viewing window. A schematic of the test setup is shown in Figure 78 and a photo of the chamber is shown in Figure 79. Thermal control was accomplished using a National Instruments USB 9211 thermocouple reader with four K-type thermocouples. Heater control was accomplished with a NI USB 6009 DAQ controlling a 250W heater mounted to the base of the chamber. A LabView Virtual Instrument (VI) was used for data acquisition and to control the heating cycle automatically.

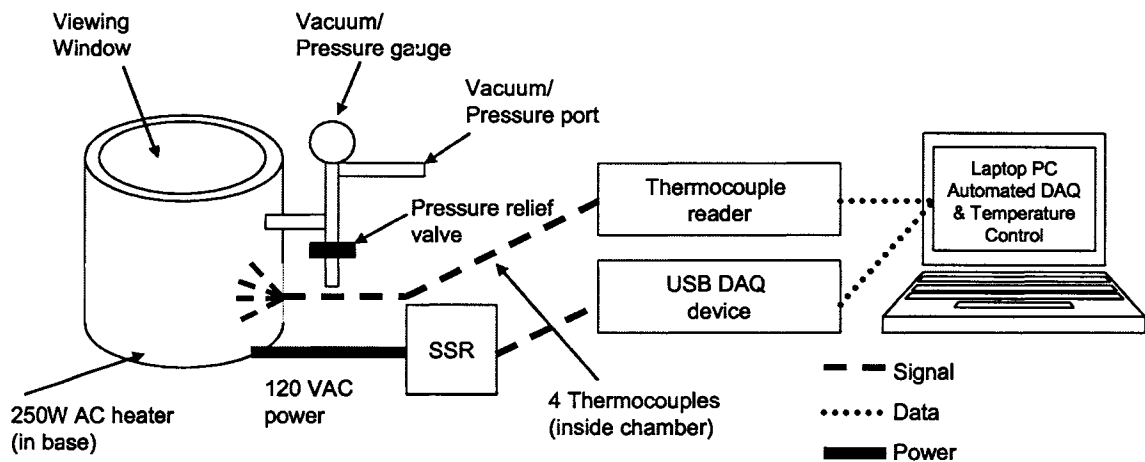


Figure 78. Schematic of the vacuum/pressure vessel test setup.

Experiments were performed by varying the chamber pressure during the intermediate dwell and during the cure cycle from a vacuum of -24 in Hg to a pressure of 50 psig (using industrial-grade N₂). The formation and behavior of bubbles was observed and changes to the cure cycle were made based on observations.

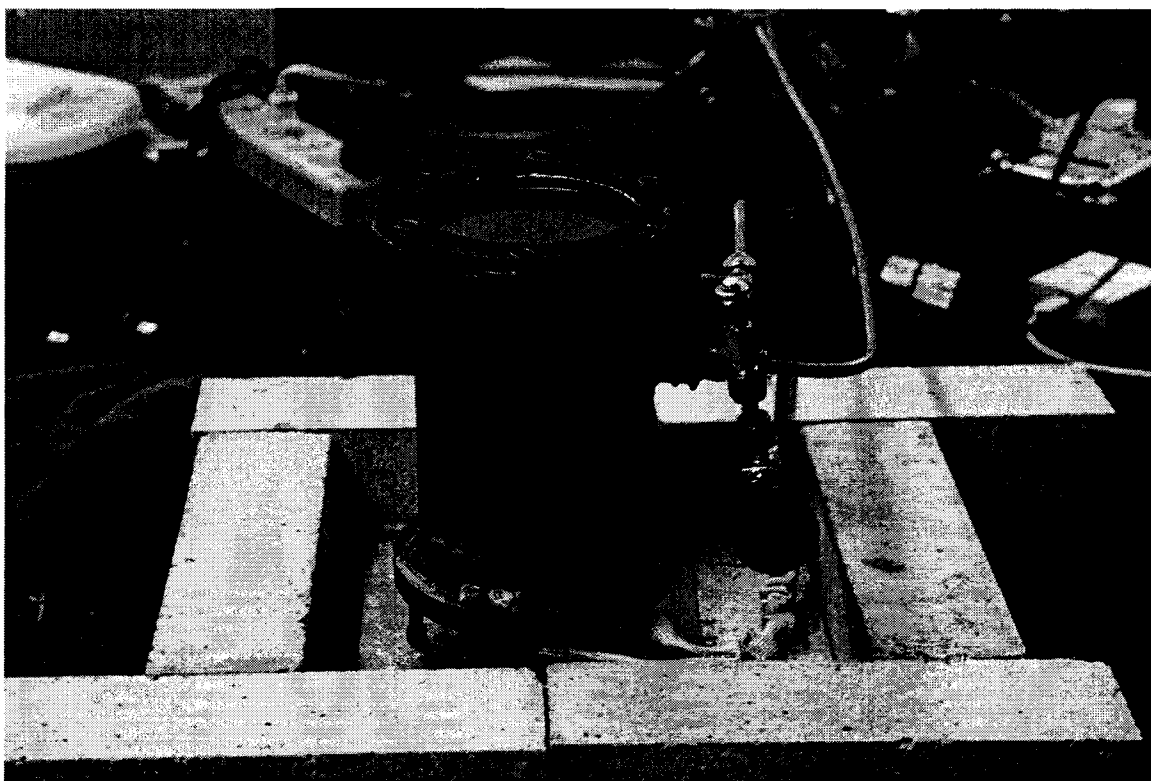


Figure 79. Photo of the vacuum/pressure chamber.

3.3.4.6 Hot Press Experiments

Hot press experiments were performed in order to quantify the feasibility of processing carbon fiber reinforced PETI-RFI without using an evacuated mold. Small 15mm disc shaped samples were prepared via melt-processing using degassed PETI-RFI and carbon fiber. Polymer and fiber were consolidated by hand in the mold. The samples were then degassed in a vacuum chamber, cooled and subsequently cured in the hot press. Fiber fraction of the samples was varied in the samples. During the cure process ramp rate and cure pressure were also varied. Samples were evaluated for void content/porosity.

3.3.4.7 Optical Microscopy

The primary purpose of the optical microscopy experiments was to determine the presence of bubbles in cured samples that might not have been visible to the naked eye. Cured samples were sectioned and prepared for metallographic inspection by mounting in epoxy, polishing and viewing using an Olympus PME-3 optical metallograph. Images were analyzed using BioScan OPTIMAS v4.02 image analysis software. Five images from random locations on each specimen were recorded and analyzed to determine void content in area percent and fiber area fraction for the reinforced samples. These results were averaged for each sample.

3.3.5 Results and Discussion

3.3.5.1 Dynamic Thermal Mechanical Analysis (DTMA)

Figure 80 shows the viscosity of PETI-RFI compared to several other injectable thermoplastics. Figure 81 is a plot of viscosity versus temperature for PETI-RFI focusing on the range with lowest viscosity. The minimum viscosity is measured between 220°C and 240°C. This result is slightly lower than previously published results, which measured minimum viscosity at 280°C¹²³. There is a clear increase in viscosity near 250°C, staying constant through about 280°C. This is contrary to the previously published information, which showed a decrease in viscosity between 250°C and 280°C⁵. It is believed that the sharp rise in viscosity at 280°C marks the beginning of the cure reaction. From this data it was determined that the optimum injection temperature for RTM of PETI-

RFI is 220°C - 240°C. Additionally, degassing of the material at the same temperature prior to processing was included to enable more rapid release of bubbles.

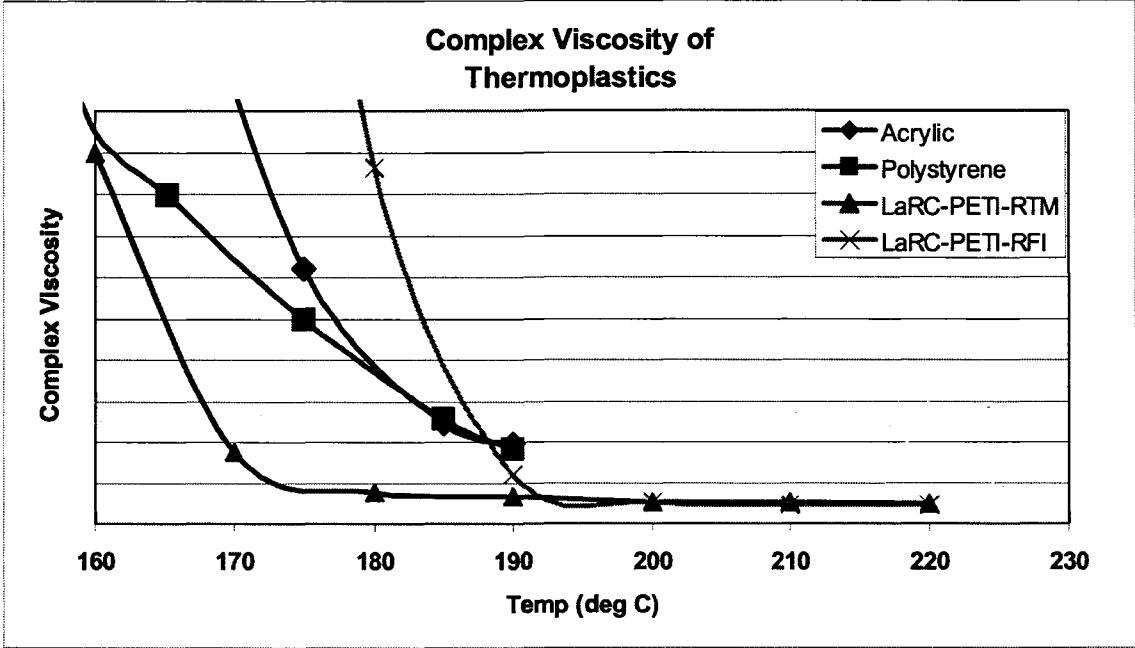


Figure 80. Relative viscosity of several thermoplastics.

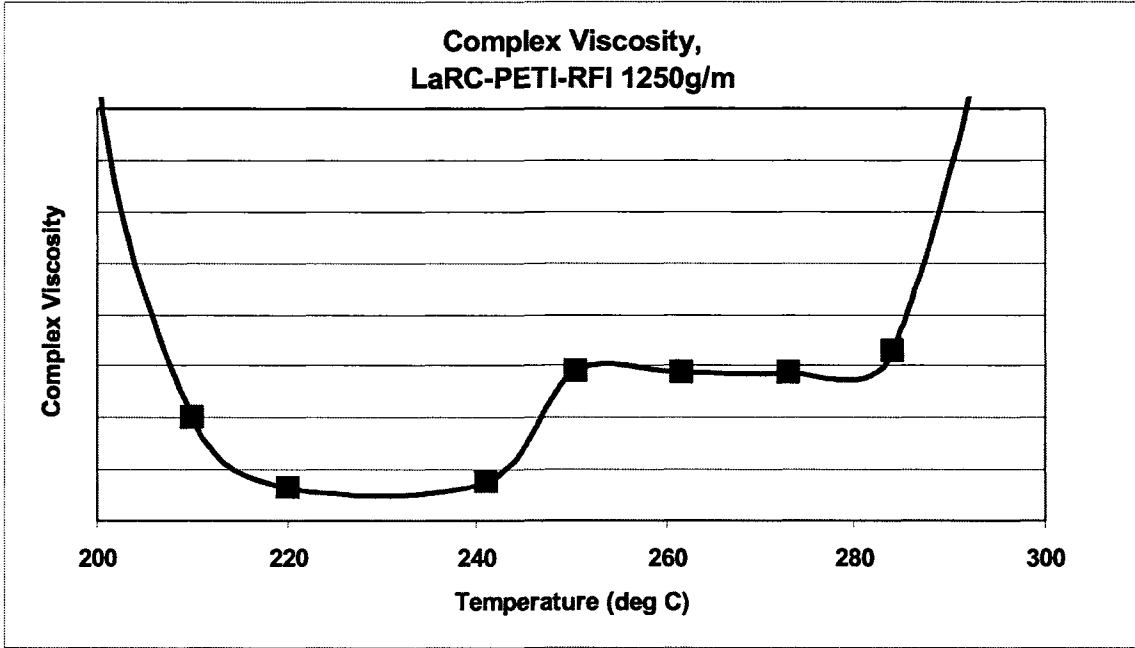


Figure 81. Viscosity versus Temperature for PETI-RFI showing minimum viscosity range.

3.3.5.2 Differential Scanning Calorimetry (DSC)

3.3.5.2.1 Effect of Ramp Rate on reaction rate

Figure 7 shows the DSC plot in $\mu\text{W}/\text{mg}$, versus time for ramp rates of $1^\circ\text{C}/\text{min}$, $2^\circ\text{C}/\text{min}$, and $3^\circ\text{C}/\text{min}$. Figure 8 shows the same data plotted versus temperature. On these plots, a higher value represents larger positive heat flux into the sample, or a more endothermic process, whereas a lower represents reduced heat flux into the sample, or a less endothermic process.

Figure 82 gives a visual representation of the relative lengths of the cure cycles that result from changing the ramp rate. It also is apparent that the faster ramp rate results in a more endothermic process. From Figure 83 it is apparent that a faster ramp rate requires a greater heat flux to maintain the sample temperature, indicating a greater reaction rate. It should also be noted that, the peak of the curve moves to lower temperatures for decreased ramp rate. Thus it is expected that a specific degree of cure will occur at lower temperatures for slower ramp rates. No attempt was made to characterize the effect of ramp rate on degree of cure.

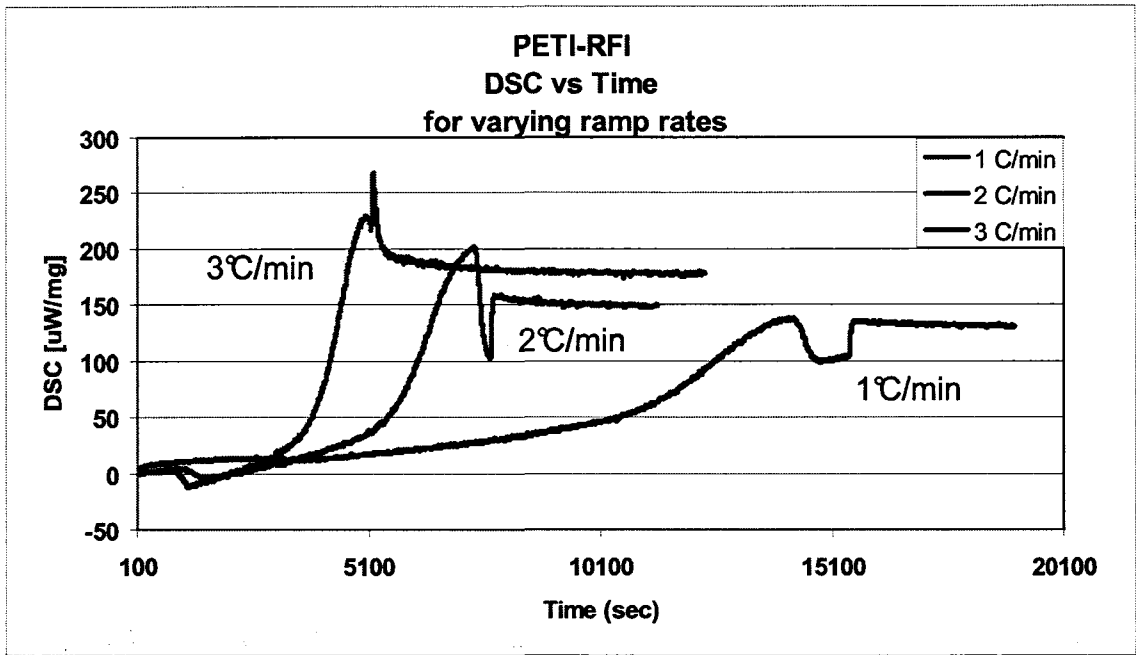


Figure 82. PETI-RFI DSC plot in uW/mg versus time for varying ramp rates.

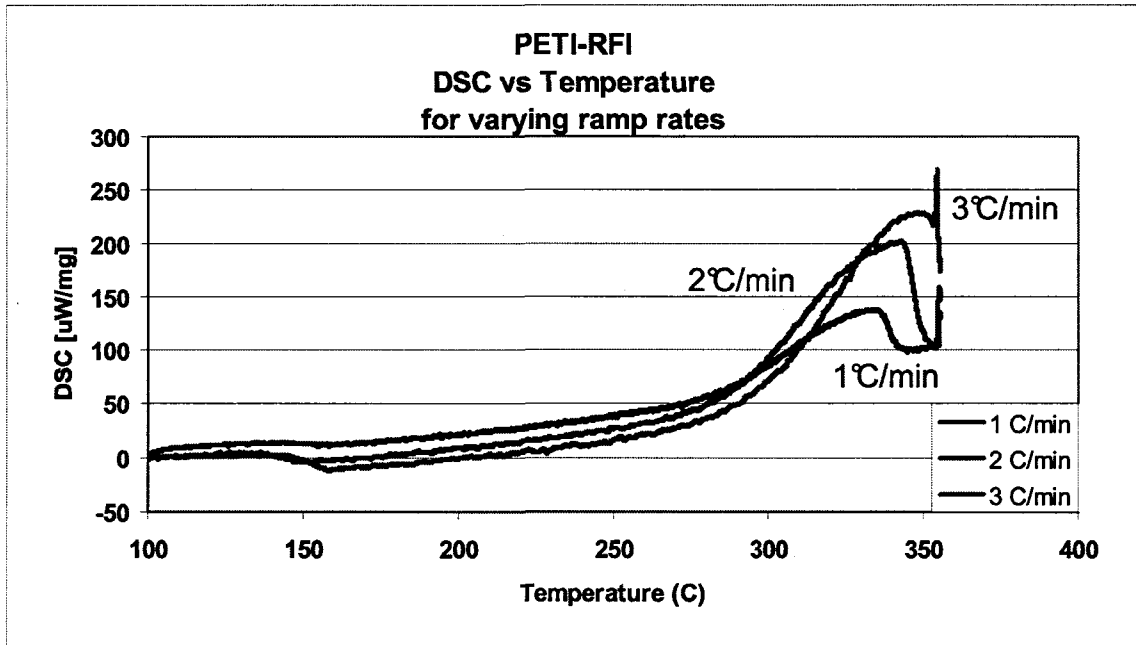


Figure 83. DSC plot in uW/mg versus temperature for varying ramp rates.

Previously published work did not focus on optimization of the cure cycle. Once injected the polymer was immediately raised to 371 °C. The current results

show that the rate of cure is affected by the cure cycle ramp rate, and that, in general slower is better when approaching the peak cure temperature.

With regards to bubble formation during the cure process, faster ramp rates produce a more energetic process, thus increasing the likelihood of void formation. In order to avoid void formation, a final ramp rate to peak cure temperature of 1°C/min was chosen for the cure cycle.

3.3.5.2.2 Effect of Peak Temperature on reaction rate

Figure 84 shows the DSC plot in $\mu\text{W}/\text{mg}$, versus temperature for peak cure temperatures of between 308°C and 388°C. Figure 85 shows the same data plotted versus time. In Figure 84, the spike at 280°C represents the change in heat flux necessary to transition from a constant ramp rate to an isotherm, and can thus be ignored. As expected, greater heat flux is required to maintain equilibrium at higher cure temperatures.

There are no sudden changes in the curve indicating that the cure reaction is stable across the cure temperature range. In Figure 85, the flat tabletop section around 2000 seconds represents the 280°C intermediate dwell during the cure cycle. In the same figure, the highest peak, near 4000 seconds, represents the most energetic portion of the cure reaction. This peak is lower in magnitude at lower cure temperatures, and greatest near 350°C. However, following the same 'ridge' line to higher temperatures, there is a sharp drop off immediately after the peak. This indicates that the cure reaction has completed, and less heat flux is required for equilibrium.

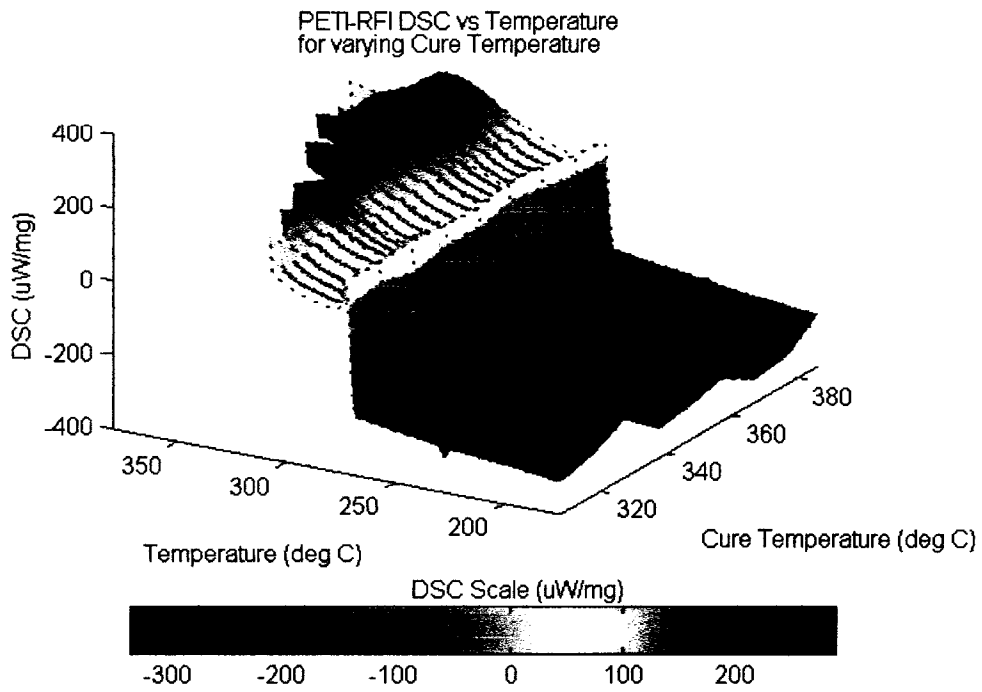


Figure 84. DSC data for PETI-RFI with varying peak temperature. Ramp rate = 3°C/min.

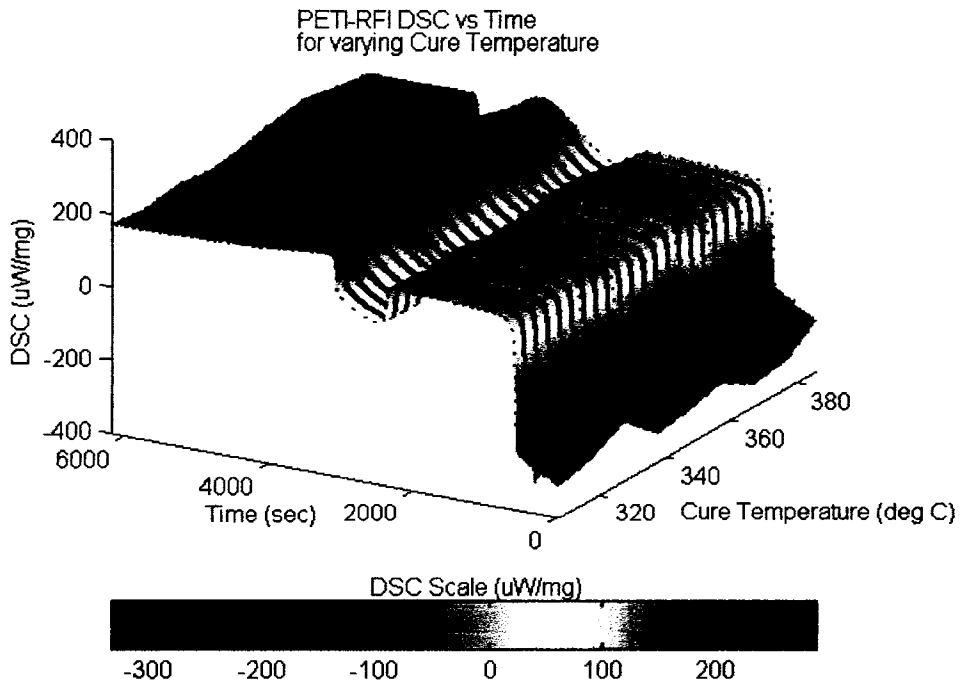


Figure 85. DSC versus time for varying peak temperature.

Thus a higher cure temperature results in a faster cure. The transition on the tail of the plots indicates the vestiges of the cure reaction. When this section of the curve reaches equilibrium, the reaction can be considered complete. Although the peak heat flux into the sample does not change considerably for the different peak temperatures, the rate at which the reaction approaches equilibrium occurs faster for the higher peak temperature, again indicating a more energetic reaction at higher temperatures.

Previous work described curing at 353°C and 371°C.¹²³ This analysis shows that it is possible to achieve a complete cure at lower temperatures. Since it is clear that the cure reaction begins near 300°C, it is possible to completely cure the polymer near 320°C. Based on the hypothesis that bubbles are formed during the more energetic cure process, these plots indicate that a lower temperature, longer cure cycle would have a lesser likelihood of producing bubbles.

3.3.5.2.3 Effect of Peak Temperature on Glass Transition Temperature (T_g)

Figure 86 shows the calculated glass transition temperature for samples of PETI RFI for varying peak cure temperatures from 310°C to 390°C. Despite the variation in peak cure temperature of 80°C, the glass transition temperature of the polymer remains in a fairly narrow range between 240 and 243 °C. This is similar, though slightly higher than the results of 236°C previously published by Criss et al. This shows that the polymer performance is insensitive to peak cure temperatures as long as those temperatures are above roughly 320°C. As a

result, the process designer has a much wider processing range to work in without changing the performance of the material.

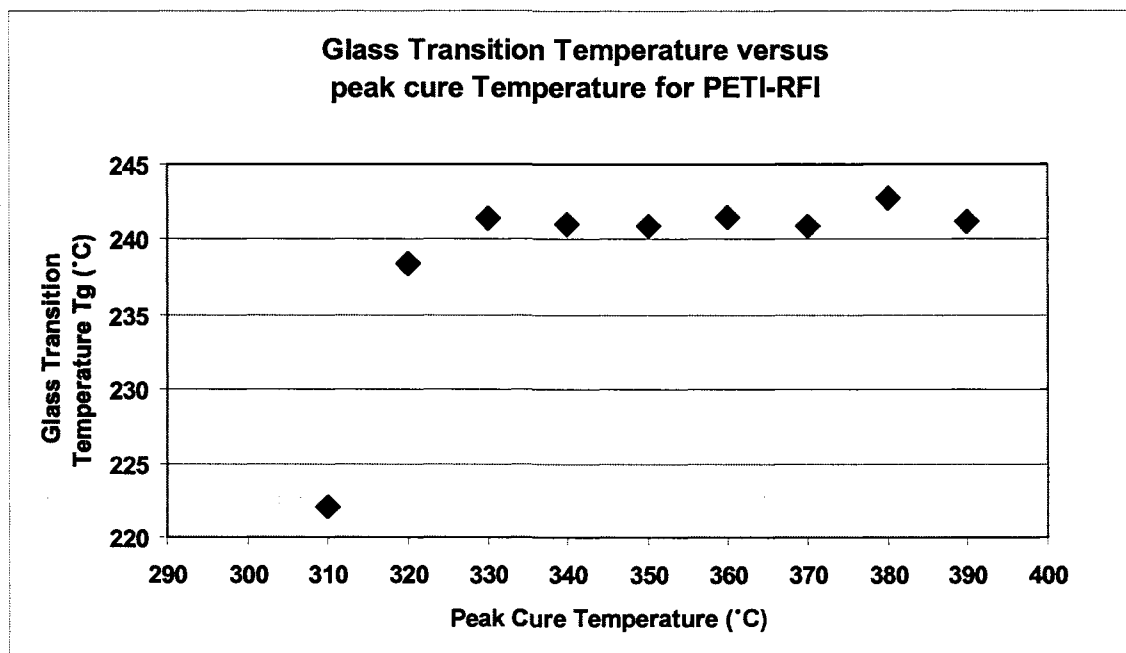


Figure 86. Glass Transition Temperature (T_g) of PETI-RFI versus peak cure temperature.

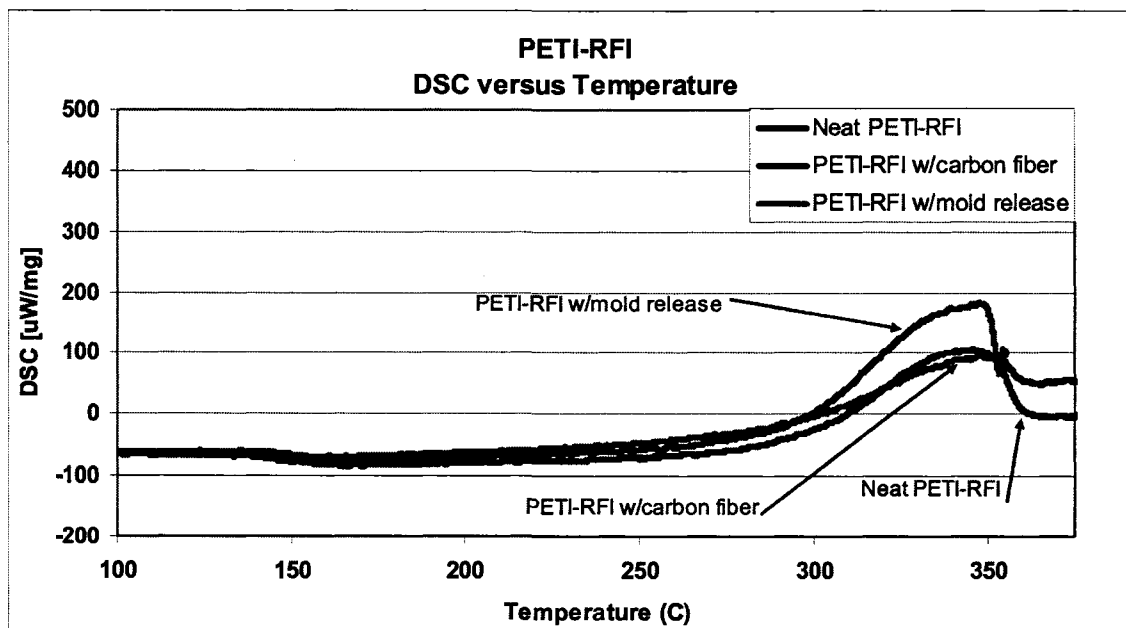


Figure 87. DSC vs. temperature for neat PETI-RFI, with mold release and with carbon fiber. Constant ramp rate of 10°C/min.

3.3.5.2.4 Interactions with Other Materials

Figure 87 is a plot of DSC versus temperature for neat PETI-RFI, PETI-RFI with carbon fiber, and PETI-RFI with mold release. Some previous work has indicated a release of some volatiles near 280°C¹²⁴. This was not observed in these samples during DSC testing. It was however, observed during the degassing experiments described later in this paper. This suggests that the products being released are relatively low molecular weight and small in proportion to the total mass.

An interaction between materials would show itself as an additional deviation from the base line PETI-RFI curve. Since the basic shape of the three curves are the same it was concluded that there is no interaction between the PETI-RFI, carbon fiber and mold release. Initial inspection of the curves might lead to the conclusion that the PETI-RFI with mold release curve is different from the other two. This is an artifact of the scale of the plot. Consequently, it was concluded that the bubbles forming during the cure process are a result of some other phenomenon, and not from an interaction between the PETI-RFI, carbon fiber and mold release.

3.3.5.3 Thermo gravimetric Analysis

Figure 88 shows a plot of mass loss (TGA) versus temperature for a cured sample of PETI-RFI as well as the slope of the TGA curve (DTG). No mass loss occurs below about 400°C. However, rapid mass loss begins above 420°C in N₂, indicating rapid decomposition of the polymer. From this data it was concluded that the maximum usable temperature of the cured polymer is approximately

400°C. This is significantly less than previously published results, which showed the base material PETI-5 stable to 550°C¹²⁵, but in line with previous results for PETI-RFI¹²³.

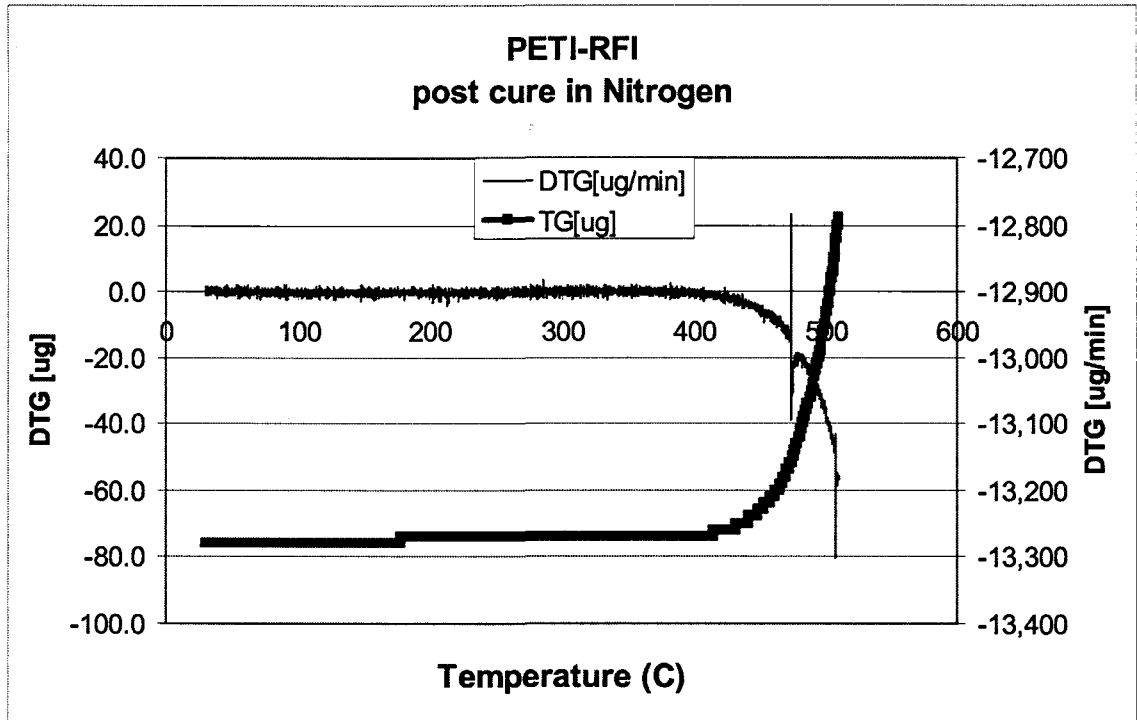


Figure 88. Thermogravimetric data for PETI-RFI.

3.3.5.4 Vacuum/Pressure Chamber Cure Cycle Experiments

A great deal of qualitative information, especially about bubble formation, was gained by observing the behavior of the polymer in the vacuum/hot plate.

These visual observations are described below:

3.3.5.4.1 Degassing:

Previous work recommends degassing PETI-RFI at 280°C for 1-2 hours under vacuum¹²³. Degassing experiments were performed to observe bubble formation and determine an appropriate degassing process. Unless otherwise

noted, experiments were performed with the chamber held at 609 torr vacuum. Temperatures were increased slowly and held at the intermediate temperatures described.

Observations of the degassing process are noted below:

- 190°C Bubbles begin to form and volume of the sample begins to increase
- 220°C Significant increase in polymer volume. Polymer is a very fine foam.
- 240°C Foam begins to collapse.
- 250°C Larger bubbles appear to form and collapse. Bubble formation appears to stop after holding at 250°C for 1 hour.
- 280°C Additional, larger bubbles appear. Holding for an additional hour appears to complete this bubble formation process

The above observations indicate that volatile gases are released from the polymer at two distinct temperatures, 250°C and 280°C. DSC and TGA analyses of the polymer did not reveal any mass loss or reactions occurring at these temperatures. This indicates 2 possibilities; 1) the bubbles are the result of entrained air captured during the melt process and/or 2) very light molecular weight volatiles, such as solvents from the manufacture process, are evaporating off. The most likely explanation is a combination of both of these two factors, but analysis of the released gases was not performed. Previously published work has recognized the release of solvents during the cure cycle¹²³. From these observations, the previously described degassing process of holding at 280°C for

1-2 hours under vacuum was deemed appropriate for removing bubbles. Ramp rate to the degassing temperature was not found to be important. However, for fiber reinforced samples it was found that rapid heating may accelerate bubble formation. If there is not a path for the release of these bubbles (i.e. the fiber acts as a barrier to bubble release) the resulting cured composite will contain voids.

3.3.5.4.2 Cure Process:

A number of experiments were undertaken to attempt to add flexibility to the cure cycle. Observations of these experiments are noted below:

It is possible to build significant flexibility into the manufacturing process, depending on need. This is especially true of the uncured thermoplastic resin. Degassed, solid resin is fairly stable. Uncured samples were left out in ambient air after degassing for 24 hours, 48 hours, and 7 days without noticeable change in the final cured sample. As a result it is possible to separate the degassing and injection processes by allowing the degassed resin to solidify at room temperature, then subsequently re-melting and injecting the resin at a later time. However, breaking the solid resin apart before re-melting will entrain air, and the polymer should be degassed again.

With respect to avoiding the formation of voids during the manufacturing process, several steps are of key importance. Failure to degas the polymer will result in a cured polymer with a high void fraction. Curing a degassed neat resin in an open mold at ambient pressure will result in a sample with surface voids. Curing neat polymer in an open mold under 275 kPa (40 psig) pressure of N₂ gas

produces a high quality sample with very low void content. Fiber reinforced samples will not consolidate under 275 kPa of N₂ gas pressure and require mechanical consolidation, such as in an evacuated hot press or under hydrostatic pressure from the injection process. Failure to do so will result in a part with significant void content.

3.3.5.5 Hot Press Experiments

A number of experiments were undertaken to determine if the same processing conditions used in the vacuum/pressure chamber could be replicated using mechanical pressure from the hot press. It was found that degassed neat polymer could be cured in the hot press under mechanical pressure as low as 700 kPa. However, the same was not true for fiber reinforced samples.

Fiber reinforced samples were manufactured by melt processing, with mechanical consolidation of fiber and polymer. Upon subsequent degassing of these samples, the rising bubbles were able to move the unconstrained fiber and/or the fibers trapped bubbles in the uncured resin. This resulted in an unconsolidated sample. When these samples were subsequently cured in the hot press, all had extremely high void content regardless of cure pressure.

3.3.5.6 Optical Microscopy

Neat polymer and carbon fiber reinforced polymer processed using the methods described in the previous section were analyzed using optical techniques to determine void area fraction and fiber area fraction where appropriate. Figure 89 is a sample of the neat polymer viewed under 1000x

optical magnification. The parallel lines in the image are polishing marks. Dark spots are voids. Table 31 documents the average void content and fiber content for carbon fiber reinforced PETI-RFI for the different cure cycles. It should be noted that average void content is in the low single digits for all three processing methods, however, failure to degas the polymer results in a large void fraction, often between 30 – 50%.



Figure 89. 1000x image of cured neat PETI-RFI polymer. The lines are polishing marks.

Figure 90 shows a sample of carbon fiber reinforced PETI-RFI at 1000x optical magnification. This sample was produced using the RTM process described above. The white ellipses are the ends of the carbon fibers, black

spots are voids. It is clear from the picture that the resin completely surrounds the fibers, indicating wetting, and the void fraction is very low. This particular sample had a void fraction of 1.1%.

Table 31. Average void content and fiber content for different processing methods of PETI-RFI.

SAMPLE NAME	MANUFACTURE METHOD	FIBER FRACTION (AREA %)	VOID CONTENT (AREA %)
P-9	RTM	41	1.5
RFI-2	Melt Process	-	2.0
RFI-V	Hot Press without degassing	-	36.0
RFI-10	Hot press	30	3.1

Figure 91 shows a sample of un-reinforced PETI-RFI at 50x optical magnification. This sample was produced using the hot press process described above without degassing the polymer first. The straight line across the bottom of the figure is the edge of the sample. This figure shows that large bubbles are present on the surface as well as throughout the thickness of the sample.

This work has resulted in the development of several possible processing options for PETI-RFI, all of which produce very good quality parts with low void content. It is also clear that failing to degas the material prior to processing will result in a marked increase in the void content of the finished part.

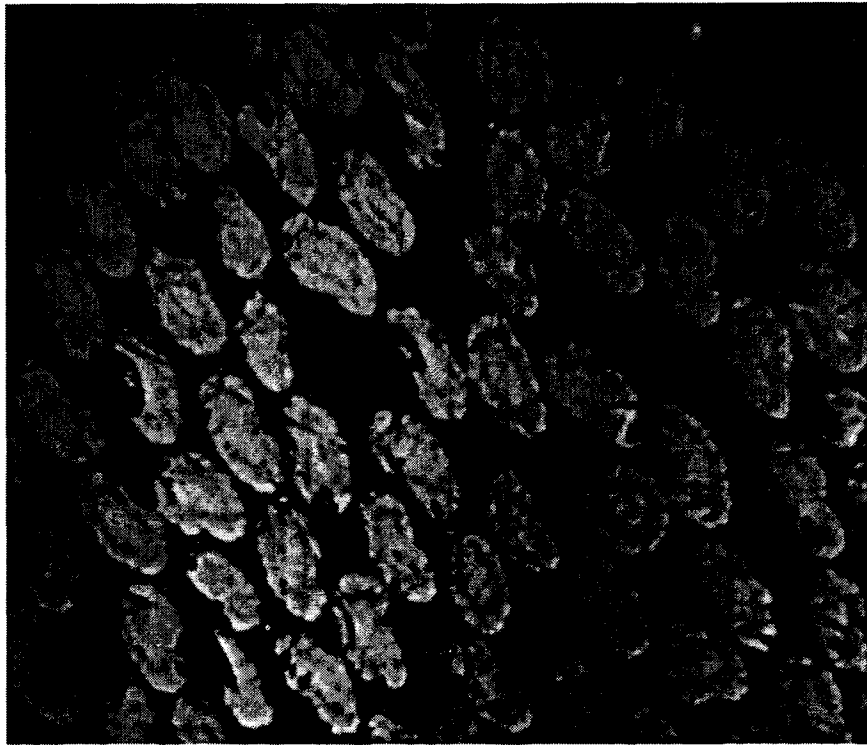


Figure 90. 1000x magnification image of PETI-RFI with carbon fiber.

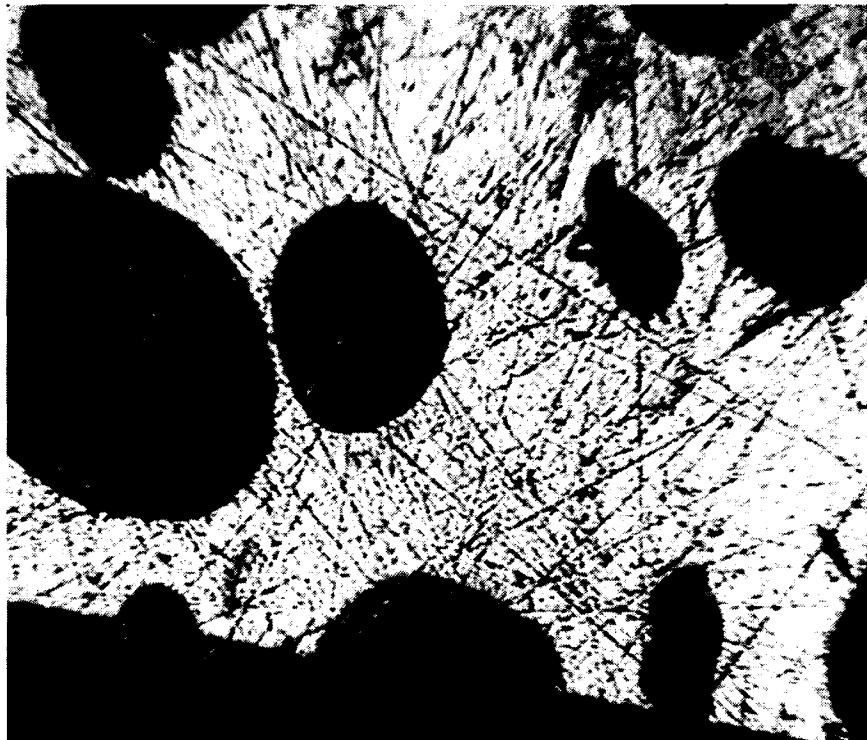


Figure 91. 50x magnification image of un-reinforced PETI-RFI. Large black spots are voids. This sample was cured without degassing.

3.3.5.7 Processing Parameters

From the observations above, several process options arose. These processes are documented below. For all cases, the final cure cycle used was:

1. Ramp from room temperature to 280°C at any rate
2. Hold at 280°C for 30 minutes
3. Ramp at 3°C/min or less to peak cure temperature (above 320°C)
4. Hold at peak cure temperature for at least one hour.

For neat polymer: (Option 1 – Melt process)

1. Degas at 280°C for 1-2 hours
2. If desired, solidify the resin.
3. Melt process the part into an open mold
4. Execute the final cure cycle under 275kPa pressure (N₂).

For neat polymer (Option 2 – Hot press)

1. Degas at 280°C for 1-2 hours
2. If desired, solidify the resin.
3. Melt process the part into an open mold
4. Execute the final cure cycle in the hot press under 700 kPa mechanical pressure.

For fiber reinforced polymer: (Option 3 – Resin Transfer Mold)

1. Degas at 280°C for 1-2 hours
2. If desired, solidify the resin.
3. Melt process and resin transfer mold the resin at 240°C into a closed, heated (280°C) mold containing a fiber preform.

4. If desired, cool and solidify the part again, keeping the part in the mold.
5. Seal the mold and execute the final cure cycle. The sealed will provide the pressure necessary for consolidation.

Cooling rate does not appear to affect the quality of the parts, though a maximum cooling rate of 10°C/min was used for all processes described. Small disc shaped samples, 15mm in diameter by 8mm thick, were manufactured using the melt processing method described above. An intake valve for an internal combustion engine was manufactured using the RTM process.

The common theme from these three processes is that the polymer must be degassed prior to processing; any process that entrains air must also be followed by degassing. During the final cure, an intermediate dwell at 280°C allows further consolidation and release of any remaining bubbles. This point was chosen because it is in the low viscosity range and is the highest temperature at which bubble formation was observed. Removing this dwell will produce a sample with voids. The final cure must be accomplished under pressure. This final cure pressure varies by the process used. For neat polymer in an open mold, 275 kPa N₂ pressure is sufficient. Hot pressing neat polymer requires a pressure of 700kPa. Curing of RTM parts can be accomplished in a closed mold without additional pressure. It is believed that heating the polymer inside the sealed mold provides enough pressure to force consolidation and produce a void free part. Internal pressure in the mold was not measured.

However, when RTM parts were cured in a mold where sealing was lost, the subsequent part contained noticeable surface voids.

3.4 Discussion of Process Development Results

A great deal of work has been done in developing the initial manufacturing process for a net-shape molded FRC intake valve. A process has been developed and demonstrated in which a single-piece fiber preform is used to fabricate a net-shape fiber reinforced intake valve using resin transfer molding. Although RTM of composite materials is not a new process, several new and unique advancements have been made.

A novel method of positively clamping and locating the fiber preform has been devised. Two concentric rings are press fit with the end of the fiber preform between them. This positively locates the fiber, prevents fiber pullout, and allows injection of the resin down the center of the fiber preform when the mold is filled. This increases the wetting of the fibers in the mold.

A method has been developed whereby prepreg inserts using PETI-RFI in the thermoplastic stage are manufactured. The inserts are placed into the mold prior to injection, during the RTM process, the insert is incorporated into the molded part. Co-curing the parts in the mold results in a net shape part. This process could also be extended by the RTM process, but before the final cure cycle. Any number of different functional inserts could be added to the part this way.

A working mold has been developed and demonstrated. Three iterations of the valve mold have been developed, each with successive improvements.

The final two designs incorporate a device for compressing fibers into the valve face, thereby increasing the fiber volume fraction and part strength. This device also serves as a perimeter vent. The final mold design incorporates a modular structure that allows the manufacture of both an intake and exhaust valve of different geometries by swapping the two pieces that form the valve face.

A manufacturing process has been demonstrated and over 20 net-shape, RTM valves have been successfully produced.

Extensive work has been done in relation to the processing of PETI-RFI. Previously described efforts to process PETI-RFI composites focused on vacuum hot pressing. Extensive material characterization using DSC, TGA and DTMA has been performed with a focus on eliminating the formation of voids during processing and curing. Additional cure experiments were performed using a vacuum/pressure chamber and hot press with the goal of adding flexibility and minimizing void formation.

DTMA experiments showed the minimum viscosity for PETI-RFI occurs between 220°C and 240°C with a rise in viscosity before 280°C. This differs from previously published results and indicates a minimum viscosity at a slightly lower temperature.

DSC experiments showed that a slower ramp rate of 1°C /min to the peak cure temperature may reduce void formation. This is done by slowing and extending the cure reaction. The cure reaction begins above 300°C and the reaction rate peaks near 350°C. Lower final cure temperatures may also reduce

void formation for the same reasons. There appear to be no interactions between the PETI-RFI polymer, carbon fiber and mold release.

T_g of PETI-RFI is near 242°C for peak cure temperatures between 330°C and 390°C. In this temperature range, the polymer is insensitive to peak cure temperature. TGA showed PETI-RFI is stable to 400°C. This is lower than that of the base material, PETI-5, but still relatively high for a polymer.

Vacuum/pressure chamber experiments showed that degassing is critical to the processing of polymer without voids. Once degassed, PETI-RFI can undergo multiple melt-freeze cycles without affecting the final cured product. Any processing that entrains air will require additional degassing to avoid void formation in the final product.

As a result of this work three additional methods of processing PETI-RFI and carbon fiber reinforced PETI-RFI have been documented. These methods are; melt processing of neat polymer with final cure under N_2 gas pressure, hot pressing of neat polymer, and resin transfer molding of fiber reinforced polymer. Hot pressing fiber reinforced PETI-RFI at ambient air pressure in an unevacuated mold produced samples of high porosity due to the presence of air entrained in the manufacture process.

All three manufacturing methods can be accomplished without the use of a high temperature vacuum bag and without the extremely high pressures described in previous work. Additional flexibility has been demonstrated by allowing intermediate cooling of the resin between the degassing, forming and

curing cycles. All three of these processes have been shown to produce parts that have excellent consolidation and void content at or below 3% by area.

As a result of this study, an understanding of the surface porosity on the carbon-fiber PETI-RFI valves mentioned in the introduction of this chapter, a better understanding of the problem was gained. Recall that the first valves manufactured had low porosity, and that void content increased with the number of valves produced. It is the opinion of the author that this was a direct result of using a 6061-T6 aluminum mold. During manufacture, the mold was carefully prepared so that all mating surfaces were flat and polished and created a seal. As mentioned above, during the manufacture process, the mold is repeatedly heated to over 300°C, effectively removing the effect of age hardening. This temperature cycling combined with the normal wear and tear of injecting, opening and closing, mold releasing and polishing the mold caused the mold to lose the ability to seal. Once this sealing capacity is lost, the PETI-RFI is effectively at ambient pressure during the cure cycle. Repeated experiments have shown that PETI-RFI must be held under pressure during cure to avoid formation of voids. This theory was confirmed when manufacturing began using the stainless steel valve mold. During the cure cycle, little or no flash was observed at any of the mold parting lines. Although pressure was not measured inside the mold, from this observation it is safe to assume that pressure was maintained in the mold during the cure cycle. Valves cured in this stainless steel mold were free of voids on the surface and in the cross section. Figure 92 is a picture of a valve cured in the stainless steel mold.

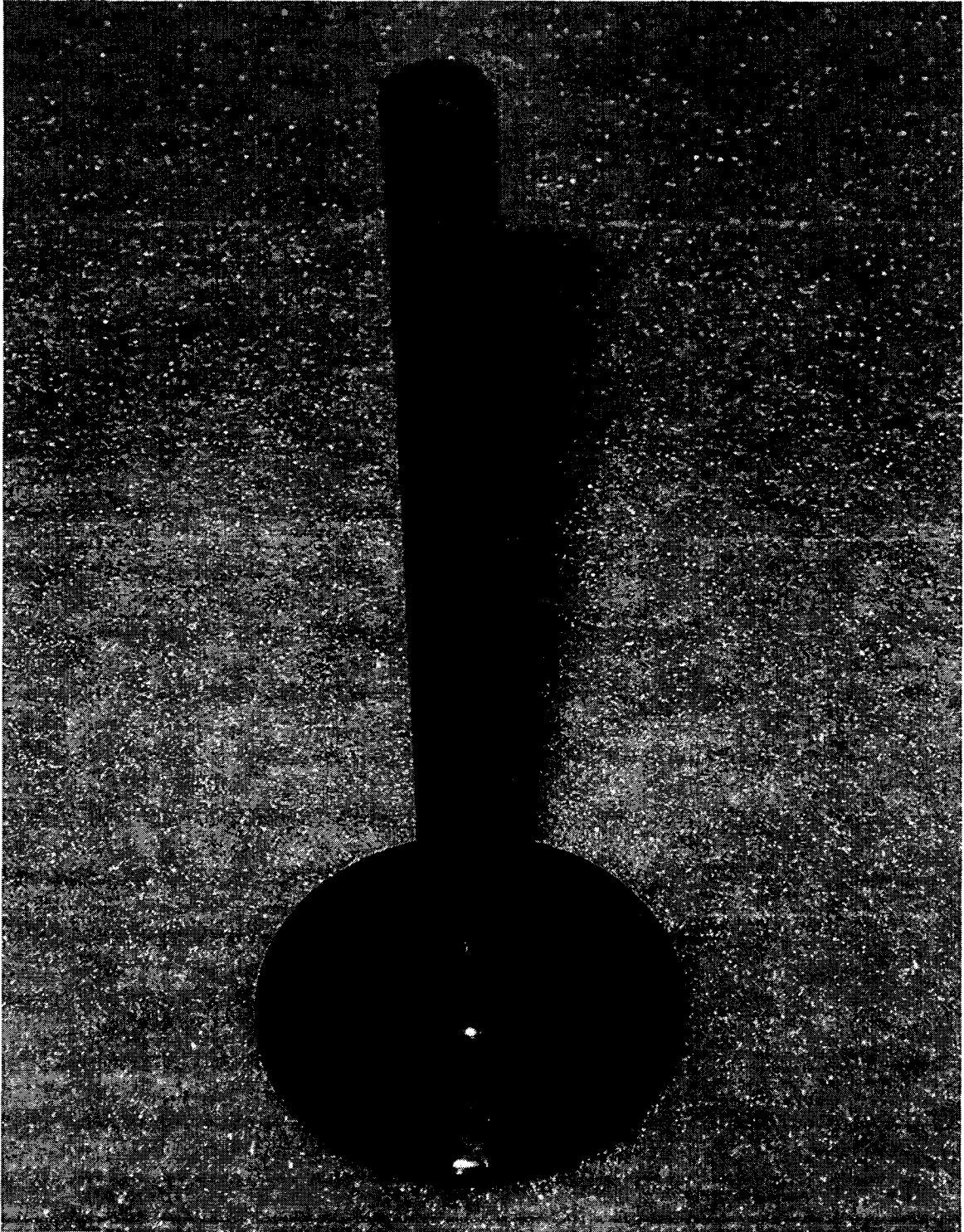


Figure 92. Carbon Fiber reinforced PETI-RFI valve cured in the stainless steel mold, free of voids.

4 Experimentation and Testing

4.1 Introduction

In order to validate the modeling described in chapter 2, and to validate the manufacturing process developed in chapter 3, a wide variety of structural, dynamic and thermal testing has been accomplished.

Validation of net shape RTM FRC intake valve structural design was conducted using initial and follow-on static testing in a tensile test load frame. Valve performance and failure modes were determined. Dynamic testing of FRC valves was conducted in a motored engine to verify performance. Fired engine testing was conducted to determine if the FRC intake valve could withstand the structural and thermal loads of operation in the combustion chamber.

Temperature measurements were taken in the running engine to aid in the determination of boundary conditions for thermal modeling, and to verify design requirements used in the initial design of the intake valve. Steady state measurements were taken at numerous points in the engine. High-sampling rate measurements were taken to determine peak temperatures and temperature fluctuations in the surface of the steel intake and exhaust valves.

In order to evaluate possible combinations of FRC and coating materials, and to verify the transient thermal modeling presented in section 2.5, in-engine

testing of small coupon samples was accomplished in a modified cylinder head in the running engine.

Details and results of each of these series of tests is presented below.

4.2 Static testing

Initial testing was conducted on two FRC valves, with follow-on testing conducted on an additional three FRC valves. The purpose of initial static testing was to apply a proof-load to the valve before doing further motored and fired testing in the engine. The purpose of the follow-on static testing was to determine the peak loads and failure modes of the FRC valve. All static testing was conducted in a screw-actuated load frame. The load frame was controlled manually. Load, crosshead displacement and extensometer displacement was recorded automatically through the use of a data acquisition system. A schematic of the test setup is shown in Figure 28, found in section 2.3.1.7.

4.2.1.1 Initial Static Testing Results

Proof-load testing was conducted on two valves. The resulting plots are shown in Figure 93 and Figure 94. Tests were run as displacement-controlled tests. Figure 93 shows crosshead displacement and load versus time for valve # P-14. It can be seen from these plots that the behavior of the valve under this load is still in the linear elastic range of the material and that no yielding occurs.

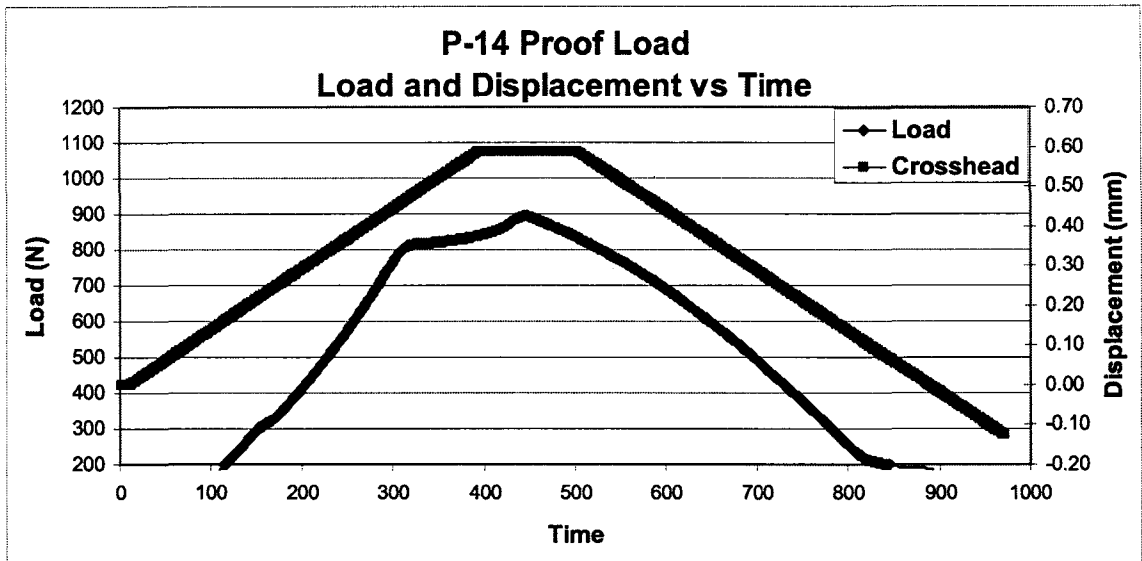


Figure 93. Valve P-14 proof-load, load and displacement vs.. time.

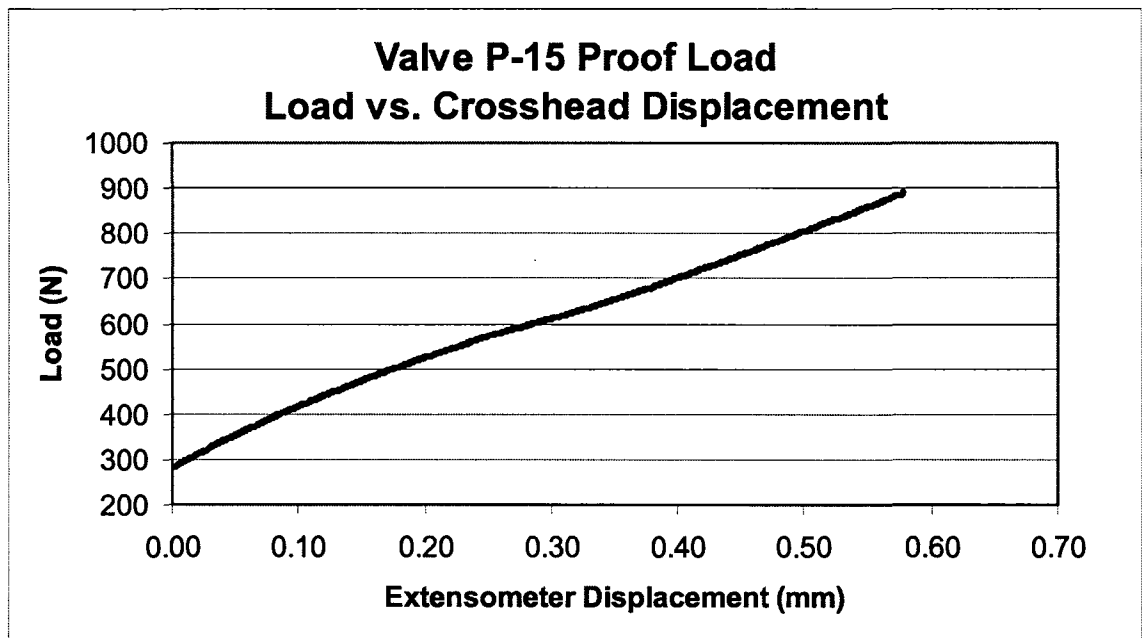


Figure 94. Valve P-15 proof-load, load vs.. crosshead displacement.

4.2.1.2 Follow-on Static Testing

Follow-on static testing was conducted on three valves. The purpose of these tests was to determine the tensile failure load and mode of the valves. The

tests were displacement controlled as in the initial tests. Valves were pulled to failure. Because multiple failure events occurred for each valve, load vs. deflection plots are difficult to read. However, plotting load and deflection vs. time shows a clearer picture of what is happening. The resulting plots are shown in Figure 95 and Figure 96.

Closer inspection of Figure 95 shows that, although crosshead displacement is increasing linearly, the load varies significantly. This is due to the fact that the keeper portion at the tip of the valve is experiencing a shear failure. Essentially the tip of the valve is being pulled through the keeper. Initial failures occurred between 900 N and 1100 N for each valve. Peak loads were between 1600 N and 2000 N. This is an order of magnitude above the tensile loads predicted during normal operation of the test engine.

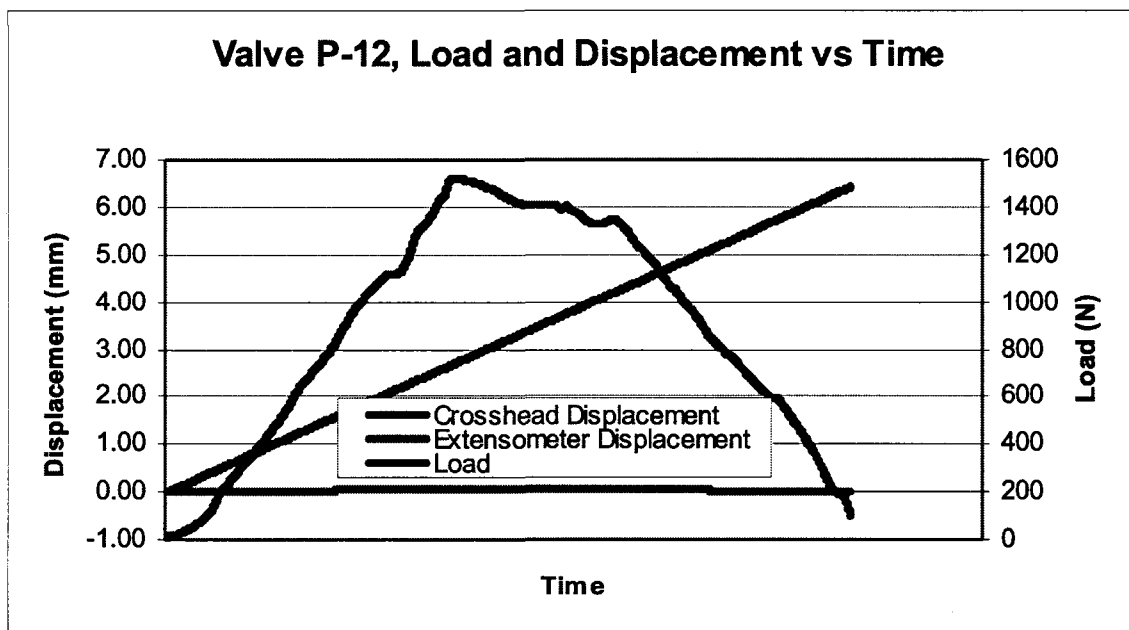


Figure 95. Valve P-12, load and displacement vs. time.

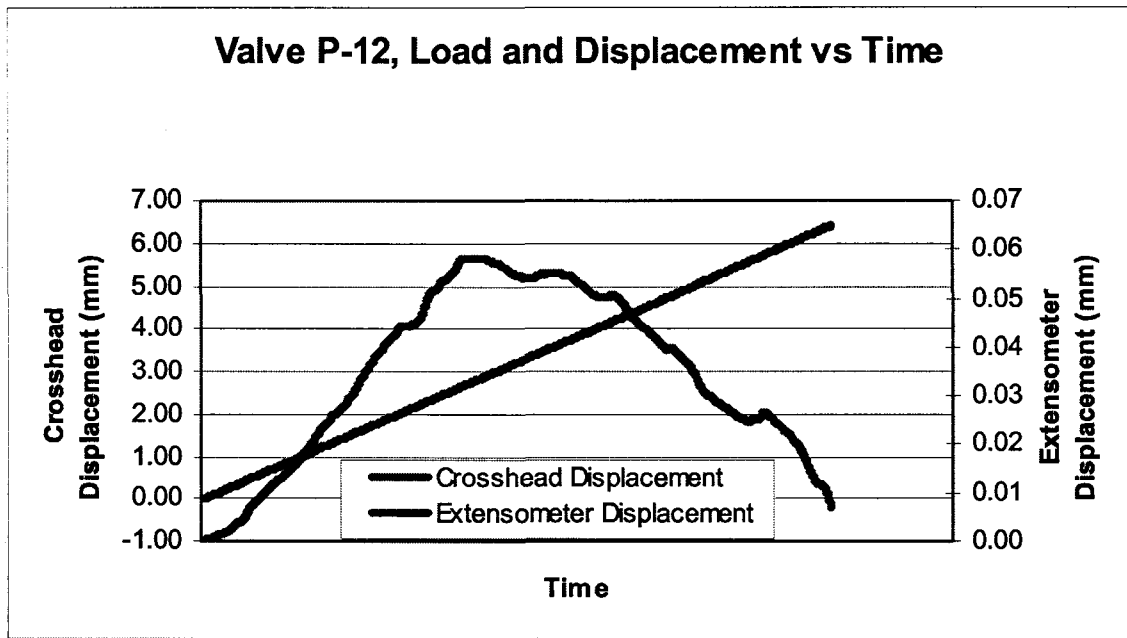


Figure 96. Valve P-12 crosshead and extensometer displacement vs.. time.

Extensometer data taken on the stem of the valve shows a similar pattern. Figure 96 shows that as the keeper fails, the load drops and the displacement of the stem section is reduced. Peak displacement in the stem also was consistent between the two tests, peaking at about 0.05 mm. Displacement in the extensometer was consistently about 1/100th that of the crosshead displacement, indicating an extremely stiff valve stem.

The failure mode demonstrated during these tests is relatively graceful. In each case, the keeper geometry on the valve stem slowly pulled through the keeper. This is a desirable failure mode. A slipping keeper will result in reduced spring tension and lost cylinder compression, presumably prompting an engine teardown. The resulting engine damage will be minimal. For most engine builders, this is much more desirable failure mode than having a valve break into pieces and rattle around in the engine.

4.3 Motored Dynamic Testing

Motored dynamic testing was conducted on two valves. The purpose of this testing was to gain confidence in the mechanical performance of the valves prior to fired engine tests. A picture of the motored test rig is shown in Figure 97. The test profile used is shown in Figure 98. Two valves were run in the motored test setup. Results are shown in Table 32. No significant wear was noted on either valve. There were no failures.

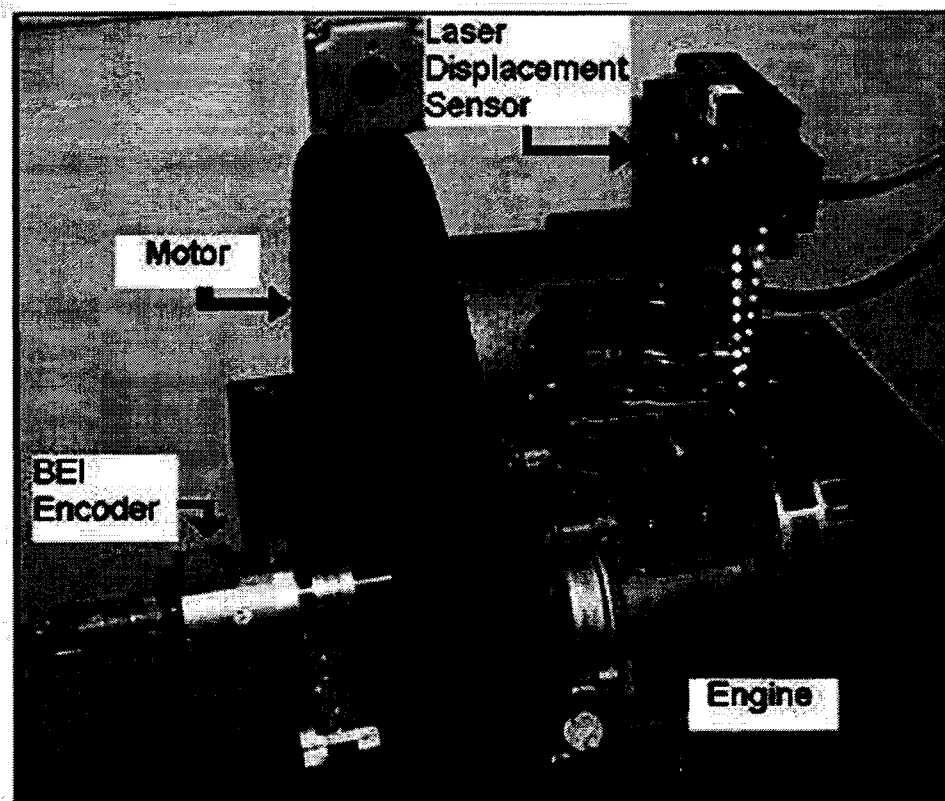


Figure 97. Motored Test Rig.

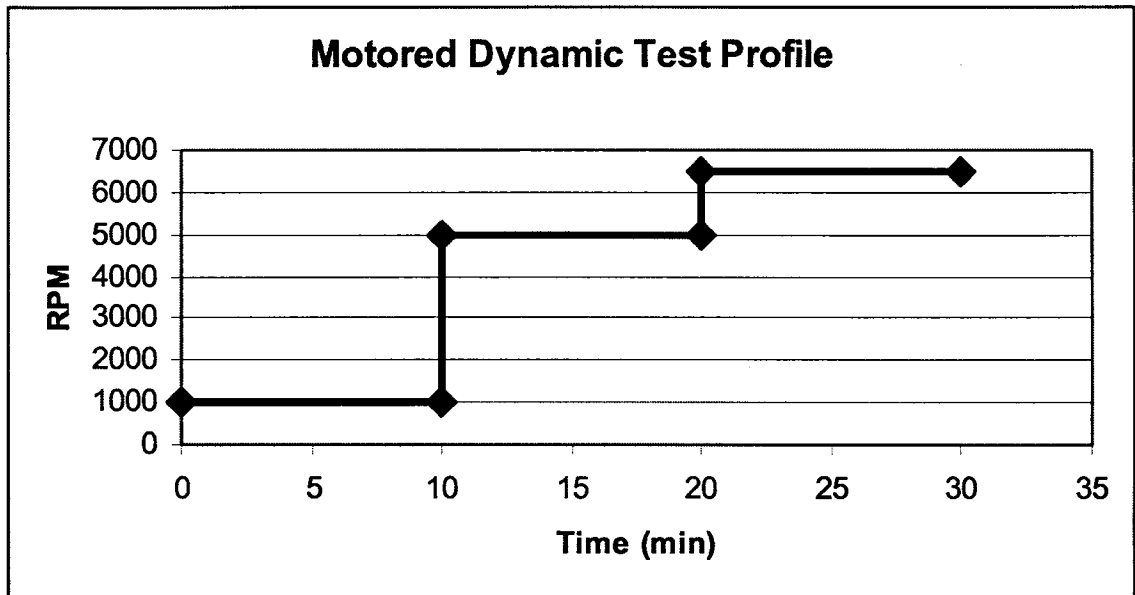


Figure 98. Dynamic Motored Test Profile.

Table 32. Motored engine test results.

VALVE NUMBER	TOTAL RUN TIME MM:SS	OBSERVED WEAR	FAILURE MODE
P-14	16:00	No noticeable	None
P-15	16:00	Keeper wear (possibly from installation)	None

4.4 Fired Engine Testing

The purpose of fired engine testing was to demonstrate the ability of the FRC valves to run in a fired engine, under load. A small hydraulic dynamometer was used for testing, shown in Figure 99. The testing profile used was:

- A 10 minute warm up at idle

- Ten minutes at the world-wide mapping point (WWMP); 1500 RPM and 2.62 bar BMEP or 3.2 ft-lbs torque.
- Ten minutes at wide-open throttle, peak power (3500 RPM, 8 ft-lb torque).
- Ten Minutes at max engine RPM.

A compression check was performed between each stage of testing.

Initial fired-engine testing was conducted on two intake valves. Results are summarized in Table 33. It proved difficult to control the engine load and RPM to the WWMP described above. This is presumably because this small engine was designed to operate at either idle or wide open throttle, and because the throttle control available on the dyno is very coarse. As a result, the total run time and average load listed in the table for valve #P-14 is approximate. A number of improvements in the test setup are under way to remedy this problem.

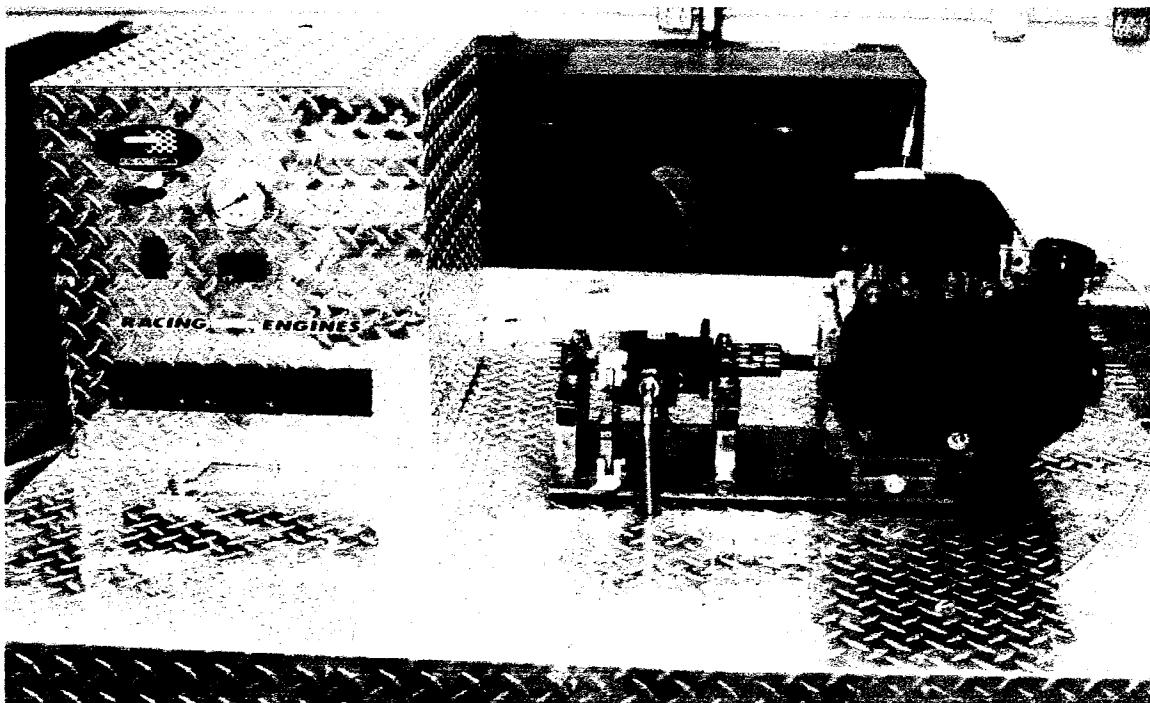


Figure 99. Small engine dynamometer used for fired engine testing.

The first valve tested idled successfully for 10 minutes. Failure occurred during the attempt to control the engine to the WWMP described above. A loss of compression caused the engine to stall. Further investigation revealed a hole burned through the face of the valve in the valve seat region.

As a result of the problems running the first valve (P-14), it was decided that the second valve should be run at idle for a substantial time, and that dyno improvements should be made before attempting to the loaded test conditions.

Table 33. Fired engine test results.

VALVE NUMBER	TOTAL RUN TIME BEFORE FAILURE HH:MM:SS	OBSERVED WEAR	FAILURE MODE
P-14	~ 00:30:00	Some seat wear	Hole burned through face
P-15	6:40:00 (1700-1900 RPM)	Small seat wear, pitting on face	None

Valve # P-15 was run at 1700-1900 RPM, with no load for over 400 consecutive minutes without failure. It should be noted that the total run time 6 hours and 40 minutes (or 400 minutes) at 1700-1900 RPM represents a ten fold performance increase over the previous published maximum run time for a composite valve. This also represents a total cyclic loading of over 400,000 cycles.



Figure 100. Valve P-14 after running engine test. Note the small hole burned from the face and exposed fiber.

4.5 Failure Analysis

Figure 100 shows the hole burned in valve # P-14. Although it is difficult to see from the photo, it appears that the matrix material decomposed while the carbon fiber stayed largely in place. This caused a leak and loss of compression.

The failure mode displayed by this valve was also graceful in that it did not lead to destruction of other engine components. It was observed during motored engine testing that the FRC valves do not rotate during engine operation the way steel valves do.

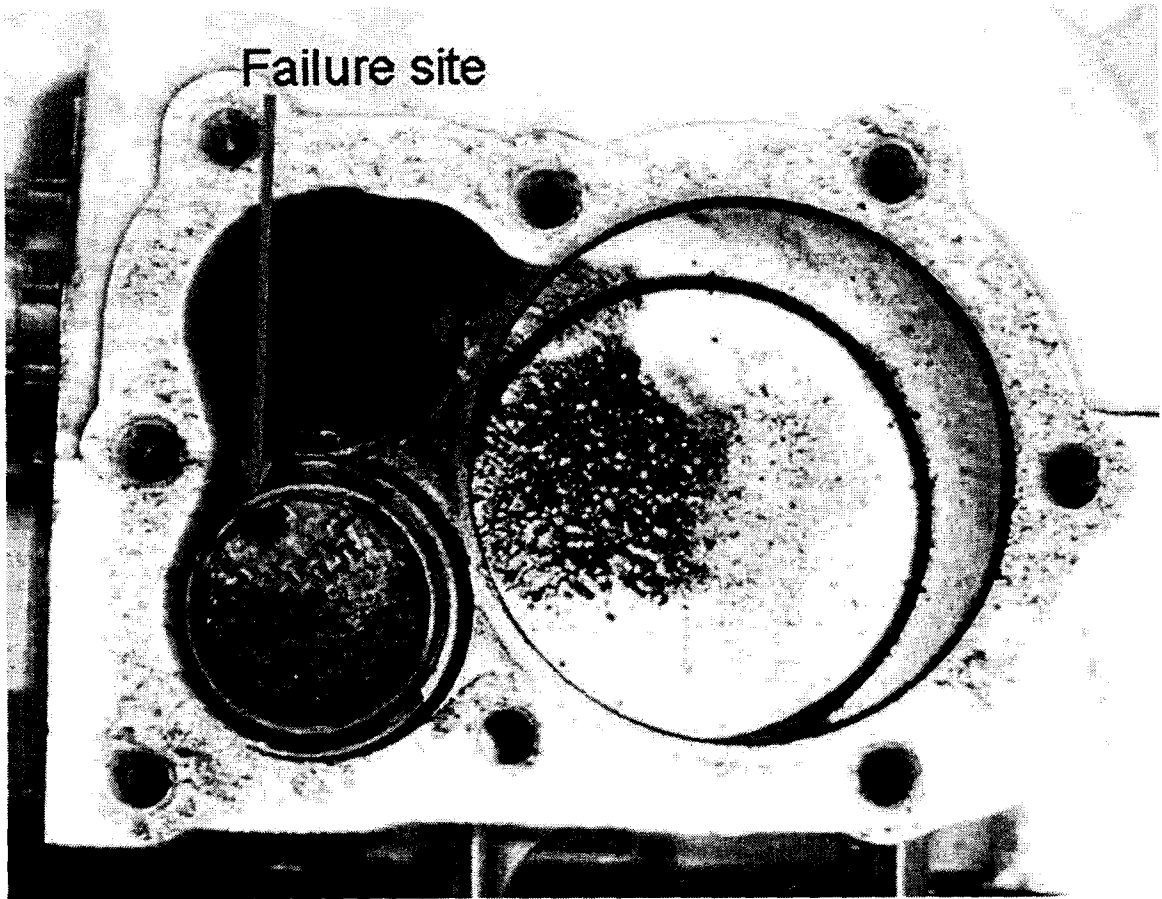


Figure 101. Valve P-14 immediately after the fired engine test. Note the location of the hole in the intake valve (bottom).

When removing the failed valve from the running engine, it was noted that the hole burned in the face was at a point on the intake valve that is closest to the exhaust valve and to the spark plug, see Figure 101. Presumably this is the hottest spot in the combustion chamber.

It appears that the thermal/oxidative environment experienced by the intake valve is more severe than anticipated from preliminary literature studies.

4.6 Temperature Measurement of Valves in an Operating Engine

4.6.1 Introduction and Background

Based on the apparent thermal degradation of the FRC valves run under load in the engine, a series of experiments were undertaken to measure the actual operating temperatures of conventional and composite valves in a running engine. Design requirements discussed in section 2.3.1, obtained from literature review, suggested that steel intake valves typically run at 350°C, exhaust valves run hotter.

4.6.1.1 Valve Temperature Measurement Techniques

As early as 1923, exhaust valve temperature measurements were being made on running gasoline engines using both thermocouples and optical pyrometers. It was noted that placing a thermocouple inside a valve and taking temperature measurements while the engine is running is extremely difficult. Exhaust valve temperatures were found by both techniques to be between 700°C and 800°C at full load¹²⁶. In 1945, measurements of exhaust valve temperature in a running supercharged diesel engine were published. Thermocouples were placed in the intake and exhaust valve and measurements of temperature inter-cycle temperature fluctuations were measured. An example of these measurements is shown in Figure 102. The steady state temperature for these diesel intake valve is between 400°C and 410°C with a fluctuation of roughly 5°C¹²⁷.

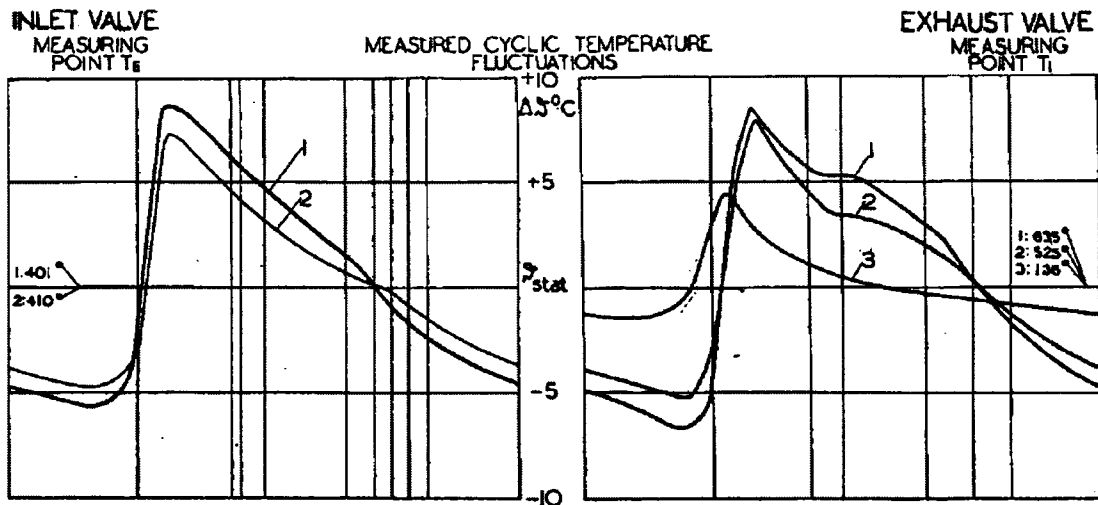


Figure 102. Fluctuations in intake and exhaust valve temperatures in a running diesel engine published in 1945¹²⁸.

In 1965, exhaust valve temperature measurements were deduced using a hardness relaxation measurement technique. Specifically designed temperature check valves were run for one hour at a load that produced maximum temperatures. Valves were removed from the engine and hardness tested, and from this hardness the operating temperature was deduced. Experiments were conducted on four, six and eight cylinder air and water cooled engines. Measured valve temperatures ranged from 668°C – 771°C (1235°F – 1420°F). Heat flow through the exhaust valve was also calculated based on temperatures. An example of this is shown in Figure 103¹²⁸. It was recognized that valve temperature is affected by a number of factors in the engine including:

- Valve size and geometry
- Engine compression ratio
- Air/Fuel ratio
- Proximity to cooling
- Valve material

- Valve stem to guide clearance
- Ignition advance

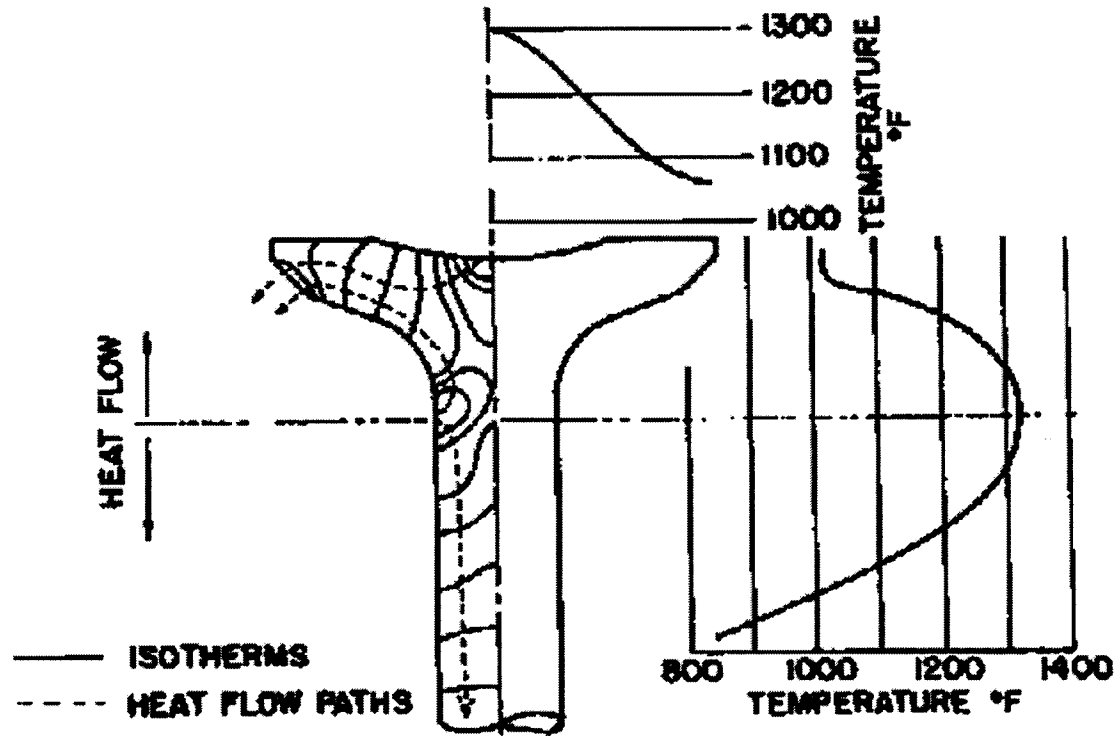


Figure 103. Exhaust valve temperature contours and heat paths¹²⁸.

Other techniques have been used to measure the temperature of the valve in a test fixture while applying boundary conditions to the valve that simulate in-engine conditions⁴⁰. Modern racing exhaust valves run at 870°C (1600°F)^{26,129}. Combinations of thermocouple temperature measurement and modeling have also been used to determine heat flux and stresses in a running exhaust valve¹³⁰.

The high operating temperatures of exhaust valves causes additional problems with corrosion¹³¹, and has caused the adoption of expensive high performance nickel steel super alloys such as Inconel and Nimonic, as standard

material for exhaust valves¹³² and the development of high performance coatings to prevent corrosion¹³³.

Unfortunately, nearly all of the information published deals with temperatures and heat flux in exhaust valves. Presumably this is because the exhaust valve is exposed to higher operating temperatures and the requirements for the intake valve are relatively “easy.” The only example found of intake valve temperatures in a gasoline engine measured temperatures at 370°C (700°F)¹³⁴. Since this is below the degradation temperature of the PETI-RFI polymer used, it is clear that this previously published data is not appropriate for the test engine. Thus a set of experiments was devised to measure the temperatures of the running valves in the test engine.

4.6.2 Experimental Setup and Procedure

4.6.2.1 Objective

Because there appeared to be a discontinuity between actual valve temperatures in running engine, and published valve temperatures for spark ignited engines, it became necessary to measure the steady state operating temperature of both the intake and exhaust valve in the running engine under varying load. Of secondary importance was measuring the valve face temperature in both steel and FRC valves to determine the peak temperature and magnitude of temperature fluctuations under peak load.

In addition, better boundary condition data was needed for thermal modeling of the valves. Data about exhaust gas temperature, valve seat temperature and cylinder head temperature was also needed.

4.6.2.2 Instrumentation of Steel Valves

Since a temperature profile for the valve was desired, multiple K-type thermocouples were placed in both the intake and exhaust valves. Four holes were drilled through the face of each valve and one hole through the stem. 32 gauge thermocouples were inserted from the back side of the valve and welded in place on the surface. Because of the nature of this process, it was difficult to control the depth of the thermocouple while welding it in place. Figure 104 show the thermocouple locations when viewed from the port side of the engine. A through hole was drilled in the valve stem and a pin inserted to prevent rotation of the valve during running, which would wrap and break the thermocouple wires. Once all five thermocouples were welded in place the face of the valve was polished flat. Valves were mounted in the engine Figure 105 shows the instrumented intake valve mounted in the engine with the cylinder head removed. Figure 106 shows both the intake and exhaust valves mounted. Bundled thermocouple wires are clearly visible exiting the side of the intake and exhaust manifolds on the right side of the picture.

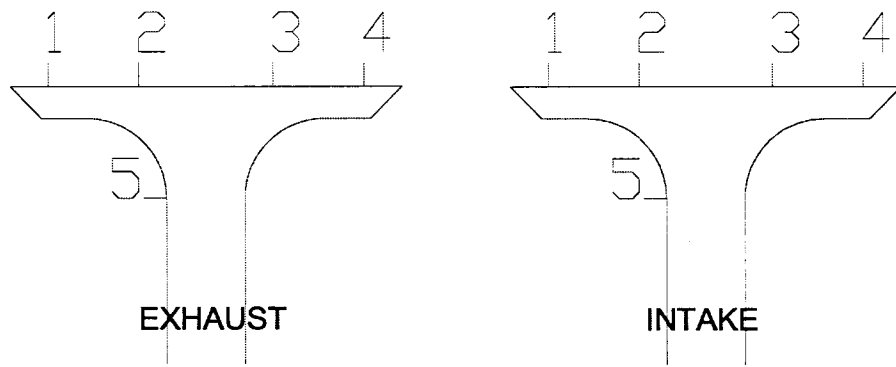


Figure 104. Exhaust and intake valve thermocouple locations.



Figure 105. Instrumented intake valve mounted in the engine.



Figure 106. Instrumented intake and exhaust valves mounted in the engine.

4.6.2.3 Instrumentation of the Engine

Additional K-type thermocouples were mounted in the engine at the following locations:

- Under the intake valve seat
- Under the exhaust valve seat
- Between valve seats
- In the cylinder head (5 locations)
- In the oil pan for monitoring oil temperature
- In the exhaust manifold for exhaust gas temperature

Figure 107 shows a diagram of the engine block with thermocouple locations marked. Figure 108 shows a picture of the cylinder head with thermocouple locations marked.

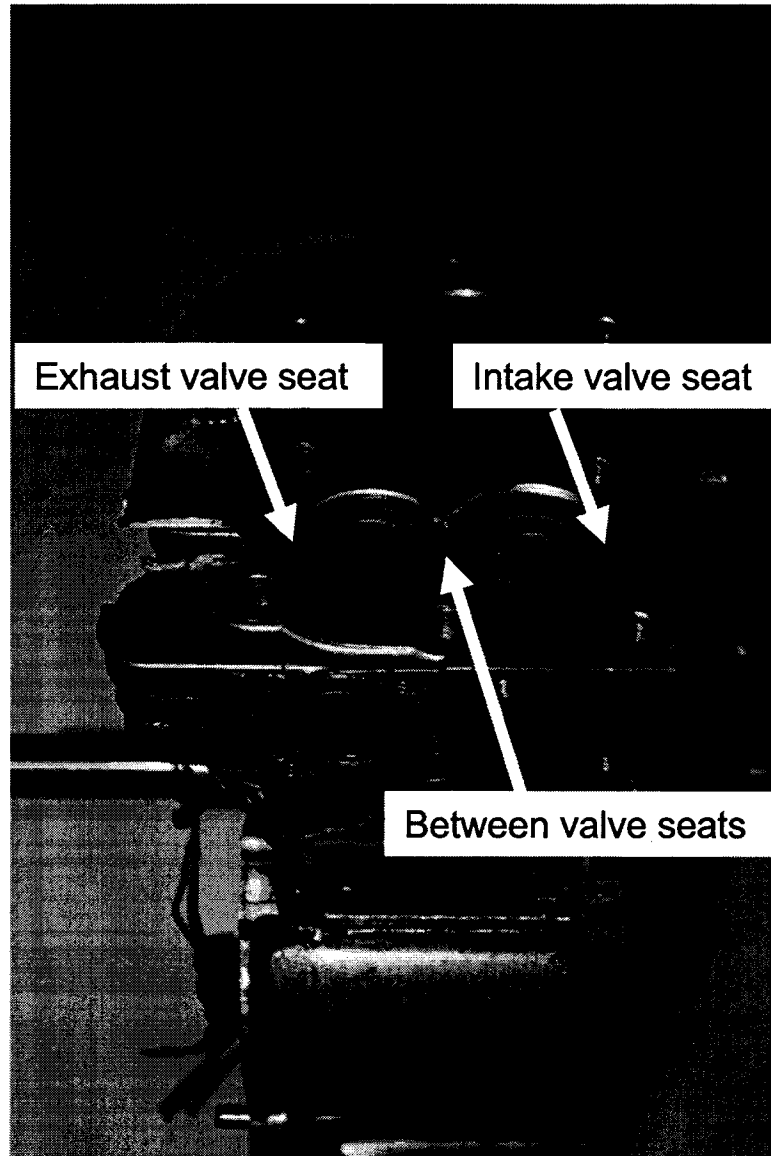


Figure 107. Engine block thermocouple locations.

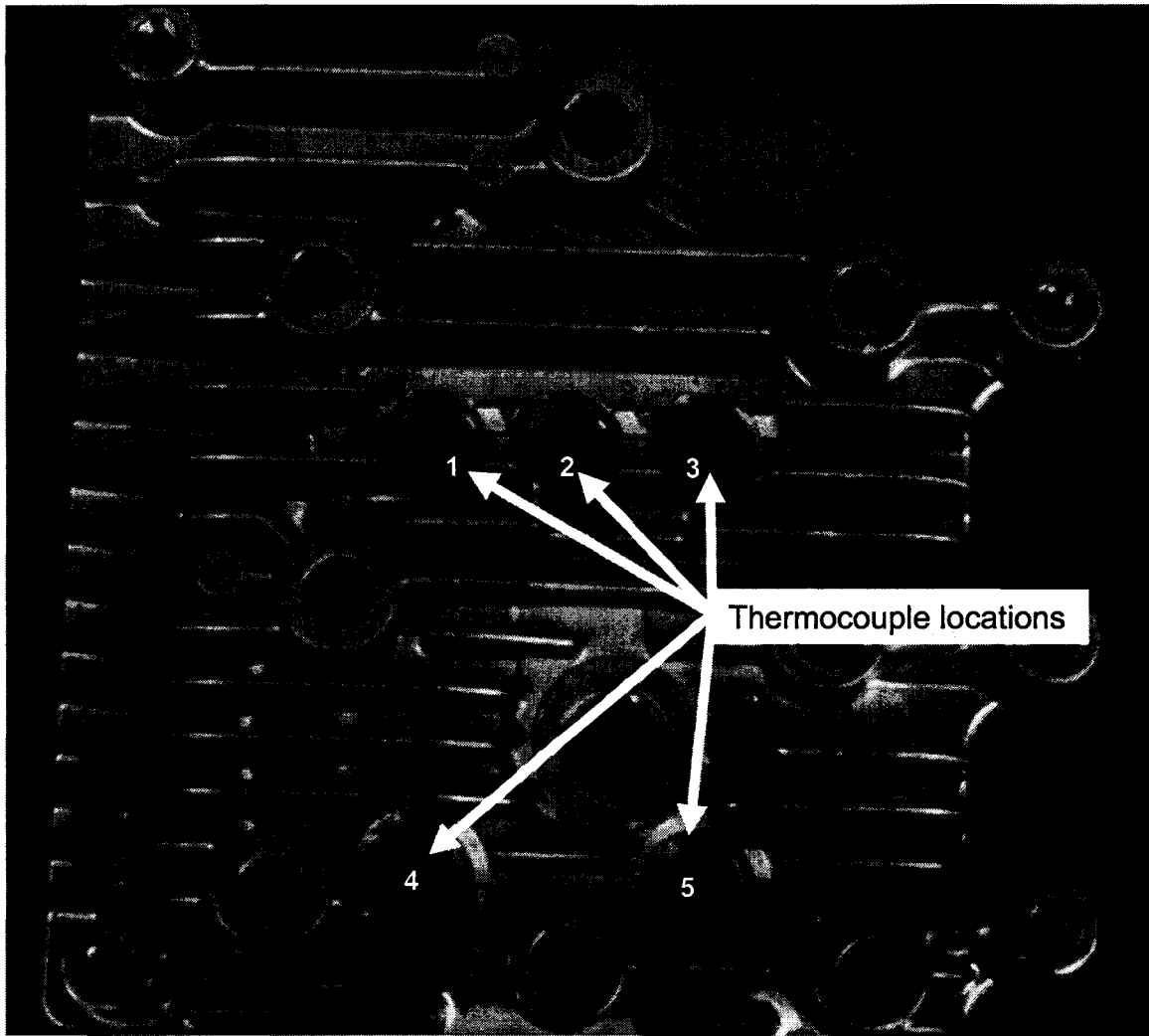


Figure 108. Cylinder head thermocouple locations.

4.6.2.4 Data Acquisition

Data acquisition was performed using a National Instruments PXI-1030 chassis connected to a SCXI-100 break out board and SCXI-1031 thermocouple reader. All data was collected using custom built LabView Virtual Instrument (VI) designed for collecting the data required for that specific test.

4.6.2.4.1 Low sampling rate (Average temperature) measurements

The objective of these tests was to get a steady-state temperature for the valves at different operating conditions. All 18 thermocouples were monitored simultaneously. Oil temperature, Exhaust gas temperature, dyno RPM and load were entered manually by the operator, and data points were recorded once the engine reached steady temperatures. A screen shot of the VI used is shown in

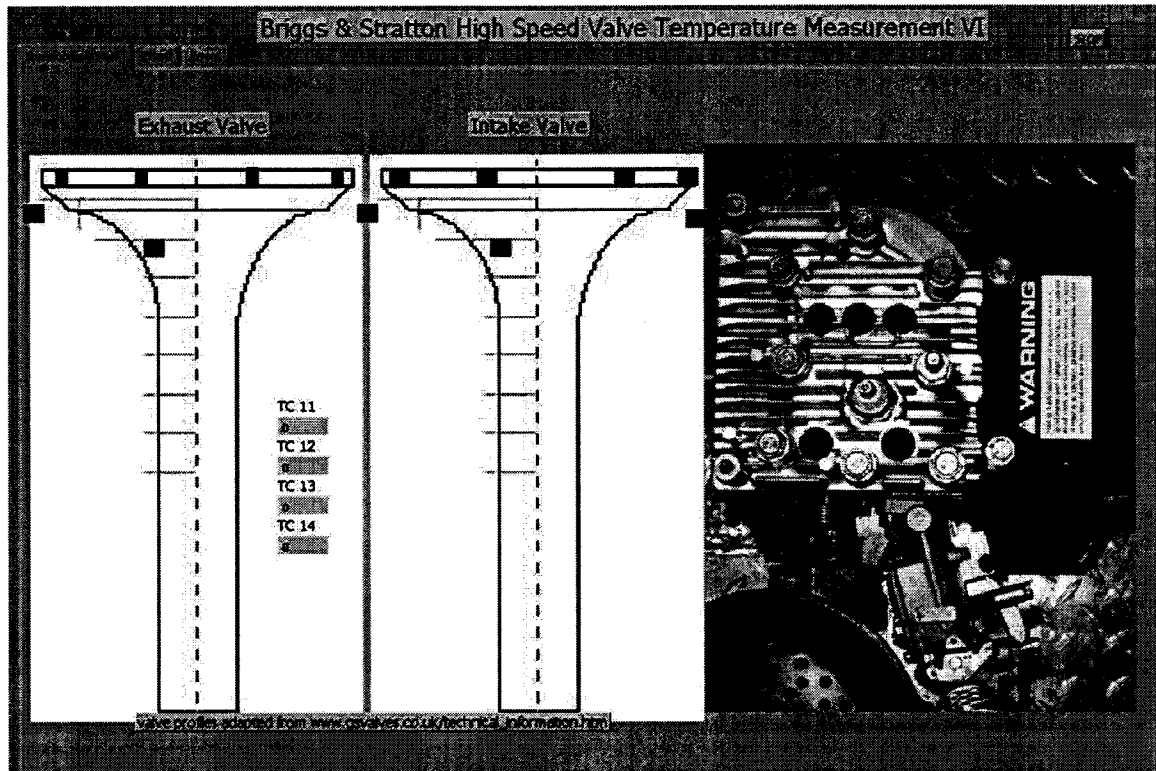


Figure 109. Screen shot of the LabView VI used for steady state valve temperature measurements.

For this set of tests, the following data acquisition parameters were used:

- Number of samples collected 2
- Sampling rate 100 Hz
- Resulting time between samples 0.005 sec

Data was written to a text file and analyzed post-test.

The test profile was generated based on the published power curve for the Briggs and Stratton Raptor engine. The published torque and horsepower curves for the test engine are shown in Figure 110. This curve was corrected for altitude. The corrected curve is shown in Figure 111.

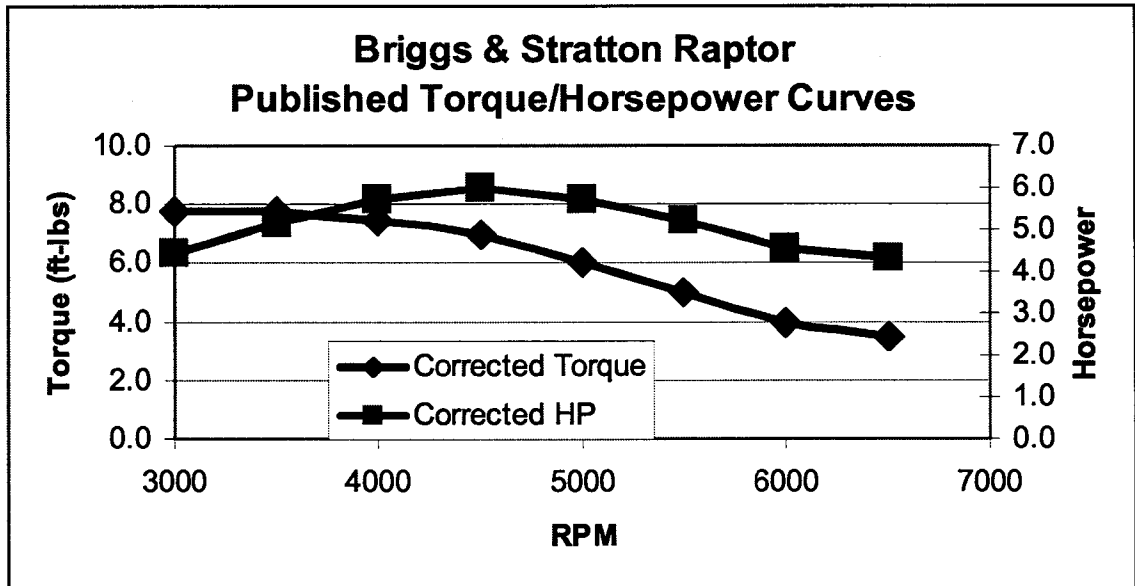


Figure 110. Briggs raptor published torque curve (reference).

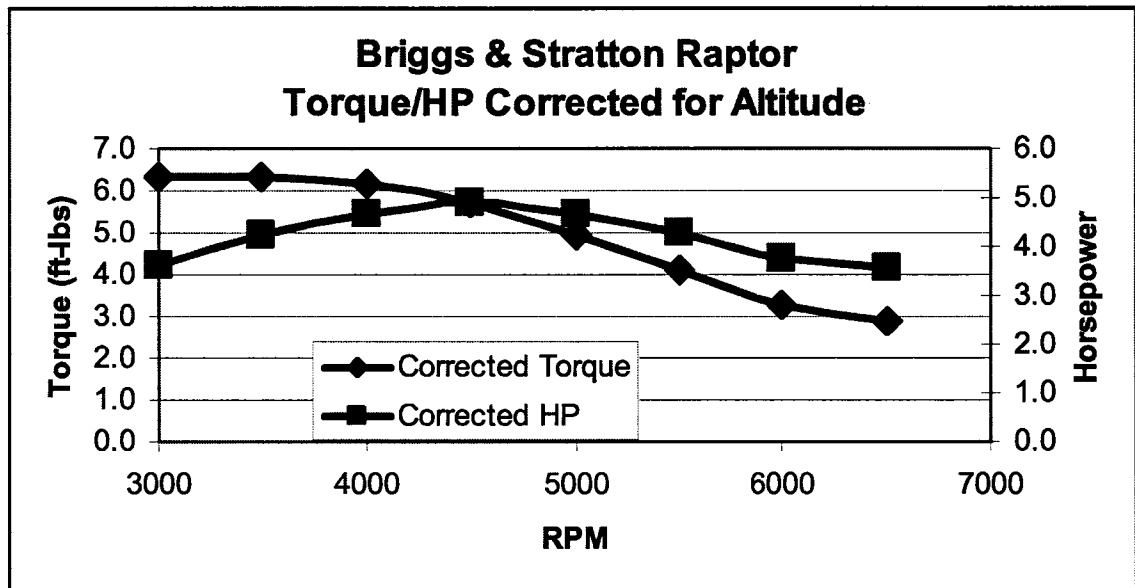


Figure 111. Briggs Raptor torque curve adjusted for altitude.

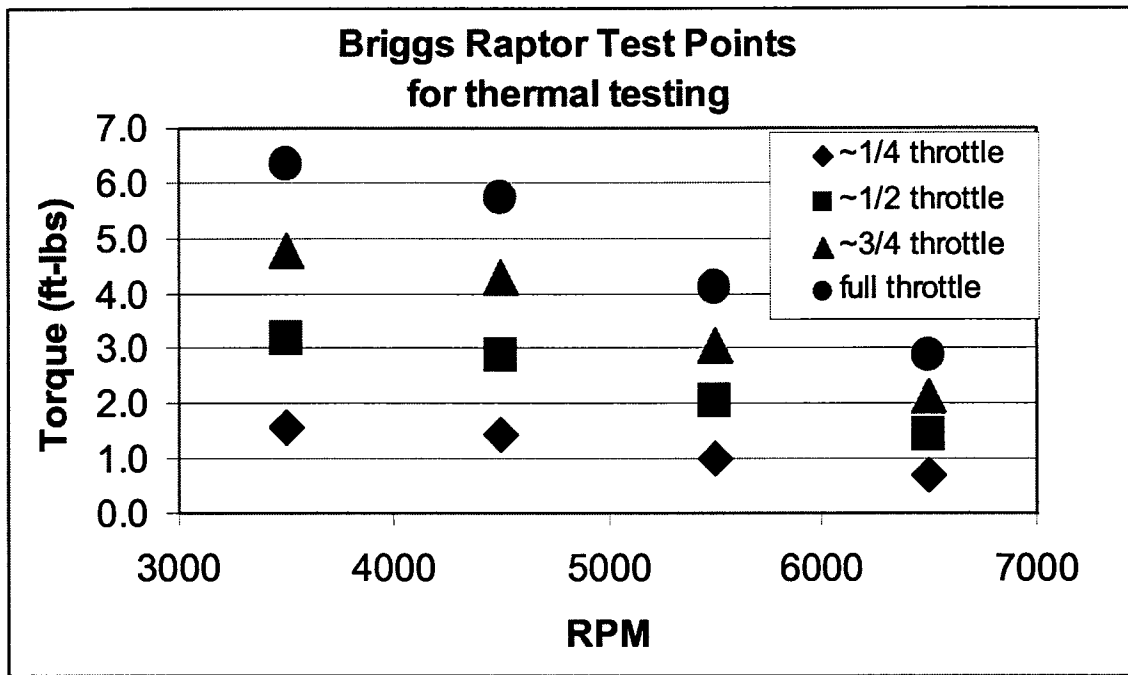


Figure 112. Briggs Raptor test points.

Approximate test points were taken periodically from this curve for $\frac{1}{4}$, $\frac{1}{2}$, $\frac{3}{4}$ and full throttle operating points. These test points are shown graphically in Figure 112 and are tabulated in Table 34.

Table 34. Briggs test points. All values are in lb-ft torque.

RPM	~ $\frac{1}{4}$ THROTTLE	~ $\frac{1}{2}$ THROTTLE	~ $\frac{3}{4}$ THROTTLE	FULL THROTTLE
3500	1.6	3.2	4.8	6.4
4500	1.4	2.9	4.3	5.7
5500	1.0	2.1	3.1	4.1
6500	0.7	1.4	2.2	2.9

After warming up the engine, the operator controlled the engine throttle and load to the desired test set point. Temperatures were monitored and, once steady state temperatures were reached, data for the test point was recorded. The engine was returned to idle and allowed to cool off.

Because the data was available, torque and RPM data were collected and measured torque vs. horsepower plots were generated.

4.6.2.4.2 High sampling rate measurements

As mentioned earlier the objective of the high sampling rate tests were two fold; 1) determine the surface operating temperature of the running valves and 2) measure the magnitude of temperature fluctuations at the surface of the valve. As a result of these different objectives, slightly different instrumentation and test procedures were used. To obtain the highest fidelity data possible, data from only one thermocouple was gathered at a time. Individual VIs were written for each valve thermocouple. The VI sampled data as fast as the hardware would allow and wrote the data to a text file for later processing. Figure 113 is an image of the high sampling rate VI.

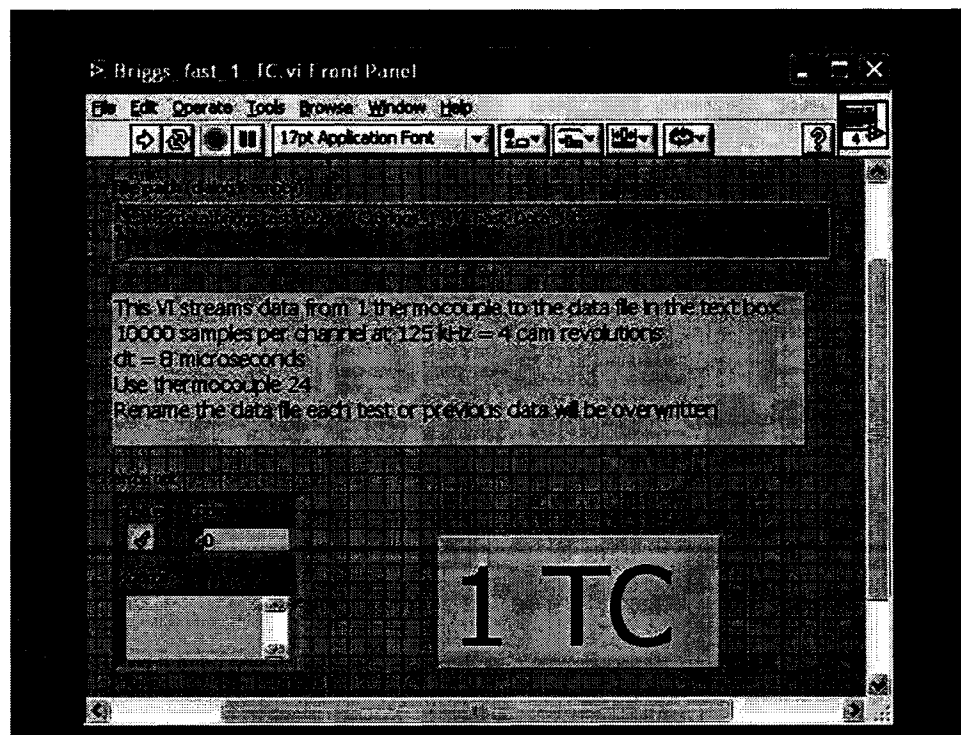


Figure 113. High-sampling rate VI.

The resulting data acquisition parameters used are shown in Table 35:

Table 35. Data acquisition parameters, single thermocouple high sampling rate, based on 5500 RPM engine speed.

Number of samples collected	10,000
Sampling rate	125 kHz
Resulting time between samples	8 μ sec
Camshaft data accuracy	0.1 degrees
Equivalent camshaft cycles	4

Because the resulting data was not collected simultaneously, and therefore not synchronized, an additional VI was written to collect data from four thermocouples simultaneously at a time at the maximum sampling rate possible. Operation was identical to the single thermocouple VIs described above, with the addition of three channels of data at the accompanying slower data acquisition rate. The resulting data acquisition parameters used are shown in Table 36:

Table 36. Data acquisition parameters for four-thermocouple high sampling rate, based on 5500 RPM engine speed.

Number of samples collected	10,000
Sampling rate	41 kHz
Resulting time between samples	24 μ sec
Camshaft data accuracy	0.4 degrees
Equivalent camshaft cycles	11.2

Because Wide Open Throttle (WOT) at full engine load represents the most severe environment seen by the valve, all tests were run at these conditions and load was used to drag the engine down to 5500 RPM

After warming up the engine, the operator controlled the engine throttle and load to the desired test set point. Temperatures were monitored and, once steady state temperatures were reached, data for the test point was recorded. The engine was returned to idle and allowed to cool off.

4.6.3 Results and Discussion

From the steady state data collection experiments, measured torque and horsepower curves were generated. These curves are shown in

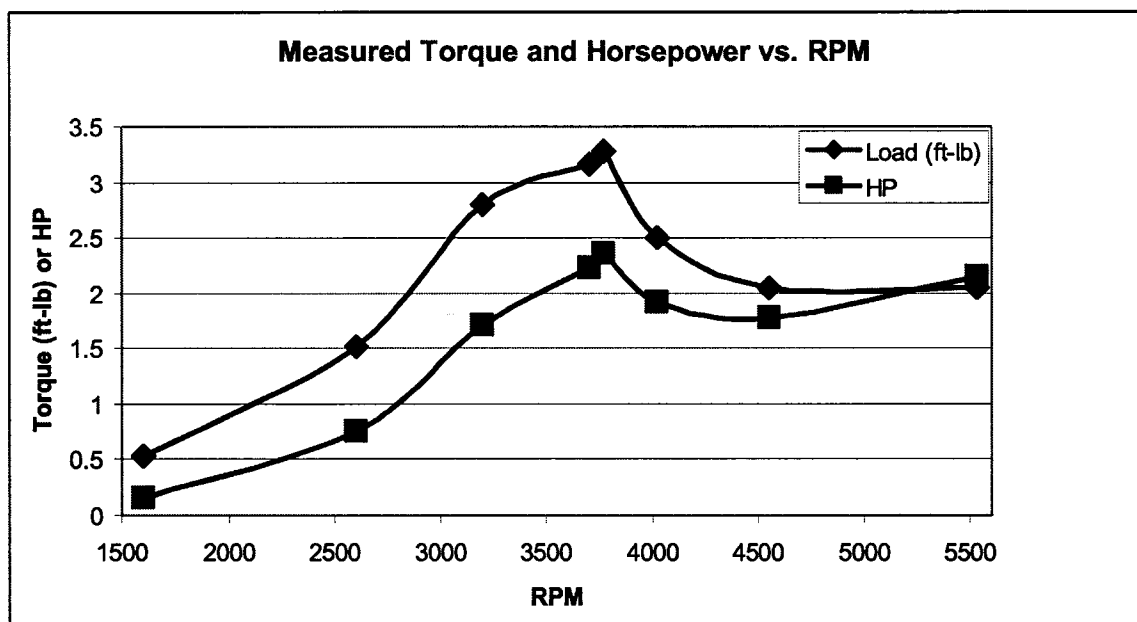


Figure 114. Measured torque and HP curves for the Briggs Raptor engine.

This data shows a roughly similar shape, with lower magnitude than the published data from Briggs and Stratton. This is not surprising considering the

relatively crude fueling system, high altitude, and rough tolerances on the engine. It does show that peak power and torque occurring at roughly 3500 RPM.

4.6.3.1 Steady State - Intake Valve Temperatures

Steady State thermocouple temperatures for the part throttle measurements of the intake valve are shown in Figure 115. Recall the thermocouple positions shown Figure 104. Thermocouples one through four are on the valve face, thermocouple five is on the back side of the valve in the intake port. It is clear that there is a temperature gradient across the face of the valve, with the center of the valve several degrees cooler than the valve seat surfaces. Temperature is also increasing with throttle position and speed as expected. These values are relative close to the intake valve temperatures published in the literature. As expected, back side temperatures remain well below face temperatures.

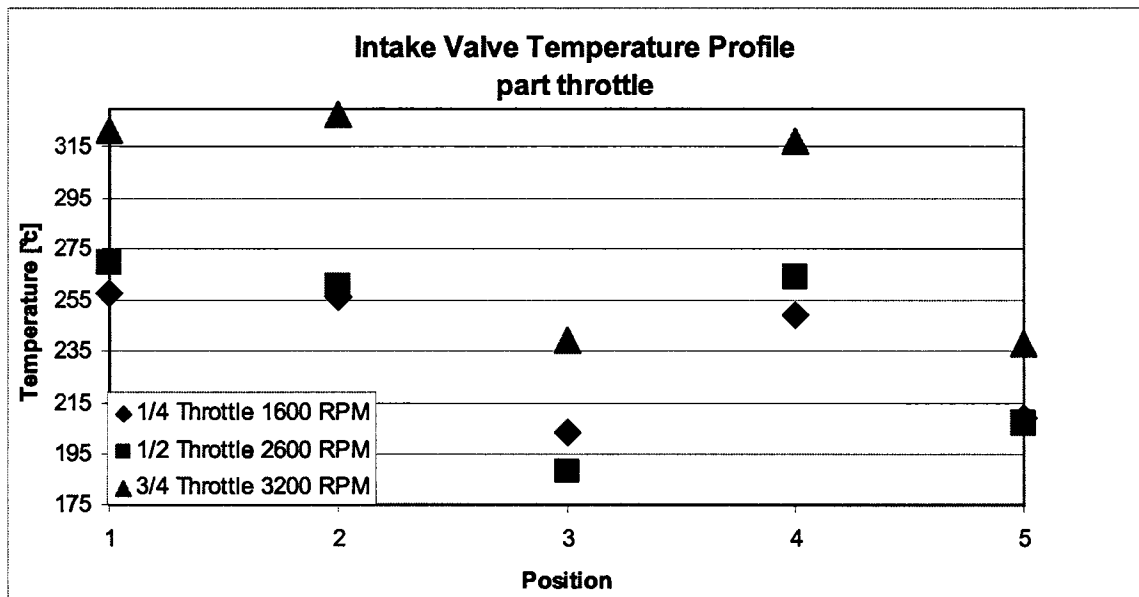


Figure 115. Intake valve temperature profiles, part throttle.

Figure 116 is thermocouple data for the WOT cases. Temperatures at WOT are nearly 100°C higher than the temperatures measured at part throttle, reaching a maximum of 425°C. The same temperature profile is seen across the valve face and back side temperatures remain well below face temperatures, though slightly higher than at part throttle operation. Temperature is again increasing with load and speed.

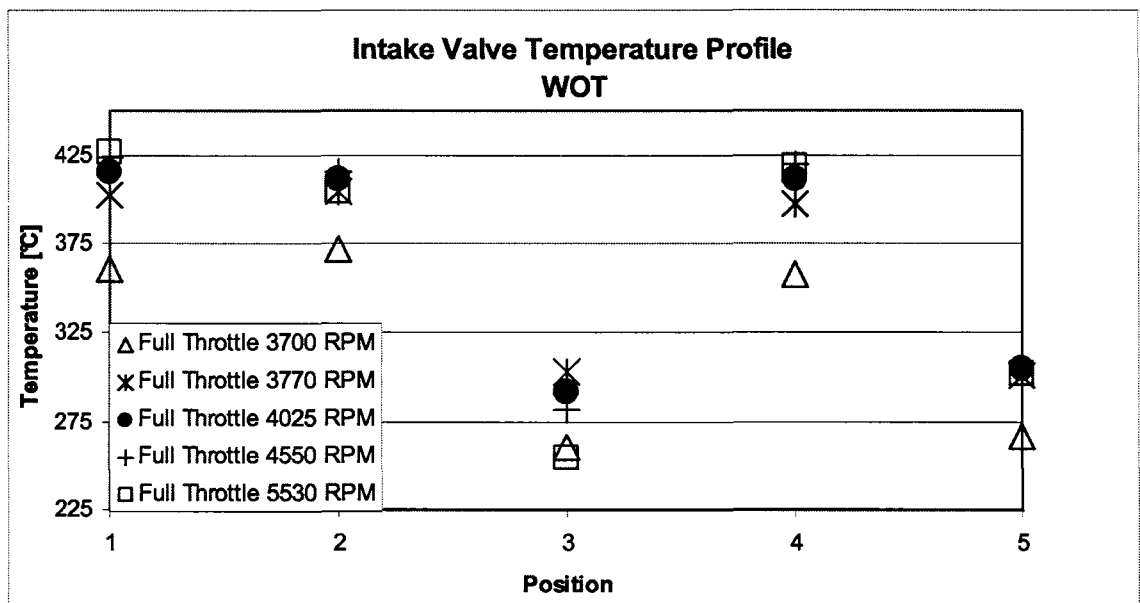


Figure 116. Intake valve temperature profiles, full throttle.

4.6.3.2 Steady State - Exhaust Valve Temperatures

Steady State thermocouple temperatures for the part throttle measurements of the exhaust valve are shown in Figure 117. Data for thermocouple 2 was not available because the thin wire broke during engine warm up. Temperatures are fairly uniform across the face of the valve. Again, temperature is also increasing with throttle position and speed as expected. These values are also relative close to the exhaust valve temperatures published

in the literature. As expected, back side temperatures remain well below face temperatures.

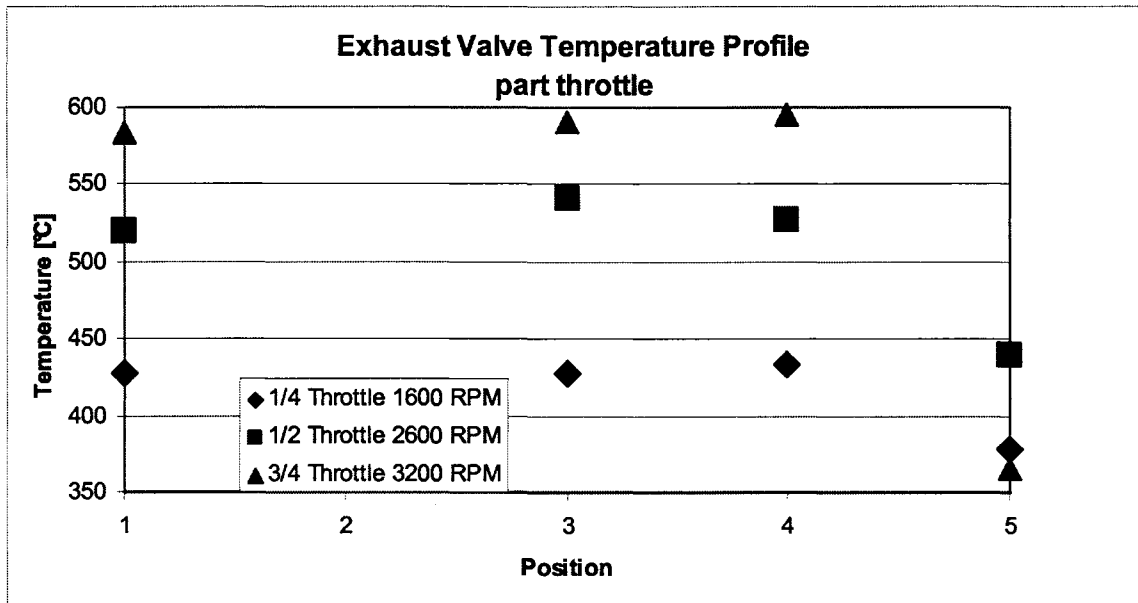


Figure 117. Exhaust Valve temperature profiles, part throttle.

Figure 118 is the exhaust valve data for the WOT cases. A temperature gradient appears across the valve face with cooler temperatures at the face and hotter temperatures at the seat. Temperatures measured at WOT are nearly 300°C higher than the temperature at part throttle. Temperatures are also much higher than those reported in the literature and even higher than those claimed for racing exhaust valves! Back side temperature also rises significantly for all RPMs and is actual higher than the measured face temperature for several cases.

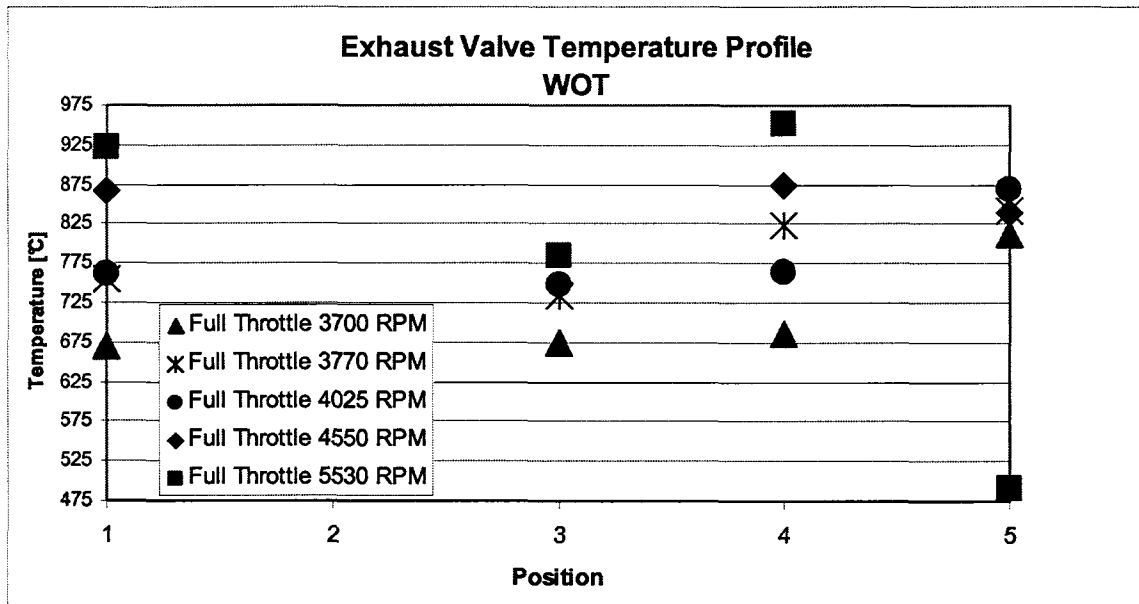


Figure 118. Exhaust valve temperature profiles, full throttle.

4.6.3.3 Steady State- Engine Temperatures

Cylinder head and valve seat temperatures were also measured. Figure 119 is a plot of these temperatures. The series numbers correspond to the locations shown in Figure 108. Most critical in these measurements is the exhaust seat temperature which peaks near 300°C. In thermal modeling of the valve, this seat temperature plays a large part in determining the valve operating temperature.

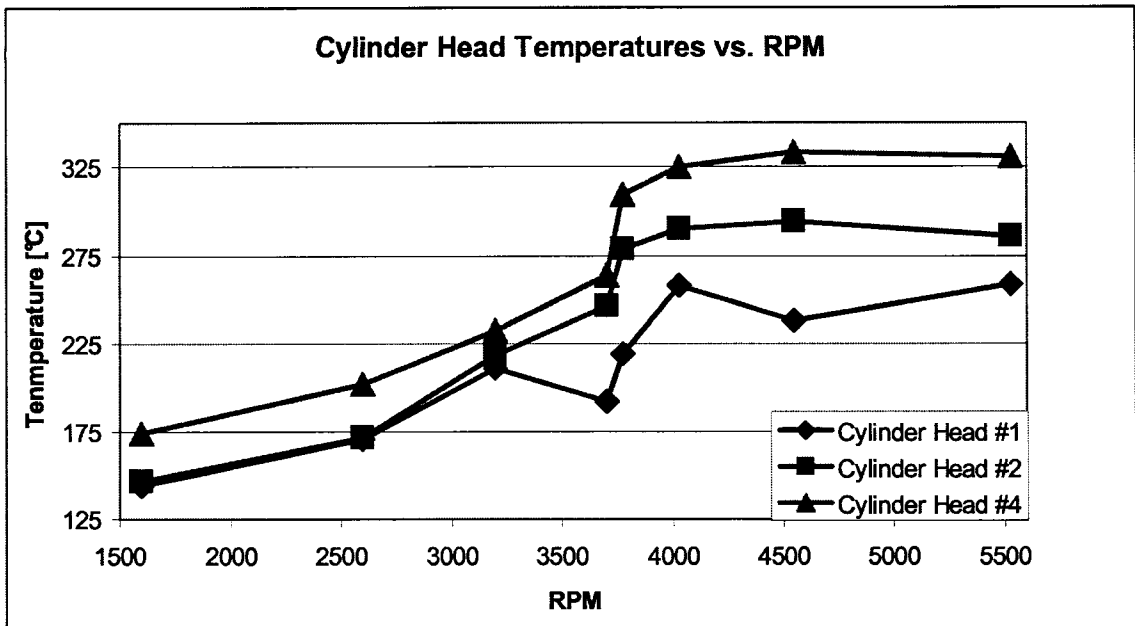


Figure 119. Cylinder head temperatures.

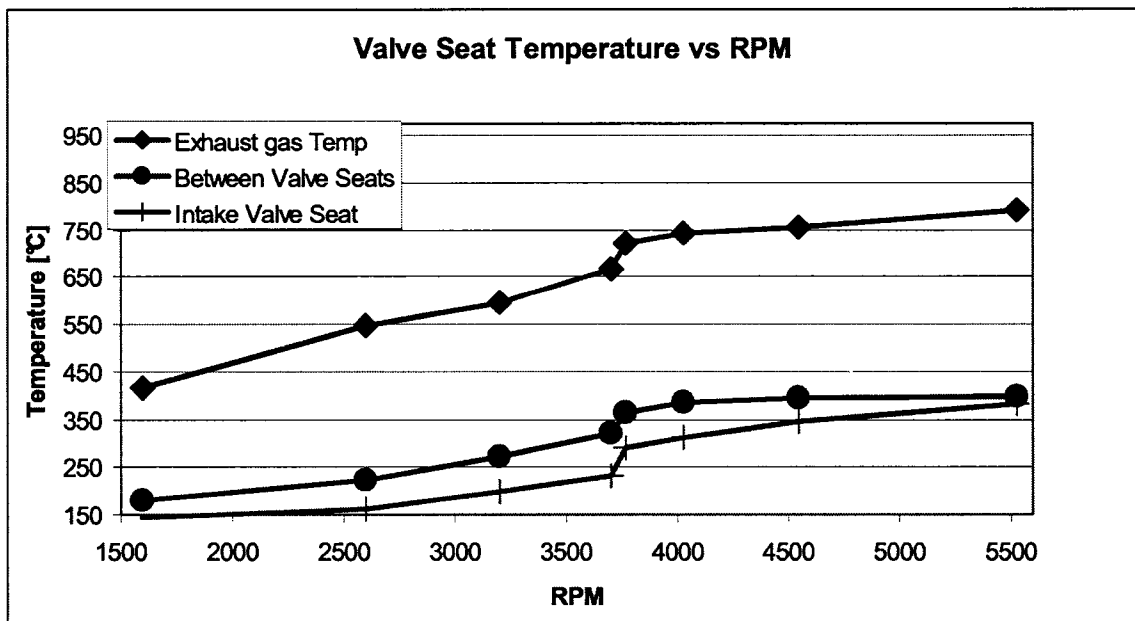


Figure 120. Valve seat temperatures vs.. RPM.

4.6.3.4 High Sampling Rate - Intake Valve Temperatures

Intake valve temperatures were measured at 125 kHz sampling rate.

During the test, engine speed was 5900 RPM at WOT and full load. Thus, the

data collected corresponds to 3.9 camshaft cycles. The results are shown in Figure 121. Only one data series is shown because, by this point in testing the other thermocouples in the valve had failed. There appears to be a lot of noise on the plot, but this is to be expected since this particular engine has a large Covariance of IMEP (COV of IMEP). In other words, the engine runs rough. Dashed lines on the plot represent the approximate time for one camshaft cycle. The mean temperature across the entire plot is 380°C. This is near the steady state values measured for the intake valve at WOT and full load for the same valve with the same thermocouples. There are two clear excursions in temperature near 0.015 seconds and 0.055 seconds. These most likely correspond to opening of the intake valve and the corresponding fresh air charge cooling the valve briefly. However this cannot be verified without synchronizing camshaft position data, which was not within the capability of this test setup. Variation in temperature while the valve is closed appears to around 40°C. Intake valve cooling of roughly 100°C occurs when the valve is open. This average valve temperature is near but slightly higher than the 370°C average temperature reported in the literature.

4.6.3.5 High Sampling Rate - Exhaust Valve Temperatures

Exhaust valve temperatures were also measured at 125 kHz. The results are shown in Figure 122. Although the temperatures are plotted on the same time scale, the data was not collected at the same time and is not synchronized. Dashed lines represent the approximate time for one camshaft revolution.

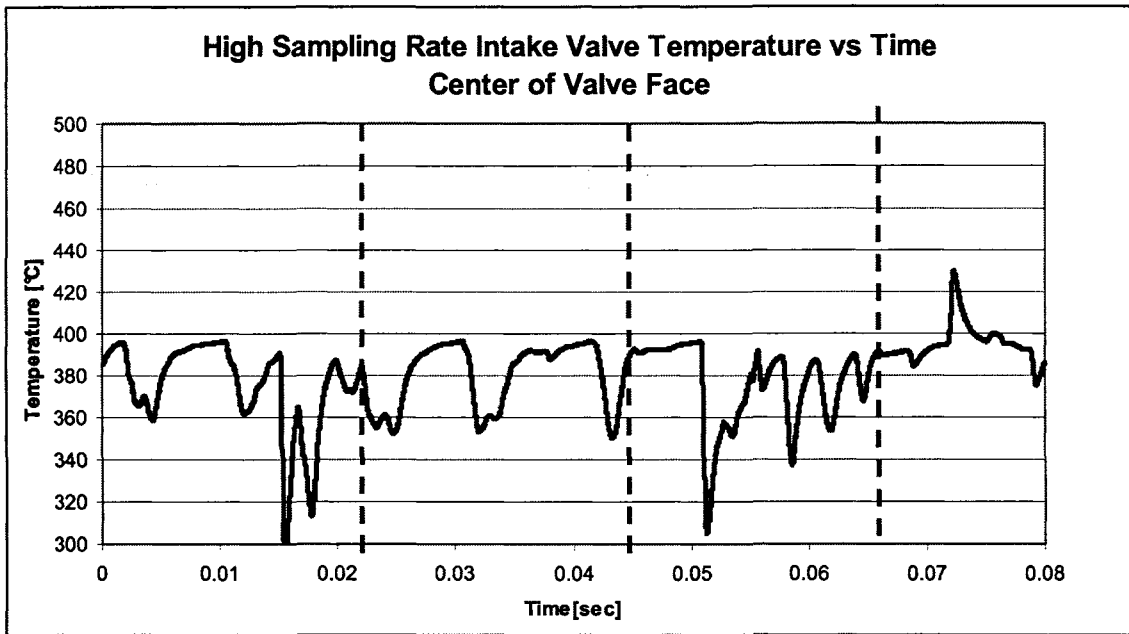


Figure 121. Intake valve temperature versus time, sampled at 125kHz.

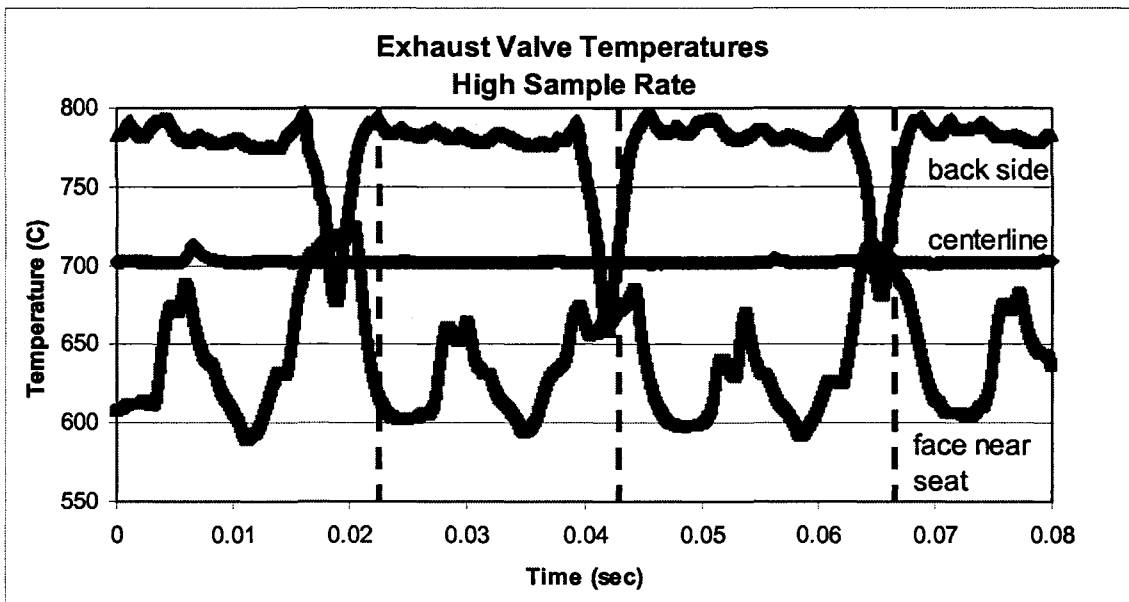


Figure 122. Exhaust Valve temperature versus time, 125kHz sampling rate, unsynchronized data

Data from the exhaust valve is much cleaner than that of the intake valve.

The nature of the data is clear from the plot. This test data was taken at 5250 RPM which corresponds to 3.5 camshaft rotations worth of data. There is a clear

difference in temperature between the front and backside of the exhaust valve. Exhaust face temperatures are lower than the backside because they are exposed to the cooling charge air for a longer period of time. The clear drops in temperature on the back side data most likely occur during valve overlap when fresh charge air is able to enter the exhaust port. Peak temperatures on the backside are slightly higher than those reported in the literature, though the overall range is similar to those reported and lower than that of racing valves. It is interesting to note that the centerline valve seat temperature stays nearly constant through the entire cycle. Valve face temperatures near the seat average 40°C lower than the temperatures at the center of the face. This is the inverse of opposite of what was seen in the steady state data. Average, minimum and maximum temperatures for the three thermocouple locations on the exhaust valve are shown in Table 37. The location numbers cited refer to the thermocouple locations shown in Figure 104.

Table 37. Minimum, maximum and average exhaust valve temperatures. 5250 RPM, WOT full load.

Location	Face Center (location 2)	Face - seat (location 1)	Backside (location 5)
Minimum	701°C	589°C	658°C
Maximum	713°C	724°C	798°C
Average	702°C	639°C	776°C

4.7 In-Engine Composite Coating Experiments

4.7.1 Introduction and Purpose

In order to provide some level of verification for the thermal analysis presented in section 2.5, a series of experiments were undertaken to assess the ability of fiber orientation and coating combinations to provide adequate thermal protection for a FRC in the combustion chamber of a running engine. In addition, an attempt was made to characterize degradation of the samples after testing. Because of the time and material involved in making a FRC valve and the challenge associated with making FRC valves from new constituent materials, it was decided that a method of testing coupon samples in the combustion chamber would be more time and cost effective. After a fair amount of trial and error, a configuration was developed which allowed testing three different samples in the engine at one time. The material and coating combinations for each sample were varied in the test matrix. Temperature measurements were made using thermocouples at the interface between FRC and coating, as well as at the back side of the sample.

4.7.2 Test Setup

In order to test coupon samples in the combustion chamber of a running engine, a test method was devised which involved drilling a stepped hole in a custom made cylinder head. Molded and coated FRC samples were placed into the stepped hole. Thermocouples were attached and the engine was run under load. Temperatures were recorded at two different locations on the sample, at

the interface and at the back-surface. A schematic of a single test sample is shown in Figure 123. A photograph of a single sample is shown in Figure 124.

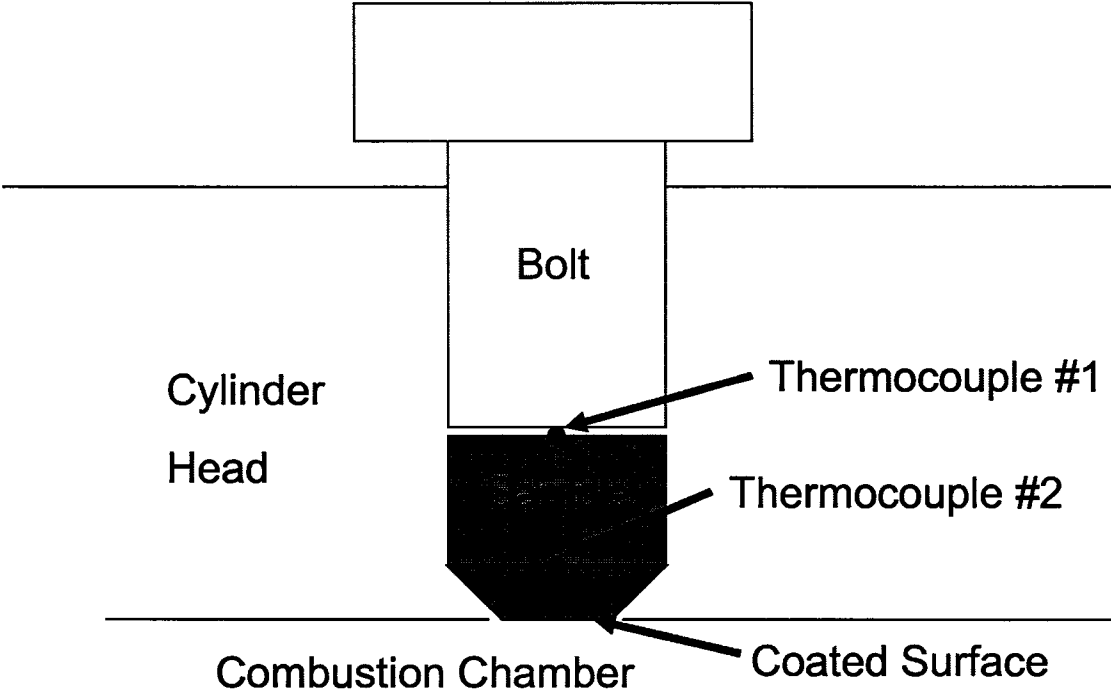


Figure 123. Schematic of coupon test setup.

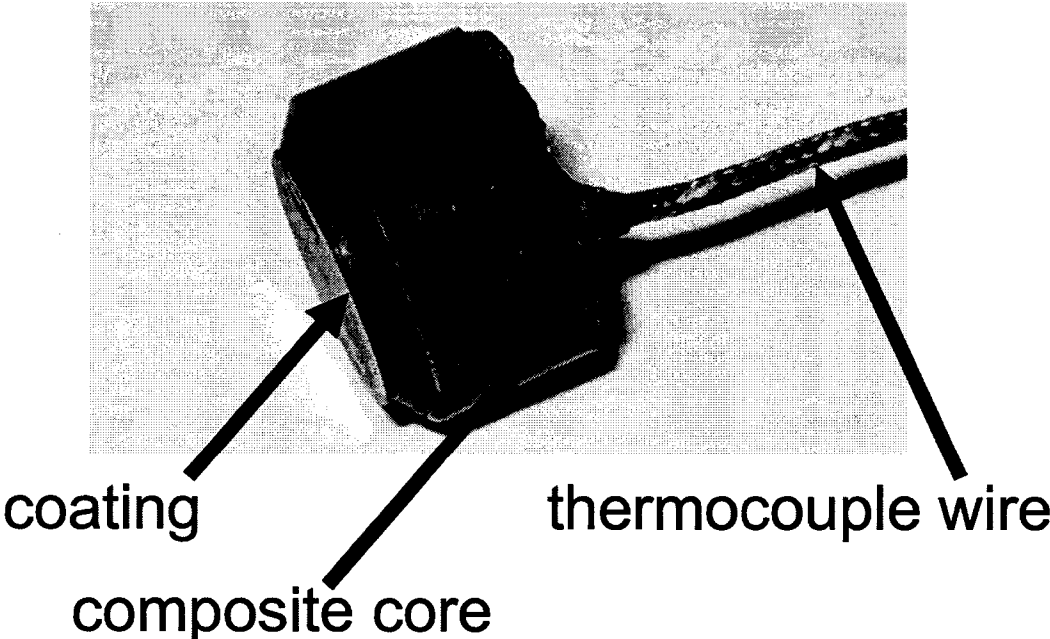


Figure 124. Photograph of a coated coupon test sample.

4.7.2.1 Test Matrix

In order to evaluate the effect of both fiber orientation and coating material on performance of the samples a test matrix was developed which varied three properties; fiber orientation, matrix material and coating material. The test matrix is shown in Table 38

In the test matrix, carbon fiber is the only fiber used. This was chosen partly because of the thermal conductivity of carbon fiber, and partly because of availability. There are three fiber orientations;

- None - no fiber (neat polymer only)
- Perpendicular - fibers are oriented perpendicular to the exposed face
- Parallel - fibers are oriented parallel to the exposed face

There are four possible coating configurations;

- None - no coating, fiber and matrix are exposed
- Stainless Steel- a stainless steel layer, 0.007 inch thick is placed on the exposed surface
- Alumina Silicate a high temperature alumina silicate disc is bonded to the sample face, thicknesses of 0.05 inch and 0.125 inch were tested
- Pyrolitic Graphite: a pyrolitic graphite disc is bonded to the sample face, thicknesses of 0.05 inch and 0.125 inch were tested

Table 38. Test matrix for in cylinder fiber orientation, matrix and coating evaluation.

Sample #	Fiber	orientation (to face)	Matrix	Coating
1	none	NA	epoxy	none
2	carbon	perpendicular	epoxy	none
3	carbon	parallel	epoxy	none
4	none	NA	epoxy	stainless steel 0.007 in
5	carbon	perpendicular	epoxy	stainless steel 0.007 in
6	carbon	parallel	epoxy	stainless steel 0.007 in
7	carbon	perpendicular	epoxy	Alumina Silicate Ceramic 0.050 in
8	carbon	parallel	epoxy	Alumina Silicate Ceramic 0.050 in
9	carbon	perpendicular	epoxy	Alumina Silicate Ceramic 0.125 in
10	carbon	parallel	epoxy	Alumina Silicate Ceramic 0.125 in
11	carbon	perpendicular	epoxy	Pyrolitic Graphite 0.125 in
12	carbon	parallel	epoxy	Pyrolitic Graphite 0.125 in
13	carbon	perpendicular	epoxy	Pyrolitic Graphite 0.050 in
14	carbon	parallel	epoxy	Pyrolitic Graphite 0.050 in
15	Al	Al	Al	Al
16	Al	Al	Al	Al
17	Al	Al	Al	Al

4.7.2.2 Sample preparation

Samples were molded in a stainless steel mold. All samples were 0.5 inch in diameter and between 0.25 in to 0.275 in thick with a 32 gauge thermocouple molded into the FRC/coating interface, or to the surface for uncoated samples.

For the manufacture of “perpendicular” fiber samples, a commercially available “100% carbon” pultruded unidirectional carbon fiber and epoxy rod with 0.5 inch outer diameter was purchased. The rod was sectioned into 0.25 inch thick discs. The discs were center drilled with a 0.050 inch diameter hole. Thermocouples were bonded into the hole using EPON 828 resin and 3140 hardener. For the purpose of modeling results, fiber was assumed to be T-300 carbon fiber.

For the manufacture of “parallel” fiber samples, a 0.25 inch thick plate of plain weave carbon fiber and epoxy was formed from 25 layers of Toray prepreg. A diamond coated abrasive hole saw was used to cut 0.4 inch diameter discs from this plate. The discs were center drilled with a 0.050 inch diameter hole. Thermocouples were bonded into the hole using EPON 828 resin and 3140 hardener. For the purpose of modeling results, fiber was also assumed to be T-300 carbon fiber.

Un-reinforced epoxy samples were made using an open mold and the same EPON 828 resin and 3140 hardener. Thermocouples were molded in place.

Samples with a stainless steel coating were made using 0.007 inch thick stainless steel. Discs were stamped from a sheet and formed to the inside

contour of the mold. Alumina silicate coated samples were made by turning discs of alumina silicate from an unfired 0.50 inch rod. Discs were then fired to reach maximum strength and service temperature. Pyrolytic graphite coated samples were made in the same way, with the exception of firing the coating material. Coating discs, fiber samples and thermocouples were then molded in place.

Because the T_g of a room temperature cured epoxy is generally relatively low, and the resulting epoxy will become soft at temperatures well below those seen inside the engine. With this in mind, epoxy samples were post cured in an oven using a progressive cure cycle that increased temperature from 50°F to 400°F in 50°F increments with a 2 hour hold at each step. Although time consuming, this succeeded in producing a sample with a much higher T_g and a noticeable increase in hardness.

4.7.2.3 Cylinder head preparation

A custom, one-inch-thick billet aluminum cylinder head was acquired from Jr Race Car Inc. in Greeley, Co. This beautiful, shiny cylinder head was then drilled with three stepped holes to allow the placement of sample. Figure 125 is a photo of the inside surface of the cylinder head with sample holes marked. Each hole is 0.40 inch in diameter, thus the exposed surface area for each sample is 0.125 in². The backside of the hole is drilled to 0.5 inch diameter with a 118° taper for seating the sample. The top (outside) of the hole is threaded with a 5/8-18 inch internal thread. Socket head hex bolts were used for mounting and holding samples in the holes and are were center drilled for routing of

thermocouple wires. This cylinder head maintains the stock compression ratio of the engine.

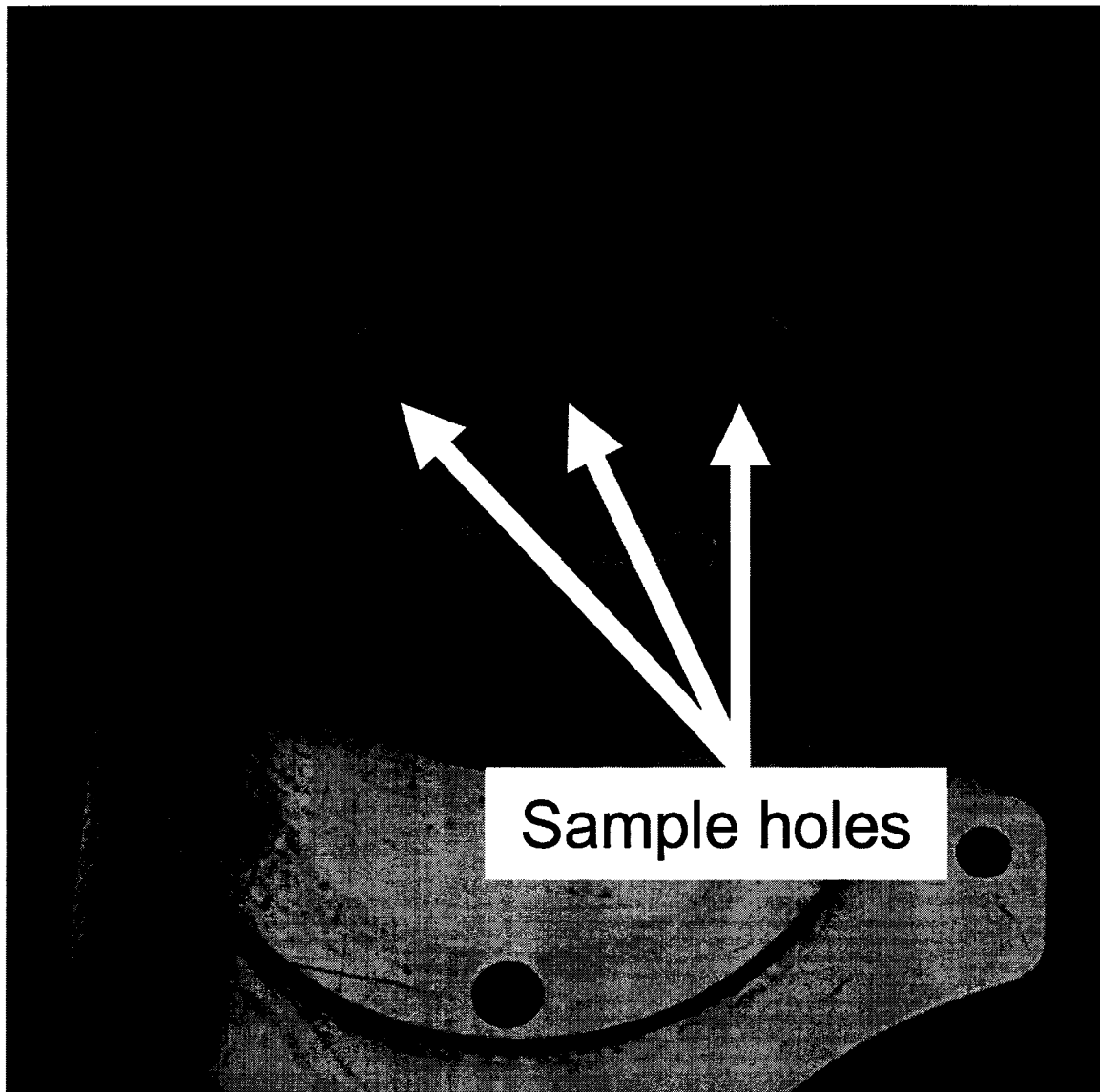


Figure 125. Modified cylinder head showing sample mounting locations.

4.7.2.4 Test Preparation

Prior to testing each sample was cleaned and weighed. A sample was placed in each hole and pressed down into the taper at the bottom of the hole. The sample is packed with conductive copper paste to fill air gaps and help with

sealing. A 5/8-18 socket head bolt is threaded into the hole, compressing the sample into the hole and sealing the hole. Thermocouple wires are threaded through a 0.01 inch diameter hole through the center of the bolt. Thermocouples are connected and the test is run.

All tests involved a five minute warm-up, followed by a one-minute run at WOT and full load after which the engine was turned off and samples were removed. If possible, samples were cleaned and weighed again to measure any weight loss due to degradation.

4.7.2.5 Data Acquisition and Instrumentation

Temperature at the FRC/coating interface and on the back side was monitored for each sample using a thermocouple. In addition, exhaust temperature was monitored for comparison. Data acquisition was done using the same National Instruments PXI 10301 chassis and SCXI 1100 thermocouple reader used for the valve testing in the previous section. Temperature was monitored continuously throughout the entire test at 100Hz sampling rate. Data was collected every 15 seconds, written to a text file and post processed once testing was finished.

4.7.3 Results and Discussion

For each sample, an estimate of material properties was made. From these material properties, the unitless values for Bi of the coating, St , of the core and Bb for the sample were calculated. Material properties used are shown in Table 39. Because sample thickness varied from sample to sample, and coating

thickness differed between materials, results were normalized for comparison. When samples of different material are compared, the unitless temperature measure Θ is used. For plots of temperature profile, the unitless length x^* is used. An example of the raw data for the alumina silicate coated samples is shown in Figure 126.

Table 39. Material properties used for in-engine coating analysis.

Material	Axial Thermal Conductivity (W/mK)
Carbon-epoxy parallel to surface	35
Carbon-epoxy perpendicular to surface	140
Epoxy	0.75
Stainless Steel	15
Alumina Silicate Ceramic	1.26
Pyrolitic Graphite	130

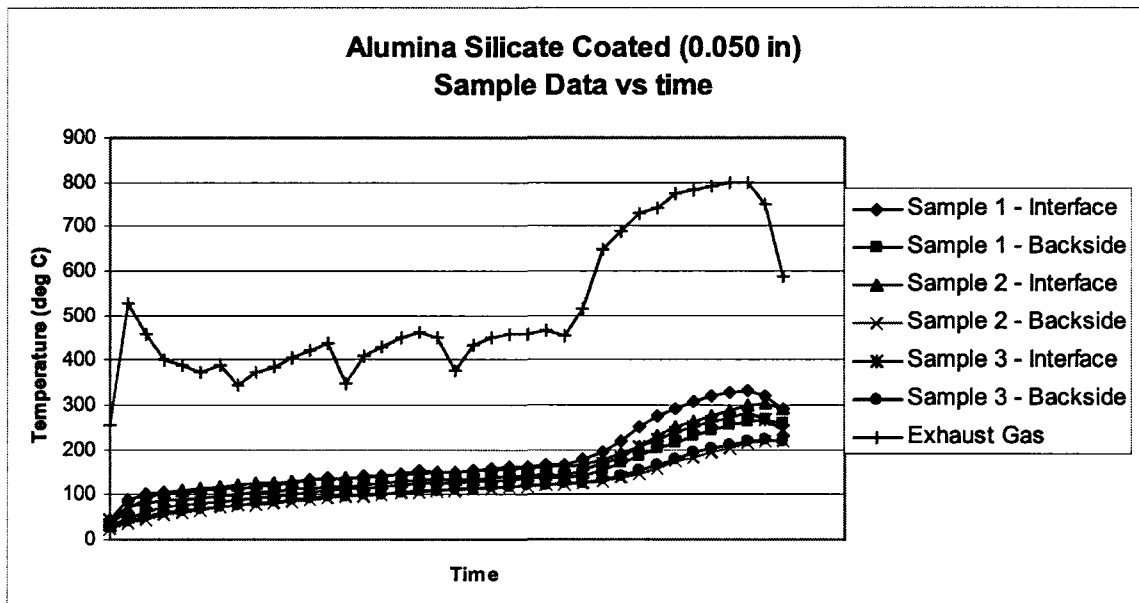


Figure 126. Raw data, temperature vs.. time for alumina silicate coated samples.

4.7.3.1 Effect of fiber orientation on temperature distribution

Data from all tests were analyzed and plotted versus exhaust gas temperature (EGT). The Temperature drop across the composite sample was calculated by subtracting the back-side temperature from the interface temperature. These results are plotted in Figure 127 for uncoated samples, Figure 128, for samples coated with 0.007 in of stainless steel coating, and Figure 129 for samples with 0.050 alumina silicate ceramic coating. In these plots, a lower value is generally better, because it indicates less of a temperature gradient across the core portion of the sample.

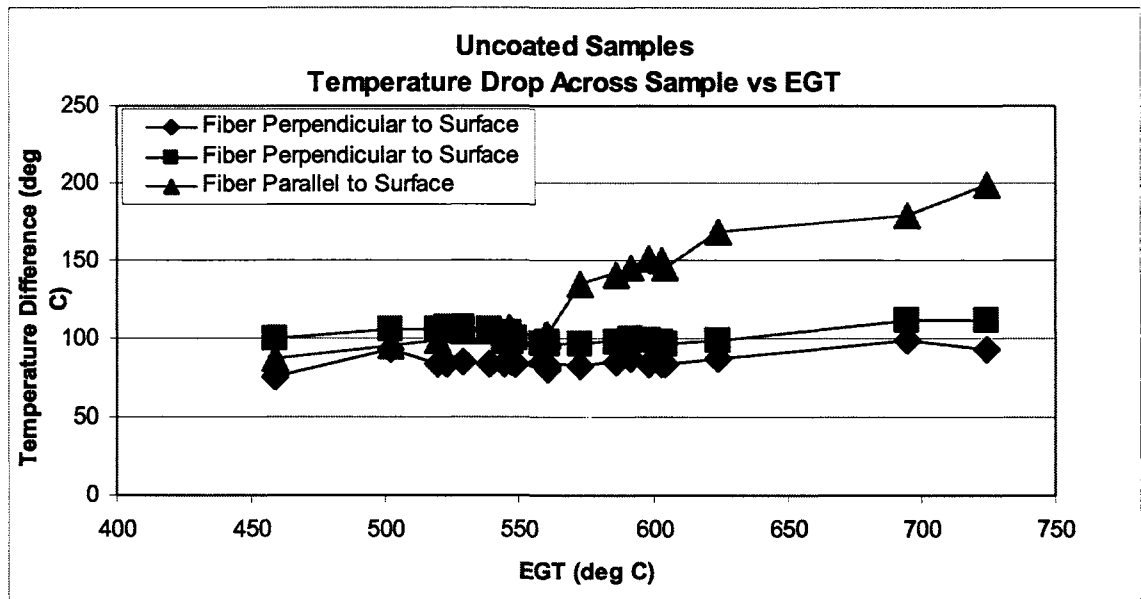


Figure 127. Effect of fiber orientation on temperature drop across the samples for uncoated samples.

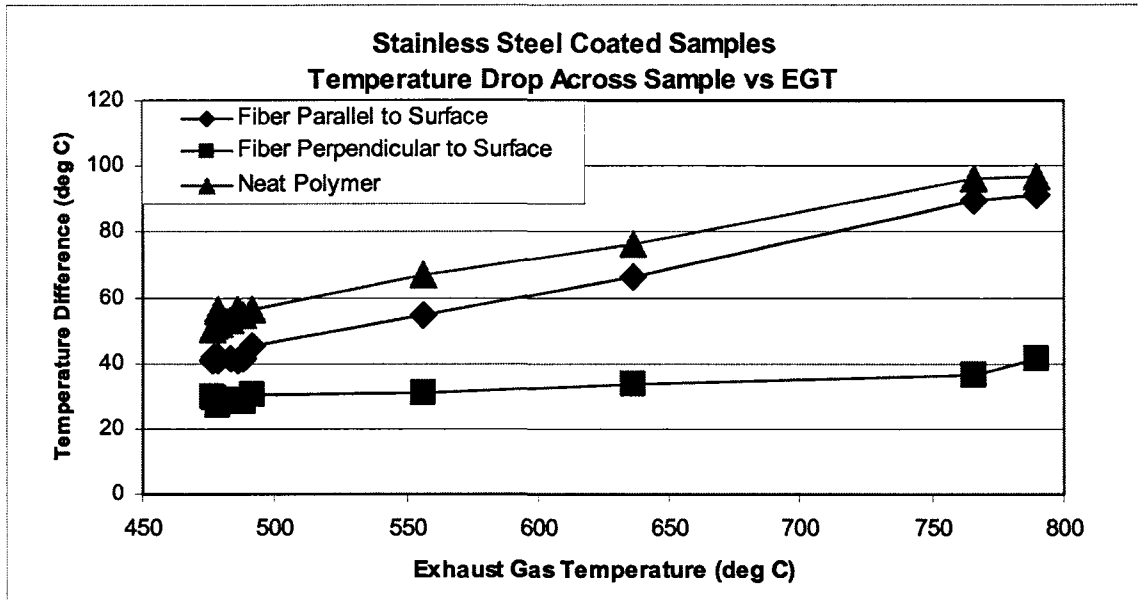


Figure 128. Effect of fiber orientation on temperature drop across the sample for stainless steel coated samples.

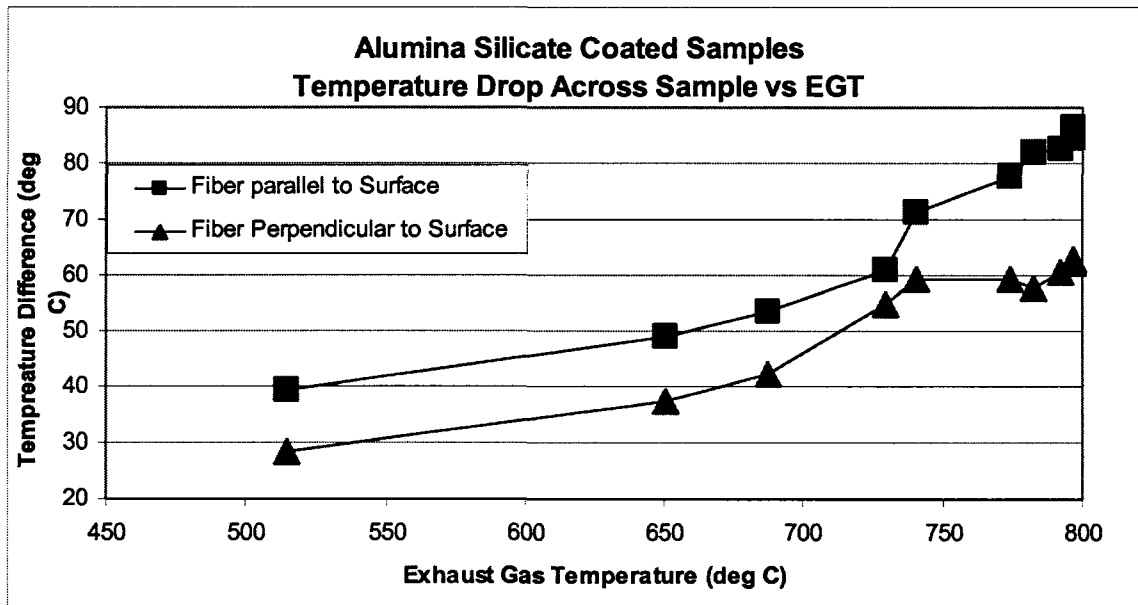


Figure 129. Effect of fiber orientation on temperature drop across the sample for alumina silicate coated samples.

For each of the sets of samples, the temperature difference increases with EGT as expected. Those samples with carbon fiber oriented parallel to the sample surface (perpendicular to the axial heat path) consistently have a larger

temperature difference across the sample than those with fibers perpendicular to the face (parallel to the heat path). This agrees with the results presented in section 2.5 and is consistent with analysis that shows a higher conductivity results in a lower temperature gradient and smaller temperature distribution across the sample. Taking a close look at Figure 128, it can be seen that the sample with fibers parallel to the surface performs only marginally better than the un-reinforced (neat) polymer.

4.7.3.2 Effect of B_b on Interface temperature

For each of the data sets, the peak EGT point was located, from this data, interface recorded. For each sample, surface temperature was assumed to be equal to EGT. Measured interface temperature vs. B_b was plotted for verification of the previous analysis and is shown in Figure 130. Thus, the data presented is the measured temperature at the boundary between the coating and core material. The data points plotted encompass the entire range of test data. The solid black line is a trend line fitted to the data and the dashed black line highlights the location of $B_b = 1$. This plot shows the same trend discussed in section in 2.5.3.1.3. That is, for $B_b < 1$, interface temperature is higher, while for $B_b > 1$, interface temperature is lower. This data was taken at WOT and peak EGT.

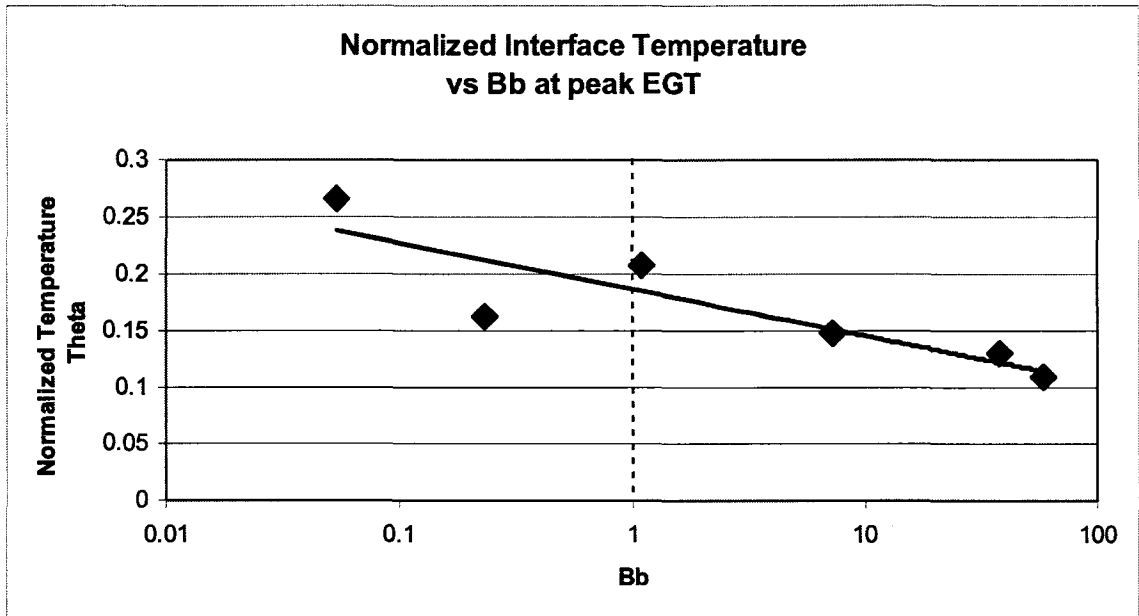


Figure 130. Interface versus Bb at peak EGT.

Because temperatures typically had not reached a steady state at the point test where maximum EGT occurred, this data analysis process was repeated using a test point with lower EGT, where the engine temperatures had reached steady state. This was typically the last data point at idle speed before the throttle was opened and load was applied. Figure 131 shows steady state interface temperature vs.. Bb. Again, the solid line is a curve fit to the data, the dashed vertical line highlights the location of Bb = 1. In order to compare this experimental result with the thermal analysis presented in section 2.5, the analysis and raw experimental data was plotted on the same plot. This plot is shown in Figure 132. The two upper curves, labeled L1/L2 = 200 and L1/L2 = 1 are the bounding curves for the geometry (aspect ratios) of the experimental samples.

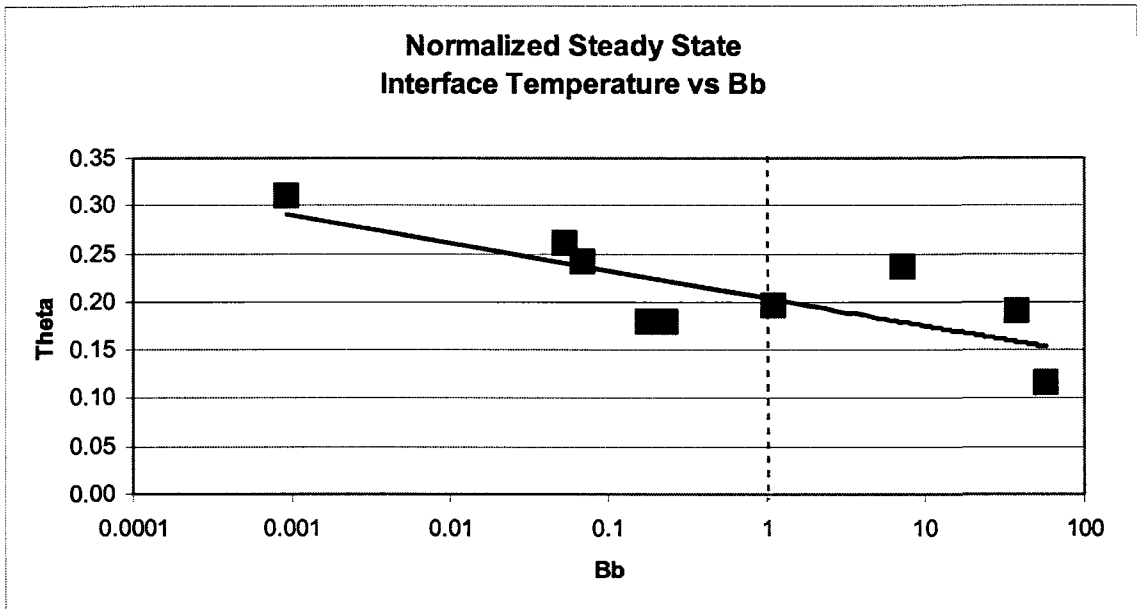


Figure 131. Steady state Interface temperature vs. Bb.

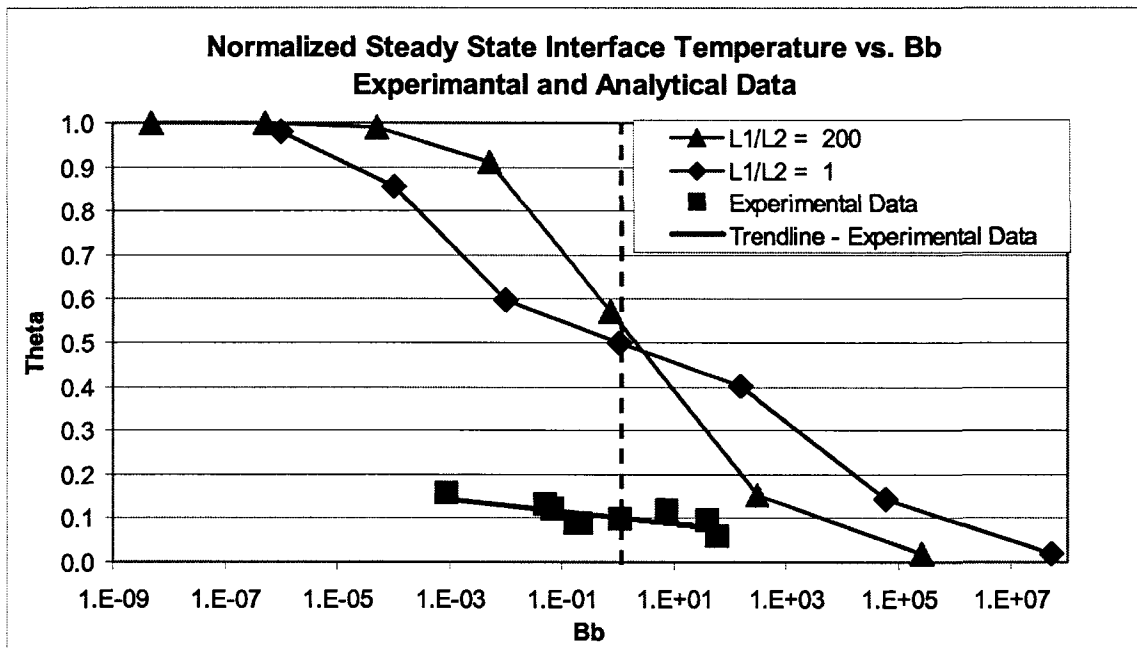


Figure 132. Bb vs.. interface temperature for analysis results and experimental test results.

Although the height of the curve is significantly lower than that presented in the analysis, the downward trend still exists. Adjusting either the assumed heat transfer coefficient in the analysis downward, or the assumed surface

temperature (equal to the EGT) for the experimental cases downward would bring the experimental and analytical curves together. To illustrate this point, the Analysis curves were adjusted downward by a factor of five. This data, combined with the experimental results, are shown in Figure 133. $Bb = 1$ is highlighted by the vertical dashed line and the trend line fitted to experimental data is the thick solid line.

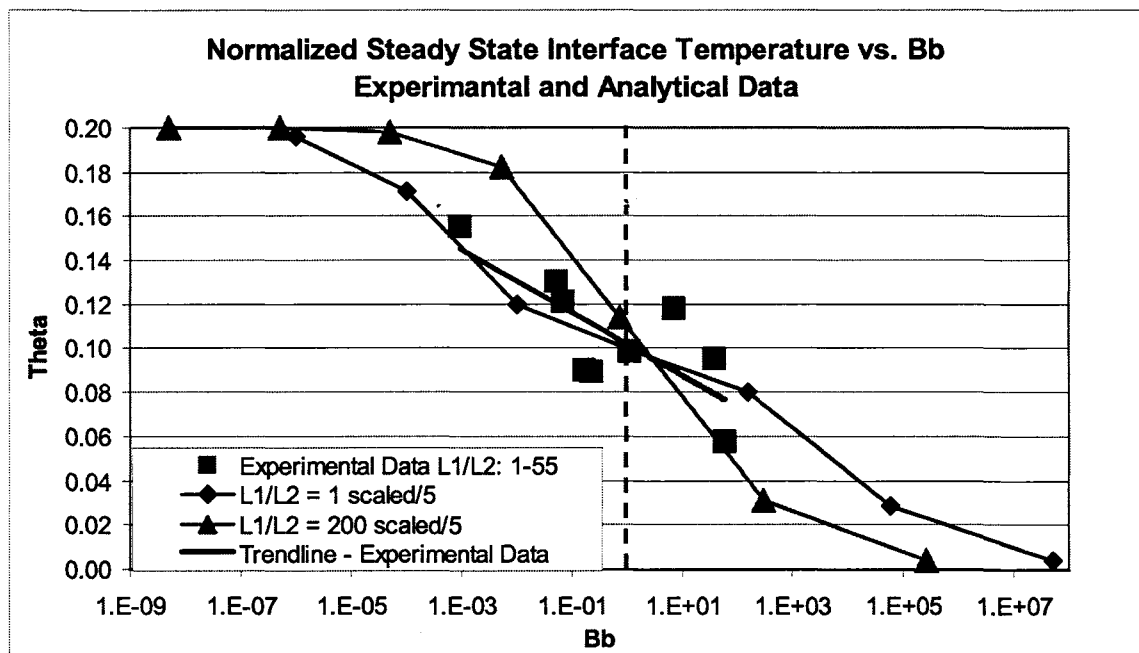


Figure 133. Interface temperature vs.. Bb, scaled analysis results and experimental data.

From Figure 133 it is clear that the trend line for the experimental data fits nicely between the two bounding curves from the analysis data. This comparison of experimental and analytical data confirms the analysis presented earlier. This data shows that using the unitless value for Bb as a predictor of relative temperature distribution in a solid material with a coating. It also shows that interface temperature, the temperature at the boundary between the coating and

core material, can be predicted based on the boundary conditions and the unitless value for B_b .

4.7.3.3 Other observations

One other significant observation was noted during disassembly of the cylinder head after testing the samples. For the samples with a stainless steel coating, the epoxy at the interface was degraded to the point that the coating material was no longer bonded to the core FRC. It appears that the FRC matrix material was exposed to temperatures higher than the degradation temperature at the interface. This is consistent with the idea that a conductive coating will transmit heat directly to the core, although these samples did not show the highest interface temperature. These samples also had the thinnest coating, which should increase the interface temperature as well. No other samples experienced this type of failure.

4.8 Discussion of Experimentation and Testing Results

Static structural proof load tensile testing of net shape FRC valves has shown the valves behavior is elastic under the loads seen during normal engine operation. Failure loading has shown a graceful, progressive failure mode that involves fiber shear-out at the keeper. Motored testing has shown that the valves can withstand dynamic loading without experiencing failure.

In engine fired testing has demonstrated that a net-shape resin transfer molded FRC valve can withstand the structural loading experienced in the combustion chamber over the entire RPM range. A FRC intake valve was run at

1700-1900 RPM under low load conditions for 400 consecutive minutes, more than ten times the previously published performance for a FRC valve. High engine load conditions caused thermal degradation in the face of the valve.

Temperature measurement of steel valves in a running engine has shown that the test engine valve temperatures are in the range of or slightly higher those reported in the literature for gasoline engines. Intake valve temperatures averages roughly 370°C – 380 °C at WOT and full load. Exhaust valve temperatures at WOT and full load are between 600°C and 800 °C depending on location. It is unclear from comparison of the steady state and high sampling rate data if the center of the exhaust valve face runs hotter or cooler than the valve seat. Arguments for either case could be made. High sampling rate measurements showed clearly the fluctuation in temperature in both the intake and exhaust valves. Both intake and exhaust valve temperatures fluctuate over 100°C depending on the location in the valve.

In-engine coupon sample testing of FRC and coating combinations has verified the thermal analysis presented in section 2.5. It is clear from the data that fiber orientation plays a major role in governing the temperature distribution across the FRC sample. Careful selection of coating materials can also substantially lower the interface temperature between coating and core FRC. The trend of interface temperature vs.. unitless ratio B_b has been verified with the analysis presented in section 2.5. Experimental data has confirmed the analysis showing that interface temperature decreases with increasing values of B_b . The experimental data trend fits well with analytical data although

magnitudes of the measured temperatures are significantly lower than those in the analytical model. This is most likely due to the selection of boundary conditions for the model and the very high value for the convective heat transfer coefficient used. It has been shown that the ratio Bb is useful for predicting the interface temperature as a function of the material properties of the coating and core material. This also implies that given the appropriate boundary conditions, the relative temperature gradient in the coating core materials can also be predicted well. This opens up a number of design possibilities for extending the usable range of FRC materials into the combustion chamber. This line of testing and analysis has shown that combinations of fiber orientation and coatings can be used to enable the use of FRC components in the in-cylinder environment.

5 Dissertation Discussion

With the stated goal of extending the usable range of FRC materials for use in the combustion chamber of an IC engine, extensive literature review, modeling and analysis, manufacturing process development and experimental testing have been accomplished.

“Structurally sound, one-piece, near net shape molded fiber reinforced composite IC engine valves can overcome the manufacturing complexities seen in previous attempts to reduce valve train reciprocating mass by using composite materials. Further, it is possible to extend the useable range of one-piece net shape resin transfer molded polymer matrix, fiber reinforced composite materials by using a combination of coatings and tailored fiber placement to withstand the structural and thermal conditions in extreme thermal oxidative environments such as the combustion chamber of an engine.”

5.1 Literature Review

An in-depth literature has been conducted that covers;

- Engine efficiency
- Documented FRC use in internal combustion engines
- Previous attempts at FRC valves for IC engines
- Resin transfer molding
- High temperature composite materials

- Processing of the high temperature polyimide, PETI-RFI
- One and two dimensional modeling of FRCs under transient thermal conditions
- Advances in thermal management of FRCs
- Advances in thermal management of FRCs with coatings
- Measurement of valve temperatures in a running IC engines

In short, many, many FRC engine components have been developed, however FRC components have had limited use in the combustion chamber of engines due largely to the difficult requirements associated with withstanding the harsh thermal, oxidative and dynamic structural loads experienced. A great deal of work has been done in modeling the thermal performance of FRCs for other applications such as spacecraft and electronics packaging. Little work has been done with regards to understanding the behavior of FRCs with coatings in an extreme transient thermal environment such as the combustion chamber. This work begins to fill that void showing analytically and experimentally that it is possible to develop a component that can meet the structural and thermal conditions that a part is exposed to in an IC engine combustion chamber.

5.2 Modeling and Analysis

Using basic mechanics, a prediction of mass reduction was made for a small aircraft engine. Using direct substitution of FRC materials for existing components, it is predicted that engine mass can be reduced by roughly 55%. A 72% mass reduction for the reciprocating mechanism is possible. Redesigning the system to take advantage of the reduced inertial loads enabled by FRC

components may enable even further mass reduction. A conservative estimate using this shows 90% mass reduction of reciprocating mass may be possible. Mass reduction in this range was demonstrated with the development of a net shape molded FRC intake valve for an IC engine that had a mass just 19% of the steel valve it replaced, a 81% mass reduction.

In development of this FRC intake valve, viable structural model for a FRC valve has been designed. Several new, novel ideas have been incorporated into this design to aid in manufacture with the goal of high-volume production. The two previous attempts at FRC valves were multi-part components bonded together. Features of the new design include:

- The fiber is designed to be a one-piece continuous fiber preform
- The finished valve is a net-shape resin transfer molded valve, minimum machining is required once removed from the mold.
- From the analysis and from follow on testing, the structural design is at least equal to that of a steel valve.

Initial transient thermal analysis using a one-dimensional flat plate with convective heat transfer showed that the decreased conductivity of the FRC matrix material causes a sharp temperature gradient near the exposed surface, increasing surface temperature. Initial results suggest that orienting conductive fibers along the heat path will help to alleviate this problem and that a temperature distribution similar to that in the steel component is attainable using FRC materials. This was later verified with in-cylinder testing of FRC samples.

A comprehensive analysis has been undertaken to quantify the effects of coating and core material combinations on the thermal performance of FRCs with axial and radial heat paths. Specific emphasis has been placed on reducing the core temperature of the FRC material.

A novel method of quantifying performance of core/coating combinations has been developed which compares the ratio the heat carrying capacity of the coating to the heat carrying capacity of the core material under convective heat transfer conditions. This ratio is referred to as Bb and is defined as:

$$Bb = \left(\frac{k_1}{L_1} \right) \left(\frac{L_2}{k_2} \right) \left(1 + h \frac{L_2}{k_2} \right) \quad \text{Equation 31}$$

Analysis results have shown that for combinations of coating and core material, $Bb < 1$ will result in a higher interface temperature and that for $Bb < 0.1$, interface temperature is effectively equal to surface temperature. In these cases, the coating material effectively transmits heat to the core. For $Bb > 1$, a large temperature gradient occurs in the coating material, effectively insulating the core material from the heat source. As seen in the one-dimensional analysis, the highly orthotropic nature of FRCs greatly affects the thermal response of the material. While orienting fibers along the heat path reduces the temperature gradient in that direction, a FRC with a large ratio of conductivities in the orthogonal directions will experience a steep temperature gradient in the direction of the lowest conductivity, typically orthogonal to the fiber direction. This can again lead to high surface temperatures and high internal thermal stresses.

The new methodology described allows the designer to more quickly focus the hone the design than by running numerous complex simulations of specific materials. This design methodology has been applied to the thermal design of a FRC intake valve. Initial estimates show that, by changing fiber type and volume fraction, and by adding a metallic coating, the peak temperature experienced by the matrix material can be reduced by several hundred degrees, making the FRC valve thermally viable.

An initial thermal management for the FRC valve face has been presented which should reduce surface temperature and reduce coating interface temperatures by roughly 80%. This solution involves increasing the conductivity of the FRC in the face, as well as adding a stainless steel barrier coating on the face of the valve.

5.3 Process Development

A great deal of work has been done in developing the initial manufacturing process for a net-shape molded FRC intake valve. A process has been developed and demonstrated in which a single-piece fiber preform is used to fabricate a net-shape fiber reinforced intake valve using resin transfer molding. Although RTM of composite materials is not a new process, several new and unique advancements have been made.

A novel method of positively clamping and locating the fiber preform has been devised. Two concentric rings are press-fit with the end of the fiber preform between them. This positively locates the fiber, prevents fiber pullout, and allows

injection of the resin down the center of the fiber preform when the mold is filled. This increases the wetting of the fibers in the mold.

A method has been developed whereby prepreg inserts using PETI-RFI in the thermoplastic stage are manufactured. The inserts are placed into the mold prior to injection. During the RTM process, the insert is incorporated into the molded part. Co-curing the parts in the mold results in a net shape part. This process could also be extended by inserting the additional functional part after the RTM process, but before the final cure cycle. Any number of different functional inserts could be added to the part this way.

A working mold has been developed and demonstrated. Three iterations of the valve mold have been developed, each with successive improvements. The final two designs incorporate a device for compressing fibers into the valve face, thereby increasing the fiber volume fraction and part strength. This device also serves as a perimeter vent. The latest mold design incorporates a modular structure that allows the manufacture of both an intake and exhaust valves of different geometries by swapping the two pieces that form the valve face. A manufacturing process has been demonstrated and over 20 net-shape, RTM valves have been successfully produced.

Extensive work has been done in relation to the processing of PETI-RFI. Previously described efforts to process PETI-RFI composites focused on vacuum hot pressing. Extensive material characterization using DSC, TGA and DTMA has been performed with a focus on eliminating the formation of voids during processing and curing. Additional cure experiments were performed using a

vacuum/pressure chamber and hot press with the goal of adding flexibility and minimizing void formation.

DTMA experiments showed the minimum viscosity for PETI-RFI occurs between 220°C and 240°C with a rise in viscosity before 280°C. This differs from previously published results and indicates a minimum viscosity at a slightly lower temperature.

DSC experiments showed that a slower ramp rate of 1°C /min to the peak cure temperature may reduce void formation. This is done by slowing and extending the cure reaction. The cure reaction begins above 300°C and the reaction rate peaks near 350°C. Lower final cure temperatures may also reduce void formation for the same reasons. No interactions were found between the PETI-RFI polymer, carbon fiber and mold release.

T_g of PETI-RFI is near 242°C for peak cure temperatures between 330°C and 390°C. In this temperature range, the polymer is insensitive to peak cure temperature. TGA showed PETI-RFI is stable to 400°C. This is lower than that of the base material, PETI-5, but still relatively high for a polymer.

Vacuum/pressure chamber experiments showed that degassing is critical to the processing of polymer without voids. Once degassed, PETI-RFI can undergo multiple melt-freeze cycles without affecting the final cured product. Any processing that entrains air will require additional degassing to avoid void formation in the final product.

As a result of this work, three additional methods of processing carbon fiber reinforced PETI-RFI have been documented. These methods are; melt

processing of neat polymer with final cure under N₂ gas pressure, hot pressing of neat polymer, and resin transfer molding of fiber reinforced polymer. Hot pressing fiber reinforced PETI-RFI at ambient air pressure in an unevacuated mold produced samples of high porosity due to the presence of air entrained in the manufacture process.

All three manufacturing methods can be accomplished without the use of a high temperature vacuum bag and without the extremely high pressures described in previous work. Additional flexibility has been demonstrated by allowing intermediate cooling of the resin between the degassing, forming and curing cycles. All three of these processes have been shown to produce parts that have excellent consolidation and void content at or below 3% by area.

5.4 Experimentation and Testing

Static structural proof load tensile testing of net shape FRC valves has shown the valves behavior is elastic under the loads seen during normal engine operation. Failure loading has shown a graceful, progressive failure mode that involves fiber shear-out at the keeper. Motored testing has shown that the valves can withstand dynamic loading without experiencing failure. These series of tests have demonstrated that a net-shape molded FRC component can withstand the dynamic structural loads required for operation in the internal combustion engine.

In engine fired testing has demonstrated that a net-shape resin transfer molded FRC valve can withstand the structural loading experienced in the combustion chamber over the entire RPM range. A FRC intake valve was run at

1700-1900 RPM under low load conditions for 400 consecutive minutes, more than ten times the previously published performance for a FRC valve. High engine load conditions caused thermal degradation in the face of the valve.

Greater understanding of the thermal requirements for in combustion chamber operation was gained through temperature measurement of steel valves in a running engine. These tests have shown that the test engine valve temperatures are in the range of or slightly higher those reported in the literature for gasoline engines. Intake valve temperatures averaged 370°C – 380 °C at WOT and full load. Exhaust valve temperatures at WOT and full load are between 600°C and 800 °C depending on location. It is unclear from comparison of the steady state and high sampling rate data if the center of the exhaust valve face runs hotter or cooler than the valve seat. Arguments for either case could be made. High sampling rate measurements showed clearly the fluctuation in temperature in both the intake and exhaust valves. Both intake and exhaust valve temperatures fluctuate over 100°C depending on the location in the valve.

In-engine coupon sample testing of FRC and coating combinations has verified the transient thermal analysis presented in section 2.5. It is clear from the data that fiber orientation plays a major role in governing the temperature distribution across the FRC sample. Careful selection of coating materials can also substantially lower the interface temperature between coating and core FRC. The trend of interface temperature vs.. unitless ratio Bb has been verified with the analysis presented in section 2.5 although magnitudes of the temperature are significantly lower than those in the model. This is most likely

due to the selection of boundary conditions for the model. This ratio is useful for predicting the interface temperature as a function of the material properties of the coating and core material. This opens up a number of design possibilities for extending the usable range of FRC materials into the combustion chamber.

Experimentation with has shown that combinations of fiber orientation and coatings can be used to enable the use of FRC components in the in-cylinder environment.

5.5 Recommendations for Future Work

In order to complete the demonstration of FRC valves for IC engines, and to extend this methodology to other components exposed to the combustion chamber, such as the cylinder, piston and rings, additional analysis and experimentation will be required. Some suggestions for research along these lines follow.

A detailed two or three dimensional transient thermal model of the steel valve in the operating engine should be developed with specific emphasis placed on refining the boundary conditions to match the experimental results achieved. Having this model available would be indispensable in evaluating the performance of fiber orientations and coating in the confines of the actual valve geometry. It would also allow a more optimized design for the valve, enabling further mass reduction. Also not discussed, but of significance is the effect of heat transfer due to radiation. Most analysis to date has neglected this effect, yet a valve running at 800-900° must be greatly effected by heat radiation of heat both into and out of the valve face.

An alternative which may be even more viable for in-engine components is the concept of a multi-layer surface for increased thermal performance. For valves and pistons two potential options are immediately apparent. First is a thicker conductive, perhaps metallic outer coating with an insulating inner coating covering a FRC core. This would provide a surface heat path, while still lowering the inner temperature of the core. This could be accomplished a number of ways. The second is the inverse of the first, an insulating outer coating, followed by a conducting second coat, covering the FRC core. This would provide the same advantage as the first option but with less heat flux allowed. This might be a more viable option for a component such as a piston or combustion chamber liner.

Inherent in the success of all of the FRC designs is the temperature of the heat sink, either in the models presented or the in the test engine. Lowering the temperature of the sink will lower the overall temperature of the entire system. Modern, liquid cooled engines have coolant operating temperatures of roughly 100°C. The current air cooled test engine reaches cylinder head temperatures of over 300°C. Simply switching to a small, water cooled test engine would have dramatic effects on component temperatures, and be more relevant in extending the technology to production engines. However, for these same reasons the current engine would continue to be a challenging test bed.

Work towards the goal of using more conventional temperature range polymers. These are simpler to work with, more readily available, and less

expensive. There are many more polymers that are structurally sound at 100°C (like Nalgene™ bottles) than at 400°C.

Valve rotation is important for number of reasons in a running engine. For reasons that are not understood, the FRC valves did not rotate during operation. Figuring out what causes this effect and how to guarantee rotation in the FRC valve would help considerably. The test setup for this research already exists in the motored test rig.

As mentioned in a number of places in this work, the extreme temperatures experienced by exhaust valves represent a much more difficult problem, especially in using polymer matrix composites. The most logical next step in pursuing this methodology for exhaust valves is to make the leap to ceramic matrix composite materials. There are a number of commercially or near-commercially available products that use a pre-ceramic polymer system with relatively low viscosities to produce a molded ceramic or ceramic matrix composite. If such products have a low enough viscosity, the process development work presented here could be easily transferable to manufacture of a fiber reinforced ceramic exhaust valve. Although mass reduction would not be quite be as great as for the PMC valve, it would still be significant.

6 Conclusions

Recall that the stated hypothesis for the research presented was:

“Structurally sound, one-piece, near net shape molded fiber reinforced polymer matrix composite IC engine valves can overcome the manufacturing complexities seen in previous attempts to reduce valve train reciprocating mass by using composite materials. Further, it is possible to extend the useable range of one-piece net shape resin transfer molded polymer matrix, fiber reinforced composite materials by using a combination of coatings and tailored fiber placement to withstand the structural and thermal conditions in extreme thermal oxidative environments such as the combustion chamber of an engine.”

In demonstrating this hypothesis to be true, a number of accomplishments and contributions have been made. An in-depth literature review has shown that FRC engine components have been demonstrated, but have not been successful in the combustion chamber due to the extreme thermal and oxidative and structural loads experienced. The two previous attempts at FRC valves were both multi-piece designs. Both involved either potential or demonstrated structural failures at the valve transition areas and acknowledgements of the need for thermal protection. Through a combination of modeling and experimentation, both the structural and thermal challenges of previous FRC valves have been overcome. Structural performance of a FRC valve has been

demonstrated in a running engine. Thermal performance of a coated FRC sample has been demonstrated in the combustion chamber of a running engine.

Accomplishments in modeling and analysis to address the structural and thermal oxidative issues identified in previous FRC poppet valve research:

- Using structural analysis, FRC mass reduction over steel components was predicted to be 70% -90%.
- A structural design for single piece-net shape molded intake valve was developed using a one-piece fiber preform. Analysis indicates a structural solution to failures noted by previous researchers.
- One-dimensional transient thermal analysis showed that FRC fiber architecture and orientation can be configured to decrease surface temperature and tailor temperature profile across a part. Based on the assumed engine boundary conditions, surface temperature was reduced by an estimated at 77°C from the initial FRC valve design.
- Detailed transient thermal analysis of FRC materials and coatings was developed to generate new guidelines for fiber orientation and selecting coating materials selection based on the unitless value, Bb.

Accomplishments in process development:

- A manufacturing method was developed for the one-piece fiber preform that addresses the process needs of resin transfer molding in addition to structural and thermal criteria. Further, the preform

developed allows optimal use of commercially available fiber forms
– unidirectional tow and braided tube.

- A series of molds were developed to allow RTM of FRC intake valves, including a modular mold which allows the manufacture of two different geometry valves from a single set of mold pieces.
- A process was developed for RTM of FRC valve using the developed carbon fiber preform and the high temperature polymer PETI-RFI as the matrix material.
- A novel method of positive locating the fiber preform in the mold using two concentric, interference fit rings was developed. This allowed injection of resin through the center of the fiber preform and eliminated migration of the preform within the mold under resin transfer pressures.
- An additional device was developed to allow compression of fibers into the valve face, increasing fiber volume and strength on the face.
- A method was developed for inserting functional inserts, in the form of fiber prepreg, into the mold prior to resin transfer molding, increasing manufacturing flexibility. This additive technique also enables the insertion of separate valve face materials as required.
- Development of detailed processing parameters for PETI-RFI was accomplished, including three new methods of processing which do not require an autoclave or vacuum bag. Additional

recommendations are made for reducing porosity of the polymer during the cure cycle of PETI-RFI.

Experimental accomplishments:

- Static structural testing has shown that the FRC valve performance is sufficient for operation under the most extreme loading conditions seen in the engine. Failure testing has shown that the failure mode of the FRC intake valve is graceful.
- Dynamic motored testing has shown that the valve design is able to withstand dynamic loading under running conditions.
- In engine fired testing of a FRC valve has set a new bench mark for FRC valve performance and demonstrated that a polymer matrix FRC valve can operate in the combustion chamber. Testing in a fired engine continuously for more than 400 minutes and in excess of 1,000,000 cycles without failure has demonstrated the potential durability of one-piece FRC valves.
- In engine steady state temperature measurements have been made of the cylinder head, valve seats, intake valve, and exhaust valve which have shown that operating temperatures for the test engine are roughly 370°C - 380°C for the intake valve and 600°C – 800°C for the exhaust valve.
- High sampling rate temperature measurements of steel intake and exhaust valves in a running engine have shown temperature

fluctuations in the face of the valve to be on the order of 100°C throughout the cycle.

- In-engine testing of FRC and coating samples has shown that the use of the unitless B_b is appropriate for predicting interface temperature and temperature profile across the sample.
- In engine static sample testing has also shown that fiber orientation has a strong effect on the temperature distribution across the sample. A 100°C temperature difference was measured between otherwise identical uncoated samples just by changing fiber orientation. For coated samples, a 50°C temperature difference was measured as an effect of changing fiber orientation.
- In addition, in-engine sample testing has shown that the appropriate combination of polymer matrix FRC and coating is capable of withstanding the thermal environment in the combustion chamber. Fiber and coating combinations have been demonstrated that reduce the peak temperature of the FRC core material by 100°C from the uncoated samples.

Most significant among these accomplishments is the development of the unitless ratio B_b . This ratio is defined as $B_b = B_i/St$, where B_i is the ratio of thermal resistance on either side of the outer surface, and St is the ratio of thermal resistance on either side of the coating-core interface. Defining this ratio allows accurate prediction of the interface temperature between the coating and core material. As a result, the temperature distribution and temperature

gradients in both the coating and core material can be accurately predicted. This is a straightforward calculation and does not require the use of any complex analyses. Analysis has shown that, for values of $Bb < 1$, interface temperature is high, and approaches the surface temperature of the part. The largest temperature gradient is in the core of the material. For values of $Bb < 1 \times 10^{-4}$, the normalized interface temperature $\Theta > 0.9$. For values of $Bb > 1$ there is a large temperature gradient in the coating. The core temperature approaches a uniform, lower temperature. For values of $Bb > 100$, the normalized interface temperature $\Theta < 0.2$.

This in depth analysis and prediction has been verified through in-engine testing of coating and core material combinations. The dependence of interface temperature on the ratio Bb has been shown to be accurate. Scaled analysis data fits very well with experimental trend line. Experimental data shows that, for values of $Bb < 0.001$ normalized temperature $\Theta > 0.3$. For values of $Bb > \sim 80$ normalized temperature $\Theta < 0.15$. This analysis and testing has shown that appropriate FRC and coating architecture can be used to lower the core temperature of the FRC to acceptable limits, allowing operation in the combustion chamber.

Through a combination of structural analysis, thermal analysis, process development, and experimentation, a net shape molded FRC component has been demonstrated that is capable of operating under the dynamic structural loading seen in the IC engine reciprocating mechanism. A manufacturing process has been developed and demonstrated to enable the production of one

piece FRC valves which meet the structural requirements, and have been demonstrated to run in an engine. The manufacturing process developed is based on processing technology proven in moderate to high volume composites production. Thermal analysis and experimentation has shown that FRC components with polymer matrix material can withstand the thermal oxidative environment seen in the combustion chamber. These facts, when combined show that a net shape molded FRC component can withstand the demanding structural and thermal loading exposed to in the combustion chamber of an internal combustion engine.

References

1. DeMeuse, Mark T. "High temperature polymer blends: an overview of the literature." *Polymers for advanced technologies* 6.2 (1995):76-82.
2. Beckmann, H, Hans-Dieter. "Fiber Reinforced Plastics Move Inside the Engine." *SAE journal of automotive engineering* 93.5 (1985):34-41.
3. Noguchi, M, M.. "Status and prospects for metal matrix composites in Japan." *Key engineering materials* 127.1 (1997):153-164.
4. Baker, A, A. R. "Ceramic and Composite Materials for Precision Engine Components." *Materials & design* 8.6 (1987):315-323.
5. Ashley, S, Steven. "Engine makers tap carbon-carbon pistons." *Mechanical engineering* 116.5 (1994):60-61.
6. Buchman, A, Alisa. "Molded carbon-carbon composites based on microcomposite technology." *Applied composite materials* 6.5 (1999):309-326.
7. <http://www.matweb.com/>
8. Loichuk, L, L. "Chemical Resistance of Graphited Plastic DG-2." *Chemical and petroleum engineering* 19.3 (1983):159-161.
9. Kuch, I, I."Advanced Composites in Vehicles - Current State and Future Prospects for Applications." *European Conference on Composite Materials.* (1990).
10. Wood, S, Stuart. "Breakthrough in Lightweighting: Composite Engine Components." *Modern plastics* 65.3 (1988):42-46.
11. Floeck, J, J.. "On the friction and wear behaviour of PAN- and pitch-carbon fiber reinforced PEEK composites." *Wear* 225 (1999):304-311.
12. Wang, H, Hengzhi. "Contrast of wear resistance between piston materials and composite." *Nanjing ligong daxue xuebao* 21.6 (1997):502-504.
13. Schmidt, J, J.. "High-strength graphites for carbon piston applications." *Carbon* 36.7 (1998):1079-1084.

14. Kuch, I, Ingo. "Potential for lightweight design of a hybrid connecting rod for automobile applications." S.A.E. transactions 100.3 (1991):578-585.
15. Dinwoodie, J, J. "Automotive Applications for MMCs Based on Short Staple Alumina Fibers." SAE Technical Paper Series (1987).
16. Theren, K, Kjell. "Advanced composite materials for road vehicles." Materials & design 11.2 (1990):71-75.
17. Chawla, Krishan K. Composite Materials Science and Engineering, Second Edition. Springer, 1998.
18. Stanglmaier, R.H. "Spec Race Engine Preparation Techniques." SAE 2004-01-3501.
19. Walke, Todd, "The Most Powerful Diesel Engine in the World!" <http://www.bath.ac.uk/~ccsshb/12cyl/>. M1rch 17 2006
20. Suematsu, Toshi, "Development of High Performance Engine for Passenger Cars." International Pacific Conference on Automotive Engineering, 1991.
21. Kajikawa, Y. "Powertrain Materials" Toyota Technical Review-Materials, vol 53 # 219, Nov 2004.
22. Mistry, K, "Theoretical modeling and simulation of piston ring assembly of an IC engine" Proceedings of the 2004 ASME/STLE international joint tribology conference, TRIB2004-64191, 2004,
23. Xu, H "Friction Predictions for piston ring-cylinder liner lubrication" Proceedings of ICEF04 2004 fall technical conference of the ASME Internal Combustion Engine Division, ICEF2004-885.
24. Juvinall, Robert C. and Kurt M. Marshek Fundamentals of Machine Component Design, 3rd Edition. New York: John Wiley & Sons, 1999.
25. Shigley, J. E and John J Eucker, "Theory of Machines and Mechanisms, 2nd ed." McGraw-Hill, 1995.
26. Katz, John F. "Open up to Profits from the latest racing valves." Performance Racing Industry, August 2005
27. Kosugi, Takashi, "Valve Motion Simulation Method for High-Speed Internal Combustion Engines." SAE 850179, Yamaha Motor Co Ltd.
28. Tominaga, T. "Development of Titanium Engine Valves for Motorcycles." SAE 2003-32-0033.

29. Sawyer, Christopher A.. "Look under the hood: you'll see everything from ceramic valves to composite spring retainers." *Chilton's automotive industries* 175.9 (1995):71-71.
30. Bamsey, Ian, "Marathon Sprinter, Profile: Mercedes Formula One V10 2005." *Race Engine Technology*, Volume 4 Issue 1, March/April 2006.
31. Anonymous, "Material Gains, State of the art, Titanium Aluminide." *Race Tech*, No 67, May 2006
32. Fukuoka, Satoshi. "Friction loss reduction by new lighter valve train system." *JSAE review* 18.2 (1997):107-111.
33. Blair, Gordon and Charles D. McCartan, "Making the Cam, Valvetrain Design part two." *Race Engine Technology*, October 2005.
34. Mufti, Riaz A. "Experimental and theoretical study of instantaneous engine valve train friction." *Journal of Tribology* 125.3 (2003):628-637.
35. Miwa, Jason, "Carbon Fiber Reinforced Composite Intake Valves for Internal Combustion Engines" M.S. thesis, Colorado State University, 2006.
36. Kurisu, Toru "A Study of Jump and Bounce in a Valve Train." SAE 910426.
37. Iritani, Takashi, "Prediction of the Dynamic Characteristics in Valve Train Design of a Diesel Engine." JSAE 2002-32-1839, SAE 20024332.
38. Miwa, Jason and Rich Buckley, "Exploring the Potential Advantages of Light-Weight Valves in Internal Combustion Engines." *Proceedings of the ASME Internal Combustion Engines Spring Conference*, Aachen Germany, 2006.
39. Collacott, R, R.A. *Gas and Oil Power* 36.430 (1941):135-137." Poppet-valve technique"
40. Danis, L, Louis J. SAE Preprints. (1973). "Engine Valve Cooling."
41. Anonymous, "TRW Automotive Fact Sheet." http://www.trw.com/images/fact_sheet_-_engine_-_feb_031.pdf, 2006
42. Anon. *Automobile*. (1911)." In the making of poppet valves."
43. Jacobs, F, F.B. "25,000,000 automotive valves annually." *Iron age* 138.7 (1936):32-36.
44. Collacott, R, R.A. *Gas and Oil Power* 36.430 (1941):135-137." Poppet-valve technique."
45. Anon. *Transport World* 106.3396 (1949):796-800." Two million valves a year!"

46. Green, R, R.E.. Machinery (London) 98.2534 (1961):1276-1284." Quantity production of poppet valves"
47. Anon. "King of Cubes Price List."
<http://www.kingofcubes.com/pricelist2.htm#Kibblewhit>. 2007
48. Kretschmer, J, J. "Composites in automotive applications - state of the art and prospects." Materials science and technology 4.9 (1988):757-767.
49. Bak, D, David J. "Molded parts make plastic engine." Design news 45.24 (1989):52-52.
50. Szigethy, N, Neil M.. "What. . . A Plastic Engine! ?." Automotive industries, the automobile 160.12 (1980):40-43.
51. Maxwell, J, J. "Do Plastic Engine Parts Make Sense?" Chartered mechanical engineer 32.4 (1985):42-44.
52. Holtzberg, M, Matthew W. "Use of Advanced Materials in Internal Combustion Engines." (1985)
53. Anon, "Lola heritage scrapbook."
<http://www.lolaheritage.co.uk/scrapbook/004/004.htm> May 26, 2007.
54. Easwaran, J, J. "Polymer composite materials for components of small I.C. engines." Proceedings of the Annual ASM/ESD Advanced Composites conference (1990):523-523.
55. Ransone, Philip, "Carbon-carbon composite piston development" American Society of Mechanical Engineers, Internal Combustion Engine Division (Publication) ICE 25.1 (1995):33-38.
56. Kowbel, W, W.. "Applications of net-shape molded carbon-carbon composites in IC engines." Journal of advanced materials 27.4 (1996):2-7.
57. Northam, G, G. Burton. "IC engine applications of carbon-carbon." Advanced engineering materials 2.9 (2000):583-586.
58. Gunyaev, G, G.M. "Using CFRP for the design of a connecting rod for automobile applications." Proceedings of the Institution of Mechanical Engineers. Part D, Journal of automobile engineering 208.1 (1994):33-36.
59. Crivelli-Visconti, I, I."Improvement in Composite Connecting Rod Design." European Conference on Composite Materials. (1990).
60. Kajikawa, Y. " Powertrain Materials" Toyota Technical Review-Materials, vol 53 # 219, Nov 2004.

- ⁶¹. Anon. Race Engine Technology, April 2005.
- ⁶². Buckley, John D. "Carbon-Carbon, an Overview." American Ceramic Society bulletin 67.2 (1988):364-368.
- ⁶³. Rice, R, Roy W. "Carbon-carbon composite IC engine valve feasibility investigation - a summary." Ceramic engineering and science proceedings 16.4 (1995):307-314.
- ⁶⁴. Bertram, Albert. "Overview of navy composite developments for thermal management." Naval engineers journal 104.3 (1992):276-285.
- ⁶⁵. www.matweb.com
- ⁶⁶. Morgan, Roger J. "Structure-property relations of bismaleimide composite matrices and durability of high temperature polymer matrix composites." International SAMPE Technical Conference 28(1996):213-224.
- ⁶⁷. Moore, Jr.. "Heat transfer across surfaces in contact -- Effects of thermal transients on one-dimensional composite slabs." United States Bureau of Standards -- Special Publication .302 (1968):787-798.
- ⁶⁸. Takeuti, Y. "Transient Thermal Stresses in a Composite Circular Cylinder Due to a Band Heat Source." Nuclear engineering and design 48.2 (1978):427-436.
- ⁶⁹. Lin, S. H. "Transient Heat Conduction in a Composite Slab with Variable Thermal Conductivity." International journal for numerical methods in engineering 14.11 (1979):1726-1731.
- ⁷⁰. Sun, C. T. "Transient Thermal Stress Analysis in Graphite/Epoxy Composite Laminates." Developments in theoretical and applied mechanics 11(1982):309-328.
- ⁷¹. Jortner, J. "Analysis of Transient Thermal Response in a Carbon-Carbon Composite." AD (1982):19-34.
- ⁷². Ishida, R. "Transient Thermal Stresses in a Composite Circular Cylinder Perfectly Bonded on the End Surfaces of Two Circular." Ingenieur-Archiv 54.4 (1984):283-290.
- ⁷³. Kardomateas, G.A. "Transient thermal stresses in cylindrically orthotropic composite tubes." Journal of applied mechanics 56.2 (1989):411-417.
- ⁷⁴. Ootao, Y. "Axisymmetric transient thermal stress analysis of a multilayered composite hollow cylinder." Journal of thermal stresses 14.2 (1991):201-213.

75. Lin, Jae-Yuh. "Radial axisymmetric transient heat conduction in composite hollow cylinders with variable thermal conductivity." *Engineering analysis with boundary elements* 10.1 (1992):27-33.
76. Abd-All, A.M. "Transient thermal stresses in a rotation non-homogeneous cylindrically orthotropic composite tubes." *Applied mathematics and computation* 105.2 (1999):253-269.
77. Shih, Wei. "Copper impregnated carbon composites for thermal management applications." *Proceedings of the International Electronics Packaging Conference*. (1995).
78. Seleznev, Maxim L. "Development of Al matrix composite components for thermal management applications." *International SAMPE Symposium and Exhibition* 44.2 (1999):1281-1291.
79. Biercuk, M.J. "Carbon nanotube composites for thermal management." *Applied physics letters* 80.15 (2002):2767-2767.
80. Huang, Hua. "Aligned carbon nanotube composite films for thermal management." *Advanced materials* 17.13 (2005):1652-1656.
81. Anon. "Carbon nanotube composites cool chips in thermal management material systems." *Advanced materials & processes* 163.3 (2005):22-22.
82. Stoessel, Chris H. "High thermal conductivity graphite copper composites with diamond coatings for thermal management packaging applications." *Materials Research Society symposia proceedings* 390(1995):147-152.
83. Cengel, Yunus. Heat Transfer, A Practical Approach, second edition. McGraw Hill, NY, 2003.
84. Zweben, Carl. "Advances in composite materials for thermal management in electronic packaging." *JOM* 50.6 (1998):47-51.
85. Pickard, Sion M. "Squeeze cast composites for thermal management of power electronic devices." *International SAMPE Symposium and Exhibition* 49(2004):4018-4030.
86. Daugherty, Mark A. "HTS current lead using a composite heat pipe." *IEEE transactions on applied superconductivity* 5.2 (1995):773-776.
87. Engle, G.B. "High thermal conductivity carbon-carbon composites for thermal management." *Proceedings of the 1993 9th International Conference on Composite Materials, ICCM/9. Part 2 (of 6)*, (1993).
88. Lin, Chun-Liang. "Thermal performance of embedded heat pipe composite sandwich panels." *A collection of technical papers on* 2(1999):1125-1134.

89. Xiao, Y. "Thermal management during the solidification of aluminum-carbon fiber composite." Proceedings of the National Heat Transfer Conference 1(2001):523-532.
90. Huang, Y, Y.D. "Thermal behavior of short fiber reinforced AlSi12CuMgNi piston alloys." Composites. Part A, Applied science and manufacturing 35.2 (2004):249-263.
91. Ashari, A.A. "Thermal spray coatings for fiber reinforced polymer composites." Proceedings of the International Thermal Spray Conference 2(1998):1255-1258.
92. Fender, T.D. "Thermal spray high performance polymer coatings." Materials technology 11.1 (1996):16-20.
93. Easwaran, J, J. "Polymer composite materials for components of small I.C. engines." Proceedings of the Annual ASM/ESD Advanced Composites Conference (1990):523-523.
94. Calder, James C. "Development of an aluminum clad carbon composite doubler for spacecraft thermal management." International SAMPE Symposium and Exhibition 49(2004):4058-4066.
95. Gibson, R.J. "Generation and effect of thermal transients in ceramic composites." Composite structures 32.1 (1995):435-444.
96. Lin, Shyh-Shyan, "Piston Ring Assembly Friction Modeling by Similarity Analysis" SAE 930794.
97. Kawamura, Hideo, "Low heat rejection engine with turbo-compound system" ASME 1995, ICE-Vol 25-1, 1995 Fall technical Conference
98. Kurisu, Toru "A Study of Jump and Bounce in a Valve Train." SAE 910426.
99. Worthen, R. P. "Temperature Controlled Engine Valves." SAE Preprints (1982):13-13.
100. Scola, Daniel A."Process characteristics of high temperature polymers and composites." International SAMPE Symposium and Exhibition 34.1 (1989):88-97.
101. Meador, Michael A. "High-temperature polymer-matrix composites." Flight-Vehicle Materials, Structures, and Dynamics - Assessment and Future Directions 2(1994):406-415.
102. Morgan, Roger J. "Structure-property relations of bismaleimide composite matrices and durability of high temperature polymer matrix composites." International SAMPE Technical Conference 28(1996):213-224.

103. Bittence, John C. "BMIS-Composites for High-Temperatures - How Hot can Polymer Composites Get?" *Advanced materials & processes* 2.1 (1986):23-26.
104. Mangalgi, P.D.. "Polymer-matrix composites for high-temperature applications." *Defence science journal* 55.2 (2005):175-193.
105. Radford, Don, "High-Temperature Capable Polymer Matrix Composites." CMMS Internal Report, 2001.
106. Agarwal & Broutman, "Analysis and Performance of Fiber Composites, second edition" John Wiley & Sons, New York, 1990.
107. Incropera, Frank P and David P. DeWitt, *Fundamentals of Heat and Mass Transfer*, 3rd edition, John Wiley & Sons, New York, 1990.
108. Vinayak, R.U. "Transient thermal conduction in rectangular fiber reinforced composite laminates." *Advanced composite materials* 4.4 (1995):327-342.
109. Zhang, Yinping. "Simple method of calculating the transient thermal performance of composite material and its applicable condition." *Science in China. Series E, Technological sciences* 43.4 (2000):344-348.
110. Hader, M.A. "Transient thermal response of a homogeneous composite thin layer exposed to a fluctuating heating source under the effect of the dual-phase-lag heat-conduction model." *International journal of thermophysics* 27.2 (2006):665-680.
111. Hader, M.A. "Thermal behavior of a thin layer carrying pulsating signals in the dual-phase-lag model." *Heat transfer engineering* 23.3 (2002):35-41.
112. Al-Nimr, M.A. "Thermal behavior of a multi-layered thin slab carrying periodic signals under the effect of the dual-phase-lag heat conduction model." *International journal of thermophysics* 25.3 (2004):949-966.
113. Balageas, D. L. "Transient Thermal Behavior of Directional Reinforced Composites: Applicability Limits of the Homogeneous Property Model." *AIAA journal* 24.1 (1986):109-114.
114. Roberts, J.C. "Transient and steady-state temperatures in hybrid high/low thermal conductivity composites." (1995).
115. Chawla, Krishan K. *Composite Materials, Science and Engineering*, Second Edition. Springer, New York, 1998.
116. Buckley, John D. "Carbon-carbon materials and composites." NASA reference publication .1254 (1992):286-286.

117. Kowbel, W, W. "Applications of net-shape molded carbon-carbon composites in IC engines." *Journal of advanced materials* 27.4 (1996):2-7.
118. DeMeuse, Mark T. "High temperature polymer blends: an overview of the literature." *Polymers for advanced technologies* 6.2 (1995):76-82.
119. Chaplin, A. "Novel hydrophobic, tough, and high temperature matrix resins for polymer composites." *Plastics, rubber, and composites processing and applications* 28.5 (1999):191-200.
120. Connell, John W., "PETIs as High-Temperature Resin-Transfer Molding Materials." *NASA Tech Briefs*, September 2005.
121. Chenock, Thomas A. Jr. "Effect of matrix material on the fracture behavior and toughness of high temperature polymer composites." *National SAMPE symposium and exhibition* 35.1 (1990):1089-1102.
122. Tang, Y. "Thermal properties of PETI-5/IM-7" *Thermochimica Acta*, 357-358, Elsevier Inc., 357-358, 2000.
123. Criss, Jim et al. "Resin Transfer Molding and Resin Infusion Fabrication of High-Temperature Composites." *SAMPE Journal*, vol 36, No 3 May, June 2000, p32-41.
124. Colton, Jonathan S. "Resin Transfer Molding of BMIs and Polyimides." *Polymer Composites*, December 1998, Vol. 19, #6.
125. Cho, Donghwan. "Characterization, properties, and processing of LaRC PETI-5 as a high-temperature sizing material II. Thermal characterization." *Journal of applied polymer science* 75.10 (2000):1278-1287.
126. Gibson, A.H. "Exhaust-valve and cylinder-head temperatures in high-speed petrol engines." *Institution of Mechanical Engineers -- Proceedings* 2.6 (1923):1045-1092.
127. Drolshammer, I. "Temperature distribution and heat flow in exhaust valves of diesel engines." *Engineers' Digest (British Edition)* 6.12 (1945):318-324.
128. Cherrie, J.M. "Factors influencing valve temperatures in passenger car engines" *Society of Automotive Engineers -- Papers*. (1965).
129. Proffit, Anne "Poppet advances." *Race Engine Technology*. issue 014, May 2006. page 38-42.
130. Worthen, Roger P. "Measurement of Valve Temperatures and Strain in a Firing Engine." *SP* (1986):85-97.

131. Wakuri, Yutaro. "On the High Temperature Corrosion of Exhaust Valve in a Diesel Engine." Bulletin of the JSME 17.112 (1974):1313-1320.
132. Neumann, William. "High Temperature Corrosion of Internal Combustion Engine Valves" AIME, Metallurgical Soc, New York, NY, USA (1985).
133. Stanglmaier, R. "An Innovative Glass-Metal Coating to provide Corrosion Resistance and a Thermal Barrier for Highly Loaded Engine Components."
134. Worthen, R. P. "Temperature Controlled Engine Valves." SAE Preprints (1982):13-13.

Appendices

Appendix 1: references for Figure 16, Figure 17, Figure 18, and Table 5

1. Bittner, D, D. "Coating of carbon fibre reinforced composite (CCC). Research, development and application." Powder Metallurgy International 24.5 (1992):291-296.
2. Kowbel, W, W. "Low cost carbon-based composite pistons." International SAMPE Symposium and Exhibition 45 (2000):664-670.
3. Ransone, Philip, "Carbon-carbon composite piston development" American Society of Mechanical Engineers, Internal Combustion Engine Division (Publication) ICE 25.1 (1995):33-38.
4. Ashley, S, Steven. "Engine makers tap carbon-carbon pistons." Mechanical engineering 116.5 (1994):60-61.
5. Buchman, A, Alisa. "Molded carbon-carbon composites based on microcomposite technology." Applied composite materials 6.5 (1999):309-326.
6. Schmidt, J, J. "High-strength graphites for carbon piston applications." Carbon 36.7 (1998):1079-1084.
7. Northam, G, G. Burton. "IC engine applications of carbon-carbon." Advanced engineering materials 2.9 (2000):583-586.
8. Rice, R, Roy W. "Carbon-carbon composite IC engine valve feasibility investigation - a summary." Ceramic engineering and science proceedings 16.4 (1995):307-314.
9. Baker, A, A. R. "Ceramic and Composite Materials for Precision Engine Components." Materials & design 8.6 (1987):315-323.
10. Menges, G, Georg. "How To Design a Connecting Rod." (1985)
11. Anonymous, "High Tech - The Way into the Nineties" Proceedings of the 7th International Conference of the Society for the Advancement of Material and Process Engineering European Chapter. Materials science monographs (1986).

12. Holtzberg, M, Matthew W. "Use of Advanced Materials in Internal Combustion Engines." (1985)
13. Noguchi, M, M. "Status and prospects for metal matrix composites in Japan." *Key engineering materials* 127.1 (1997):153-164.
14. Folgar, F, F. "Design, Fabrication and Performance of Fiber FP/Metal Matrix Composite Connecting Rods." *International SAMPE Symposium and Exhibition* 32 (1987):1559-1568.
15. Sala, G, Giuseppe. "Technology-driven design of MMC squeeze cast connecting-rods." *Science and technology of advanced materials* 3.1 (2002):45-57.
16. Ebisawa, M, Masuo. "Production process of metal matrix composite (MMC) engine block." *SAE technical paper series* (1991).
17. Goddard, D, David M. "Graphite/Magnesium Composites for Advanced Lightweight Rotart Engines." *SAE technical paper series* (1986).
18. Keribar, R, Rifat. "Investigation of structural effects of fiber matrix reinforcement in aluminum diesel pistons." *S.A.E. transactions* 99.5 (1990):622-641.
19. Afonso, A, Alexandre. "Development of fiber reinforced aluminum alloy for diesel piston applications." *S.A.E. transactions* 100.5 (1991):629-637.
20. Zweben, C, Carl. "Limitless world of composites." *Chemtech* 18.12 (1988):733-737.
21. Belousov, I, I.Ya. "Promising technology and equipment for manufacturing billets for composite pistons of internal combustion engines (ICE) of a new generation, using the liquid stamping method." *TYAZHELOE MASHINOSTROENIE* .5 (1998):45-47.
22. Salzar, R, Robert S. "Design considerations for rotating laminated metal-matrix-composite shafts." *Composites science and technology* 59.6 (1999):883-896.
23. Dwivedi, R, R. "Applications of metal matrix composites in high performance racing engines." *SAE technical paper series* (1991):1-11.
24. Pidira, M. Development of low-cost, interconnected matrix composites for valve seat application, 2002, *International Conference High Performance*,
25. Wood, S, Stuart. "Breakthrough in Lightweighting: Composite Engine Components." *Modern plastics* 65.3 (1988):42-46.

26. Maxwell, J, J. "Do Plastic Engine Parts Make Sense?" Chartered mechanical engineer 32.4 (1985):42-44.
27. Beckmann, H, Hans-Dieter. "Fiber Reinforced Plastics Move Inside the Engine." SAE journal of automotive engineering 93.5 (1985):34-41.
28. Kretschmer, J "Load Bearing Parts in Ground Car Vehicles out of Fibre Reinforced Plastics." Materials science monographs (1986):1-13.
29. Anon. "Plastics Enter the Engine." Engineering 227.3 (1987):14-15.
30. Theren, K, Kjell. "Advanced composite materials for road vehicles." Materials & design 11.2 (1990):71-75.
31. Wieslach, H "Stand und Entwicklungstendenzen beim Herstellen von Pleueln" Werkstatt und Betrieb, 1990 vol 123 # 12,
32. Crivelli-Visconti, I, I."Improvement in Composite Connecting Rod Design." European Conference on Composite Materials. (1990).
33. Easwaran, J, J. "Polymer composite materials for components of small I.C. engines." Proceedings of the Annual ASM/ESD Advanced Composites Conference (1990):523-523.
34. Kuch, I, I."Advanced Composites in Vehicles - Current State and Future Prospects for Applications." European Conference on Composite Materials. (1990).
35. Malkan, S, Sanjiv R. "Three-dimensionally braided preform for a composite connecting rod. Concept development and demonstration." Journal of reinforced plastics and composites 10.2 (1991):167-183.
36. Gunyaev, G, G.M. "Using CFRP for the design of a connecting rod for automobile applications." Proceedings of the Institution of Mechanical Engineers. Part D, Journal of automobile engineering 208.1 (1994):33-36.
37. Holtzberg, M, Matthew W. "Use of Advanced Materials in Internal Combustion Engines." (1985)
38. Not used
39. Guimond, D, David P. "Composite V-6 diesel engine concept." SAE technical paper series (1992):1-7. SAE 920084
40. Cho, Toshoku. "Manufacture of Carbon-Carbon Composites by using Fine Coke and its Properties." ASTM special technical publication (1985):443-455.

41. Cho, D, Durk Hyun. "Manufacture of one-piece automotive drive shafts with aluminum and composite materials." *Composite structures* 38.1 (1997):309-319.
42. Szigethy, N, Neil M. "What. . . A Plastic Engine! ?." *Automotive industries, the automobile* 160.12 (1980):40-43.
43. Murphy, J, J. S. "Engine Components, Gear Box and Transmission" (1982):1-1.
44. Anon. "Technical note: 2.3-litre 16V engine for Ford Galaxy." *International journal of vehicle design* 18.5 (1997):574-580.
45. Zhang, L, Li. "Development of composite engine blocks for automobiles." *Bing gong xue bao* 20.2 (1999):186-188.
46. Kajikawa, Y. "Powertrain Materials" *Toyota Technical Review-Materials*, vol 53 # 219, Nov 2004.
47. Anon. "The Ultimate Cup Motor" *Race Engine Technology*, Winter 2003.
48. Anon – *Race Engine Technology*, Issue 08, June 2005.

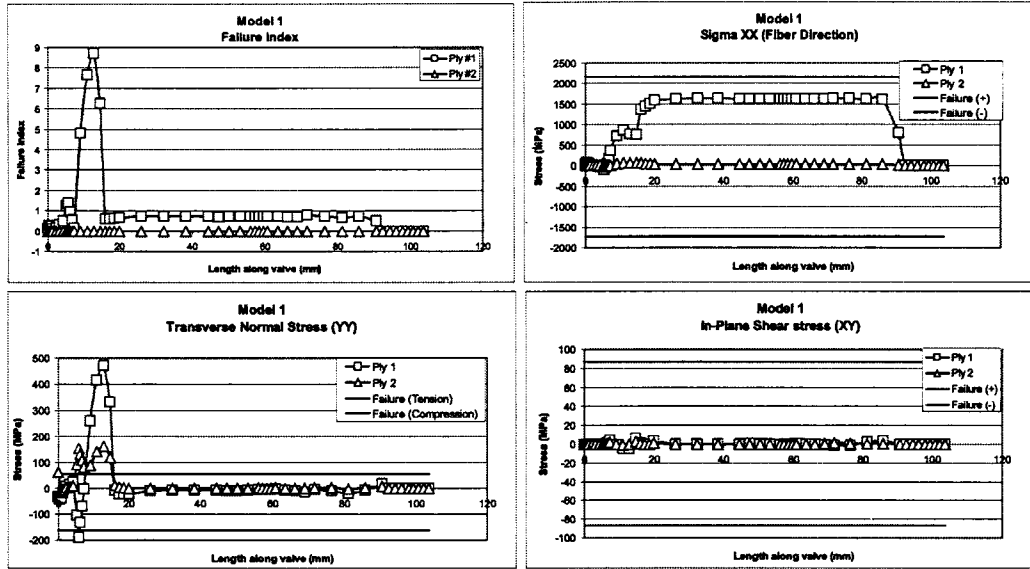
Appendix 2: tabulated mass reduction by material substitution

Results applied to lycoming engine

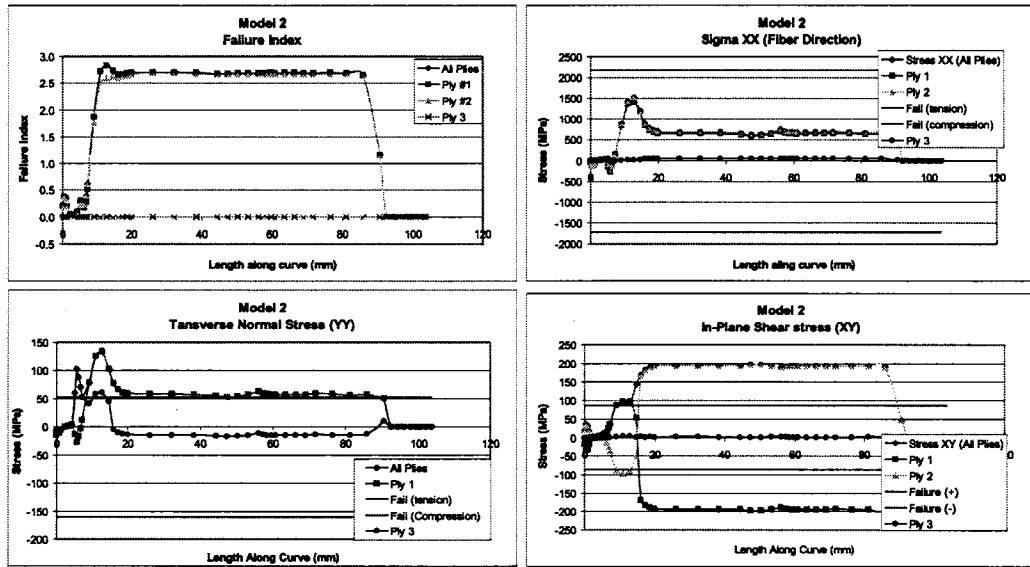
	Total weight	Original material	Material substituted	Category	
alternator	13.00	multiple	None	starter/alternator	
starter	17.00	multiple	None	starter/alternator	
Total starter/alternator	30.00			Total starter/alternator	30.00
gearing	0.00	Al	PMC	accessories	
oil sump	23.50	Al	PMC	accessories	
pushrod tubes	1.00	Al	PMC	accessories	
Total Accessories	24.50			Total Accessories	12.50
exhaust pre turbo	13.00	steel	None	air/exhaust	
intake cast tube	4.50	Al	PMC	air/exhaust	
more exhaust	4.50	steel	PMC	air/exhaust	
turbo	47.50	steel	C-C	air/exhaust	
Total air/exhaust	69.50			Total air/exhaust	26.51
accessory cover	10.00	Al	PMC	covers	
another air cover	4.00	steel	PMC	covers	
covers, air flow	13.00	steel	PMC	covers	
valve covers	3.50	steel	PMC	covers	
Total covers	30.50			Total covers	8.59
dist cap wires	5.00	PVC/wire	none	miscellaneous	
distributors	7.50	multiple	none	miscellaneous	
Fuel injector	7.00	multiple	none	miscellaneous	
fuel lines	2.50	steel	pmc	miscellaneous	
misc hardware nuts bolts	26.00	steel	none	miscellaneous	
total miscellaneous	48.00			total miscellaneous	45.93
cam followers	2.50	steel	C-C	recip	
connecting rods	12.00	steel	pmc	recip	
exhaust valve	1.82	steel	C-C	recip	
intake valve	2.03	steel	C-C	recip	
piston	18.00	Al	C-C	recip	
pushrods	3.00	steel	pmc	recip	
wrist pins	10.50	steel	pmc	recip	
rocker arms	3.50	al	PMC	recip	
total recip	53.35			total recip	16.71
camshaft	4.50	steel	c-c	rotating	
crankshaft	67.50	stainless steel	pmc	rotating	
crankshaft counterbalance	9.00	steel	mmc	rotating	
ring gear	10.00	steel	mmc	rotating	
total rotating	91.00			total rotating	50.18
Crank case	82.00	Al	mmc	structure	
cylinder/head	165.00	Al and steel	mmc	structure	
journal bearings	0.00	steel	none	structure	
mounts	4.40	al	PMC	structure	
thru bolts	6.00	steel	none	structure	
total structure	257.40			total structure	82.34
total mass	604.25			Total "reduced" mass	272.75

Appendix 3: Stress Plots for FRC valve structural design

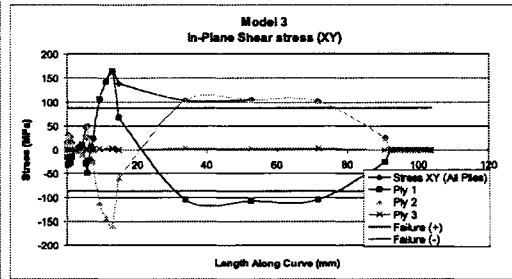
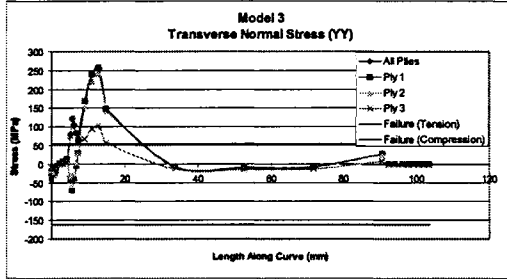
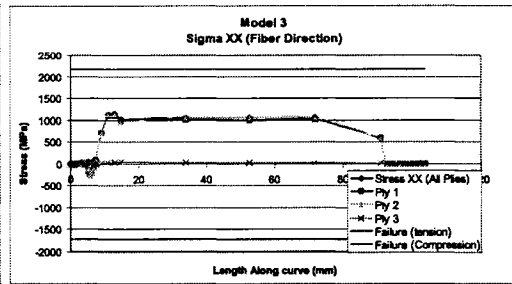
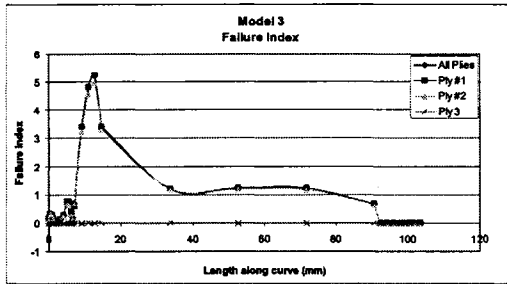
Model 1



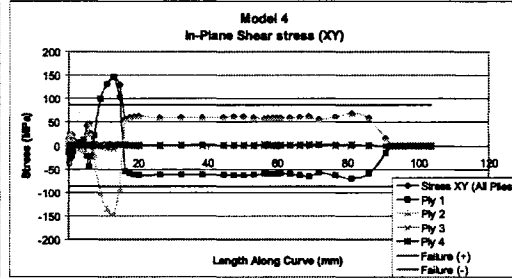
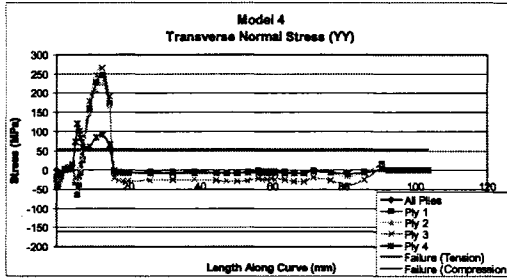
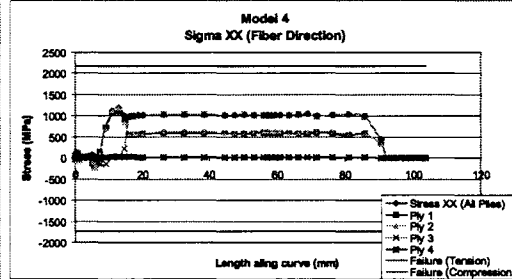
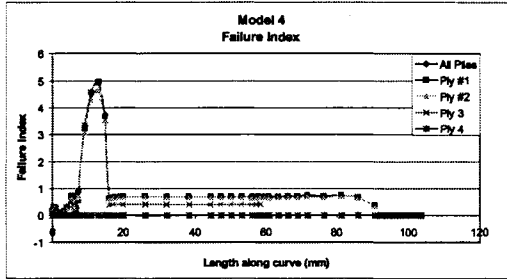
Model 2



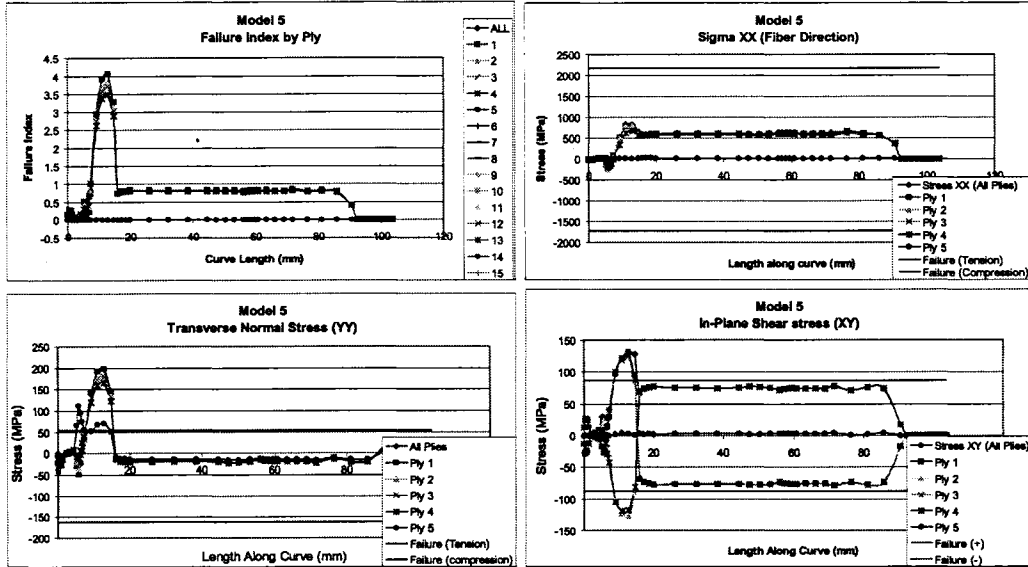
Model 3



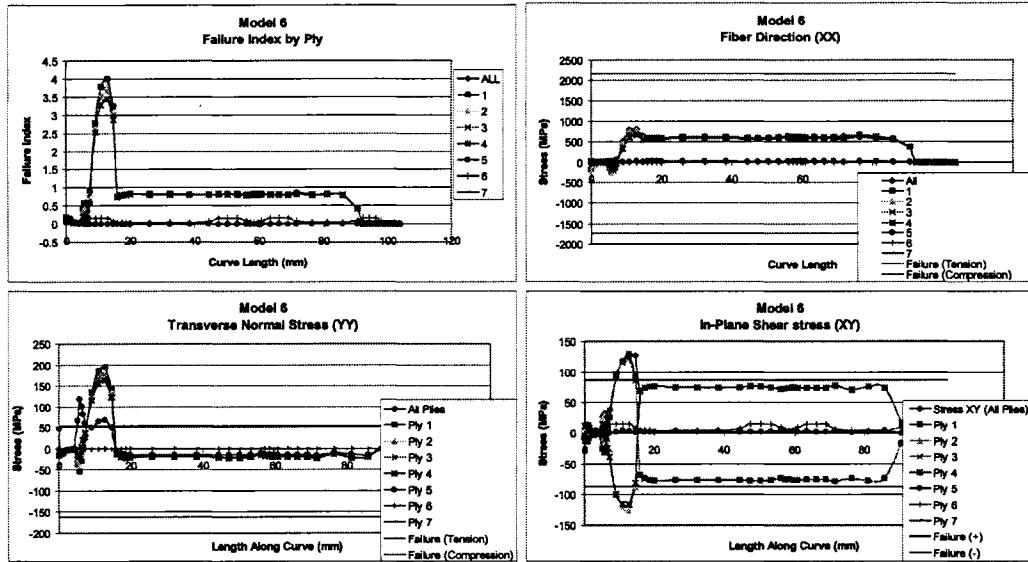
Model 4



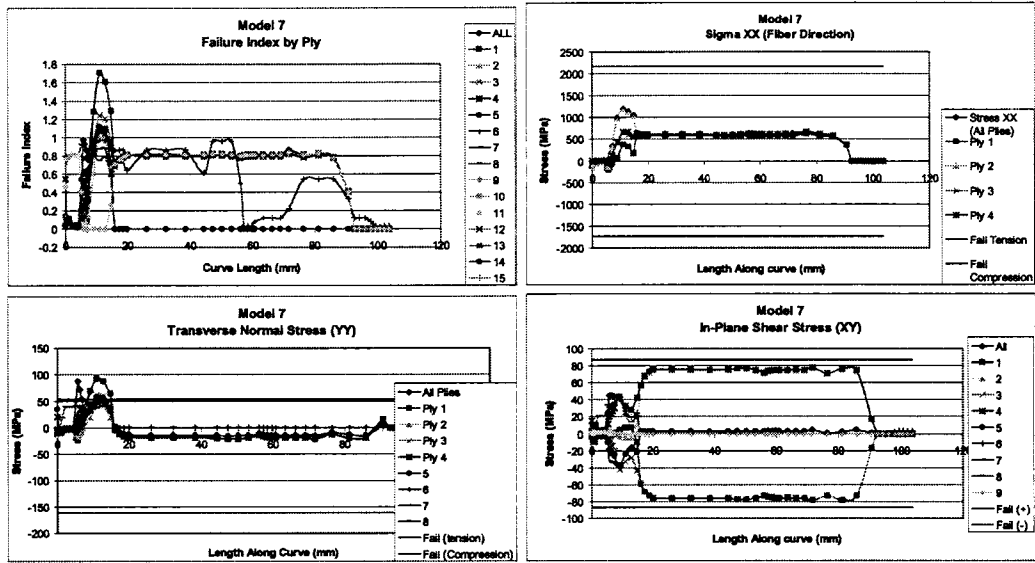
Model 5



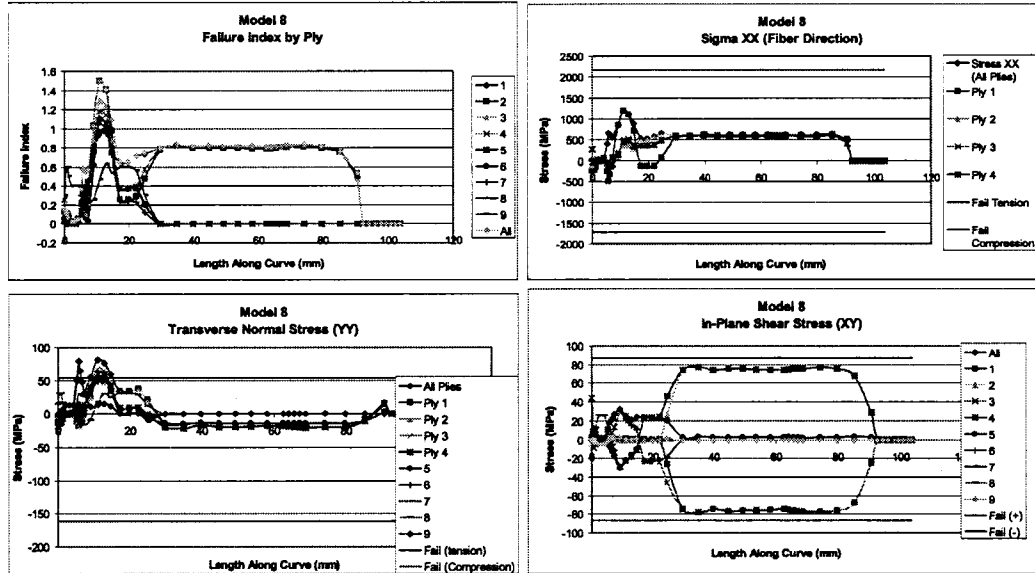
Model 6



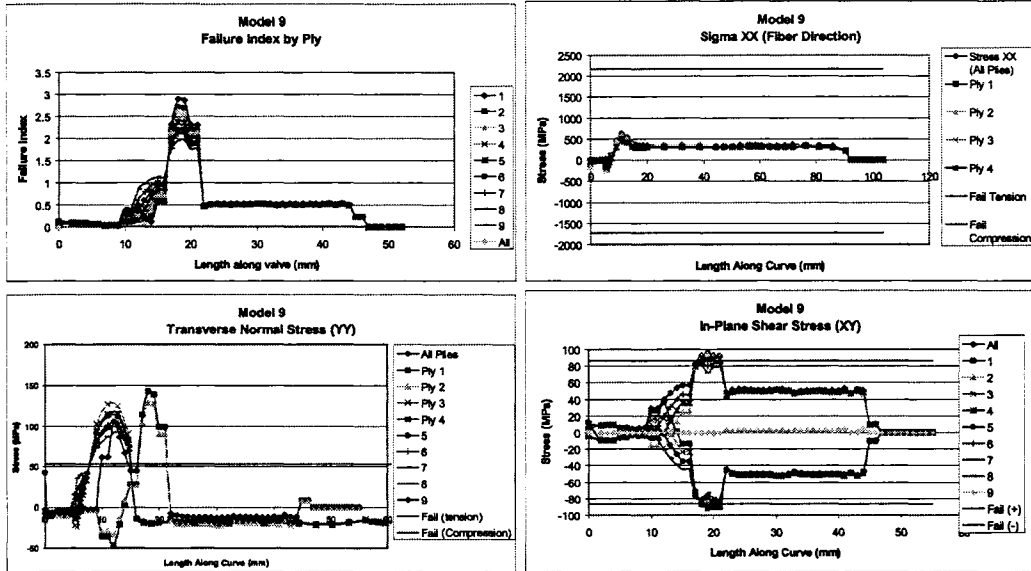
Model 7



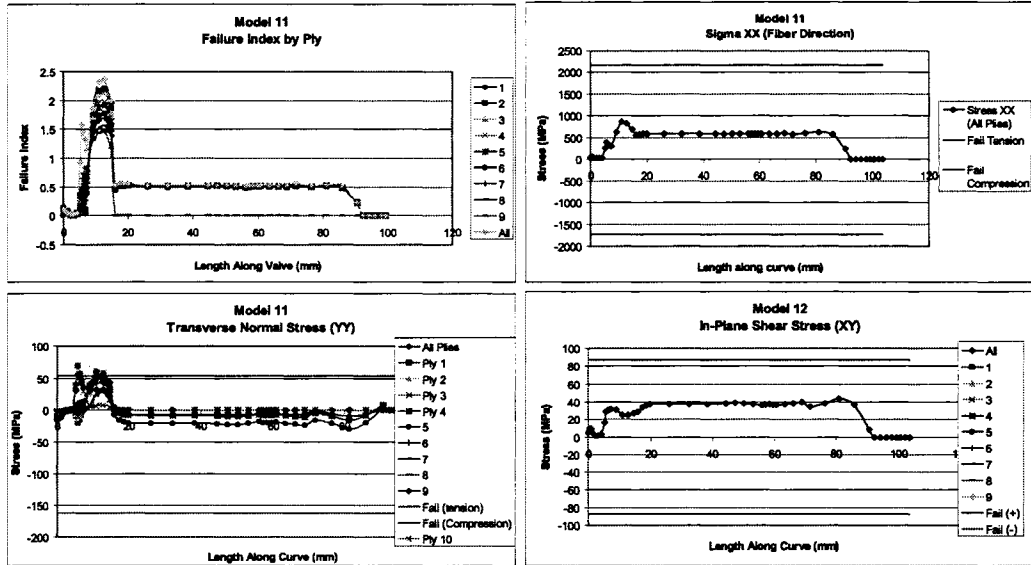
Model 8



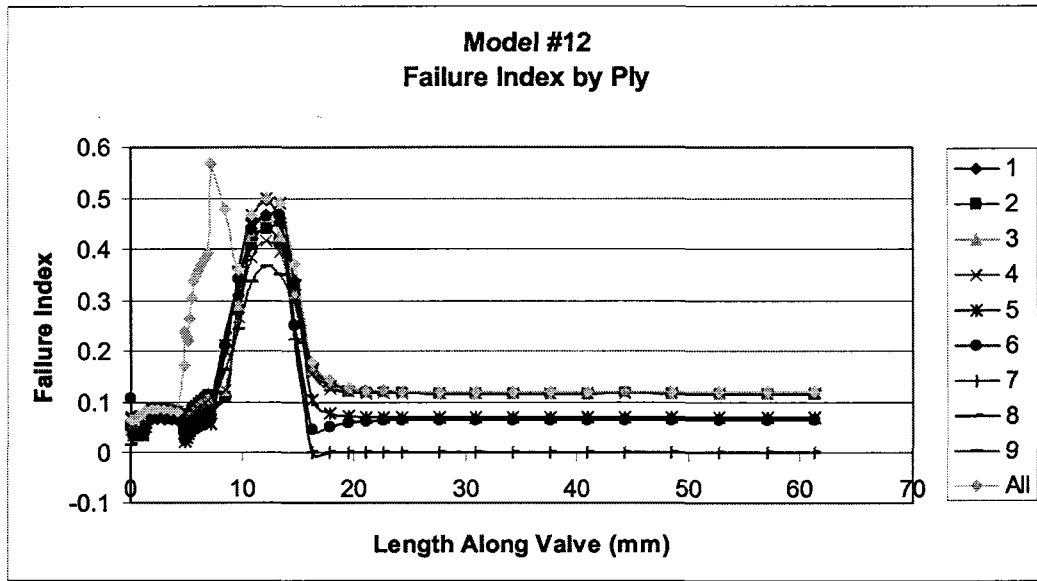
Model 9



Model 11



Model 12



Appendix 4: Complete Thermal Analysis Plans

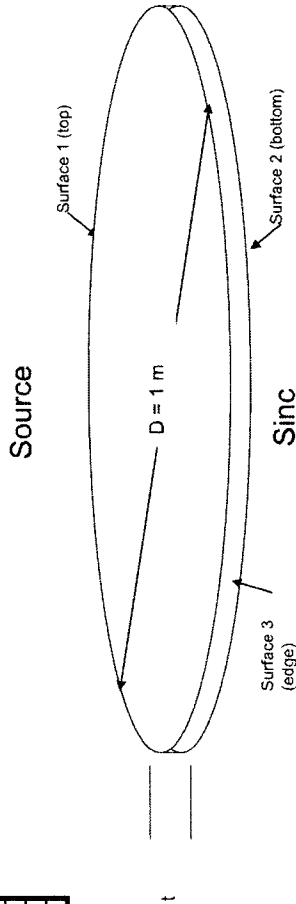
5/29/2007 22:27

Study Name: 1: Thin Isotropic Solid

Heat Path: Axial		(THESE SHOULD NEVER CHANGE)	
Model Dimensions			
Diameter	1 m	1000 mm	
Core thickness	0.002 m	2 mm	
Coating thickness	m	0 mm	

Initial Conditions:	
Initial Temperature	300 K
T _{gas}	1300 K

Boundary conditions:		Surface Areas (m ²)
surface 1	h (W/m ² K)	0.7854
surface 2	T _{gas} (K)	0.0063
surface 3		0.7854



$$F_0 = t' = \frac{c \rho}{L^2}$$

$$Bi = \frac{hL}{k}$$

$$\alpha = \frac{k}{\rho \cdot c_p}$$

Material	k (W/mK)	density (kg/m ³)	Specific Heat, cp (J/kgK)	thermal diffusivity, alpha (m ² /s)	Bi	Fo (0.01 sec)	Fo (0.1 sec)	Fo (1.0 sec)
thin iso a 1	0.001	10	1000	1.00E-07	1000	2.50E-04	2.50E-03	2.50E-02
thin iso a 2	0.01	10	1000	1.00E-06	100	2.50E-03	2.50E-02	2.50E-01
thin iso a 3	0.1	10	1000	1.00E-05	10	2.50E-02	2.50E-01	2.50E+00
thin iso a 4	1	10	1000	1.00E-04	1	2.50E-01	2.50E+00	2.50E+01
thin iso a 5	10	10	1000	1.00E-03	0.1	2.50E+00	2.50E+01	2.50E+02
thin iso a 6	100	10	1000	1.00E-02	0.01	2.50E+01	2.50E+02	2.50E+03
thin iso a 7	1000	10	1000	1.00E-01	0.001	2.50E+02	2.50E+03	2.50E+04

Analyses:

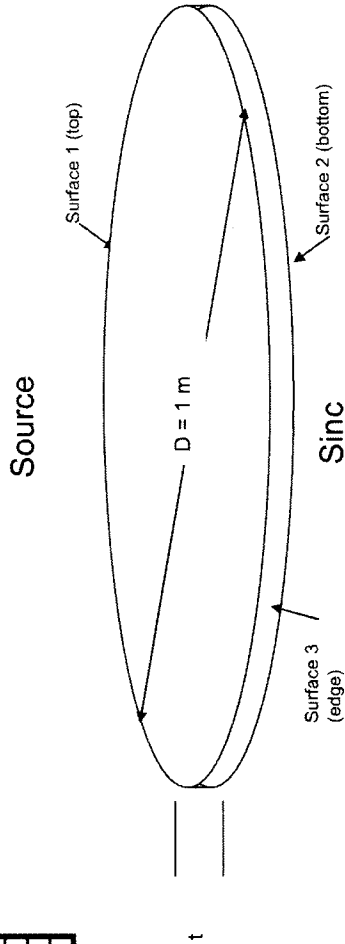
Study Name: 2: Thin Isotropic Solid
Heat Path: Radial

5/29/2007 22:27

Model Dimensions	(THESE SHOULD NEVER CHANGE)	
Diameter	1 m	1000 mm
Core thickness	0.002 m	2 mm
Coating thickness	m	0 mm

Initial Conditions:	
Initial Temperature	200 K
T_gas	1200 K

Boundary conditions:			
	h (W/m^2K)	Tgas (K)	Surface Areas (m^2)
surface 1	500	1200	0.7854
surface 2	0	200 (insulated)	0.0063
surface 3	62500	200	0.7854



Analyses:

Material	k (W/mK)	density (kg/m^3)	Specific Heat, cp (J/kgK)	thermal diffusivity, alpha (m^2/s)	Bi	Fo (0.01 sec)	Fo (0.1 sec)	Fo (1.0 sec)
thin iso r_1	0.001	10	1000	0.0000001	1000	2.50E-04	2.50E-03	2.50E-02
thin iso r_2	0.01	10	1000	0.000001	100	2.50E-03	2.50E-02	2.50E-01
thin iso r_3	0.1	10	1000	0.00001	10	2.50E-02	2.50E-01	2.50E+00
thin iso r_4	1	10	1000	0.0001	1	2.50E-01	2.50E+00	2.50E+01
thin iso r_5	10	10	1000	0.001	0.1	2.50E+00	2.50E+01	2.50E+02
thin iso r_6	100	10	1000	0.01	0.01	2.50E+01	2.50E+02	2.50E+03
thin iso r_7	1000	10	1000	0.1	0.001	2.50E+02	2.50E+03	2.50E+04

$$\alpha = \frac{k}{\rho \cdot c_p}$$

$$F_0 = t^* = \frac{\alpha t}{L^2}$$

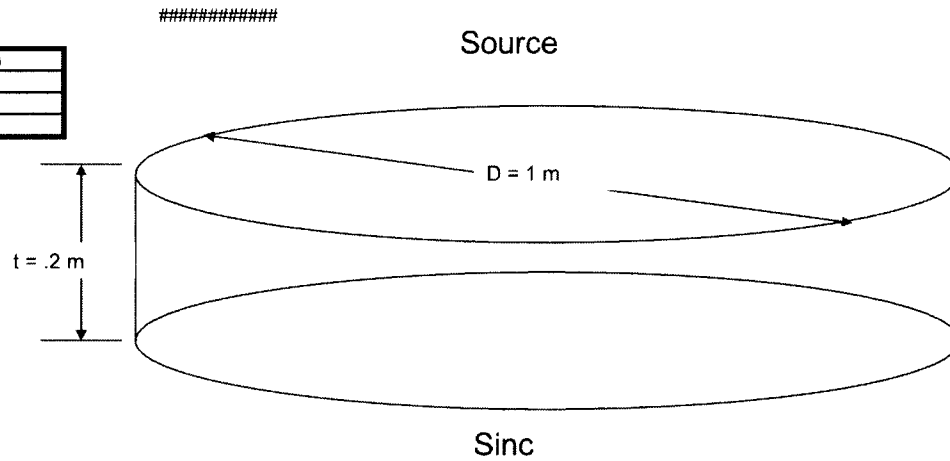
$$Bi = \frac{hL_c}{k}$$

Study Name: 4: Thick Isotropic Solid
Heat Path: Radial

Model Dimensions		(THESE SHOULD NEVER CHANGE)	
Diameter	1 m	1000 mm	
Core thickness	0.2 m	200 mm	
Coating thickness	m	0 mm	

Initial Conditions:	
Initial Temperature	200 K
T _{gas}	1200 K

Boundary conditions:			
	h (W/m ² K)	T _{gas} (K)	Surface Areas (m ²)
surface 1	500	1200	0.7854
surface 2	0	200 (Insulated)	0.0063
surface 3	625	200	0.7854



Analyses:

Material	k (W/mK)	density (kg/m ³)	Specific Heat, cp (J/kgK)	thermal diffusivity, alpha (m ² /s)	Bi	Fo (0.01 sec)	Fo (0.1 sec)	Fo (1.0 sec)	Fo (10 sec)	Fo (100 sec)
thick iso r 1	0.001	10	1000	0.0000001	100000	2.50E-08	2.50E-07	2.50E-06	2.50E-05	2.50E-04
thick iso r 2	0.01	10	1000	0.000001	10000	2.50E-07	2.50E-06	2.50E-05	2.50E-04	2.50E-03
thick iso r 3	0.1	10	1000	0.00001	1000	2.50E-06	2.50E-05	2.50E-04	2.50E-03	2.50E-02
thick iso r 4	1	10	1000	0.0001	100	2.50E-05	2.50E-04	2.50E-03	2.50E-02	2.50E-01
thick iso r 5	10	10	1000	0.001	10	2.50E-04	2.50E-03	2.50E-02	2.50E-01	2.50E+00
thick iso r 6	100	10	1000	0.01	1	2.50E-03	2.50E-02	2.50E-01	2.50E+00	2.50E+01
thick iso r 7	1000	10	1000	0.1	0.1	2.50E-02	2.50E-01	2.50E+00	2.50E+01	2.50E+02

$$\alpha = \frac{k}{\rho \cdot c_p}$$

$$Bi = \frac{hL_c}{k}$$

$$F_0 = t^* = \frac{\alpha t}{L^2}$$

5/29/2007 22:27

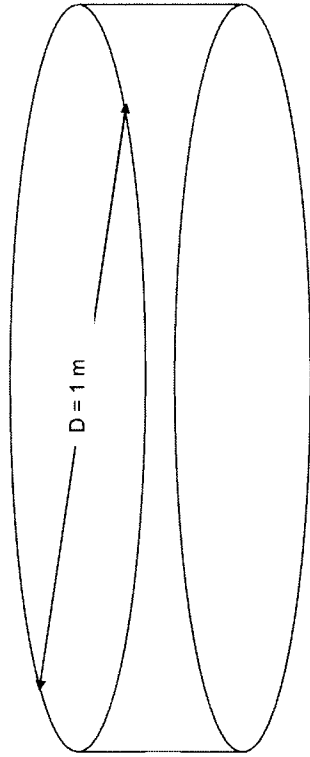
Study Name: 3: Thick Isotropic Solid
Heat Path: Axial

Model Dimensions (THESE SHOULD NEVER CHANGE)	
Diameter	1 m
Core thickness	0.2 m
Coating thickness	0 mm

Initial Conditions:	
Initial Temperatur	300 K
T _{gas}	1300 K

Boundary conditions:	
h (W/m ² K)	T _{gas} (K)
surface 1	500
surface 2	300
surface 3	0 (Insulated)
	Surface Areas (m ²)
	0.7854
	0.6283
	0.7854

Source



Sinc

$$\alpha = \frac{k}{\rho \cdot c_p}$$

$$F_0 = t' = \frac{\alpha t}{L^2}$$

$$Bi = \frac{hL_c}{k}$$

Material	k (W/mK)	density (kg/m ³)	Specific Heat, cp (J/kgK)	thermal diffusivity, alpha (m ² /s)	Bi	Fo (0.01 sec)	Fo (0.1 sec)	Fo (1.0 sec)
thick iso a 1	0.001	10	1000	1E-07	100000	2.50E-08	2.50E-07	2.50E-06
thick iso a 2	0.01	10	1000	0.000001	10000	2.50E-07	2.50E-06	2.50E-05
thick iso a 3	0.1	10	1000	0.00001	1000	2.50E-06	2.50E-05	2.50E-04
thick iso a 4	1	10	1000	0.0001	100	2.50E-05	2.50E-04	2.50E-03
thick iso a 5	10	10	1000	0.001	10	2.50E-04	2.50E-03	2.50E-02
thick iso a 6	100	10	1000	0.01	1	2.50E-03	2.50E-02	2.50E-01
thick iso a 7	1000	10	1000	0.1	0.1	2.50E-02	2.50E-01	2.50E+00

Analyses:

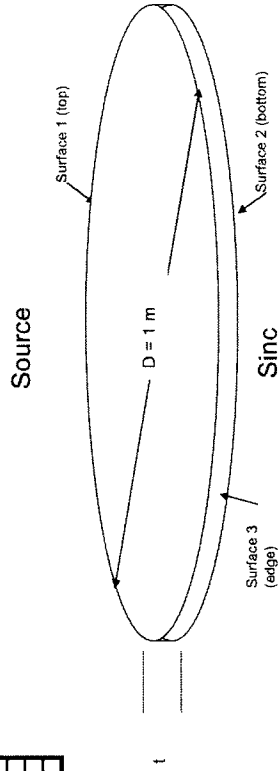
5/29/2007 22:27

Study Name: 5: Thin Isotropic Solid with coating
Heat Path: Axial

Model Dimensions		[THESE SHOULD NEVER CHANGE]	
Diameter	1 m	1000 mm	
Core thickness	0.002 m	2 mm	
Coating thickness	0.0001 m	0.1 mm	

Initial Conditions:	
Initial Temperature	300 K
T_gas	1300 K

Boundary conditions:		
h (W/m^2K)	T_gas (K)	Surface Areas (m^2)
surface 1	1300	500 0.7854
surface 2	500	300 0.0063
surface 3	0	300 (insulated) 0.7854



Analyses:

Test Name	Coating material name	Core Material name	k-coating (W/mK)	k-core (W/mK)	density (kg/m^3) [core and coating]	Specific Heat, (α) (J/kgK) [coating and core]	coating thermal diffusivity, alpha (m^2/s)	core thermal diffusivity, alpha (m^2/s)
thin_iso_coat_a_1	iso_7	iso_1	1000	0.001	10	1000	1.00E-01	1.E-07
thin_iso_coat_a_2	iso_6	iso_2	100	0.01	10	1000	1.00E-02	1.E-08
thin_iso_coat_a_3	iso_5	iso_3	10	0.1	10	1000	1.00E-03	1.E-09
thin_iso_coat_a_5	iso_3	iso_5	0.1	10	10	1000	1.00E-05	1.E-03
thin_iso_coat_a_6	iso_2	iso_6	0.01	100	10	1000	1.00E-06	1.E-02
thin_iso_coat_a_7	iso_1	iso_7	0.001	1000	10	1000	1.00E-07	1.E-01

$$F_0 = i^* = \frac{at}{L^2}$$

$$Bi = \frac{hL_c}{k}$$

$$\alpha = \frac{k}{\rho \cdot c_p}$$

$$Bi^*_{core} = \left(\frac{L_{core}}{h} / k_{core} \right) \left(\frac{1}{h} + \frac{L_{mat}}{k_{mat}} / k_{coat} \right)$$

Calculations for future reference:

Test Name	Bi-coating	Bi-core	Ratio k_coating/k_core	Ratio alpha_coating/alpha_core	Fo-coat	Fo-core	Fo-coat/Fo-core
thin_iso_coat_a_1	0.0005	1.0E+03	1.E+08	1.E+06	0.1 sec	1.0 sec	0.01 sec
thin_iso_coat_a_2	0.0005	1.0E+02	1.E+04	1.E+04	2.50E-03	2.50E-02	4.00E+08
thin_iso_coat_a_3	0.0005	1.0E+01	1.E+02	1.E+02	2.50E-02	2.50E-01	4.00E+08
thin_iso_coat_a_5	0.5	6.7E-02	7.5E+00	1.E-02	2.50E+00	2.50E+01	4.00E+00
thin_iso_coat_a_6	5	1.7E-03	3.0E+03	1.E-04	2.50E+01	2.50E+02	4.00E-02
thin_iso_coat_a_7	50	2.0E-05	2.6E+06	1.E-06	2.50E+02	2.50E+03	4.00E-04

5/28/2007 22:27

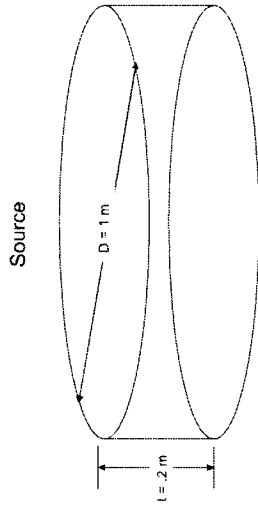
Study Name: 7: Thick isotropic solid with coating

Heat Path: Axial

Modal Dimensions		[THESE SHOULD NEVER CHANGE]	
Diameter	1 m	1000 mm	
Core thickness	0.2 m	200 mm	
Coating thickness	0.0001 m	0.1 mm	

Initial Conditions:	
Initial Temperature	300 K
L gas	300 K

Boundary conditions:	
h (W/m ² *K)	Surface
500	1300
500	900
0	300 (insulated)
	0.7854



Sinc

Test Name	Coating material name	Core Material name	k-coating (W/mk)	k-core (W/mk)	density (kg/m ³)	Specific Heat, core and coating (J/kgK)	coating thermal diffusivity, alpha (m ² /s)	core thermal diffusivity, alpha (m ² /s)
thick iso coat a 1	iso 7	iso 1	1000	0.001	10	1000	1E-01	1E-07
thick iso coat a 2	iso 6	iso 2	100	0.01	10	1000	1E-02	1E-08
thick iso coat a 3	iso 5	iso 3	10	0.1	10	1000	1E-03	1E-09
thick iso coat a 4	iso 4	iso 4	10	0.1	10	1000	1E-03	1E-09
thick iso coat a 5	iso 3	iso 5	0.1	10	10	1000	1E-05	1E-10
thick iso coat a 6	iso 2	iso 6	0.01	100	10	1000	1E-06	1E-11
thick iso coat a 7	iso 1	iso 7	0.001	1000	10	1000	1E-07	1E-12

$$Fo_{core} = \frac{\alpha t}{L^2}$$

$$Bi = \frac{hL}{k}$$

$$\alpha = \frac{k}{\rho c_p}$$

$$Bi^*_{conv} = \left(\frac{c_{conv} k_{conv}}{h} + L_{conv} \right) \frac{h}{k}$$

Calculations for future reference

| Test Name | Bi-coat | Bi-core | Bi-coat/alpha-coat | Ratio k-coat/k-core | Ratio alpha-coat/alpha-core | Fo-coat | Fo-core | Fo-coat/Fo-core | |
|--------------------|---------|---------|--------------------|---------------------|-----------------------------|----------|----------|-----------------|-----------------|-----------------|-----------------|-----------------|-----------------|-----------------|-----------------|-----------------|-----------------|-----------------|---------|
| thick iso coat a 1 | 0.0001 | 1.0E+03 | 1E-08 | 1E-04 | 1E-08 | 0.01 sec | 0.01 sec | 1.0E+01 | 1.0E+01 |
| thick iso coat a 2 | 0.0001 | 1.0E+04 | 1E-08 | 1E-04 | 1E-08 | 0.01 sec | 0.01 sec | 1.0E+01 | 1.0E+01 |
| thick iso coat a 3 | 0.0001 | 1.0E+05 | 1E-08 | 1E-04 | 1E-08 | 0.01 sec | 0.01 sec | 1.0E+01 | 1.0E+01 |
| thick iso coat a 4 | 0.0001 | 1.0E+06 | 1E-08 | 1E-04 | 1E-08 | 0.01 sec | 0.01 sec | 1.0E+01 | 1.0E+01 |
| thick iso coat a 5 | 0.0001 | 7.5E+02 | 1E-02 | 1E-02 | 1E-02 | 0.01 sec | 0.01 sec | 1.0E+01 | 1.0E+01 |
| thick iso coat a 6 | 0.0001 | 3.0E+01 | 1E-04 | 1E-04 | 1E-04 | 0.01 sec | 0.01 sec | 1.0E+01 | 1.0E+01 |
| thick iso coat a 7 | 0.0001 | 2.0E+04 | 1E-06 | 1E-06 | 1E-06 | 0.01 sec | 0.01 sec | 1.0E+01 | 1.0E+01 |

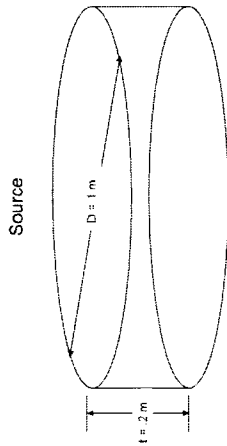
5/1/2007 12:27

Sheet Name: B: Thick Isotropic Solids with Coating
 Heat Path: Radial

Geometrical Dimensions	
Radius	1 m
Coating thickness	0.002 m
Substrate thickness	0.002 m
Substrate radius	1 m

Initial Conditions	
Initial Temperature	300 K
Initial Heat Flux	1300 W/m ²

Boundary conditions	
Surface 1	h = 2500 W/m ² K, T _{amb} = 300 K, Surface Area = 0.000314 m ²
Surface 2	h = 2500 W/m ² K, T _{amb} = 300 K, Surface Area = 0.000314 m ²
Surface 3	h = 2500 W/m ² K, T _{amb} = 300 K, Surface Area = 0.000314 m ²



Test Name	Coating material	Coating thickness (m)	Substrate material	Substrate thickness (m)	Substrate radius (m)	Substrate density (kg/m ³)	Substrate thermal conductivity (W/mK)	Substrate thermal diffusivity (m ² /s)	Substrate thermal expansion coefficient (1/K)
Thick Iso Coat 1	AlN	0.001	AlN	0.001	1	3000	1000	1E-05	1E-05
Thick Iso Coat 2	AlN	0.002	AlN	0.002	1	3000	1000	1E-05	1E-05
Thick Iso Coat 3	AlN	0.003	AlN	0.003	1	3000	1000	1E-05	1E-05
Thick Iso Coat 4	AlN	0.004	AlN	0.004	1	3000	1000	1E-05	1E-05
Thick Iso Coat 5	AlN	0.005	AlN	0.005	1	3000	1000	1E-05	1E-05
Thick Iso Coat 6	AlN	0.006	AlN	0.006	1	3000	1000	1E-05	1E-05
Thick Iso Coat 7	AlN	0.007	AlN	0.007	1	3000	1000	1E-05	1E-05

Sink

$$h_{eff} = \frac{1}{\frac{1}{h} + \frac{t_c}{k_c} + \frac{t_s}{k_s}}$$

Calculations for future reference:

Test Name	Coating material	Coating thickness (m)	Substrate material	Substrate thickness (m)	Substrate radius (m)	Substrate density (kg/m ³)	Substrate thermal conductivity (W/mK)	Substrate thermal diffusivity (m ² /s)	Substrate thermal expansion coefficient (1/K)
Thick Iso Coat 1	AlN	0.001	AlN	0.001	1	3000	1000	1E-05	1E-05
Thick Iso Coat 2	AlN	0.002	AlN	0.002	1	3000	1000	1E-05	1E-05
Thick Iso Coat 3	AlN	0.003	AlN	0.003	1	3000	1000	1E-05	1E-05
Thick Iso Coat 4	AlN	0.004	AlN	0.004	1	3000	1000	1E-05	1E-05
Thick Iso Coat 5	AlN	0.005	AlN	0.005	1	3000	1000	1E-05	1E-05
Thick Iso Coat 6	AlN	0.006	AlN	0.006	1	3000	1000	1E-05	1E-05
Thick Iso Coat 7	AlN	0.007	AlN	0.007	1	3000	1000	1E-05	1E-05

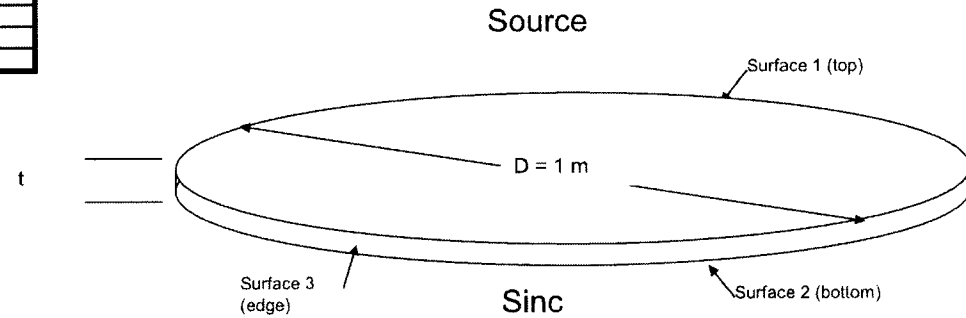
Study Name: 9: Thin Orthotropic Solid
Heat Path: Axial

5/29/2007 22:35

Model Dimensions		(THESE SHOULD NEVER CHANGE)	
Diameter	1 m	1000 mm	
Core thickness	0.002 m	2 mm	
Coating thickness	m	0 mm	

Initial Conditions:	
Initial Temperature	300 K
T _{gas}	1300 K

Boundary conditions:			
	h (W/m^2K)	T _{gas} (K)	Surface Area (m^2)
surface 1	500	1300	0.7854
surface 2	500	300	0.0063
surface 3	0	300 (insulated)	0.7854



Analyses:

Material	Core material	k-axial	k-radial	ratio k _{axial} /k _{radial}	Bi	Fo (0.01 sec)	Fo (0.1 sec)	Fo (1.0 sec)
thin ortho a 1	ortho 1	100	0.1	1.00E+03	1.00E-02	2.5E+01	2.5E+02	2.5E+03
thin ortho a 2	ortho 2	10	1	1.00E+01	1.00E-01	2.5E+00	2.5E+01	2.5E+02
thin ortho a 3	ortho 3	1	10	1.00E-01	1.00E+00	2.5E-01	2.5E+00	2.5E+01
thin ortho a 4	ortho 4	0.1	100	1.00E-03	1.00E+01	2.5E-02	2.5E-01	2.5E+00

$$\alpha = \frac{k}{\rho \cdot c_p}$$

$$F_o = t^* = \frac{\alpha t}{L^2}$$

$$Bi = \frac{hL_c}{k}$$

Study Name: 10: Thin Orthotropic Solid
Heat Path: Radial

5/29/2007 22:35

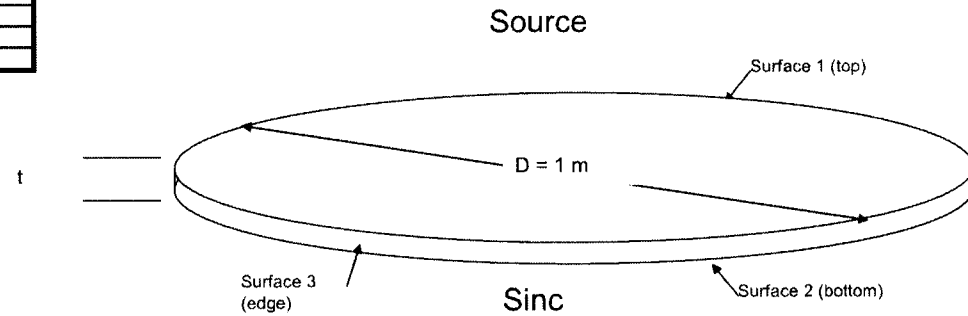
Model Dimensions				(THESE SHOULD NEVER CHANGE)			
Diameter	1	m	1000	mm			
Core thickness	0.002	m	2	mm			
Coating thickness		m	0	mm			

Initial Conditions:	
Initial Temperature	300 K
T_gas	1300 K

Boundary conditions:			
	h (W/m^2K)	Tgas (K)	Surface Areas (m^2)
surface 1	500	1300	0.7854
surface 2	0	300 (Insulated)	0.0063
surface 3	62500	300	0.7854

Analyses:

Material	Core material	k-axial	k-radial	ratio k_axial/k_radial	Bi	Fo (0.01 sec)	Fo (0.1 sec)	Fo (1.0 sec)
thin_ortho_r_1	ortho_1	100	0.1	1.00E+03	1.00E-02	2.5E+01	2.5E+02	2.5E+03
thin_ortho_r_2	ortho_2	10	1	1.00E+01	1.00E-01	2.5E+00	2.5E+01	2.5E+02
thin_ortho_r_3	ortho_3	1	10	1.00E-01	1.00E+00	2.5E-01	2.5E+00	2.5E+01
thin_ortho_r_4	ortho_4	0.1	100	1.00E-03	1.00E+01	2.5E-02	2.5E-01	2.5E+00



$$\alpha = \frac{k}{\rho \cdot c_p}$$

$$F_o = t^* = \frac{\alpha t}{L^2}$$

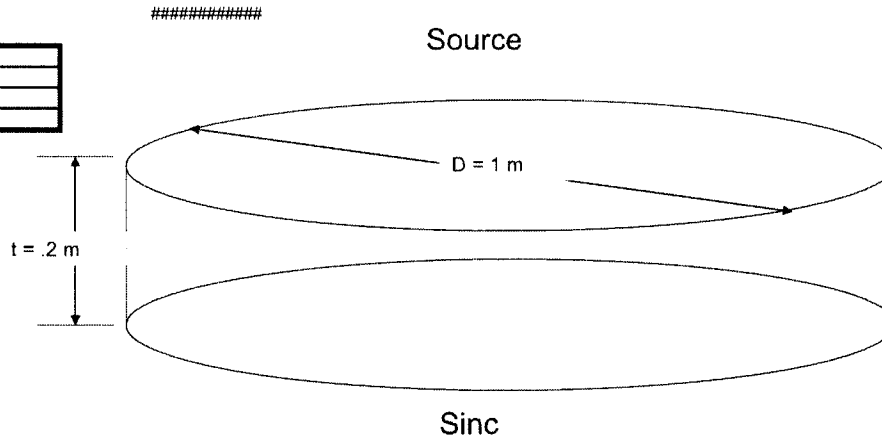
$$Bi = \frac{hL_c}{k}$$

Study Name: 11: Thick Orthotropic Solid
Heat Path: Axial

Model Dimensions (THESE SHOULD NEVER CHANGE)			
Diameter	1 m	1000 mm	
Core thickness	0.2 m	200 mm	
Coating thickness	m	0 mm	

Initial Conditions:	
Initial Temperatur	300 K
T_gas	1300 K

Boundary conditions:			
	h (W/m^2K)	Tgas (K)	Surface Areas (m^2)
surface 1	500	1300	0.7854
surface 2	500	300	0.6283
surface 3	0	300 (Insulated)	0.7854



Analyses:

Material	Core material	k-axial	k-radial	ratio k_axial/k_radial	Bi	Fo (0.01 sec)	Fo (0.1 sec)	Fo (1.0 sec)	Fo (10 sec)	Fo (100 sec)
thick_ortho_a_1	ortho_1	100	0.1	1.00E+03	1.00E+00	2.5E-03	2.5E-02	2.5E-01	2.5E+00	2.5E+01
thick_ortho_a_2	ortho_2	10	1	1.00E+01	1.00E+01	2.5E-04	2.5E-03	2.5E-02	2.5E-01	2.5E+00
thick_ortho_a_3	ortho_3	1	10	1.00E-01	1.00E+02	2.5E-05	2.5E-04	2.5E-03	2.5E-02	2.5E-01
thick_ortho_a_4	ortho_4	0.1	100	1.00E-03	1.00E+03	2.5E-06	2.5E-05	2.5E-04	2.5E-03	2.5E-02

$$\alpha = \frac{k}{\rho \cdot c_p}$$

$$Fo = t^* = \frac{\alpha}{L^2}$$

$$Bi = \frac{hL_c}{k}$$

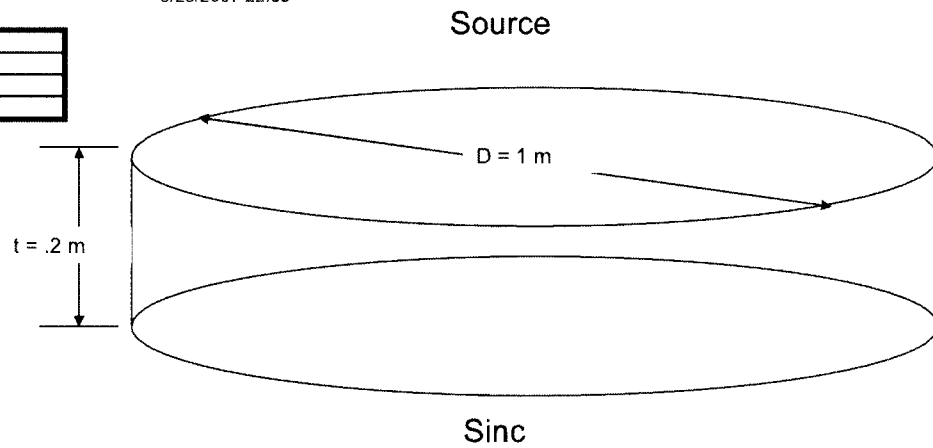
Study Name: 12: Thick Orthotropic Solid
Heat Path: Radial

5/29/2007 22:35

Model Dimensions (THESE SHOULD NEVER CHANGE)			
Diameter	1	m	1000
Core thickness	0.2	m	200
Coating thickness		m	0

Initial Conditions:	
Initial Temperatur	300
T_gas	1300

Boundary conditions:			
	h (W/m^2)	Tgas (K)	Surface Areas (m^2)
surface 1	500	1300	0.7854
surface 2	0	300	insulated 0.6283
surface 3	625	300	0.7854



Analyses:

Material	Core material	k-axial	k-radial	ratio k_axial/k_radial	Bi	Fo (0.01 sec)	Fo (0.1 sec)	Fo (1.0 sec)	Fo (10 sec)	Fo (100 sec)
thick_ortho_r_1	ortho_1	100	0.1	1.00E+03	1.00E+00	2.5E-03	2.5E-02	2.5E-01	2.5E+00	2.5E+01
thick_ortho_r_2	ortho_2	10	1	1.00E+01	1.00E+01	2.5E-04	2.5E-03	2.5E-02	2.5E-01	2.5E+00
thick_ortho_r_3	ortho_3	1	10	1.00E-01	1.00E+02	2.5E-05	2.5E-04	2.5E-03	2.5E-02	2.5E-01
thick_ortho_r_4	ortho_4	0.1	100	1.00E-03	1.00E+03	2.5E-06	2.5E-05	2.5E-04	2.5E-03	2.5E-02

$$\alpha = \frac{k}{\rho \cdot c_p}$$

$$F_o = i^* = \frac{\alpha t}{L^2}$$

$$Bi = \frac{hL_c}{k}$$

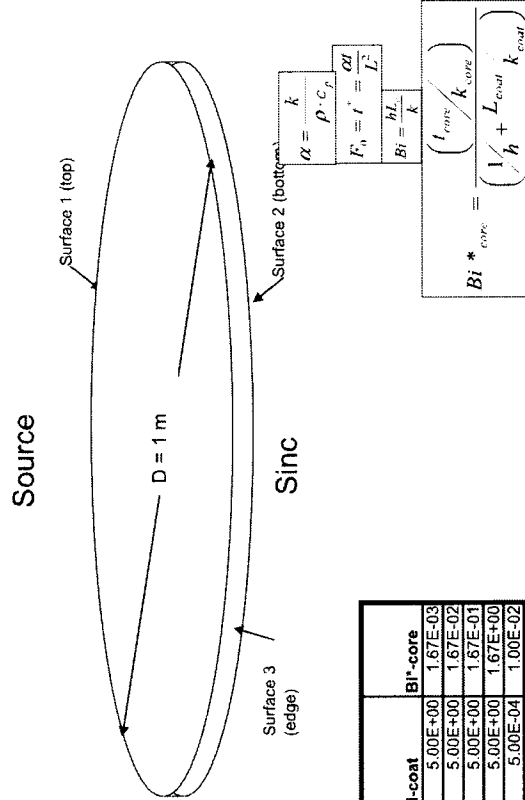
Study Name: 13: Thin orthotropic solid with coating
Heat Path: Axial

Modal Dimensions	(THESE SHOULD NEVER CHANGE)
Diameter	1 m 1000 mm
Core thickness	0.002 m 2 mm
Coating thickness	0.0001 m 0.1 mm

Initial Conditions:	
Initial Temperature	300 K
T _{gas}	1300 K

Boundary conditions:	h (W/m ² K)	T _{gas} (K)	Surface Areas (m ²)
surface 1	500	1300	0.7854
surface 2	500	300	0.0063
surface 3	0	300 (Insulated)	0.7854

#####



Material:	Core	Coating	Ratio	BI-coat	BI-core
thin_ortho_coat_a	material	k-axial	k-radial	k-coating	k-coating / k-axial
1	ortho_1	100	0.1 iso_2	1.00E-02	1.00E-04
2	ortho_2	10	1 iso_2	1.00E-02	1.00E-03
3	ortho_3	1	10 iso_2	1.00E-02	1.00E-02
4	ortho_4	0.1	100 iso_2	1.00E-02	1.00E-01
5	ortho_1	100	0.1 iso_6	1.00E+02	1.00E+00
6	ortho_2	10	1 iso_6	1.00E+02	1.00E+01
7	ortho_3	1	10 iso_6	1.00E+02	1.00E+02
8	ortho_4	0.1	100 iso_6	1.00E+02	1.00E+03

Calculations for future use

Material:	Fo-coat (0.01 sec)	Fo-coat (0.1 sec)	Fo-coat (1.0 sec)	Fo-core (0.1 sec)	Fo-core (1.0 sec)	Fo-coat/ Fo-core (0.1 sec)	Fo-coat/ Fo-core (1.0 sec)
1	1.00E+00	1.00E+01	1.00E+02	2.5E+01	2.5E+02	4.0E-02	4.0E-02
2	1.00E+00	1.00E+01	1.00E+02	2.5E+00	2.5E+01	4.0E-01	4.0E-01
3	1.00E+00	1.00E+01	1.00E+02	2.5E-01	2.5E+00	4.0E+00	4.0E+00
4	1.00E+00	1.00E+01	1.00E+02	2.5E-02	2.5E+01	4.0E+01	4.0E+01
5	1.00E+04	1.00E+05	1.00E+06	2.5E+01	2.5E+02	4.0E+02	4.0E+02
6	1.00E+04	1.00E+05	1.00E+06	2.5E+00	2.5E+01	4.0E+03	4.0E+03
7	1.00E+04	1.00E+05	1.00E+06	2.5E-01	2.5E+00	4.0E+04	4.0E+04
8	1.00E+04	1.00E+05	1.00E+06	2.5E-02	2.5E+01	4.0E+05	4.0E+05

5/29/2007 22:35

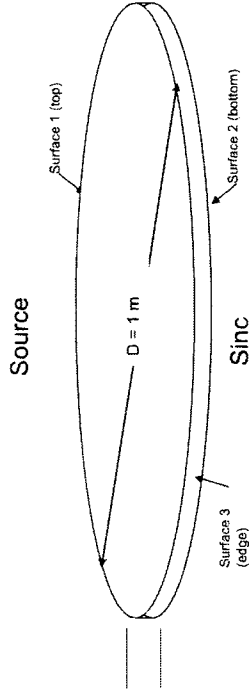
Study Name: 14: Thin orthotropic solid with coating

Heat Path: Radial

Model Dimensions		(THESE SHOULD NEVER CHANGE)	
Diameter	1 m	1000	mm
Core thickness	0.002 m	2	mm
Coating thickness	0.0001 m	0.1	mm

Initial Conditions:	
Initial Temperature	300 K
T _{gas}	1300 K

Boundary conditions:		Surface Areas (m ²)	
surface 1	h (W/m ² K) 500	T _{gas} (K) 1300	0.7854
surface 2	0	300 Insulated	0.0063
surface 3	62500	300	0.7854



$$\alpha = \frac{k}{p \cdot c \cdot B}$$

$$F_n = r = \frac{\alpha}{L}$$

$$Bi = \frac{hL}{k}$$

$$Bi^*_{conv} = \left(\frac{L_{conv}/k_{conv}}{L/h + L_{conv}/k_{conv}} \right)$$

Analysis:

Material:	Core	k-axial	k-radial	coating	k coating	ratio k coating / k axial	Bi-coat-axial	ratio k coating / k radial	Bi*-coating axial	Bi-coat-radial	Bi*-core-radial	Bb axial	Bi-coat-radial	Bi*-core-radial	Bb radial
1	ortho 1	100	0.1	iso 2	1.00E-02	1.00E-04	5.00E+00	1.00E-01	1.67E-03	2.50E+04	1.00E-01	3.00E+03	2.50E+04	1.00E-01	2.50E+05
2	ortho 2	10	10	iso 2	1.00E-02	1.00E-03	5.00E+00	1.00E-02	1.67E-02	2.50E+04	1.00E-02	3.00E+02	2.50E+04	1.00E-02	2.50E+06
3	ortho 3	1	10	iso 2	1.00E-02	1.00E-02	5.00E+00	1.00E-03	1.67E-01	2.50E+04	1.00E-03	3.00E+01	2.50E+04	1.00E-03	2.50E+07
4	ortho 4	0.1	100	iso 2	1.00E-02	1.00E-01	5.00E+00	1.00E-04	1.67E+00	2.50E+04	1.00E-04	3.00E+00	2.50E+04	1.00E-04	2.50E+08
5	ortho 1	100	0.1	iso 6	1.00E+02	1.00E+00	5.00E+04	1.00E+03	1.00E+02	2.50E+00	7.14E+02	5.00E+02	2.50E+00	7.14E+02	3.50E+03
6	ortho 2	10	10	iso 6	1.00E+02	1.00E+01	5.00E+04	1.00E+02	1.00E+01	2.50E+00	7.14E+01	5.00E+03	2.50E+00	7.14E+01	3.50E+02
7	ortho 3	1	100	iso 6	1.00E+02	1.00E+02	5.00E+04	1.00E+01	1.00E+00	2.50E+00	7.14E+00	5.00E+04	2.50E+00	7.14E+00	3.50E+01
8	ortho 4	0.1	100	iso 6	1.00E+02	1.00E+03	5.00E+04	1.00E+00	1.00E+01	2.50E+00	7.14E+01	5.00E+05	2.50E+00	7.14E+01	3.50E+00

Calculations for future use

Material:	thin_ortho_coat_r	Fo-coat (0.1 sec)	Fo-coat (1.0 sec)	Fo-coat (0.1 sec)	Fo-coat (1.0 sec)	Fo-core-axial (0.01 sec)	Fo-core-axial (1.0 sec)	Fo-core-radial (0.01 sec)	Fo-core-radial (1.0 sec)	Fo-coat/ Fo-core-axial (0.1 sec)	Fo-coat/ Fo-core-axial (1.0 sec)	Fo-coat/ Fo-core-radial (0.1 sec)	Fo-coat/ Fo-core-radial (1.0 sec)
1	1.00E-04	1.00E-03	1.00E-02	2.5E-02	2.5E-03	2.5E-02	2.5E-01	2.5E-02	2.5E-01	4.00E-06	4.00E-06	4.00E-03	4.00E-03
2	1.00E-04	1.00E-03	1.00E-02	2.5E+00	2.5E+01	2.5E+02	2.5E+01	2.5E+02	2.5E+01	4.00E-05	4.00E-05	4.00E-04	4.00E-04
3	1.00E-04	1.00E-03	1.00E-02	2.5E-01	2.5E-01	2.5E+00	2.5E+01	2.5E+02	2.5E+01	4.00E-04	4.00E-04	4.00E-05	4.00E-05
4	1.00E-04	1.00E-03	1.00E-02	2.5E-01	2.5E-01	2.5E+00	2.5E+01	2.5E+03	2.5E+01	4.00E-03	4.00E-03	4.00E-06	4.00E-06
5	1.00E+00	1.00E+01	1.00E+02	2.5E+01	2.5E+02	2.5E+03	2.5E+01	2.5E+02	2.5E+01	4.00E-02	4.00E-02	4.00E-01	4.00E-01
6	1.00E+00	1.00E+01	1.00E+02	2.5E+00	2.5E+01	2.5E+02	2.5E+01	2.5E+02	2.5E+01	4.00E-01	4.00E-01	4.00E+00	4.00E+00
7	1.00E+00	1.00E+01	1.00E+02	2.5E+01	2.5E+01	2.5E+01	2.5E+01	2.5E+02	2.5E+01	4.00E+00	4.00E+00	4.00E-01	4.00E-01
8	1.00E+00	1.00E+01	1.00E+02	2.5E-02	2.5E-01	2.5E+00	2.5E+01	2.5E+03	2.5E-02	4.00E-01	4.00E-01	4.00E-02	4.00E-02

5/29/2007 22:35

Study Name: 15: Thick orthotropic solid with coating

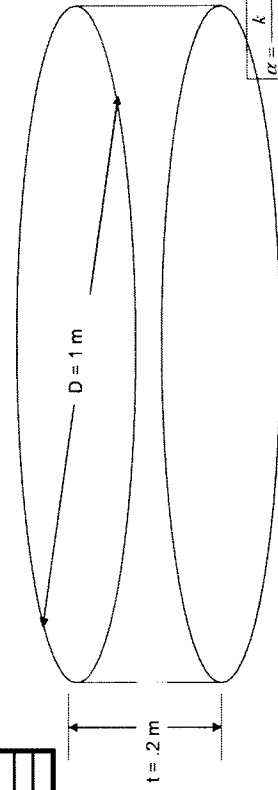
Heat Path: Axial

Model Dimensions		(THESE SHOULD NEVER CHANGE)	
Diameter	1 m	1000 mm	
Core thickness	0.2 m	200 mm	
Coating thickness	0.0001 m	0.1 mm	

Initial Conditions:	
Initial Temperature	300 K
T _{gas}	1300 K

Boundary conditions:	
h (W/m ² K)	Surface
Area (m ²)	0.7854
Surface 1	500
Surface 2	300
Surface 3	0
	300
	Inclined
	0.7854

Source



Sinc

$$\alpha = \frac{k}{\rho \cdot c_p}$$

$$Fo_{core} = \frac{t_{core}^2}{L_c^2} \frac{\alpha}{k_{core}}$$

$$Bi = \frac{h L_c}{k}$$

$$Bi^*_{core} = \left(\frac{t_{core}}{h} + \frac{L_{out}}{k_{out}} \right) \frac{\alpha}{k_{core}}$$

Analyses:

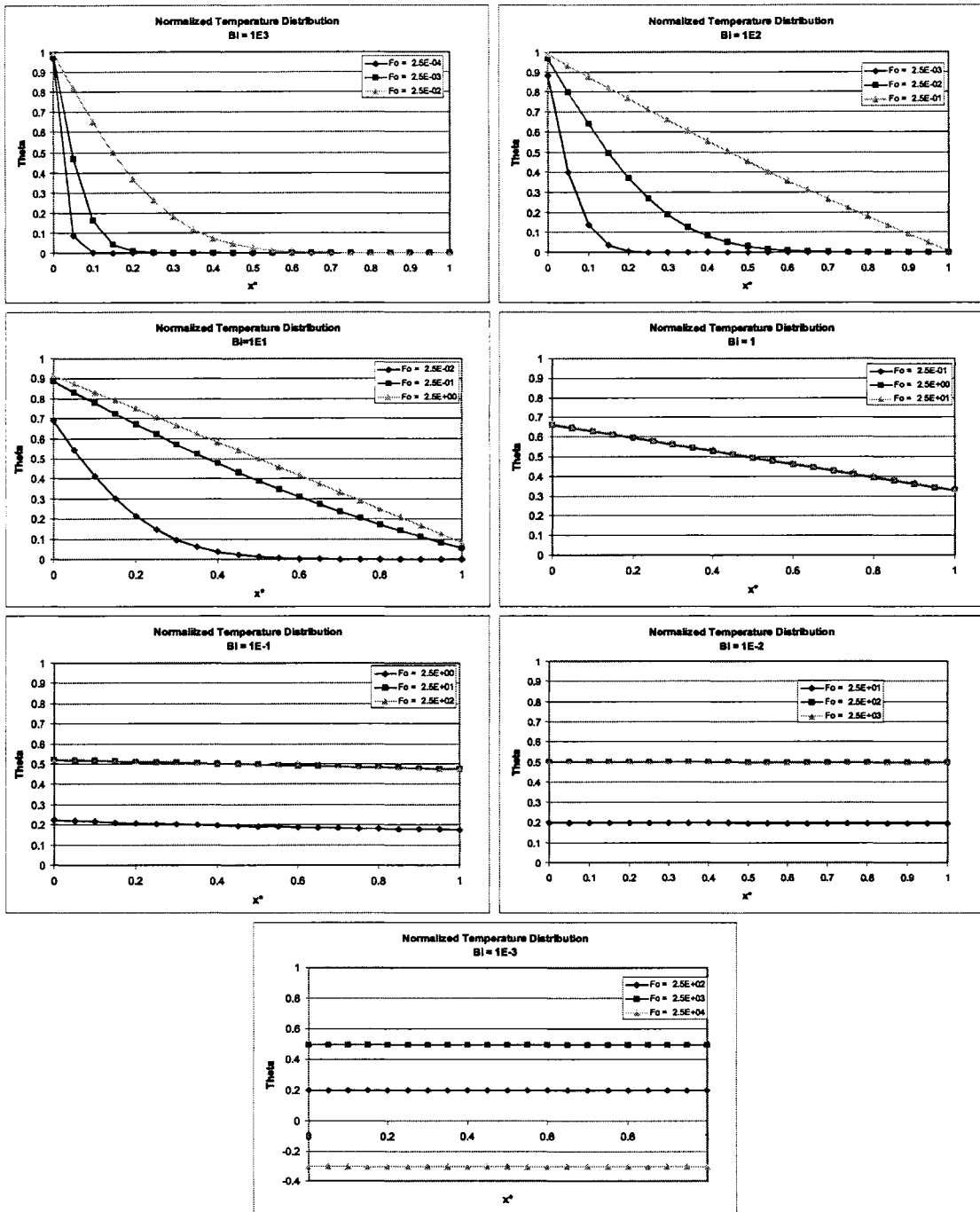
Material:	thick_ortho_coat_a	Core material	k-axial	k-radial	k-coating	coating	ratio	k-coating / k-axial	Bi-coat
1	ortho_1	100	0.1	iso_2	1.00E-02	1.00E-04	5.00E+00	1.00E-02	5.00E+00
2	ortho_2	10	10	iso_2	1.00E-02	1.00E-03	5.00E+00	1.00E-02	5.00E+00
3	ortho_3	1	10	iso_2	1.00E-02	1.00E-02	5.00E+00	1.00E-02	5.00E+00
4	ortho_4	0.1	100	iso_2	1.00E-02	1.00E-01	5.00E+00	1.00E-02	5.00E+00
5	ortho_1	100	0.1	iso_6	1.00E+02	1.00E+00	5.00E-04	1.00E+02	5.00E-04
6	ortho_2	10	10	iso_6	1.00E+02	1.00E+01	5.00E-04	1.00E+02	5.00E-04
7	ortho_3	1	10	iso_6	1.00E+02	1.00E+02	5.00E-04	1.00E+02	5.00E-04
8	ortho_4	0.1	100	iso_6	1.00E+02	1.00E+03	5.00E-04	1.00E+02	5.00E-04

Calculations for future use

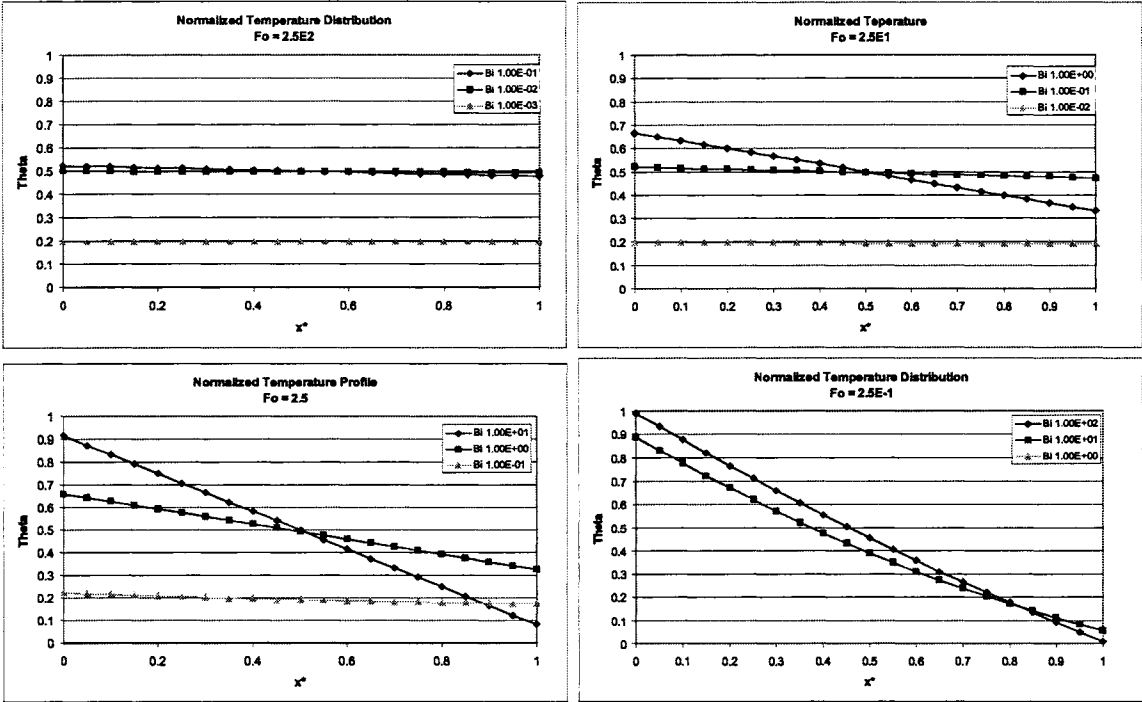
Material:	thick_ortho_coat_a	Fo-coat (0.01 sec)	Fo-coat (0.1 sec)	Fo-coat (1.0 sec)	Fo-coat (10 sec)	Fo-coat (100 sec)	Fo-core (0.01 sec) axial	Fo-core (0.1 sec) axial	Fo-core (1.0 sec) axial	Fo-core (10 sec) axial	Fo-core (100 sec) axial	Fo-coat/ Fo-core (0.01 sec)	Fo-coat/ Fo-core (0.1 sec)	Fo-coat/ Fo-core (1.0 sec)	Fo-coat/ Fo-core (10 sec)	Fo-coat/ Fo-core (100 sec)
1	ortho_1	1.00E+00	1.00E+01	1.00E+02	1.00E+03	1.00E+04	2.5E-03	2.5E-02	2.5E-01	2.5E+00	2.5E+01	4.00E+02	4.00E+02	4.00E+02	4.00E+02	4.00E+02
2	ortho_2	1.00E+00	1.00E+01	1.00E+02	1.00E+03	1.00E+04	2.5E-04	2.5E-03	2.5E-02	2.5E-01	2.5E+00	4.00E+03	4.00E+03	4.00E+03	4.00E+03	4.00E+03
3	ortho_3	1.00E+00	1.00E+01	1.00E+02	1.00E+03	1.00E+04	2.5E-05	2.5E-04	2.5E-03	2.5E-02	2.5E-01	4.00E+04	4.00E+04	4.00E+04	4.00E+04	4.00E+04
4	ortho_4	1.00E+00	1.00E+01	1.00E+02	1.00E+03	1.00E+04	2.5E-06	2.5E-05	2.5E-04	2.5E-03	2.5E-02	4.00E+05	4.00E+05	4.00E+05	4.00E+05	4.00E+05
5	ortho_1	1.00E+04	1.00E+05	1.00E+06	1.00E+07	1.00E+08	2.5E-03	2.5E-02	2.5E-01	2.5E+00	2.5E+01	4.00E+06	4.00E+06	4.00E+06	4.00E+06	4.00E+06
6	ortho_2	1.00E+04	1.00E+05	1.00E+06	1.00E+07	1.00E+08	2.5E-04	2.5E-03	2.5E-02	2.5E-01	2.5E+00	4.00E+07	4.00E+07	4.00E+07	4.00E+07	4.00E+07
7	ortho_3	1.00E+04	1.00E+05	1.00E+06	1.00E+07	1.00E+08	2.5E-05	2.5E-04	2.5E-03	2.5E-02	2.5E-01	4.00E+08	4.00E+08	4.00E+08	4.00E+08	4.00E+08
8	ortho_4	1.00E+04	1.00E+05	1.00E+06	1.00E+07	1.00E+08	2.5E-06	2.5E-05	2.5E-04	2.5E-03	2.5E-02	4.00E+09	4.00E+09	4.00E+09	4.00E+09	4.00E+09

Appendix 5: Normalized data for axial heat path cases

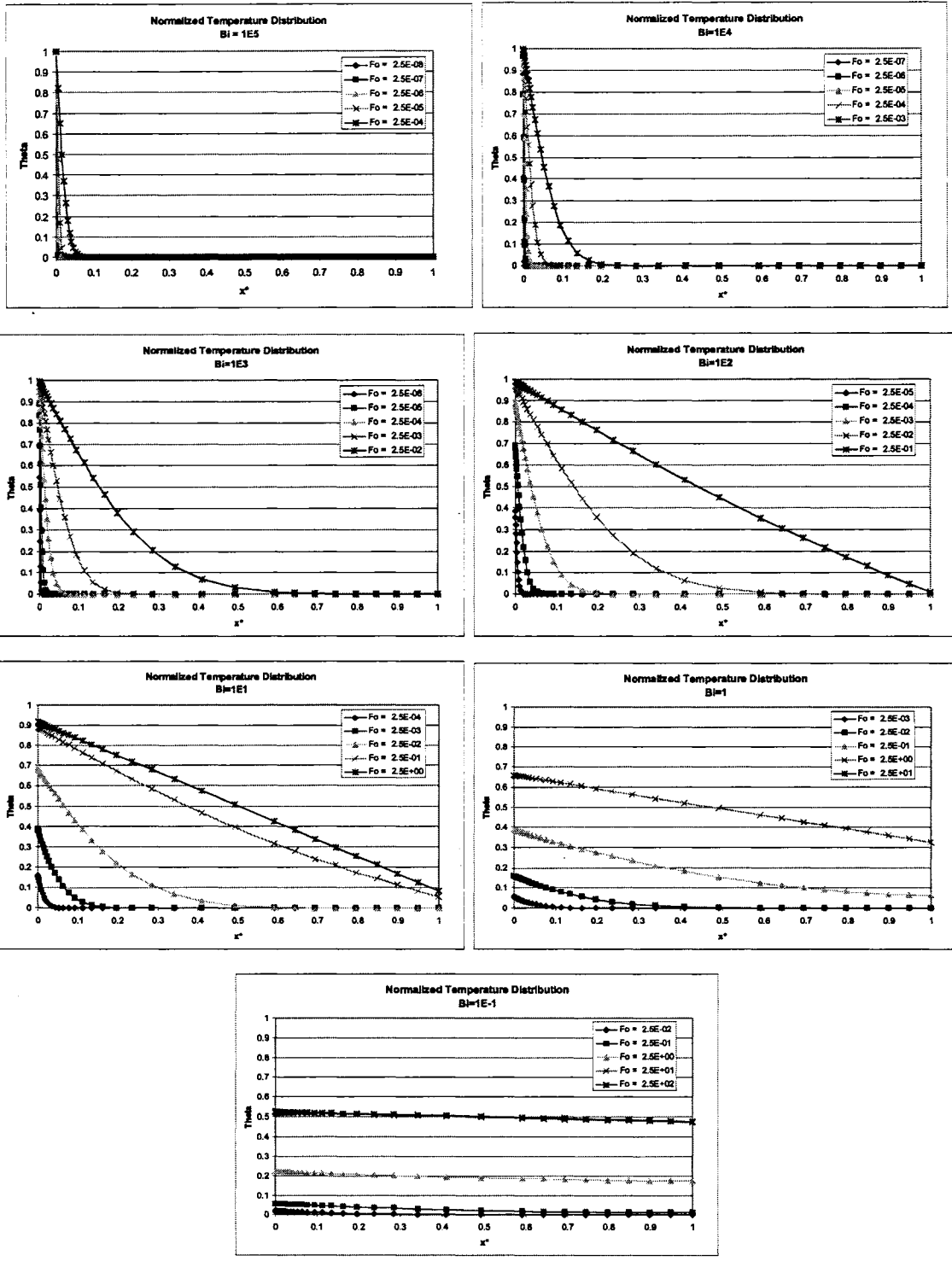
Case 1: thin-iso-a normalized plots



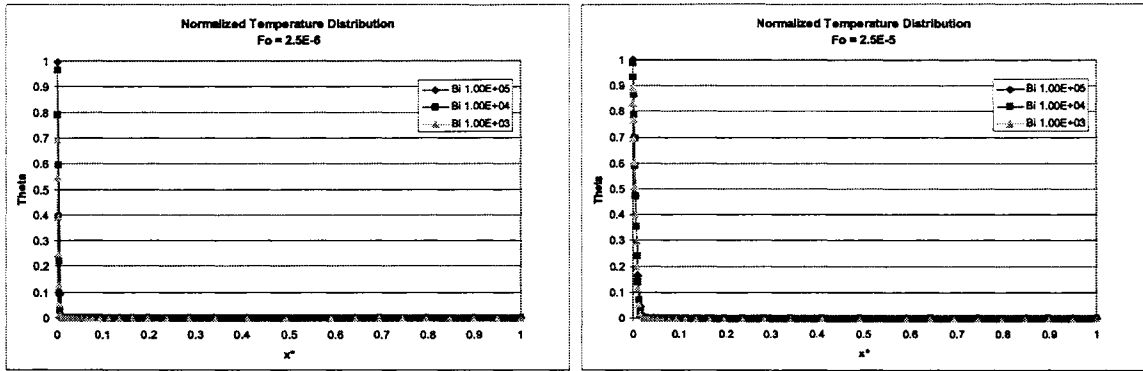
Case 1: thin-iso-a normalized plots



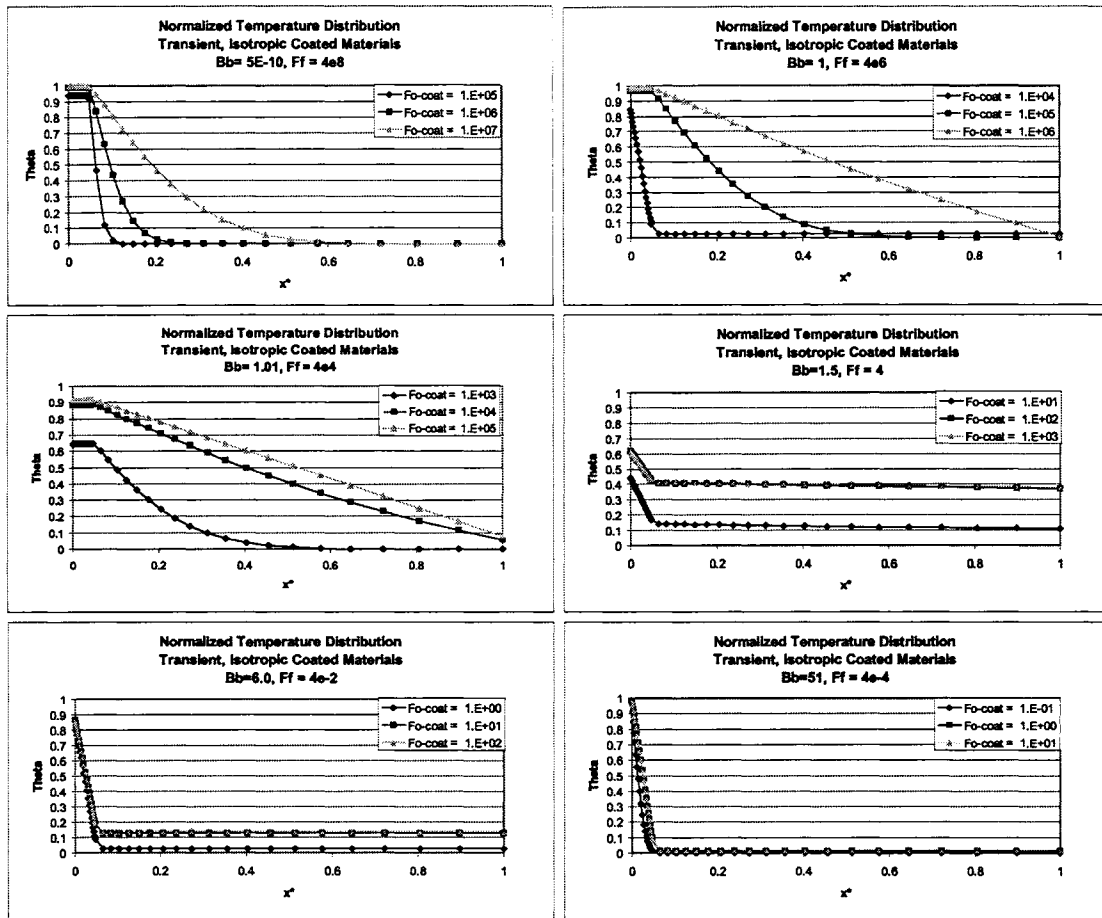
Case 3: thick-iso-a normalized plots



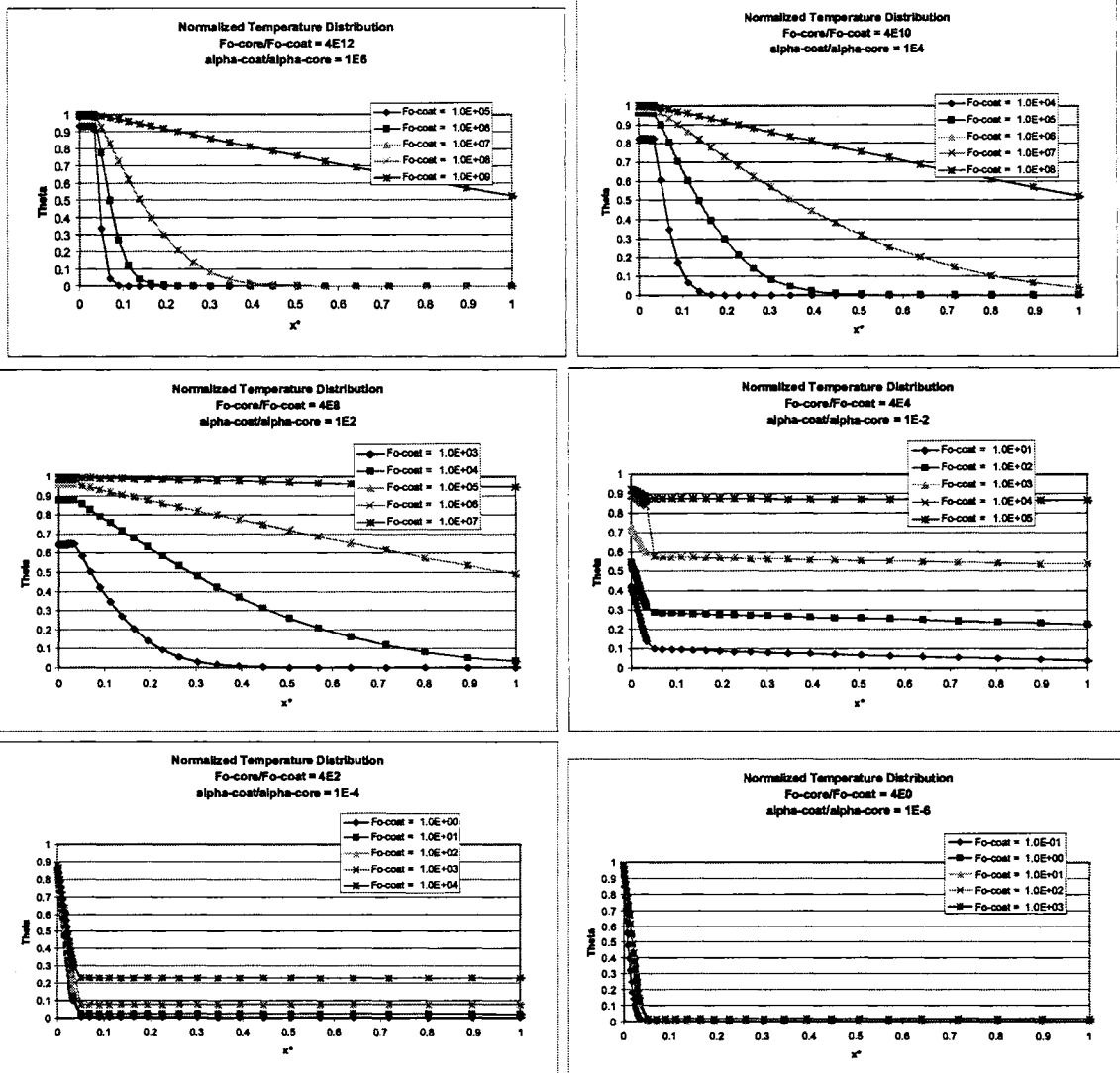
Case 3: thick-iso-a normalized plots



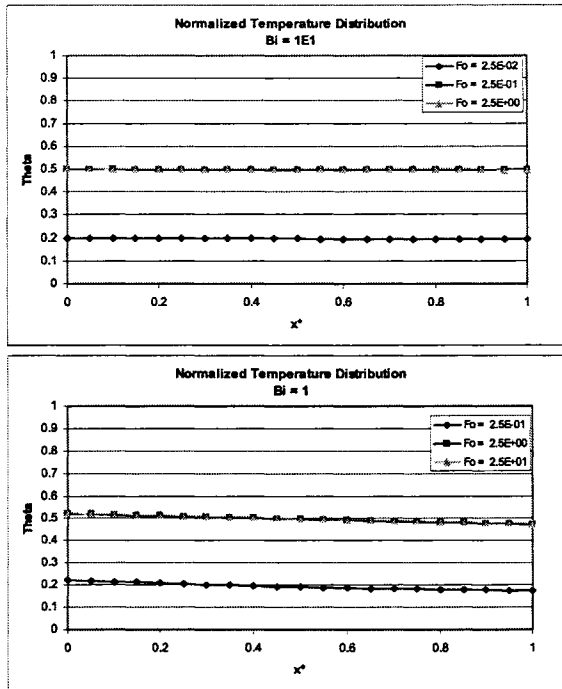
Case 5: thin-iso-coat-a normalized plots



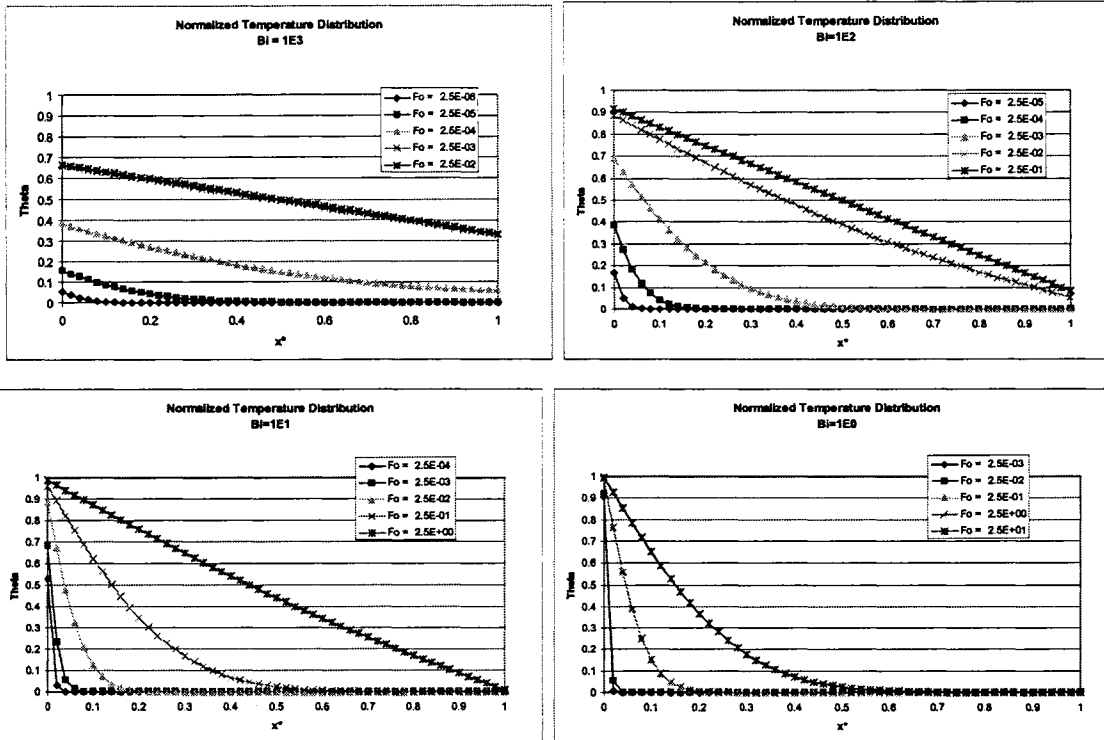
Case 7: thick-iso-coat-a normalized plots



Case 9: thin-ortho-a normalized plots

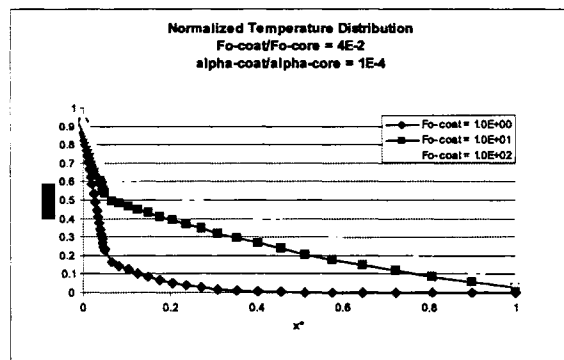
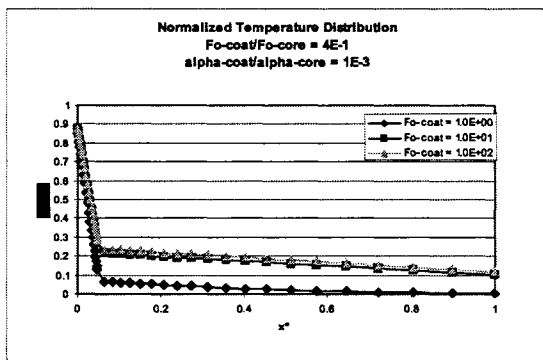
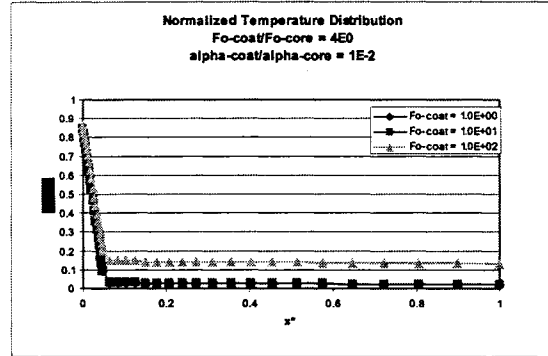
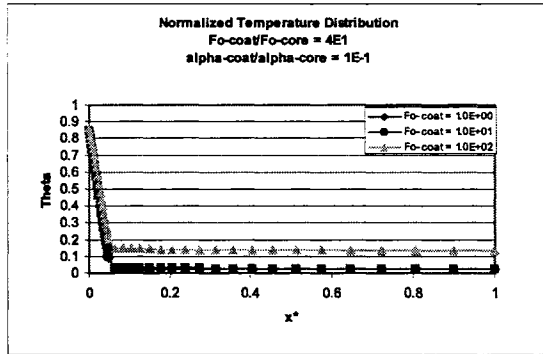


Case 11: thick-ortho-a normalized plots



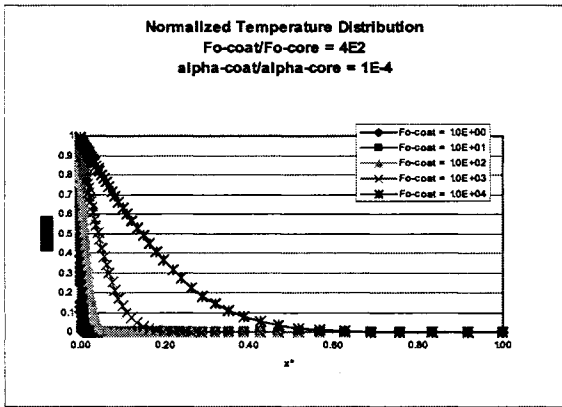
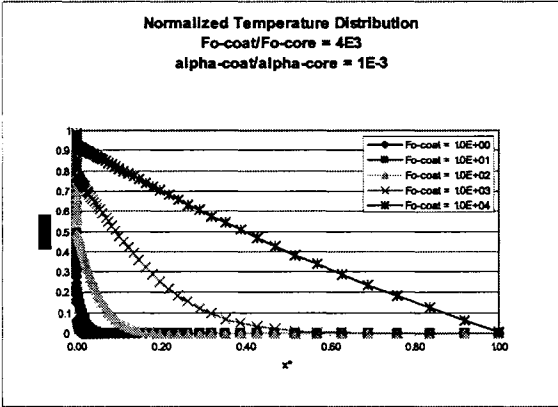
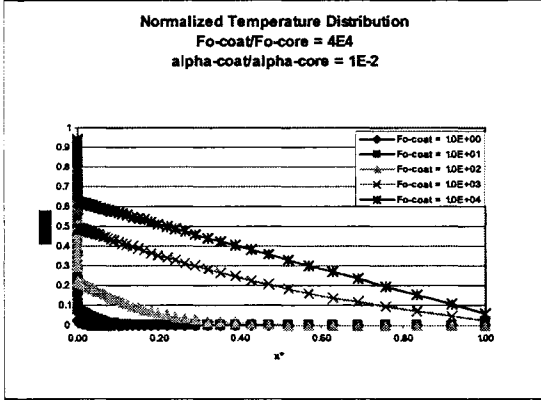
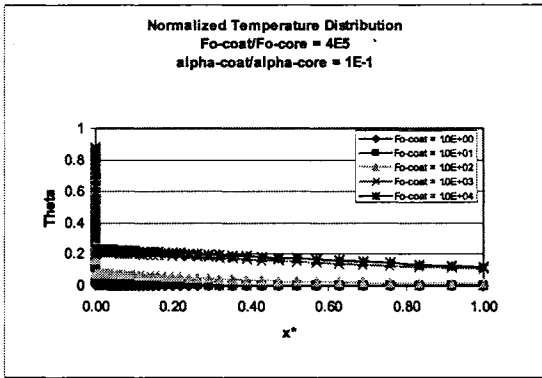
Case 13: thin-ortho-coat-a normalized plots

Insulating Coating



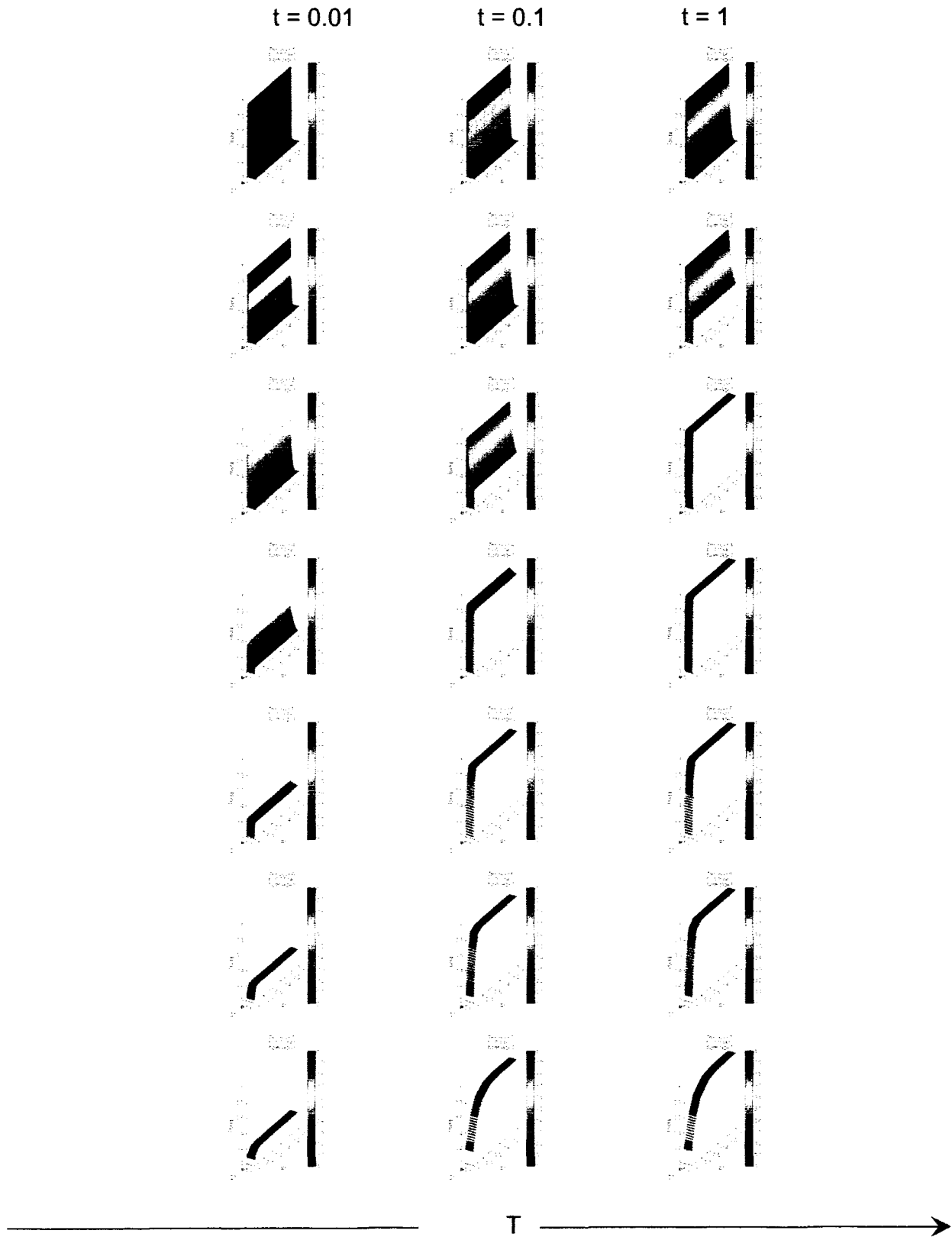
Case 15: thick-ortho-coat-a normalized plots

Insulating Coating

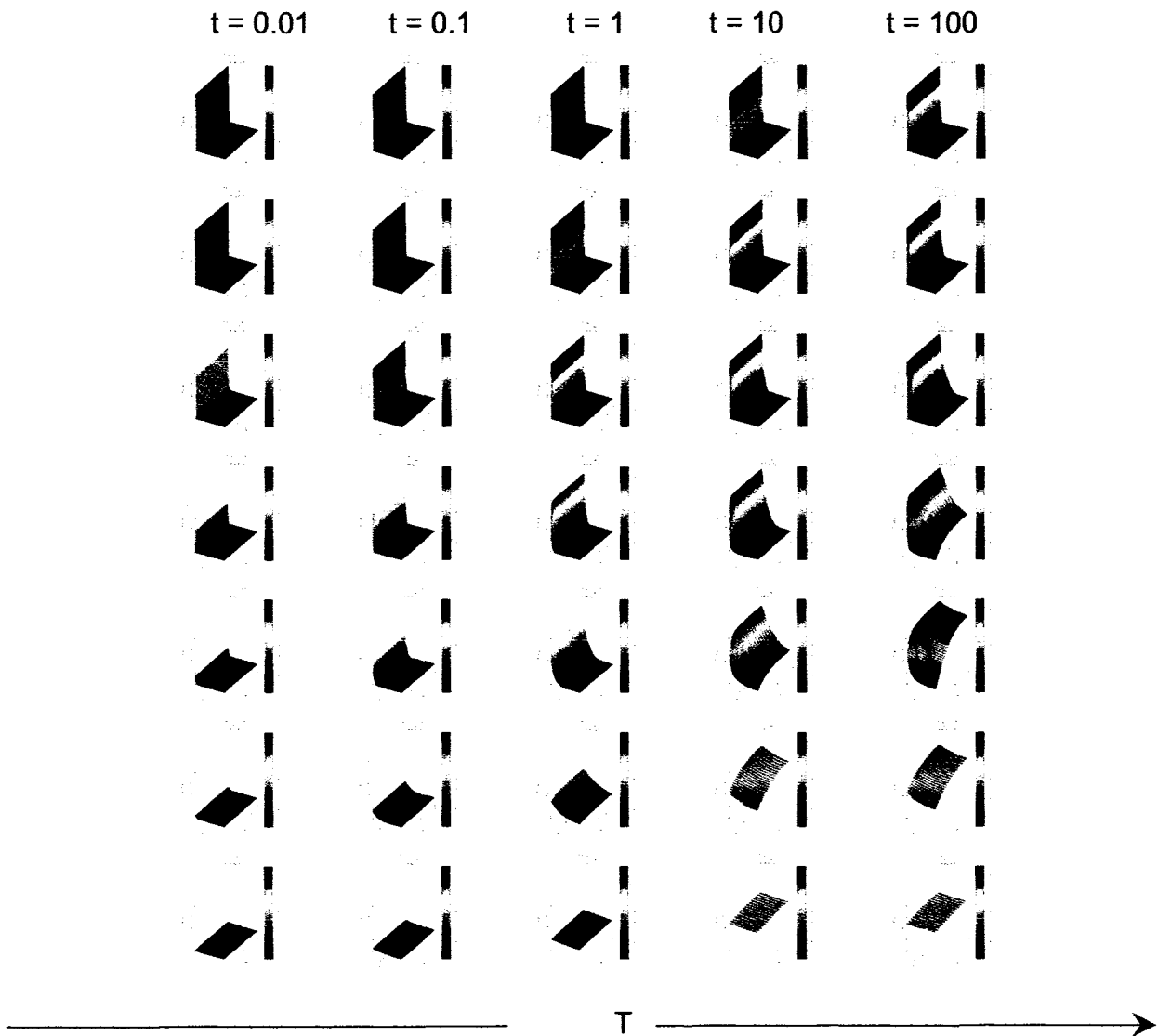


Appendix 6: Normalized data for radial heat path cases

Case 2: Thin-iso-r-summary plots

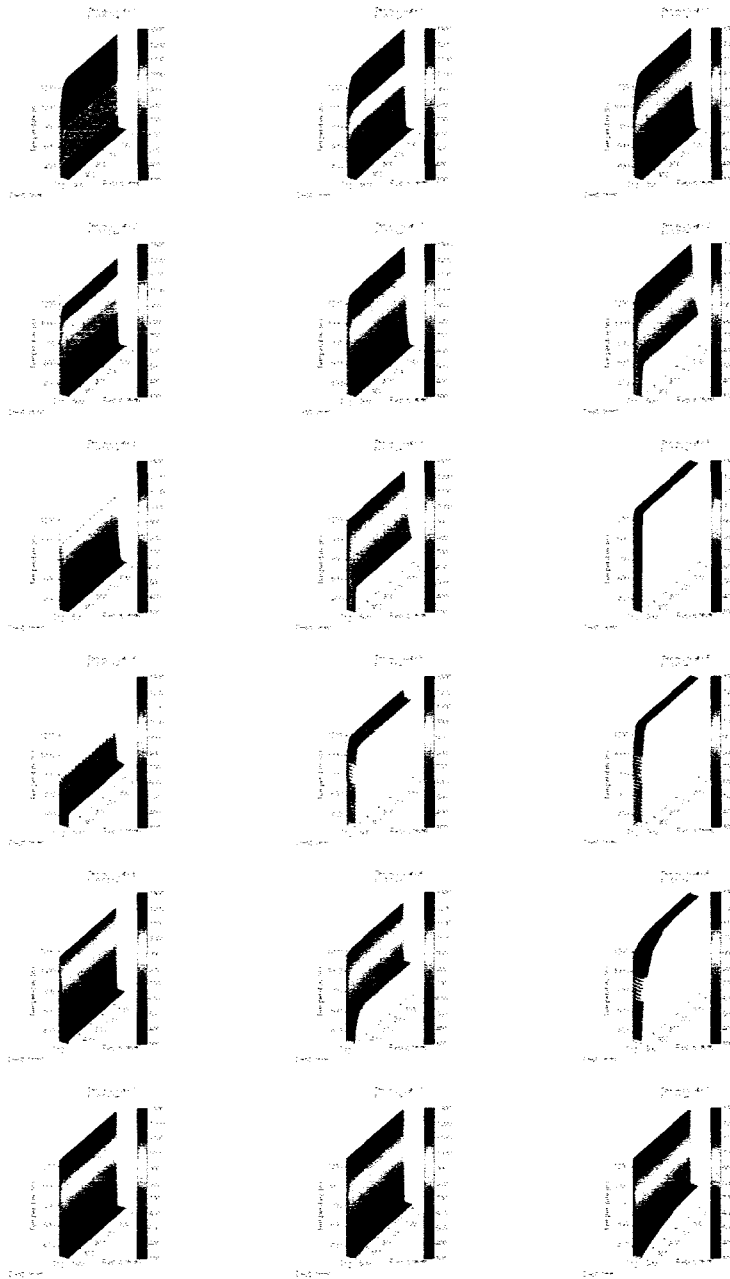


Case 4: Thick-iso-r normalized plots



Case 6: Thin-iso-coat-r summary plots

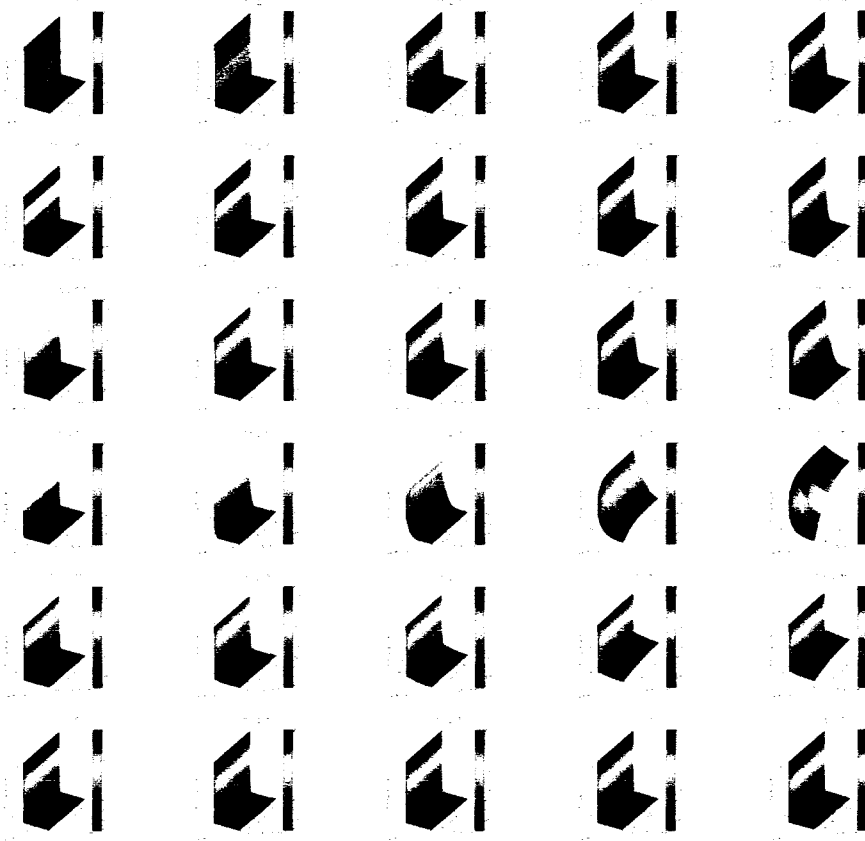
t = 0.01 sec t = 0.1 sec t = 1.0 sec



T →

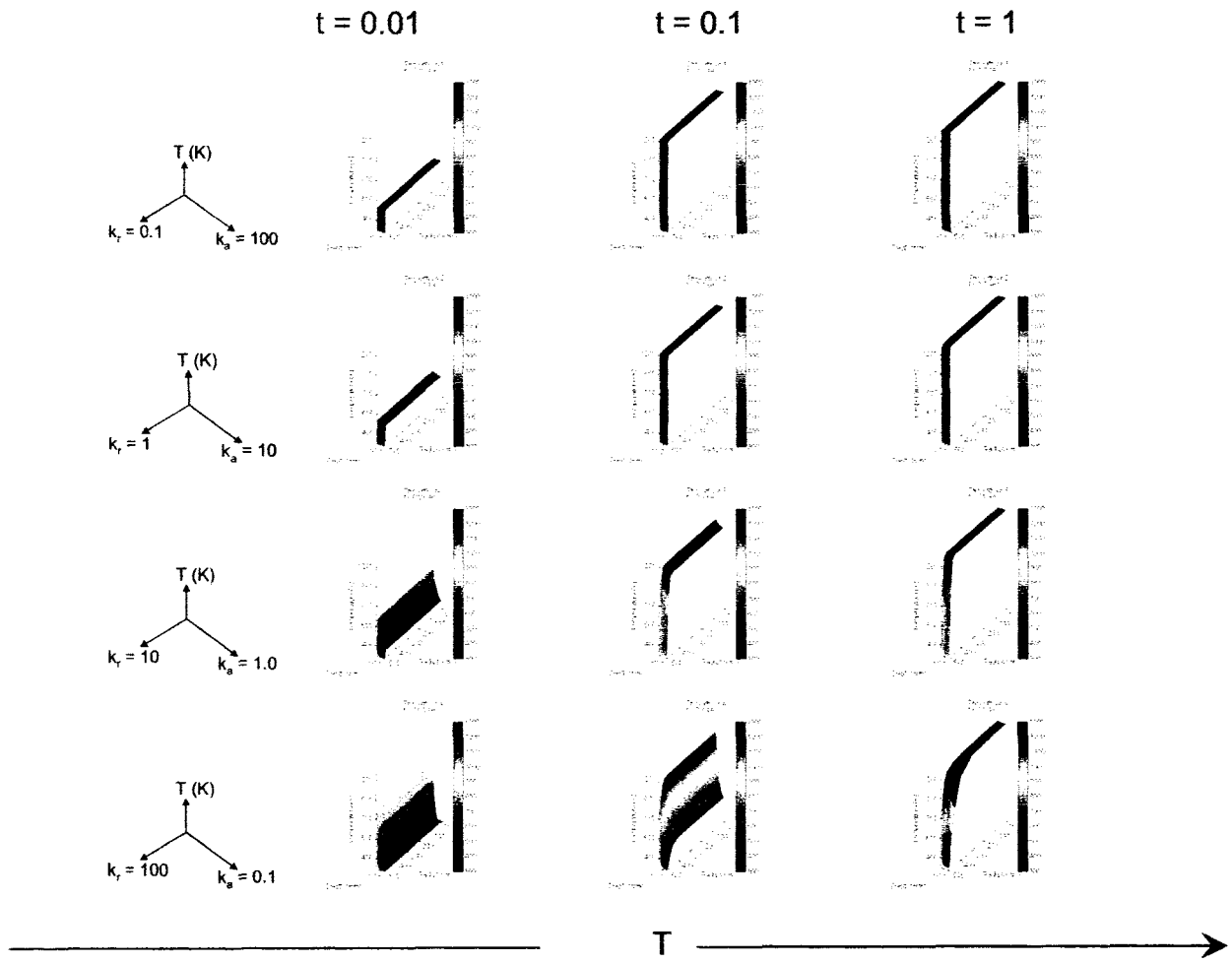
Case 8: Thick-iso-coat-r summary plots

t = 0.01 sec t = 0.1 sec t = 1.0 sec t = 10 sec t = 100 sec

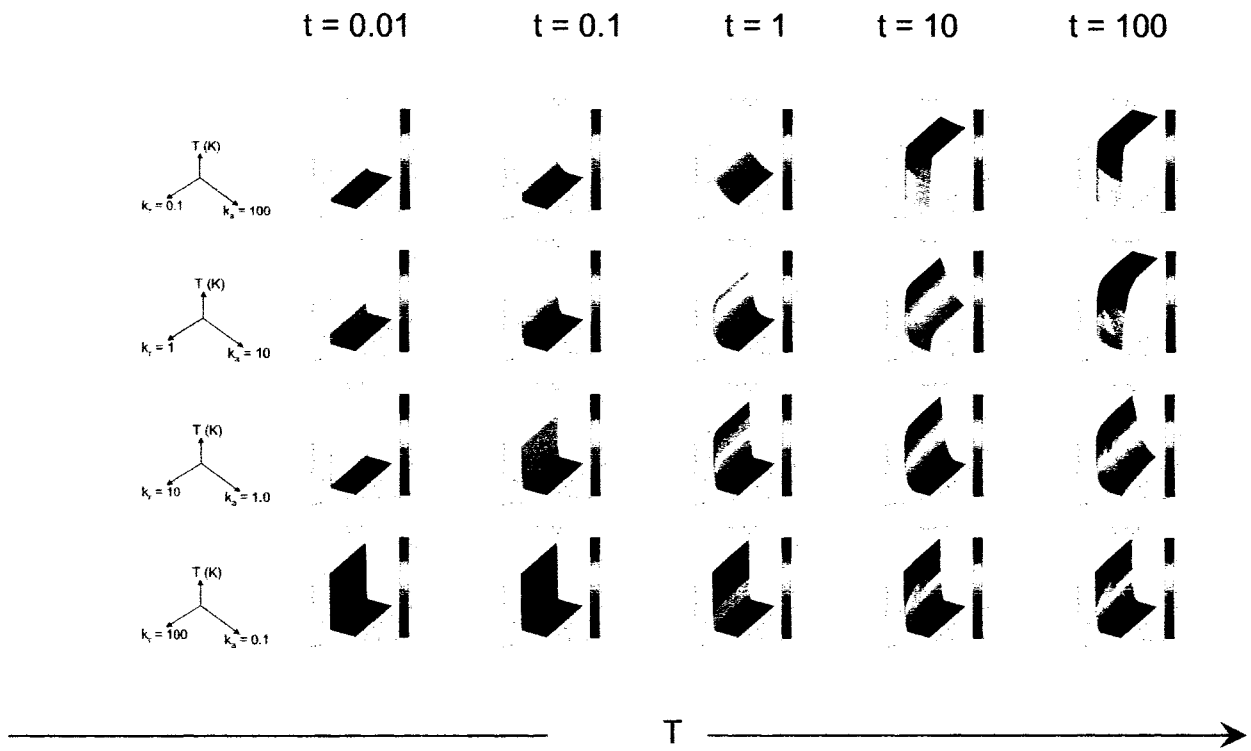


————— T —————>

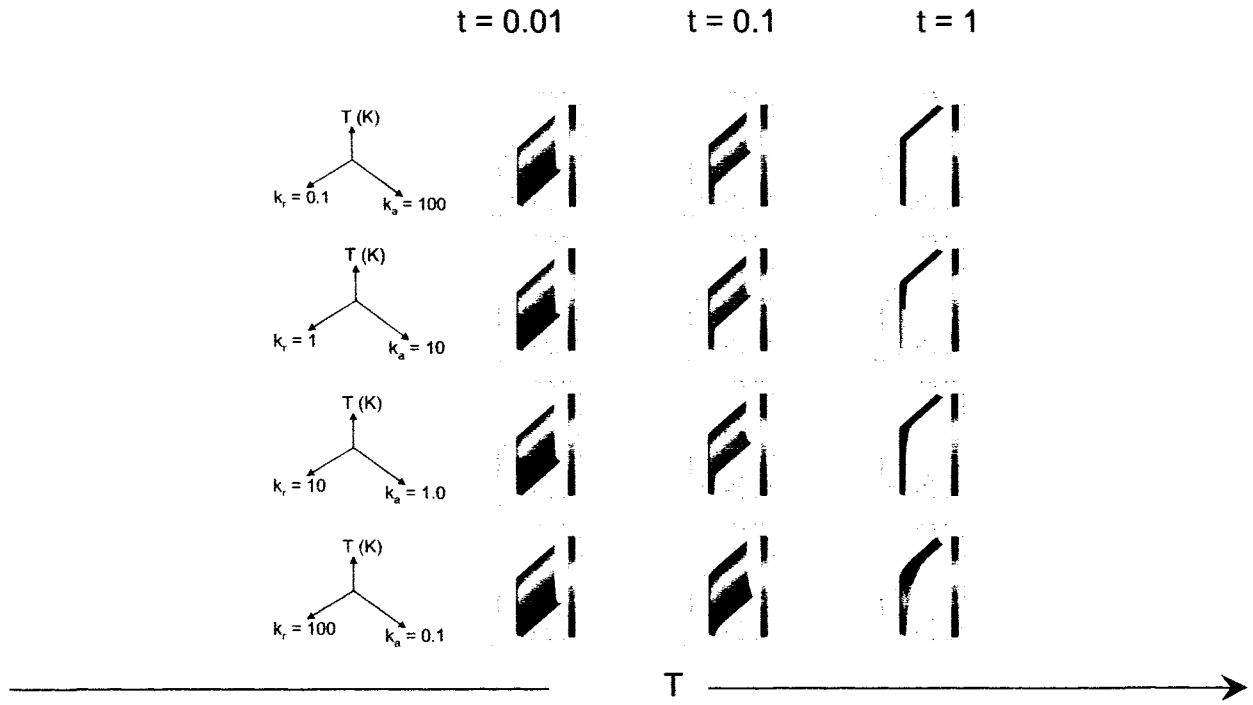
Case 10: Thin-ortho-r-summary plots



Case 12: Thick-ortho-r-summary plots



Case 14: Thin-ortho-coat-r-summary plots
 Coating = iso_2 (Insulator)

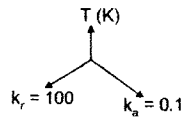
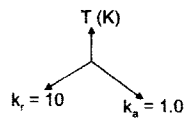
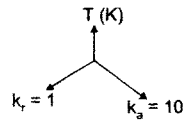
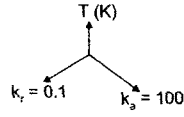


Case14: Thin-ortho-coat-r-summary plots
 Coating = iso_6 (Conductor)

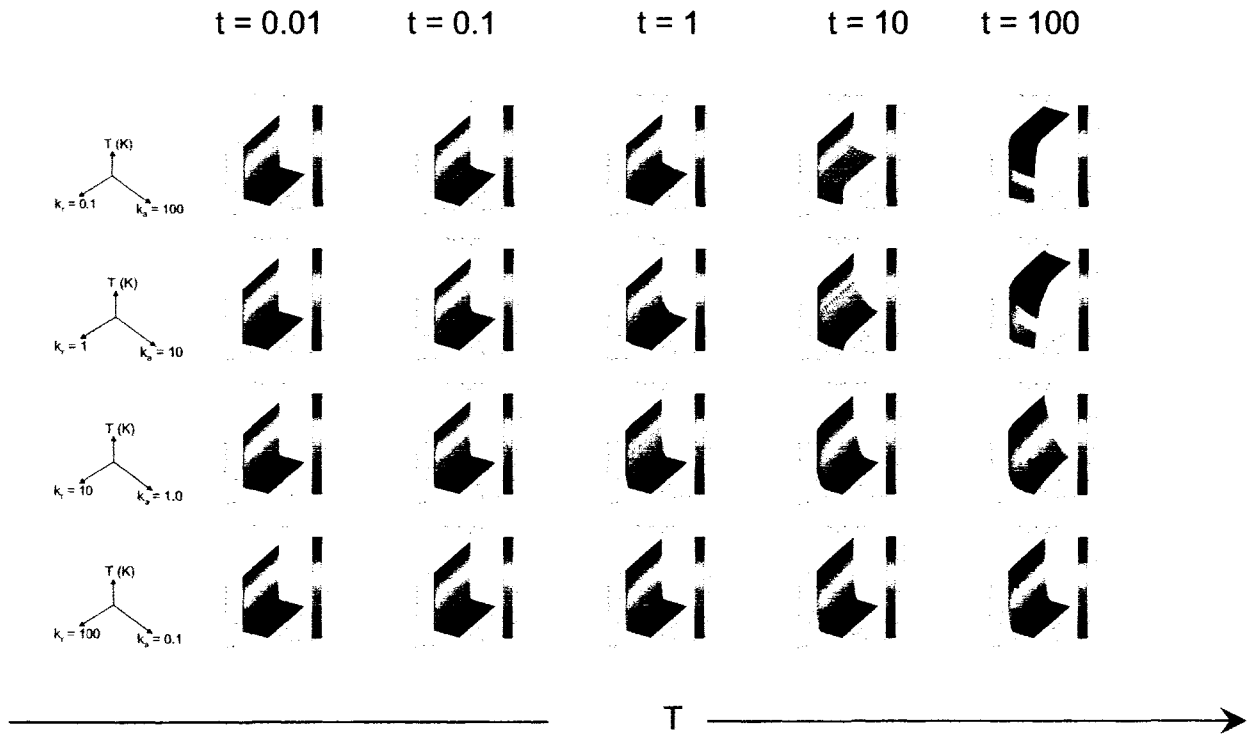
t = 0.01

t = 0.1

t = 1



Case 16: Thick-ortho-coat-r-summary plots
 Coating = iso_2 (Insulator)



Case 16: Thick-ortho-coat-r-summary plots
 Coating = iso_6 (Conductor)

